Experiments in single molecule localization microscopy: Towards detecting single molecules using incoherent digital holography

by

Abhijit Marar

(Under the Direction of Peter Alexander Kner)

Abstract

Holography was invented by Dennis Gabor in 1948 for which he was awarded the Nobel Prize in Physics in 1971. A hologram (portmanteau of the Greek words 'holos' meaning whole, and 'gramma', meaning record) is a physical recording of an interference pattern which retains the phase information of a three-dimensional (3D) object, and thus its depth information. The interference pattern is usually obtained by combining an object wave and a reference wave which are mutually coherent (i.e. the waves coming from various points of the object are statistically correlated). However, most of the imaging performed in biological research uses fluorescent light which is inherently incoherent. Creating holograms with incoherent light relies on the principle of self-interference of light, where beams originating from the same point source are interfered with each other since they are mutually coherent. This technique of interfering incoherent light with itself to create holograms is called self-interference digital holography (SIDH). SIDH has been used for imaging biological samples, however it has been limited to very bright samples.

In this dissertation we explore the possibility of using SIDH in low-light conditions, particularly to detect single molecules used in single molecule localization microscopy (SMLM). We demonstrate the application of SIDH to localize the position of point-like single emitters with high precision over large axial ranges. We describe the development of a novel 3D imaging system that uses incoherent digital holography to image single emitters under low-light conditions over a large axial range. We demonstrate SIDH of particles emitting $\approx$ 50,000 photons over a 20 μm axial range, and show that particles emitting as few as 10,000 detected photons can be localized. Here we detect 0.2 photons per pixel, below the quantum level of visibility. To benchmark digital holography as a 3D imaging technique, we derive the theoretical limit of localization precision and compare the calculated precision to the 3D single molecule localization precision of different Point Spread Functions.

Index words: Fluorescence microscopy, Super-resolution microscopy, Single molecule localization microscopy, Incoherent digital holography, Self-interference digital holography, Light-sheet microscopy

Experiments in single molecule localization microscopy: Towards detecting single molecules using incoherent digital holography

by

Abhijit Marar

B.S., University of Illinois at Urbana-Champaign, 2013
M.Sc., Ruperto-Carola University of Heidelberg, Germany, 2015

A Dissertation Submitted to the Graduate Faculty of the
University of Georgia in Partial Fulfillment of the Requirements for the Degree.

Doctor of Philosophy

Athens, Georgia

2020

Experiments in single molecule localization microscopy: Towards detecting single molecules using incoherent digital holography

by

Abhijit Marar

Major Professor:	Peter A. Kner
Committee:	Mable P. Fok
	Luke J. Mortensen
	Rabindranath De La Fuente

Electronic Version Approved:

Ron Walcott
Dean of the Graduate School
The University of Georgia
December 2020

CONTENTS

List of Figures

CHAPTER 1

INTRODUCTION

Every development in the history of the microscope can be attributed to humanity's intellectual goal to see better (higher magnification, better contrast, enhanced resolution), faster and deeper, in particular, the biological world. The original inventor of the microscope remains questionable; however, credit is generally given to Hans Janssen (1534-1592), Zaccharias Janssen (1587-1638) and Hans Lippershey (1570-1619), three Dutch spectacle makers who, around the turn of the 17th century, placed two lenses in a tube and observed the image was magnified. In 1661, Marcello Malpighi (1628-1694) published the *De Pulmonibus Observatones Anatomicae*, where he studied the dried lung of a frog and observed the traces of blood that marked the vessels (Castiglioni, 1947). Malpighi's discovery of capillaries was the first time the microscope was used for a genuinely scientific purpose. Despite earlier microscopic observations and discoveries, it was not until 1665 when Robert Hooke (1635-1703) published *Micrographia* (Hooke, 1665), that the importance of the microscope was significantly increased. Using his compound microscope and an oil lamp as a light source, Hooke observed everything from lice to weeds. He observed the eye and the morphology of the common fly while also describing the fruiting structure of molds. Hooke's most famous microscopical observation was his study of small openings in thin slices of cork tissue. It is to these small openings in the cork that he attached the term *cell* for the first time. In his book, Hooke importantly noted that the single-lens microscope; which was heavily used by his contemporary Antonie van Leeuwenhoek (1632-1723) to observe single bacterial cells and other microorganisms, provided images of superior quality compared to the compound microscope. The superior image quality of the single-lens microscope was because of its lower susceptibility to optical aberrations. The direct observation of the microscopic world enabled the possibility to study life at small scales and established microscopy as an essential tool in the life sciences. Over the next several decades, many significant advances were made in physics, specifically optics and glass chemistry and manufacturing that helped the compound microscope to attain the look of the modern optical microscope.

1.1 The diffraction limit

DIFFRACTION   In 1828, John Herschel in his article on light for the *Encyclopedia Metropolitana* had, for the first time, described the appearance of a bright star under high magnification as a perfectly round disk (Herschel, 1828) instead of a well-focused point. He comments as follows:

"...the star is then seen (in favourable circumstances of tranquil atmosphere, uniform temperature, etc.) as a perfectly round, well-defined planetary disc, surrounded by two, three, or more alternately dark and bright rings, which, if examined attentively, are seen to be slightly coloured at their borders. They succeed each other nearly at equal intervals round the central disc...."

Herschel's observation was provided with a complete theoretical explanation by George B. Airy in 1835. In his article in the Transactions of the Cambridge Philosophical Society, he concluded that the best-focused spot of light that was attainable with a perfect lens with a circular aperture was limited by the diffraction of light (Airy, 1835). The pattern that was described by Herschel and later explained in detail by Airy is called the Airy pattern, and the bright central spot (*"well-defined planetary disc"*) in the center is called the Airy disk.

The Airy pattern is not only seen in astronomy but also microscopy and can be best understood by examining a point-like source emitter that is brought to focus in a microscope. As light from the source emitter passes through the microscope

1. Only a portion of the wavefront propagates after interaction with every element due to their finite size.

2. The light bends at the edges of the encountered optical elements due to the finite size of the apertures and limited collection angle.

This bending of light when it passes through an aperture of finite size is called diffraction. Diffraction effectively increases the area over which the rays can intersect each other and interfere constructively to form an image, consequently degrading the image of the point-source to take the form of an Airy pattern instead of being focused to a point. The image of a point-source in 3D formed by an optical system is called the point-spread function (PSF) of the optical system and serves as the *signature* of the optical system. Such behavior of an optical system to broaden the image of the object under consideration has direct consequences on the resolving power of a microscope. Instead of looking at a point-source, if we were to now look at a continuous object tagged with multiple point-sources (e.g., fluorescently labeled antibodies) as is commonly done in fluorescence microscopy, the broadened images (i.e., the PSF of every single point-source) would overlap and blur the image of the continuous object.

ABBE'S LIMIT   Although the effects of diffraction and its implications for resolution were known for a while; it was not until later that it was discussed in detail. In 1869, Émile Verdet was possibly the first person to explicitly mention that telescopes were limited in their resolution by diffraction (Verdet, 1869). Verdet derived the resolution limit for telescopes in terms of the viewing angle and the
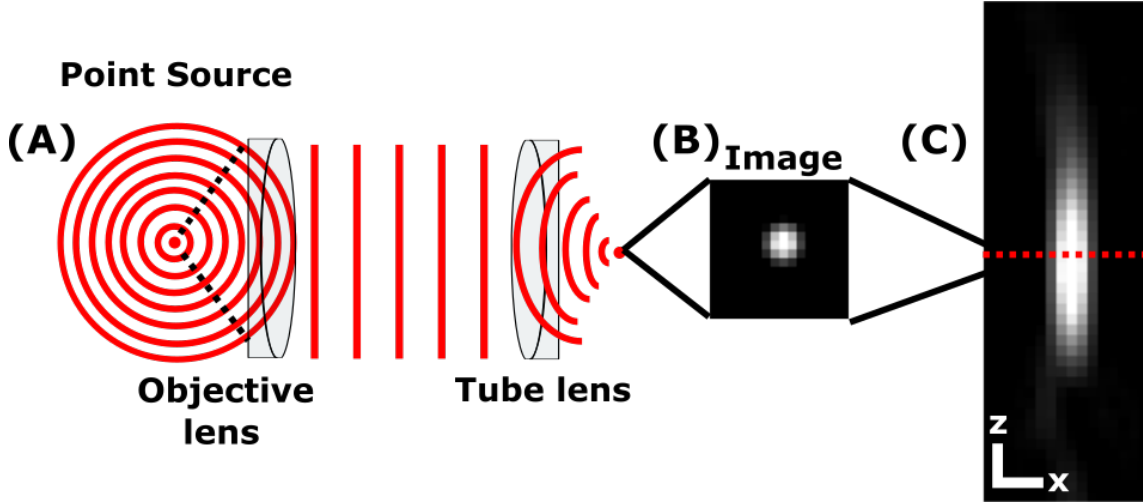
Figure 1.1: **Diffraction and point-spread function.** a) Only a portion of the total wavefront emitted by a source propagates through the microscope due to the finite extent of the components. This causes the image of a point formed by the microscope to be broader than the source. b) The image of a point source is described by the Point-Spread function (PSF). Imaged onto the camera, it appears as a pixelated Gaussian. c) The 3D PSF is extended along the axial direction and occupies a much larger area than it does in the lateral direction.

lens diameter. For a circular aperture, Verdet found that $\sin \omega = 0.819\lambda/R$, where ω denotes the viewing angle of the first bright ring, λ denotes the wavelength of light used and R denotes the radius of the aperture. He considered the resolution limit to be $1/2(\omega)$.

The resolution limit for an optical microscope was for the first time extensively discussed by Ernst Abbe in 1873. In this work, Abbe explicitly states the resolution limit of microscopic images to be half the wavelength of blue light (Abbe, 1873). Based on the diffraction of (coherent) light through a grating and its subsequent imaging through a microscope, Abbe described in words his famous formula:

$$d_{Abbe(xy)} = \frac{\lambda}{2\, n sin(\alpha)} \tag{1.1}$$

where $d_{Abbe(xy)}$ is the minimal resolvable distance in the lateral dimension (xy), λ is the wavelength of light used to view the sample, n is the refractive index between the sample and the objective lens, and α is the half-angle of the microscope's objective. The product of the refractive index and the sine of α is more commonly called the numerical aperture (NA): NA = $n sin(\alpha)$.

In his article, Abbe envisioned the microscopic object as a diffraction grating. When the illuminating light passes through the object (i.e., the diffraction grating), the light diffracts at every groove of the grating and travels in different directions. At each groove, the light can be thought of as a spherical wave propagating beyond the grating (Huygens-Fresnel principle). The spherical waves originating

from each groove differ only in their phase and therefore interfere constructively and destructively at a particular distance away from the grating, thus forming an image. Abbe concluded that the image of each groove on the grating could be resolved only if a sufficient number of diffraction orders (0th and 1st) pass through the finite-sized back-aperture of the microscope objective. It was not until later that Abbe realized that his theory also applied to self-luminous objects (e.g., fluorescent nano-particles) (Abbe, 1880).

Detailed experimental tests of Abbe's theory can be found in an article published by J.W. Stephenson in 1877 (Stephenson, 1877).

RAYLEIGH'S CRITERION   Almost two decades after Abbe's seminal work was published, Lord Rayleigh in 1896, published an article extensively discussing the resolution of microscopes (Rayleigh, 1896). In his article, Lord Rayleigh discussed both illuminated objects as well as self-luminous objects while extending his investigations to different objects. Rayleigh examined two point-sources close to each other and defined a criterion - called the Rayleigh criterion - for the minimal distance between them at which their images (PSF's) can still be discriminated. Since the PSF of an optical system takes the form of an Airy pattern as mentioned above, the Rayleigh criterion is based on the mathematical expression of the Airy pattern. According to the criterion, the two sources are only discernible if the distance in between them is greater than the distance between the maximum intensity of the Airy pattern and the first minimum, leading to:

$$d_{Rayleigh} = \frac{0.61\,\lambda}{NA} \qquad (1.2)$$

where λ is the wavelength of light used to view the sample, and NA is the numerical aperture of the objective lens. Rayleigh's criterion holds well for the human eyes but is not necessarily true for detectors that are very sensitive to small intensity variations such as modern cameras. Over the years, several other criteria have been introduced (e.g., the Sparrow criterion) to overcome such bottlenecks; however, the values of the resolution limit remain close to each other.

DIFFRACTION LIMIT IN Z   In the axial (z) dimension, the Airy disk forms an elliptical pattern, thus making the axial resolution worse than the lateral resolution. The elongated geometry of the PSF along the axial dimension arises from the nature of the non-symmetrical wavefront that emerges from the microscope objective. The Abbe diffraction limit in the axial dimension is given by

$$d_{Abbe(z)} = \frac{2\,\lambda}{NA^2} \qquad (1.3)$$

It can be seen from Eq. 1.3, that the dependency of the z resolution on the numerical aperture (NA) is squared. For instance, using a 100x objective of NA = 1.4 and green light (550 nm), the lateral resolution of an optical microscope is limited to 200 nm whereas the axial resolution limit is on the order of 500 nm.

In this chapter I will introduce the different microscopy techniques that have been developed to image at resolutions beyond the diffraction limit. I introduce the concept of fluorescence and how it is used in optical microscopy. I briefly discuss different super-resolution techniques used with fluorescence microscopy. Furthermore, I talk about the practical details that need to be considered when performing super-resolution imaging using single molecule localization microscopy (SMLM).

1.2 Beyond the diffraction barrier

Over the years several efforts were made to circumvent the resolution limit. It is apparent from the criteria mentioned earlier that the size of the PSF can be decreased (in effect reducing the resolution limit) by either increasing the NA of the objective lens or decreasing the wavelength of light used for imaging. The NA of a single objective lens, however, cannot be increased infinitely primarily due to the physical limitation of the angle of the cone of light that the objective can capture (i.e., For an objective lens with an NA of 1.4, the collection angle is already $\sim 70°$). High NA objectives have the added disadvantage that the spherical aberration; usually caused by refractive index mismatch between the sample medium and the immersion medium, is more severe as it scales with the NA of the objective lens. The other approach to reduce the size of the PSF involves abandoning the visible spectrum of light altogether. This approach has been successfully demonstrated in UV (Brand et al., 1997) and X-ray microscopy (Kirz et al., 1995; Miao et al., 2008). Although these techniques have been shown to achieve higher-resolution, the optical setups involved in these techniques are highly complex, and the use of such low wavelengths do not allow for the imaging of living samples due to the harmful effects of the high-energy radiation. Electron microscopy (Ruska, 1934, 1987) is another such technique that takes advantage of the reduction in wavelength to improve the resolution limit. Electron microscopes provide resolution in the angstrom regime by using electrons with very short de Broglie wavelength; however, they can be used for imaging only thin samples or surfaces. Furthermore, the sample is required to be placed in a vacuum chamber, thus making it impossible to image under physiological conditions.

Although light microscopy forces us to work in a particular wavelength regime (450-680 nm), the vast array of highly specific markers available for the study of various cellular processes, and versatility in sample preparation protocols makes light microscopy a very attractive tool for studying biological specimens under physiological conditions. A myriad of techniques have, therefore, been developed to shift and break the diffraction barrier using light in the visible wavelength (S. W. Hell, 2007; B. Huang et al., 2010; B. Huang et al., 2009; Wu & Shroff, 2018).

CONFOCAL MICROSCOPY Among far-field fluorescence microscopy techniques, the confocal microscope (Davidovits & Egger, 1969; Marvin, 1961) is one of the most widely used tools in the life sciences (Pawley, 2010). Unlike a wide-field microscope, where the entire sample is illuminated at once, a confocal microscope focuses the laser light onto a small part of the sample which is then scanned across the entire area of the biological specimen to produce an image. In addition, the light emitted from the focused part of the sample is imaged onto a pinhole which rejects the out-of-focus

light from the sample, at the expense of collected intensity. The combination of a focused laser for excitation and a pinhole for detection allows for a $\sqrt{2}$ improvement in the lateral resolution (Wilson, 2011). However, since confocal microscopy requires scanning the sample to form an image (as opposed to wide-field microscopy, where the entire image of the sample captured in a single exposure), the image acquisition is slower. Furthermore, practical limits to the size of the pinhole and low light level makes it challenging to achieve the theoretical resolution enhancement (G. Cox & Sheppard, 2004). Therefore, instead of improving the resolution, the main advantage of confocal microscopy over wide-field microscopy is the reduction of the out-of-focus fluorescence background, thereby enabling optical sectioning in 3D imaging (Wilson, 1989).

MULTIPHOTON MICROSCOPY   Another promising approach considered to extend the diffraction limit was multiphoton microscopy (Denk et al., 1990; Zipfel et al., 2003). In multiphoton microscopy, the effective size of the excitation PSF can be decreased by exploiting the non-linear absorption processes at longer wavelengths. However, this reduction in the PSF size is offset by the increased wavelength of the excitation light. Although the theoretically calculated resolution of a multiphoton microscope does not surpass that of a confocal microscope (Gu & Sheppard, 1995), it provides excellent optical sectioning (Zipfel et al., 2003) and improved imaging depth due to the decreased scattering occurring at longer wavelengths.

MICROSCOPY USING OPPOSING OBJECTIVES   Both confocal and multiphoton microscopy reduce the effective size of the PSF; however, the resolution improvement is restricted to the lateral dimension. In the axial dimension, the PSF remains elongated and occupies a larger area compared to the lateral dimension. The elongated shape of the PSF in the axial dimension is due to the fact that even though, the light emitted from a point-like emitter radiates outward in all directions, the microscope objective collects light only from one side of the emitter. The collection of light through an objective from only one side of a sample results in a large amount of information loss, in effect leading to a PSF that is elongated in the axial direction. As described earlier, the Abbe limit in z varies inversely with the square of the NA (i.e., the amount of light collected). Although the NA of a single objective lens cannot be increased indefinitely, the effective NA of an optical system can be increased by collecting more light from the sample. This increment in the collected light can be brought about by imaging the sample using two opposing objectives which would collect light from the full spherical angle around the sample, thereby reducing the axial size of the PSF substantially. The first manifestation of this idea called 4Pi-microscopy (S. Hell & Stelzer, 1992) was implemented on a confocal microscope with the use of two-photon excitation. The resolution can be further improved by focusing the illumination spot of the confocal microscope using both objectives at the same time. By using the interference between the two illumination spots, a more spherical illumination spot can be created, which further decreases the effective size of the PSF. The idea of using two opposing objectives has also been demonstrated on a wide-field microscope (Bailey et al., 1993; M. G. Gustafsson et al., 1995, 1996, 1999). In this case, the interference between the two illumination beams creates an intensity pattern across the axial direction, which in turn extends the bandwidth of the microscope.

Both, 4Pi-microscopy and I⁵M have been able to achieve an axial resolution of $\sim$ 100nm which is a significant improvement over the wide-field axial resolution.

STRUCTURED ILLUMINATION MICROSCOPY (SIM)   Another technique used to extend the diffraction barrier relies on illuminating the sample with patterned or structured light. This technique exploits the fact that when a sample is illuminated with structured light, the spatial frequencies of the illumination pattern mix with those of the sample and shift the high-frequency information (i.e., high-resolution details of the sample) within the optical bandpass of the objective lens. This phenomenon manifests itself in the form of Moiré Fringes (Amidror, 2009; Oster & Nishijima, 1963), due to which the high-frequency information from the sample that was unable to pass through the objective is now detectable and can be extracted and computationally treated, leading to an image with enhanced information content in real space. The principle of using patterned illumination to increase the axial resolution of microscopes was first shown using two objectives as mentioned above in what is called standing wave microscopy (Bailey et al., 1993; Bailey et al., 1994). Structured illumination has also been used to provide optical sectioning using a 2D grid pattern (M. Neil et al., 1998; M. A. Neil et al., 1997). Furthermore, in addition to improved axial resolution and optical sectioning, periodic illumination patterns can be created in the lateral direction (Frohn et al., 2000; M. G. Gustafsson, 2000; Heintzmann & Cremer, 1999) and in both directions (M. G. Gustafsson et al., 2008), thereby enhancing the resolution by a factor of two. Because the illumination pattern is projected through the objective lens, it is also limited by the diffraction of light. Therefore, the resolution enhancement in SIM is limited to a two-fold improvement. Using SIM for biological imaging, a resolution of $\sim$ 100 nm in the lateral dimensions (M. G. Gustafsson, 2000) and $\sim$ 300 nm in the axial dimension (M. G. Gustafsson et al., 2008; Schermelleh et al., 2008) has been achieved.

The methods mentioned above have proved that it is possible to image below the diffraction barrier using wavelengths from the visible spectrum of light. The advantage of these purely optical techniques is that they do not rely on the properties of the fluorescent labels and can be performed with virtually any fluorescent probe. It can be seen that by combining I⁵M and SIM, one can produce an isotropic PSF which would result in an image with $\sim$ 100 nm resolution in all three dimensions. This concept has been successfully demonstrated in a technique dubbed I⁵S (Shao et al., 2008). Although the resolution enhancement using the aforementioned techniques shows a significant improvement, these techniques merely shift the diffraction barrier instead of breaking it. The resolution limit in these techniques, albeit lower, continues to be governed by the diffraction of light.

BREAKING THE DIFFRACTION BARRIER   It has been argued that in order to fundamentally overcome the Abbe limit and break the diffraction barrier, a microscopy method must have the potential to achieve infinite resolution (S. W. Hell, 2003). Edward Synge, in 1928, published the first paper challenging the diffraction barrier and theorized a resolution well below the diffraction limit (Synge, 1928). His idea has since been come to be known as scanning near-field optical microscopy (SNOM/NSOM). The method proposed the use of a sub-diffraction aperture to image the surface of a sample using visible light. However, Synge' idea was not practically realized until 1972 when

Ash and Nichols demonstrated a resolution of $\lambda/60$ in a scanning near-field microwave microscope using 3 cm radiation (Ash & Nicholls, 1972). In 1984, two groups, independently, further refined the microscope developed by Ash and Nichols, achieving sub-100 nm resolution (Lewis et al., 1984; Pohl et al., 1984). SNOM circumvents the diffraction limit by ensuring that the size of the aperture and the distance between the size and the aperture are less than the wavelength of light used for imaging. The aperture or probe can be used for either exciting the sample with evanescent waves or to collect them or both. Evanescent or non-propagating fields exist only near the surface of the object and carry the high-frequency (high-resolution) information about the object, thereby leading to an improved resolution which is limited only by the dimensions of the aperture and the sample-to-aperture distance. Because SNOM is a near-field technique, the aperture is required to be positioned very close (10-100 nm) away from the surface of the sample and does not allow probing the specimen in 3D making it a surface scanning technique. A multitude of non-optical surface scanning techniques have been developed over the years (Binnig et al., 1986; Binnig & Rohrer, 1983; Hansma et al., 1989; Hayazawa et al., 2000; Stöckle et al., 2000) to facilitate high resolution imaging. Most of these techniques are used for imaging surfaces; however, some have been demonstrated to achieve molecular resolution on biological samples (Müller et al., 2009).

HYPERLENSES   Another near-field approach that promises to enhance the optical resolution makes the use of hyperlenses (Veselago, 1968). A hyperlens is an anisotropic lens consisting of negative refractive index materials (Pendry, 2000; Veselago, 1967). When placed close to the sample, the hyperlens converts evanescent waves into propagating waves, which can then be imaged in the far-field (Z. Liu et al., 2007). However, hyperlenses also need to be placed very close to the sample even if their image can be magnified in the far field.

To overcome these shortcomings, several far-field methods have been developed to break the diffraction barrier. Far-field imaging techniques are most desirable for imaging objects that contain fine structures, but are large compared to the wavelength of light used to illuminate the sample. Biological samples fall in this category of objects since they span across various size scales but contain features that scale in the molecular regime. These methods can be divided into two types of approaches: the deterministic approaches such as stimulated emission depletion (STED) microscopy (S. W. Hell & Wichmann, 1994; Klar & Hell, 1999), saturated structured illumination microscopy (SSIM, M. G. Gustafsson, 2005; Heintzmann et al., 2002), etc. and the stochastic approaches such as single-molecule localization microscopy (SMLM, Betzig et al., 2006; Hess et al., 2006; Rust et al., 2006) and super-resolution optical functional imaging (SOFI, Dertinger et al., 2009). These far-field super-resolution techniques, in addition to complex optics, take into consideration the photophysics (or photochemistry) of the fluorescent molecules that label the sample. Therefore, further discussion of these techniques warrants a discussion on fluorescence microscopy.
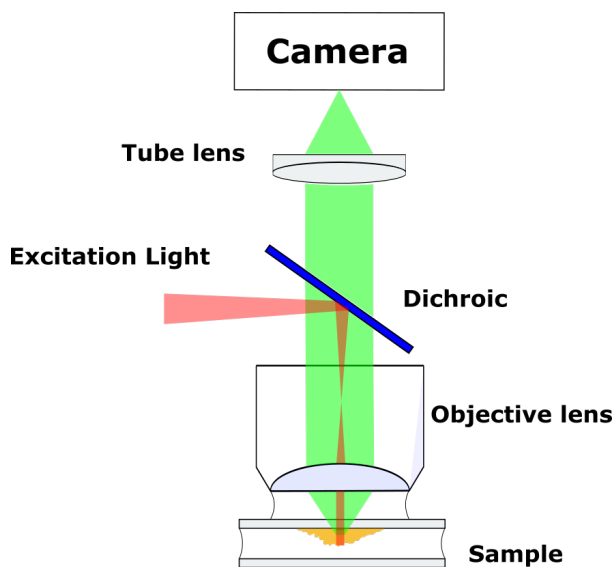
Figure 1.2: **Diagram of a Fluorescence Microscope.** The Dichroic mirror in a fluorescence microscope separates the excitation light from the light emitted from the sample which is imaged onto the camera.

1.3 Fluorescence microscopy

FLUORESCENCE Fluorescence was first observed by John Herschel in 1845 when he saw that quinine; which is present in tonic water, emits blue light after absorbing ultraviolet light from the sun (Herschel, 1845). Although inexplicable at the time, Herschel reported the unusual phenomenon in his article to the Philosophical Transactions of the Royal Society of London. In his report, he comments:

"The sulphate of quinine is well known to be of extremely sparing solubility in water. It is however easily and copiously soluble in tartaric acid. Equal weights of the sulphate and of crystallised tartaric acid, rubbed up together with addition of a very little water, dissolve entirely and immediately. It is this solution, largely diluted, which exhibits the optical phenomenon in question. Though perfectly transparent and colourless when held between the eye and the light, or a white object, it yet exhibits in certain aspects, and under certain incidences of the light, an extremely vivid and beautiful celestial blue colour...."

In 1852, George Stokes published an article reporting detailed experimental studies of organic (including quinine) and inorganic samples, clearly identifying a phenomenon he called dispersive reflection (Stokes, 1852). In his article, Stokes importantly noted that the wavelength of the dispersed light was always longer than the wavelength of the original light; an observation which later came to be known as *Stokes Law*. When moving a solution of quinine through a solar spectrum, Stokes noticed that the

solution of quinine remained invisible while passing through all the colors, except beyond the violet portion of the spectrum. He comments:

"It was certainly a curious sight to see the tube instantaneously light up when plunged into the invisible rays: it was literally darkness visible. Altogether the phenomenon had something of an unearthly appearance."

Stokes also noted that light dispersed from the fluid in all directions as if it were self-luminous. Although he originally called the phenomenon true dispersive reflection in the paper, he wrote in a footnote:

"I confess I do not like this term. I am almost inclined to coin a word, and call the appearance fluorescence, from fluorspar, as the analogous term opalescence is derived from the name of a mineral."

Stokes Law turns out to be quite convenient for optical microscopy since it enables the separation of the excitation light (i.e., light used to illuminate the sample) from the weak fluorescence light (i.e., light being emitted by the sample), thereby reducing the background and improving image contrast. In a modern epi-fluorescence microscope, this is achieved with the help of a dichroic mirror, which was first developed by Evgenii Brumberg (Brumberg, 1959) for ultraviolet (UV) light and later refined by Johann Sebastiaan Ploem (Ploem, 1967) for light in the visible spectrum. Ploem later went on to collaborate with the Ernst Leitz company to construct the first inverted microscope with epi-illumination combined with optical filters and the dichroic mirror in a single unit (the filter cube).

Since its early development, fluorescence microscopy has been closely related to the field of fluorescent labeling. The observed autofluorescence from a sample is often weak and results in reduced image contrast. The field of Immunofluorescence was first conceptualized in 1941 (Coons et al., 1941) and subsequently demonstrated experimentally (Coons & Kaplan, 1950) by labeling antibodies with a fluorophore and binding them to their antigen. This technique resulted in the highly specific fluorescent staining of the biological specimen (due to antigen-antibody specificity).

In 1962, Osamo Shimomura discovered the green fluorescent protein (GFP) while purifying the bioluminescent protein aequorin from the jellyfish *Aequoria victoria* (Shimomura et al., 1962). This was followed by extensive cloning in the following decades paving the way for experiments to assess its utility as an in vivo tag for proteins. Almost three decades after Shimomura's discovery, it was shown that GFP could fluoresce when expressed in bacteria and worm cells (Chalfie et al., 1994). This development was instantly recognized as a significant breakthrough in cell biology. Soon after that, several efforts were made to improve the spectral and fluorescent characteristics over the wild-type GFP and developed mutations with different excitation and emission spectra throughout the visible spectra (Heim & Tsien, 1996; Tsien, 1998). The ongoing development of fluorescent molecules with distinct excitation/emission spectra and improved brightness and photostability (Dempsey et al., 2009; Dempsey et al., 2011) have made fluorescence microscopy a mainstay of biological and biomedical laboratories.

STATE TRANSITIONS IN A SINGLE MOLECULE   In a quantum mechanical description, a molecule is characterized by different energy bands. These energy bands correspond to electronic, vibrational, and rotational states. The configuration of the energy levels and energy differences depends
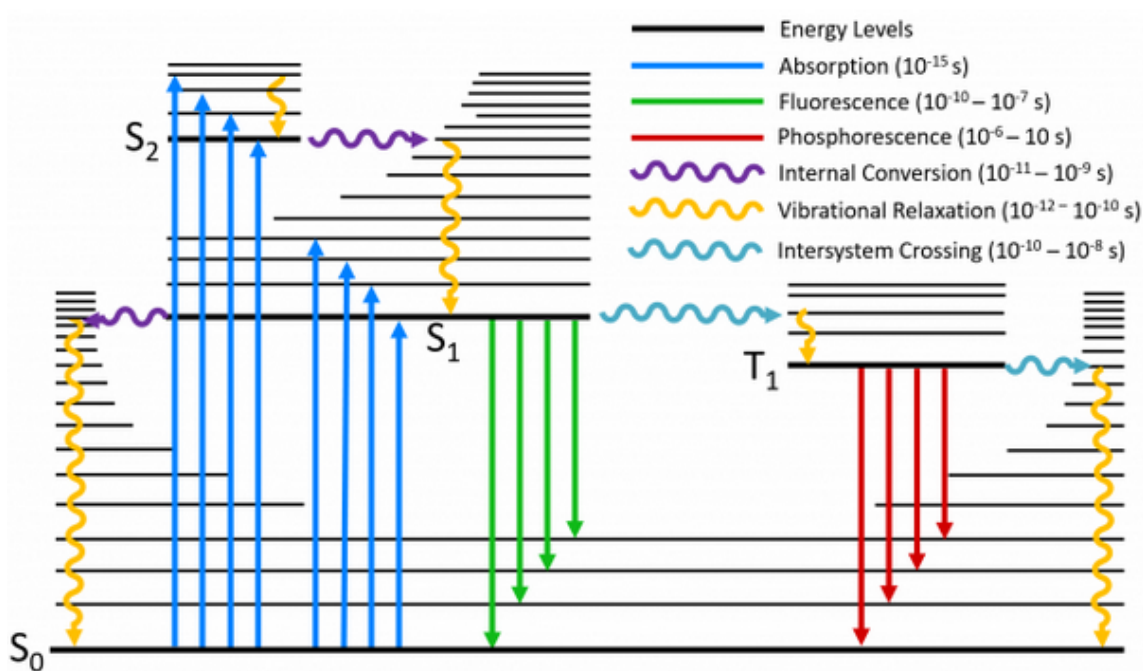
Figure 1.3: **Jablonski diagram depicting molecular energy levels and transitions.** A thermally stable molecule goes to the excited state (S_1/S_2) upon absorbing a photon with energy equal to the energy bandgap. From the excited state the molecule can undergo vibrational relaxation (VR), and either fluoresce or undergo non-radiative relaxation after internal conversion. There is also a non-zero probability for the fluorophore to experience intersystem crossing into a dark triplet state (T_1) and subsequently return to the ground state via phosphorescence or non-radiative relaxation. Additional higher energy states are not shown. Reprinted from https://www.edinst.com/blog/jablonski-diagram/.

on the structure of the molecule. When a substance emits light, it is called luminescence, and this occurs due to the relaxation of an electronically excited molecule. Luminescence can further be divided into two groups: fluorescence and phosphorescence, depending on the nature of the excited state. Both these processes can be best understood by looking at a three-state system consisting of a singlet ground state S_0, singlet excited state S_1 and a triplet state T_1 using a Jablonksi diagram (Jabłoński, 1935) as shown in Fig. 1.3. At each of these electronic energy levels, the electrons can exist in a number of vibrational energy levels. In a thermally stable molecule, both the electrons reside in the ground state and have opposite spins. For a molecule to generate luminescence, it must absorb energy (radiation) equal to the band gap between the ground state and the excited state. Following light absorption, an electron is excited to one of the higher vibrational levels in the excited energy state S_1. When the molecule is in this phase, it rapidly relaxes (non-radiatively) to the lowest vibrational level of S_1. This

process is called *vibrational relaxation* (or *internal conversion* when the transition occurs between vibrational states of two different electronics states due to overlap between the states) and typically occurs within 10^{-12} s or less. Since the electron in the singlet excite state S_1 is paired (by opposite spin) to the electron in the ground state S_0, the transition $S_1 \rightarrow S_0$ is spin allowed and occurs rapidly with the emission of a red-shifted photon (radiative relaxation), thereby entering a vibrationally excited state of S_0. Finally, the electron relaxes quickly into the vibrational ground state of S_0. The emission of a light caused due to the transition from $S_1 \rightarrow S_0$ is called fluorescence and has lifetimes typically near 10^{-8} s.

The process of fluorescence in a molecule competes with non-radiative relaxation (i.e., vibrations or collisions). For a molecule to fluoresce efficiently, it is necessary that its ground state S_0 has a low density of vibrational states at the S_1 energy level. This reduces the chances of non-radiative decay through the S_0 vibrational manifold. The radiative quantum yield of a molecule q_r is given by

$$q_r = \frac{k_r}{k_r + k_{nr}} \tag{1.4}$$

where k_r is the radiative decay rate and k_{nr} is the non-radiative decay rate.

If the torque acting on the spin of the electron in the S_1 state is non-zero, then the electron can undergo a spin conversion to the first triplet state T_1. This process is called *intersystem crossing*. Since the electron in the triplet state T_1 has the same spin orientation as the ground-state electron, the transition $T_1 \rightarrow S_0$ is forbidden and takes place over a much longer lifetime (milliseconds to seconds). Emission due to radiative relaxation from T_1 is termed *phosphorescence*, and is generally shifted to longer wavelengths (lower energy) relative to fluorescence. Accordingly the radiative quantum yield for this process is given by

$$q_r = \frac{k_r}{k_r + k_{nr} + k_{isc}} \tag{1.5}$$

where k_r is the radiative decay rate and k_{nr} is the non-radiative decay rate and k_{isc} is the intersystem crossing rate constant. The rate constants for triplet emission are several orders of magnitude smaller than those for fluorescence and thus the decay from $T_1 \rightarrow S_0$ is usually non-radiative. Repeated entry into and exit from the triplet state T_1 appears as blinking of the fluorescent molecule. Blinking can also be observed on longer timescales due to molecular interactions with oxidants and reductants used in blink microscopy (Cordes et al., 2009; Duim et al., 2011; van de Linde et al., 2008; Vogelsang et al., 2009).

When an electron undergoes intersystem crossing, the fluorescent molecule is turned off and is in its dark state. However, this removal is transient and lasts only the duration of the triplet state lifetime. Eventually, all molecules completely cease to fluoresce because the electron has been permanently removed from its singlet manifold. This is typically due to the cleaving of covalent bonds or non-specific reaction between the fluorescent molecule and its surrounding environment (singlet oxygen). This process is called *photobleaching* and the number of excitation cycles to achieve full bleaching varies depending on the specific structure of the molecule. Photobleaching is especially a problem

in time-lapse microscopy as it complicates the observation of fluorescent molecules over extended periods.

1.4 Stimulated emission depletion microscopy
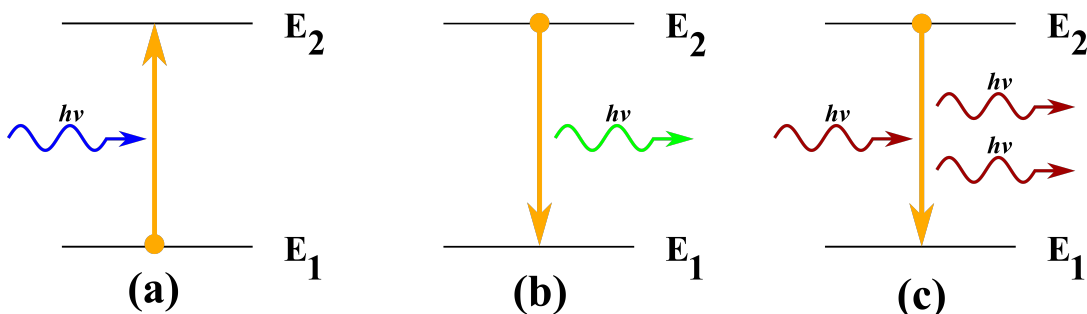
Figure 1.4: **Jablonski diagram of the molecular states and transitions involved in STED microscopy.** (a) The electron in a thermally stable fluorophore is excited from the ground state E_1 to the excited state E_2 by absorption of a photon of the excitation light. (b) Fluorescence: A red-shifted photon is emitted when the electron from the excited state E_2 transitions back down to the ground state E_1 forming an electron pair as described earlier. (c) Stimulated emission forces the transition from E_2 to E_1, thereby sending the fluorophore to the dark state. This transition can emit photons of a wavelength that is different from that of the fluorescent photons.

Stimulated emission depletion (STED) microscopy (S. W. Hell & Wichmann, 1994; Klar & Hell, 1999), like confocal microscopy, is a scanning technique that uses a second, red-shifted laser (STED beam/depletion beam/de-excitation beam) to suppress the fluorescence emission from the molecules located off the center of the excitation beam. This process effectively reduces the size of the effective PSF, thereby enhancing the resolution of the optical system. The suppression of the molecules into a non-fluorescing state is achieved by de-exciting the molecules via stimulated emission (Einstein, 1917; Kopfermann & Ladenburg, 1928; Maiman et al., 1961; Schawlow & Townes, 1958). The process of stimulated emission can be understood using a Jablonski diagram shown in Fig. 1.4. When the sample, is illuminated using the excitation laser, the fluorescent molecule is excited from the ground state S_0 to a higher vibrational state of S_1. The molecule then undergoes non-radiative relaxation to the lowest vibrational state of S_1 within picoseconds. At this point, if the molecule were to absorb another photon (STED beam) that matched the energy difference between S_0 and S_1, it would de-excite to the ground state S_0 while emitting a photon at the same wavelength as that of the absorbed photon (i.e., same wavelength as STED beam). Hence, the fluorophore is essentially confined to the ground state S_0, which is equivalent to switching off the fluorescing ability of the molecule (S. W. Hell et al., 2009). It is imperative that the wavelength of the STED beam is red-shifted relative to the emission spectrum of the fluorescing molecule for three reasons:

1. Stimulated emission will not occur if the de-excitation wavelength is near the absorption spectrum of the fluorescing molecule.

2. The excitation cross-section must be small at the de-excitation wavelength otherwise the experimenter risks exciting the molecule instead of only stimulating the $S_1 \to S_0$ transition.

3. The spontaneous and stimulated emissions can be spectrally separated by stimulating the $S_1 \to S_0$ transition at the red end of the emission spectrum.
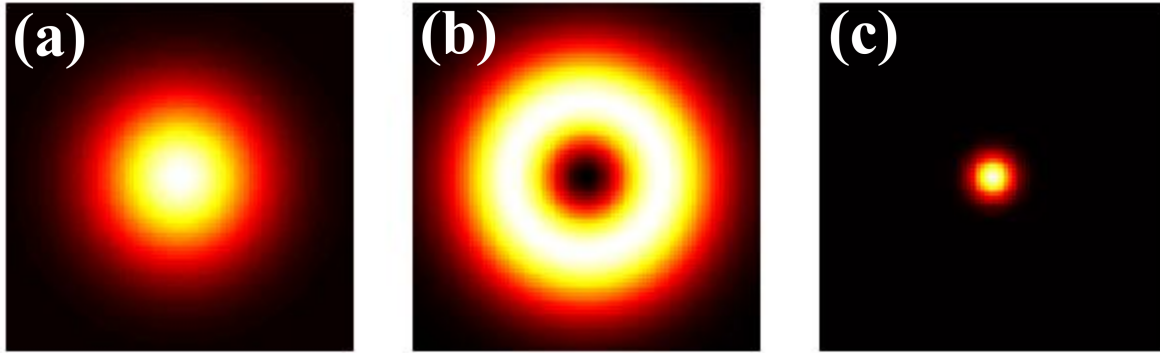
Figure 1.5: **Configuration of the two beams in a STED microscope.** Overlaying a Gaussian excitation focus (a) with a toroidal de-excitation focus (b) results in a small region of remaining fluorescence (c). This small region is the effective PSF (point spread function) of a STED microscope. Reprinted from Lagrue, 2014

The pattern of the STED beam is typically generated by placing a phase mask in the path of the laser used for the de-excitation of fluorescent molecules. The most commonly used shape of the STED beam (for both 2D and 3D imaging) is a toroid ("donut"). By superimposing a focused STED beam on the excitation beam, the fluorophores in the periphery of the excitation beam are switched off using stimulated emission leaving only the fluorophores in the very center (i.e., where the STED beam has zero-intensity) in a fluorescing state, therefore creating a 3D PSF that is smaller (size depends on the intensity of STED beam) than the PSF of a conventional widefield microscope (Klar et al., 2000). Fig. 1.5 illustrates the creation of an effectively smaller PSF using the donut beam. STED microscopy has been shown to achieve a lateral resolution of $\sim$ 30nm (Westphal & Hell, 2005). STED can also be employed in 4Pi microscopy (STED-4Pi), resulting in an axial resolution of 30-40 nm (Dyba & Hell, 2002). STED microscopy is the first far-field method to break the diffraction barrier as its resolution no longer depends on diffraction but the size of the zero-intensity volume of the toroidal beam. The size of the zero-intensity volume decreases with increasing intensity of the depletion beam, thereby decreasing the minimally resolvable distance. The resolution of the optical system, in this case, is given by

$$d_{min} \approx \frac{\lambda}{2\,NA\sqrt{1 + I/I_{sat}}} \tag{1.6}$$

where d_{min} is the full-width half max (FWHM) of the fluorescence intensity distribution in the area that remains fluorescing, λ is the wavelength of the light used to excite the sample, NA is the numerical aperture of the objective lens, I is the maximal intensity of the depletion laser and I_{sat} is the saturation intensity of the fluorescent molecule. The saturation intensity is a fluorophore-characteristic constant which depends on the absorption cross-section and fluorescent lifetime of the molecule. At the saturation intensity I_{sat}, half of the excited fluorescent molecules are forced to the ground state S_o by stimulated emission.

Since the resolution in STED microscopy is only limited by the power of the depletion beam, it is theoretically possible to achieve unlimited resolution. However, in order to achieve high resolutions ($d_{min} \leq 50$ nm), the intensity required from the depletion beam is sufficient to bleach the fluorophores (often > 1 GW/cm²) (Blom & Widengren, 2017). Furthermore, the strong power of the depletion beam results in phototoxicity induced in the sample when performing live-cell imaging. In order to address these issues, a more general scheme has been formalized with the name of RESOLFT (reversible saturable optical fluorescence transitions) microscopy (S. W. Hell, 2007). RESOLFT exploits the phenomenon of saturable depletion using photoswitchable fluorescent molecules to suppress the fluorescence at the periphery of the excitation spot. When the molecule is turned off by sending the electron to the triplet state, the technique is called ground-state depletion (GSD, Bretschneider et al., 2007; S. W. Hell & Kroug, 1995). RESOLFT has been demonstrated to achieve sub-100 nm resolution using photoswitchable proteins at low laser intensities (depletion laser intensity of $\sim$ 600 W/cm²) (Hofmann et al., 2005).

Because the excitation spot must be very small in order to attain high resolutions using STED, the time required to scan the entire sample increases as the required resolution increases owing to longer imaging times. However, like the confocal microscope, the speed can be optimized by limiting the imaging to the region of interest. Finally, it is essential to note that STED microscopes are complex instruments, partly due to the requirement of precise alignment of the two beams. This has limited the development of STED microscopy to specialized groups.

1.5 Saturated structured illumination microscopy

Like in RESOLFT, the concept of employing saturable processes can also be applied to structured illumination microscopy (SIM) to exploit the non-linear response of a fluorescent molecule to very high intensities of the structured excitation light. When the intensity of the excitation laser is very high, the molecule is immediately excited to the singlet state every time it returns to the ground state, thereby making the fluorescence lifetime the limiting factor of the fluorescence emission rate. Consequently, the fluorescent intensity of the fluorescent molecule is saturated and is no longer proportional to the excitation intensity. When the sample is illuminated with a sinusoidal pattern at very high intensities, the peaks of the sinusoidal pattern plateau, whereas fluorescence emission is still absent from the zero points of the excitation pattern. The 2D pattern at this point is no longer a perfect sinusoid and contains higher-order spatial frequencies. The overlaying of such an excitation pattern on the high

spatial frequencies of the sample effectively shift the high-resolution features of the sample into the bandpass of the microscope's objective. Similar to STED, the resolution now is no longer limited by diffraction but by the level of fluorescence saturation that can be practically achieved.

Saturated structured illumination microscopy (SSIM) was theoretically studied under the name of the saturated patterned excitation microscopy (SPEM, Heintzmann et al., 2002) and later experimentally demonstrated to achieve 50 nm resolution under the name of non-linear structured illumination microscopy (NL-SIM, M. G. Gustafsson, 2005). Although SSIM provides theoretically unlimited resolution, the requirement of strong saturation results in photobleaching and phototoxicity in the sample (Gur et al., 2011). These issues have been overcome by exploiting photoswitchable proteins (Li et al., 2015; Rego et al., 2012), making SSIM a viable option for sub-100 nm live-cell imaging. Reconstruction of images using SSIM requires more images, thus making it slower than linear-SIM. As in the case of STED, SIM microscopes require precise alignment and therefore require expert hands in the handling of the microscope and also the analysis after data collection.

1.6 Single-molecule localization microscopy

The idea of circumventing the diffraction limit by optically isolating individual molecules that label the sample was first theorized in 1985 (Burns et al., 1985), which was subsequently followed by a theoretical framework describing the process for single-molecule imaging (Betzig, 1995). Since the first single-molecules were detected optically almost three decades ago (Betzig & Chichester, 1993; W. Moerner & Basche, 1993; W. E. Moerner & Kador, 1989; Xie, 1996), it is now conventional to use single molecules in a variety of biophysical studies in the life sciences. In addition to imaging, single-molecules have been used in particle tracking experiments, making it possible to follow the trajectory of proteins (Sako et al., 2000) and determine their mode of motion (T. Schmidt et al., 1996) with nanometer accuracy. The basic principles and applications of single-molecule imaging and tracking have been the subject of many reviews (Baddeley & Bewersdorf, 2018; Manzo & Garcia-Parajo, 2015; Sauer & Heilemann, 2017; Shashkova & Leake, 2017; von Diezmann et al., 2017).

DETECTION AND LOCALIZATION OF SINGLE MOLECULES Fluorescence from single molecules can be detected by using the appropriate excitation sources and fluorescence filters with a wide-field microscope employing an objective lens and a sensitive electron-multiplying charge-coupled device (EMCCD) or scientific complementary metal-oxide-semiconductor (sCMOS) camera. The excitation source is used to pump up the molecule to the excited state. During the molecule's transition back to the ground state, a fluorescent photon is emitted, which is spectrally filtered using fluorescence filters. The fluorescent photon makes its way to the camera to generate electron-hole pairs in the electronic detector array. These electron-hole pairs are subsequently converted to digital counts by the camera's readout circuitry.

In high precision experiments, the most common models used to represent an isotropic point source (emitting light in all directions) are the Richard-Wolf model (Richards & Wolf, 1959) and the Gibson-Lanni model (Gibson & Lanni, 1992). These models are very accurate and account for

various factors that have to be considered namely the NA of the objective lens, materials that are placed between the sample and lens and the dipole moment of the light source. However, the mathematical formulations used in these models are complicated, and therefore the 2D PSF of the microscope (mathematically expressed as the Airy function) is often approximated with a Gaussian function

$$I(x, y) = I_0 \, exp\left(\frac{-(x - \theta_x)^2 - (y - \theta_y)^2}{2 \, w^2}\right) + bg \tag{1.7}$$

where I_0 is the amplitude of the Gaussian function, (θ_x, θ_y) is the center position of the Gaussian function, w is the standard deviation (width) of the Gaussian function and bg is the background offset in the image. Eq. 1.7, describes how the signal $I(x, y)$ on camera pixel (x, y) depends on the coordinates of the fluorophore (θ_x, θ_y), its peak intensity I_0 and the background in the experiment.
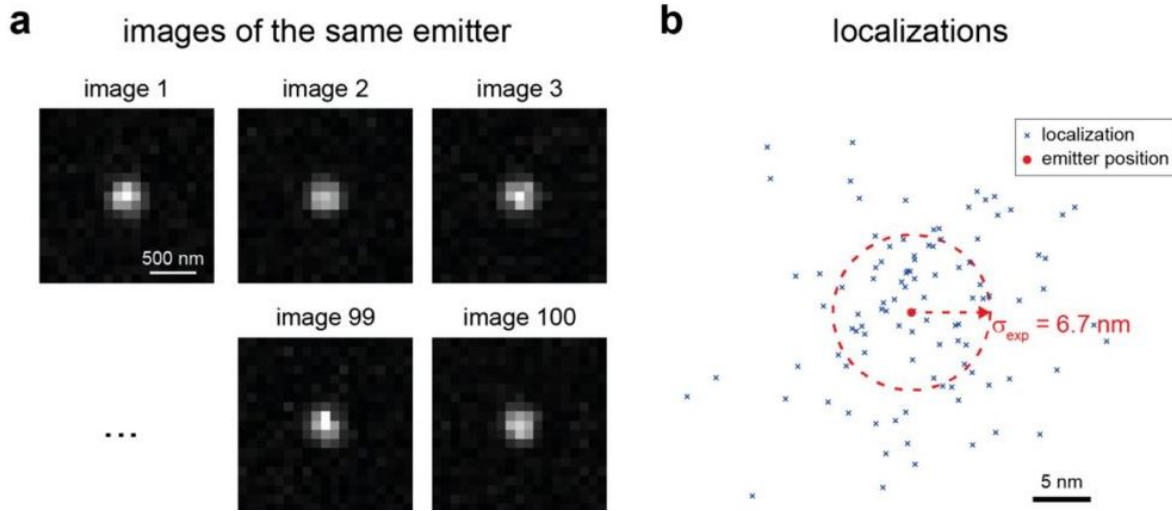
Figure 1.6: **Experimental procedure to calculate localization precision**. (a) 100 simulated images of the sample single emitter (b) The localizations obtained from each image in (a) and the localization precision σ_{exp} calculated from the variance of the localizations as described in Eqn. 1.8. Reprinted from Deschout, 2017.

Suppose a fluorescent emitter lies at position $(\theta_x, \theta_y, \theta_z)$ in the sample. If the true position of the emitter θ_x is estimated multiple times, the precision, σ_x, with which the emitter can be localized describes the spread of these estimates $\theta_{x,i}$ around its mean values $\overline{\theta_x}$. The precision with which an emitter has been localized is given by

$$\sigma_x = \sqrt{\frac{1}{n-1} \sum_{i=1}^{n} (\theta_{x,i} - \overline{\theta_x})^2} \tag{1.8}$$

where n is the number of estimates. Sometimes the localization precision is represented by the full-width at half-maximum (FWHM) of the measurement distribution. In the case of a Gaussian mea-

surement distribution, the $FWHM_x$ is related to the standard deviation σ_x as

$$FWHM_x = 2\sqrt{2\,ln\,2}\,\sigma_x \approx 2.355\,\sigma_x \qquad (1.9)$$

Similar expression can be written for the localization precision in the other dimensions θ_y and θ_z. Fig. 1.6 illustrates the process of calculating the experimental localization precision. The localization precision is essentially determined by the number of photons that make up the image. The number of photons arriving at the camera in a certain time interval follows a Poisson distribution. The standard deviation of this Poisson distribution is called *Poisson noise* or *shot noise*. In a system that is only affected by shot noise, the limit on the localization precision in this simplified case (Ober et al., 2004b; R. E. Thompson et al., 2002) is given by

$$\sigma_x \geq \frac{w}{\sqrt{N}} \qquad (1.10)$$

where N is the total number of photons detected and w is the standard deviation of the Gaussian function. However, when calculating the localization precision of experimental data, it is important to take into consideration factors other than the shot noise such as, pixelation effects from the detector and other sources of noise (readout noise, fluorescence background, etc.). In this case the localization precision is given by (Mortensen et al., 2010; Rieger & Stallinga, 2014; R. E. Thompson et al., 2002)

$$\sigma_x = \sqrt{\frac{w_a^2}{N}\left(\frac{16}{9} + \frac{8\,\pi\,w_a^2\,b^2}{N\,a^2}\right)} \qquad (1.11)$$

where $w_a^2 = w^2 + a^2/12$ is the effective size of the Gaussian spot after pixelation, a is the size of the pixel at the detector, b is the number of background photons per pixel, N is the total number of photons detected and w is the standard deviation of the Gaussian function. Single molecules typically yield 500-5000 photons producing typical experimental localization precisions of $\sim$ 5-20 nm depending on the background conditions, which is ten times smaller than the width of the diffraction-limited spot.

IMAGING WITH RESOLUTION BEYOND THE DIFFRACTION BARRIER USING SINGLE-MOLECULES   The central idea behind localization-based microscopy techniques is to effectively decrease the density of fluorescent molecules in the on (fluorescent) state at a particular moment in time, thereby making it possible to resolve each fluorescing molecule individually. Exploiting the state transitions available in many fluorescent molecules, several "blinking" mechanisms have been employed to demonstrate optical imaging using single molecules beyond the diffraction limit (Betzig et al., 2006; Hess et al., 2006; Rust et al., 2006; Sharonov & Hochstrasser, 2006). Although the specific molecular transitions involved in each of these techniques vary from one another, the fundamental idea remains the same in all of them. The molecules are switched between their on/off (fluorescent/dark) state via active photocontrol such that only a sparse subset of molecules
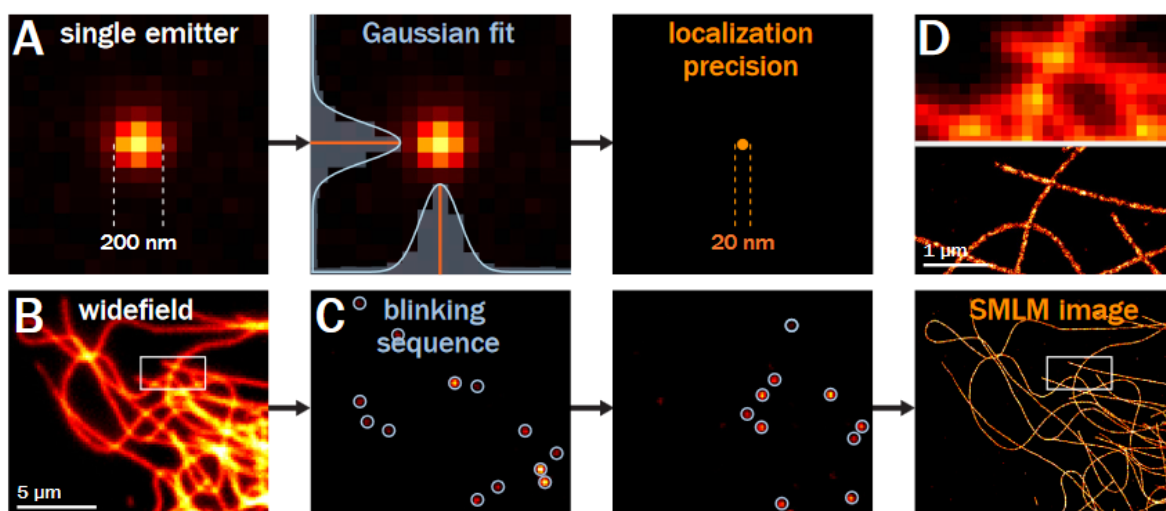
Figure 1.7: **Principle of Single Molecule Localization Microscopy (SMLM)**. (a) Diffraction limited image of a single emitter showing the ~ 200 nm width of the PSF (left) that is fitted using Gaussian curves (center) to determine its position with a ~ 20 nm precision (right). (b) Epifluorescence image of microtubules in a COS cell. (c) During SMLM acquisition, the fluorescent molecules labeling the biological specimen are turned on (fluroescent state) and off (dark state) thereby inducing a blinking behavior (left and center). Thousands of such frames are recorded which are then fitted as shown in (a) to provide precise estimates of the molecular positions. After all the frames are fitted, the final image is rendered using a Gaussian at each estimated molecular position, thereby providing a superresolution image of (b) (right). (d) Zoomed images of the highlighted boxes in the wide-field image (b) and the superresolution image showing the gain in resolution. Reprinted with permission from Jimenez et al., 2019.

emit fluorescence during each acquisition. During the next acquisition, another subset of molecules is activated or allowed to emit. The cycle repeats until all molecules are exhausted (i.e., photobleached) or the structure has been sampled sufficiently to prevent aliasing. The recorded images of the single-molecules from each acquisition are then localized with high precision. The estimated positions of the single molecules can then be used to reconstruct an image of the sample with resolution beyond the diffraction limit. Fig. 1.7 is an illustration describing the process of SMLM. In order to reduce the density of fluorescing molecules during each acquisition, the experimenter is required to actively control the laser intensities, choose laser wavelengths, and in some cases introduce chemical additives. Details regarding the various chemical mechanisms for photocontrol are beyond the scope of this dissertation, but several reviews cover these topics in great detail (Lew et al., 2012; M. A. Thompson et al., 2012).

RESOLUTION Resolution in SMLM, is a difficult quantity to assess; however, two parameters play an important role in determining the resolution of the final rendered image: the number of
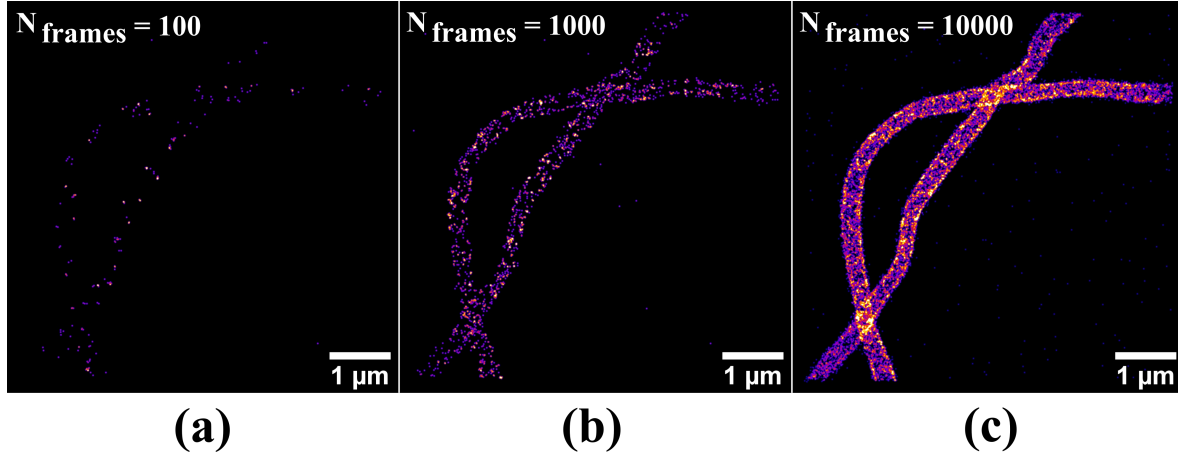
Figure 1.8: **Effect of sampling on resolution of SMLM images**. Simulated SMLM superresolution images of the endoplasmic reticulum (ER) reconstructed from (a) 100 raw frames (b) 1000 raw frames (c) 10000 raw frames.

photons collected per localization event and the density with which the sample is labeled. Since the localization precision scales inversely with $\sqrt{N}$ (see Eq. 1.10), in order to obtain an image where the molecules have been localized with high precision, the fluorescent molecule used to label the sample must emit as many photons per localization event as possible. In addition to collecting a high number of photons, it is imperative that the structure under investigation be labeled adequately so that it can be sampled enough to form a representative image. Similarly, stopping an SMLM experiment before enough localizations have been recorded leads to an under-sampled image. Fig. 1.8 illustrates the need for adequately sampling the structure of interest in SMLM. The structures are clearly visible if enough frames are acquired, but do not give a reliable impression when only a hundred frames are analysed. Similar results are observed when the biological specimen under study is not labeled adequately. According to the Nyquist-Shannon sampling theorem (Nyquist, 1928; Shannon, 1949), the biological structure must be sampled at a rate of at least twice the desired image resolution, therefore, the resolution of an SMLM image cannot be higher than two times the average spacing of the localizations (Shim et al., 2012; Shroff et al., 2008)

$$R_{Nyquist} = \frac{2}{\left(\frac{L}{a}\right)^{\frac{1}{d}}} \tag{1.12}$$

where $R_{Nyquist}$ is the Nyquist resolution, L is the total number of localizations, a is the area of the structure of interest and d is the dimension (d = 1,2,3). Notably, L/a is the density of the localizations. Eq. 1.12 underestimates the resolution if the localization precision is not significantly smaller than the mean localization spacing. To account for the localization precision, a modification has been

proposed to approximate the image resolution by the following formula (Legant et al., 2016)

$$R = \sqrt{R_{Nyquist}^2 + \sigma^2} \qquad\qquad (1.13)$$

where R is the overall resolution of the image and σ is the localization precision.

These approximations, however do not account for additional sources of errors, such as the size of the linker, the non-uniform density or the blinking stochasticity. The resolution is often approximated by calculating FWHM curves on biological structures and comparing them to their known widths, for instance synaptonemal complex or more commonly microtubules. This approach, however is unreliable when the structure of the biological specimen is unknown. Furthermore, such measurements are usually performed at the best part of the rendered image and by no means serve as the constant resolution of the entire reconstruction. Another approach that is commonly used to measure the resolution in localization microscopy is called the Fourier ring correlation (FRC, Banterle et al., 2013; Nieuwenhuizen et al., 2013). Originally developed for electron microscopy, FRC uses two independent subsets of the localization table (table consisting the recorded positions of the individual molecules) to reconstruct two superresolution images. These images are subsequently compared in the Fourier space to determine the spatial frequency cut-off beyond which the images lack similarity. The resolution of the image is then defined as the inverse of the threshold frequency. For further discussion on the definition of resolution in SMLM, the reader is directed to the supplementary information of Legant et al., 2016 and the review Demmerle et al., 2015.

PRACTICAL CONSIDERATIONS WHEN CONDUCTING SMLM EXPERIMENTS   A particular advantage of localization microscopy over the other superresolution techniques is the simplicity in the optics of the microscope. SMLM can be performed on any wide-field microscope as long as it satisfies three fundamental criteria: high stability, sufficient laser power and efficient photon collection.

STABILITY   Imaging a biological specimen using SMLM can take anywhere from tens of minutes to a couple of hours, depending on the number of frames required to gather the appropriate number of localizations. Since the localization precision is in the order of few to tens of nanometers, it is crucial that the microscope undergoes minimal drift in all three dimensions. Drift in the imaging system during acquisition can cause the final rendered image to appear smeared. Although technology has made it possible to use highly stable ($\sim 1\,nm$ precision) stages on microscopes, it is impossible to completely avoid drift caused due to thermal expansion and mechanical relaxation. Several strategies have been employed to calculate and correct the drift in an optical system, including using the positions of the single molecules post-localization (Mlodzianoski et al., 2011), real-time correction using correlation of bright-field images (McGorty et al., 2013), fiducial markers (Grover et al., 2015; Gustavsson et al., 2018; Ma et al., 2017), or an electrically tunable lens (Tafteh et al., 2016). One of the more common methods for live axial drift correction makes the use of an infra-red laser reflected in total internal reflection (TIR) at the coverslip. The reflected beam from the laser is measured with a photo-detector

in closed-loop with the objective lens holder (Jones et al., 2011). An open source implementation of this system is available under the name *PgFocus* (Bellve et al., 2014).
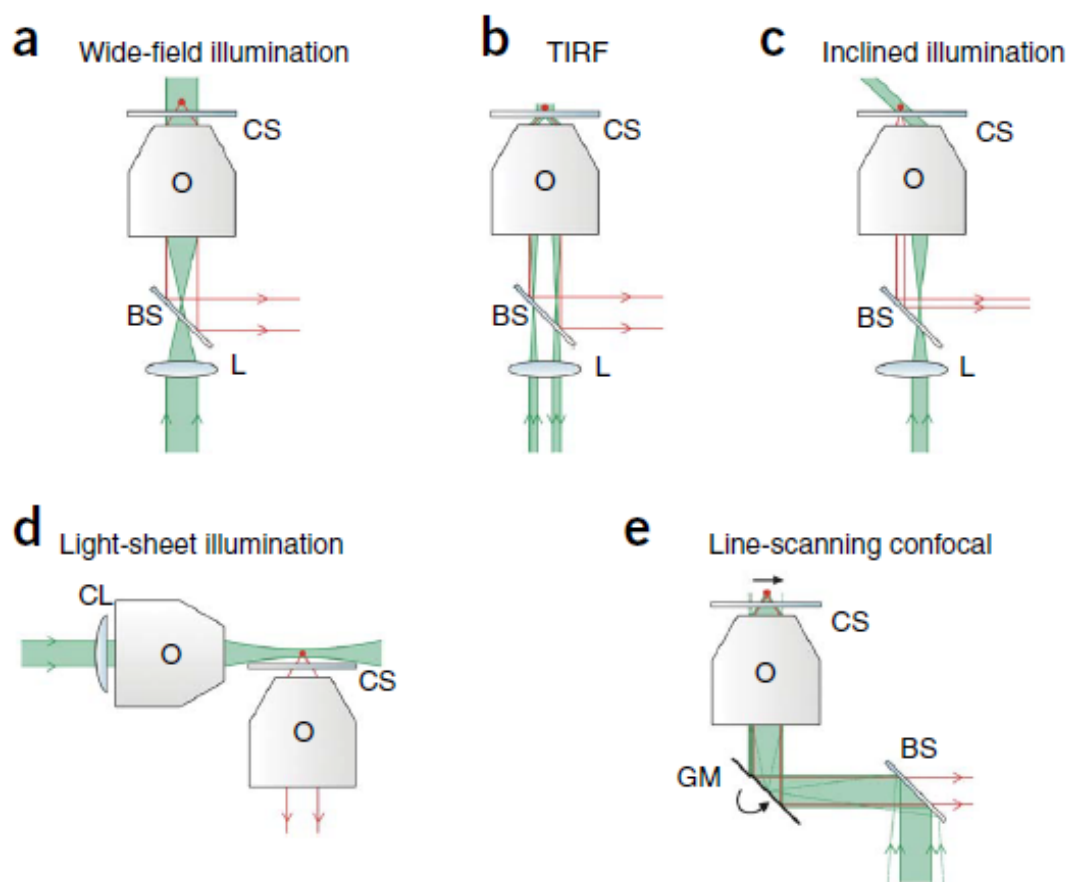
Figure 1.9: **Different illumination schemes in SPT and SMLM. CS: Coverslip, O: Objective lens, BS: Dichroic beam splitter, GM: Galvanometric mirros, CL: Cylindrical lens, L: Lenses** (a) In wide-field or epifluorescence illumination all planes above and below the focal plane receive excitation light (green), resulting in substantial out-of-focus fluorescence. (b) TIRF illumination reflects all the energy from the excitation laser at the coverslip letting only evanescent waves to pass through into the specimen, thereby reducing out-of-focus fluorescence when imaging structures that are very near the coverslip. (c) In oblique illumination the excitation light comes out a sharp angle, therefore only illuminating a part of the sample. Oblique illumination provides superior contrast compared to wide-field illumination and can be used to structures far away from the coverslip by changing the off-center distance at which the beam enters the back focal plane of the objective lens. (d) Light sheet illumination creates a sheet of light at the focal plane of the objective lens used to collect the fluorescence light (red). This allows only a thin part of the sample to be illuminated when imaging thick samples, thereby reducing out-of-focus light. (e) By focusing the light at a small volume of the sample, SMLM and SPT can be performed using a confocal microscope. Reprinted with permission from Deschout et al., 2014

ILLUMINATION   The power of the laser used to excite a single molecule must be sufficient enough so that the molecule can undergo the state transitions required for blinking. The laser power used for an SMLM experiment depends mainly on the type of fluorescent label used. In addition to collecting the maximum number of photons from the molecule, the intensity of the laser must be optimized to match the speed of the switching cycles with the camera exposure time. Typically an SMLM microscope must have the capability to deliver tens of kW/cm² to the sample at multiple wavelengths. A flexible microscope would, in addition to epi-illumination, include the possibility of illuminating the sample in total internal reflection (TIR, Axelrod et al., 1984) and in light sheet mode (Huisken et al., 2004; Siedentopf & Zsigmondy, 1902) to facilitate the imaging of thick samples and to reduce the background due to out-of-focus fluorescence. In order to implement TIR, the objective must have a large collection angle (NA > 1.33 for a water solution). The light from the laser is then focused at the edge of the back focal plane of the objective lens so that the the beam interacts with the coverslip at an angle greater than the critical angle. This way all the energy from the laser beam is reflected at the interface of the coverslip and the specimen, allowing only the evanescent wave to pass through into the specimen thus illuminating it close to the coverslip. The laser intensity reduces sharply with distance away from the coverslip ($\sim > 200$ nm), thereby drastically reducing the background. Since the localization precision in SMLM is highly dependent on the background of the image, TIR has been used extensively (Betzig et al., 2006; Hess et al., 2006; Sharonov & Hochstrasser, 2006). It is important to note that the weaker laser intensity at the periphery of the evanescent wave is not sufficient enough to switch off the emitters, thus introducing a background haze. Therefore TIRF illumination is only used when the structures in the specimen are well separated axially permitting efficient background reduction. Since TIRF is primarily used for looking at structures only at the surface of the coverslip, a technique similar to TIRF has been developed that facilitates SMLM at low background levels deeper inside the biological specimen (Tokunaga et al., 2008). There are various implementations of light sheet illumination for inverted microscopes which can be used for SMLM (Gebhardt et al., 2013; Greiss et al., 2016; Gustavsson et al., 2018; Meddens et al., 2016; Yang et al., 2019). Light sheet illumination, as it is named, creates a sheet of light in the biological specimen so that only a thin volume of the sample is illuminated. By bringing the illuminated part of the specimen into focus using the collection objective, the detector is exposed to light only from the part of the sample that is in focus, thereby dramatically reducing the out-of-focus background. This is particularly useful when the specimen under study is thick ($> 10\ \mu$m) and the experiment requires the preservation of the structural integrity of the biological specimen.

CAMERA   Single molecules typically emit 500-5000 (Fluorescent proteins: 500-1000 photons, Alexa dyes: 1000-5000 photons) photons. In order to localize single molecules within tens of nanometers it is important that the microscope is equipped with a very sensitive detector. Most SMLM experiments typically use an electron multiplying charge coupled device (EMCCD), due to their high quantum efficiency (i.e., their capacity to transform incident photons into electrons that can be measured). Advances in camera development have made it possible to use scientific metal-oxide semiconductors (sCMOS) as an alternative type of camera sensor for SMLM experiments. sCMOS

cameras now offer larger sensors, lower noise and high quantum efficiency. Futhermore, the architecture of sCMOS cameras allow for a much faster frame rate than the EMCCD. However, since the readout noise in sCMOS cameras is pixel-dependent, more complex noise modelling is required to properly estimate the number of photons detected during analyses of SMLM images (F. Huang et al., 2013; S. Liu et al., 2017).

ABERRATION CORRECTION   The quality of an optical system is determined by the quality of its PSF. Imperfections in the optical elements that make up the microscope can cause optical aberrations in the system. Aberrations distort the optical wavefront originating from the sample, thereby degrading the PSF of the system and consequently the localization precision (Coles et al., 2016). In addition to aberrations inherent in the system, the biological sample can also be a source of aberrations due its the non-homogeneous refractive index. Furthermore the refractive index mismatch between the immersion medium and the sample is also detrimental to the quality of the PSF (S. Hell et al., 1993; Hiraoka et al., 1990). Using adaptive optics, which was originally developed for astronomy (Merkle et al., 1989; Rousset et al., 1990), the degraded PSF of an optical microscope can be corrected by compensating for the distortions in the wave-front caused due to the reasons mentioned earlier (Booth, 2007). The aberrations in an optical system can be corrected by either sensing the wavefront and correcting for the distortions in the wavefront or by measuring certain metrics in the image itself to determine the required correction. In a sensor-based system, the wavefront sensor measures the departure of the wavefront from a perfect one by imaging a single bright object, typically a fluorescent bead in the sample or the focus of a laser. The wavefront sensor is then used in closed-loop with a wavefront correction device to manipulate the local phase of the wavefront, thereby guiding it towards a perfect wavefront. In an image-based adaptive optics system, the corrections are based on image-based metrics instead of a wavefront sensor. The closed-loop with the correction device maximizes the metric iteratively. Recently adaptive optics has been used successfully in SMLM to improve the localization precision when imaging deep into a biological specimen (Burke et al., 2015; Izeddin, El Beheiry, et al., 2012; Mlodzianoski et al., 2018; Tehrani et al., 2015; Tehrani et al., 2017).

ROTATIONAL FREEDOM OF MOLECULES   The localization algorithms used in SMLM approximate the emission patterns of a single-molecule to be that of an isotropic emitter or a monopole. However, this assumption is not accurate as the emission pattern of a single-molecule has been shown to behave like that of a dipole. Therefore, the monopole or scalar approximations made when studying the emission patterns of a single-molecule lead to large localization errors in SMLM (Lew et al., 2013) especially when orientation of molecule is constrained. Although it has been shown that for a typical sample, with flexible linkers, the population of non-freely rotating molecules is negligible (Backlund et al., 2013), care must be taken to image samples without orientation-induced bias. A promising solution to overcome the limitation caused by the rotational freedom of molecules, involves imaging only the azimuthally polarized light (Backlund et al., 2016; Lew & Moerner, 2014), as it does not carry any bias, as opposed to the radially polarized light. A detailed theoretical description of the emission

patterns of fluorescent dipole emitters can be found in Chandler et al., 2019a and Chandler et al., 2019b.

IMAGE ANALYSIS   In SMLM, the algorithms used to precisely measure the position of single molecules from raw camera frames have a fundamental effect on the resolution and fidelity of the final rendered superresolution image (A. Small & Stahlheber, 2014). The complete process involved in the rendering of a final superresolution SMLM image can be divided into five stages: detection of single molecules from raw camera frames, fitting and localization of detected candidates, processing of positions of localized molecules (eg. drift correction, density filtering, intensity thresholding), rendering of the localizations and finally the analysis of the statistics/spatial distributions. The detection step involves identifying the local maxima in each image after it is subjected to an intensity threshold. This gives the user the approximate estimates of the positions of the single molecules. The intensity thresholding minimizes the number of false-positives detected due to noise or background. The detected single-molecules are subsequently centered on a user-defined region of interest (ROI) and run through a fitting algorithm. Several fitting algorithms have been developed to find accurate position of the molecules by using different statistical tools (H. P. Babcock & Zhuang, 2017; S. Cox et al., 2012; Parthasarathy, 2012; Smith et al., 2010). This is typically the slowest part of the entire process and thus preference should be given to algorithms that run on graphic cards (GPU) instead of the central processing unit (CPU). The Cramér-Rao lower bound is defined as the uniform lower bound on the covariance for any unbiased estimation strategy. If a localization algorithm can reach the threoretical CRLB, it means the algorithm has attained its best-case limit of localization precision. Therefore, care must be taken when choosing a localization algorithm so that it can reach the theoretical limit of the CRLB (Chao et al., 2016). Once the fitting is done, a table of the localization results is compiled. The output of each localization event consists of the (estimated) position, number of emitted photons, number of background photons and the localization precision. At this point all post-processing steps such as drift correction, removal of bad localizations (i.e., localizations with precision > 20 nm), etc. are performed before finally rendering the superresolution image. The rendering of the final image is done by representing each localization as a point or a Gaussian at their measured position (Baddeley et al., 2010). A multitude of softwares have been developed and published to aid non-expert users to perform these steps easily (Henriques et al., 2010; Köthe et al., 2014; Ovesný et al., 2014). In addition to the user-friendly softwares, there are several softwares that vary by their performance under different imaging conditions (eg. low density vs high density imaging, performance of different 3D fitting routines, noise modeling, etc.) (Sage et al., 2019). Single-molecule localization algorithms and their effects on SMLM images have been the subject of several reviews (Burgert et al., 2015; Deschout et al., 2014; Durisic et al., 2014; Erdélyi et al., 2015; Rees et al., 2013; Rieger et al., 2014; A. R. Small & Parthasarathy, 2014).

MULTI-EMITTER FITTING ALGORITHMS   An important requirement in SMLM experiments is the control over the density of single-molecules in the fluorescing state during the acquisition of a single frame. If too many molecules are in the on state, it is nearly impossible to cut out an ROI

with a single-molecule in its center for the fitting step. An alternative solution to the high density of fluorescing molecules has been the development of fitting algorithms that can localize multiple molecules from overlapping PSF images. Methods that can handle images with higher density of fluorescing molecules can be classified into those that output a list of positions (H. Babcock et al., 2012; Holden et al., 2011; F. Huang et al., 2011; Wang et al., 2012) (similar to the aforementioned PSF fitting algorithms) and those that provide density maps with resolution on the scale of the localization precision (S. Cox et al., 2012; Deng et al., 2014; Hu et al., 2013; Marsh et al., 2018; Mukamel et al., 2012; Zhu et al., 2012). Algorithms that output a list of the molecular positions are similar to the algorithms that fit single molecules, except that the model now is a sum of PSFs from molecules that are no longer well-separated. When fitting such complex models, care must be taken to avoid overfitting or additing parameters to the model without conveying additional information about the physical nature of the sample. Methods that directly develop the fluorophore density map estimate the fluorophore concentration on a grid that is several times finer than that of the camera's pixel grid. These methods require precise knowledge of the noise and single-molecule blinking statistics.

THREE DIMENSIONAL (3D) IMAGING OF SINGLE MOLECULES The three dimensional (3D) nature of the biological world makes it important to develop SMLM instruments that can provide 3D positional information of the single molecules labeling the sample. As a single emitter changes its axial position relative to the focal plane of the objective lens, the shape of the 2D PSF of a standard fluorescence microscope changes very slowly. If the PSF of a standard fluorescent microscope were to be used for 3D imaging, this would result in very poor localization precision when estimating the axial position of the emitter because of the small change in the PSF shape relative to the axial movement of the emitter. In addition to the slow change in PSF shape, the PSF is symmetric above and below the focal plane making it difficult to assign a precise and unique axial position to the emitter along the axial dimension. Due to the above stated limitations of the standard Gaussian PSF, various techniques have been developed to facilitate 3D single molecule imaging. For the most part, these techniques can be classified by the optical principle they employ and fall under three categories: *PSF engineering*, *multifocal imaging* and *interferometric imaging*.

PSF ENGINEERING PSF engineering relies on altering the PSF of the microscope to encode the axial position of an emitter in its shape. This is done by placing an optical element (e.g. deformable mirror (DM), spatial light modulator (SLM), phase masks) in the detection path at a plane conjugate to the back focal plane (BFP) of the objective lens. This alters the phase of the local wavefront at the BFP consequently altering the shape of the PSF at the image/sensor plane. The phase changes made to the wavefront at the BFP are translation invariant which means that every point in the field of view will show the same altered PSF. Wavefront modification introduces additional costs and complexity in the system and requires precise alignment of the optical system. Although phase masks tend to be a more cost-effective alternative to SLMs and DMs, phase masks are non-adaptive. On the other hand, SLMs and DMs can be used to display a large variety of patterns that can generate different PSFs and can additionally correct for aberrations in the system.

Using this principle, a large number of engineered PSFs have been developed to aid 3D SMLM and single-particle tracking (SPT). The main difference between the PSFs are the axial range over which they allow 3D imaging (i.e. how far in 'z' can one see without moving the stage or the sample) and the axial localization precision with which the position of the emitter can be estimated. One of the most commonly used engineered PSFs, primarily because of it simplicity, is called the astigmatic PSF (B. Huang et al., 2008) (axial range: 800 nm, lateral precision: 20-30 nm, axial precision: 66 nm). The easiest way to alter the PSF shape to an astigmatic PSF is by placing a cylindrical lens in the detection path of the microscope (Kao & Verkman, 1994). This introduces astigmatism in the system and produces an elliptical PSF that is no longer symmetric above and below the focal plane thus allowing one to assign a unique axial position to the emitter along the axial dimension over the entire focal depth. Other implementations of the astigmatic PSF involve the use a DM (Izeddin, El Beheiry, et al., 2012; Xu et al., 2015) to introduce astigmatism in the system. Although the astigmatic PSF allows for 3D SMLM and SPT, the axial range over which it allows for 3D imaging remains limited to 800 nm. In order to increase the axial range other designs have been developed such as, the rotating double-helix PSF (Pavani et al., 2009) (axial range: 2-3 μm, axial precision: 21 nm) the corkscrew PSF (Lew et al., 2011), the phase ramp PSF (Baddeley, Cannell, et al., 2011), the self-bending PSF (Jia et al., 2014) and most recently the saddle-point/tetrapod PSF's (axial range: 3-20 μm, axial precision: 36 nm using the 3 μm tetrapod) (Shechtman et al., 2014; Shechtman et al., 2015). All these engineered PSF's have distinct features that change rapidly with defocus thus encoding the axial position of the emitter however they span different axial ranges (800 nm - 20 μm).

In addition to the axial range, the axial localization precision is another parameter that is considered when choosing an engineered PSF to perform 3D SMLM or 3D SPT. The different engineered PSFs mentioned above provide different values for axial precision. Although the axial localization precision of an engineered PSF depends on the optical setup and the experimental conditions, it is routine to calculate the Cramér-Rao lower bound (CRLB) (Cover & Thomas, 2012; Kay, 1993; Rao, 1973) whenever a new PSF engineering technique is developed. The CRLB provides the lower limit of precision with which the position of the emitter can be estimated. This quantity is useful because it (1) serves as a benchmark to which the precision provided by a particular estimator can be compared, thus indicating how much room there might be for improvement and (2) by calculating the quantity for a particular estimator under different experimental conditions, the lower bound helps in designing experiments where various parameters of the optical setup can be varied to achieve the desired level of precision. Several experimental and theoretical studies have been published that compare the CRLB values for different PSF engineering techniques (Badieirostami et al., 2010; Middendorff et al., 2008; Mlodzianoski et al., 2009; Zhou & Carles, 2020).

MULTIFOCAL IMAGING   The 3D positional information of a single-emitter in a sample can also be achieved by imaging multiple axial planes at different heights at the same time. This technique is known as multifocal or multiplane imaging. The simplest realization of this technique is achieved by splitting the light from the emitter equally between two arms and imaging the two arms on two separate cameras (axial range: 800 nm, axial precision: 75 nm) (Juette et al., 2008; Ram et al., 2008).

One of the arms is longer than the other, thus introducing defocus in the system. Since the two arms image different planes of the sample, there is no longer any uncertainty on the position of the molecule with respect to the reference plane. The concept of multifocal imaging can be extended to more than two arms (Prabhat et al., 2006) and multiple objectives (Ram et al., 2009), however for high-NA optics, refocusing by displacing the camera introduces spherical aberration for larger displacements (Botcherby et al., 2007).

Diffractive optics analogous to those used in PSF engineering can be used to get around the problem of optical aberrations in multifocal microscopy (Abrahamsson et al., 2013; Blanchard & Greenaway, 1999; Dalgarno et al., 2010; Hajj et al., 2014). The diffractive optical element (DOE), which is placed in the detection path of the microscope, diffracts the image into many orders with different phase terms. The different phases caused due to the DOE closely mimic axial displacement within the sample, avoiding aberrations. Although diffraction gratings account for a substantial loss of signal ($\sim 25\%$) and precise alignment, multifocal microscopy using diffraction gratings has resulted in simultaneous imaging of nine different planes spanning an axial range of 4 μm (Abrahamsson et al., 2016). One of the major drawbacks of the use of DOE's in multifocal microscopy is the loss of signal when imaging over large axial ranges. This is especially seen at the extremities of the axial range, where the signal from the emitter is split among planes that are significantly away from focus to provide any useful information. This causes a degradation in the localization precision since it is adversely affected by a decrease in the number of signal photons. To improve the axial localization precision over large axial ranges, multifocal imaging using DOE's has been combined with astigmatism (Hajj et al., 2016; Oudjedi et al., 2016). While, multifocal imaging using a single objective and two arms can be realized fairly simply, the extension of this concept to multiple axial planes increases the complexity of the setup and the analysis significantly.

INTERFEROMETRIC IMAGING   Another approach that has been commonly used in determining the 3D positional information of single-emitters uses the phase of the light being emitted from a single-molecule. Since the light emitted from a single fluorescent emitter is self-coherent, it can be interfered with itself and the relative phase delay can be used to estimate the axial position of the single-emitter. This is achieved by using a 4Pi optical arrangement, where light from a single-emitter is collected using two opposing objectives above and below the sample. The light collected from both the objectives is then combined and subsequently separated into different channels. By introducing a relative phase delay ψ_n between the light from the two objectives, different effective displacements of the emitter are sampled in each channels n. The total intensity detected from the molecule in each channel n can then be shown to have the relationship

$$I_n \propto 1 + cos(2kz + \psi_n) \qquad (1.14)$$

where z is the axial position relative to focus. Due to the axial interference fringes introduced to the PSF by combining the two paths, the images in the different channels have different intensities given by Eqn. 1.14. The ratio of the intensities in the different channels depends on the axial position of the

emitter within the sample. If the emitter were to be axially displaced with respect to the two objective lenses, the path lengths in each of the channels would change thereby changing the intensities of the images in each of the channels. The z position of the emitter can be extracted within an axial slice by measuring intensities in each of the channels. For a two-channel interferometric setup, $n \in (1, 2)$, with relative phase delays $\psi = (0, \pi)$, the z position of the emitter can be estimated from Eqn. 1.14 and is given as

$$z = \frac{1}{2k} cos^{-1} \left(\frac{I_1 - I_2}{I_1 + I_2} \right) \tag{1.15}$$

Since the total intensities of the PSF slices vary sinusoidally, to estimate the position of the emitter unambiguously, it is important to perform phase unwrapping to determine the axial slice within which the emitter rests. Interference based 3D localization microscopy has been realized in setups that use three (N. C. Schmidt et al., 2018; Shtengel et al., 2009) or four detection (Aquino et al., 2011; F. Huang et al., 2016; Middendorff et al., 2008) paths with relative phase delays of $2\pi/3$ or $\pi/3$ respectively. One approach to avoid the ambiguity in estimating the axial position of the emitter involves placing a deformable mirror (DM) on each arm of the 4Pi microscope and introducing astigmatism in the system (F. Huang et al., 2016). The change in the lateral size of the PSF due to the astigmatism allows one to estimate the slice of the periodical intensity pattern in which the emitter can be found. Whole-cell, high-resolution interferometric imaging over a range of 10 μm has been achieved using such a setup. Since the axial position is dependent on the interference of light passing through the two objectives, interference based localization microscopy techniques provide very high lateral ($\sigma_{xy} < 10nm$) and axial ($\sigma_z < 5nm$) precision (Shtengel et al., 2009). However, it must be noted that, while interferometric based techniques provide high precision, the systems require complex alignment and maintenance procedures. Since a difference in path length between the two imaging arms will reflect in the intensity of the images, it is imperative that the two imaging arms holding the objectives are stabilized to nanoscale tolerances over a path length on the order of 1 m.

3D single molecule imaging has been extensively explored and has been a major area of development in localization based microscopy. Several methods have been developed that perform axial localization by using other properties such as the intensity gradient of the excitation field (Fu et al., 2016), the near-field coupling of the emission to the coverslip (Bourg et al., 2015; Dasgupta et al., 2020; Deschamps et al., 2014), or the latent information of intrinsic aberrations of an ordinary microscope (Copeland et al., 2020). Recently SMLM has also been performed using light-field microscopy where the 3D position of the molecule is obtained by capturing both the spatial and angular information of the light emitted from the sample (Sims et al., 2020). An excellent review discussing the challenges of 3D localization microscopy and commonly used existing techniques can be found in von Diezmann et al., 2017 and Zhou et al., 2019. In chapter 3, I introduce a new and simple approach to 3D localization.

OUTLOOK   Although the optical setup in SMLM is much simpler than SIM or STED, the success of an SMLM experiment relies on the precise combination of carefully optimized factors such as the labeling efficiency, choice of fluorescent probes, an optical system with minimized drift and aberrations, the right illumination setup to ensure reduced background and artifact free image anal-

ysis. In addition, the buffer chemistry has to be optimized to ensure satisfactory blinking rates of the molecules. This can take months to come together and demands good expertise, both on sample preparation and during data acquisition and analysis. Not all biological questions benefit from imaging using SMLM. An increase in resolution obtained using SIM/NL-SIM or STED might be sufficient and can help avoid months of optimization of parameters required for SMLM. A particularly attractive feature of SMLM is the ability to perform vast number of analyses on the localization table to extract meaningful quantitative information about the biological specimen under investigation. The ability to perform quantitative experiments on nanoscale features is where SMLM has proven to be extremely valuable.

1.7 Scope of this dissertation

Despite there being several methods for performing 3D localization microscopy, most users turn to PSF engineering using an astigmatic PSF. This is primarily due to its simplicity since this can be achieved by placing a single cylindrical lens in the emission path. The simplicity in an astigmatic setup comes with the drawback of poorer axial localization precision (compared to the lateral localization precision) and a short axial range ($\sim$ 800 nm). Imaging samples larger than $\sim$ 1 μm using the astigmatic system requires moving some part of the microscope thereby jeopardizing the stability of the system. Other techniques that provide higher axial precision and larger axial ranges are often expensive, complex to build, operate and analyze. During my PhD, I explored a fundamentally new method to perform 3D localization microscopy based on the principle of self-interference digital holography (SIDH). This approach has the potential to achieve nanometer scale localization precision over a range of 20-25 μm. In chapter 2, I describe the theory of SIDH. In chapter 3, I describe a simple optical system necessary to implement 3D localization microscopy using SIDH and the proof-of-principle experiments using 100 and 40 nm fluorescent nanospheres. This work was published in Marar and Kner, 2020b. In chapter 4, I calculate the theoretical limit of localization precision of our proposed 3D imaging technique by calculating the Cramér-Rao lower bound (CRLB) and compare the calculated theoretical precision to the 3D single molecule localization precision of different PSF's.

Chapter 2

Theory of Self-Interference Digital Holography

Holography was invented by Dennis Gabor in 1948 while working to improve the resolution of an electron microscope which was degraded due to the aberrations introduced by the electron lens. Gabor realized that the diffraction pattern of the electron beam contained information about the amplitude and phase of the electron wave and could be used to optically synthesize the field of the object. Gabor's realization could be extended to visible light optics for image formation. This was greatly beneficial, since visible light optics was easier to implement and lot more advanced than electron optics. He named the new imaging technique holography, due to its ability to record the whole optical field of the object (Gabor, 1948).

The principle of holography was immediately applied for recording and imaging using visible light (Rogers, 1952), however, development in the field was stymied during the next decade because light sources available at the time were not truly coherent and could not provide high quality interference contrast. The invention of the laser in 1960 (Basov & Prokhorov, 1954; Maiman, 1960; Schawlow & Townes, 1958), helped overcome this barrier. During the same time, Emmett Leith and Juris Upatnieks decided to duplicate Gabor's work using an off-axis illumination setup with a separate reference wave (Leith & Upatnieks, 1962, 1963, 1964) which resulted in the first laser transmission hologram of 3D objects. The new setup eliminated the problem of the zero-order and twin images which existed in Gabor's on-axis configuration. Following the invention of the laser and the off-axis configuration, many new techniques and applications of holography were subsequently developed. Comprehensive reviews discussing the different applications of holography can be found in Hariharan, 1996 and Kim, 2010.

This chapter provides an outline of the theory behind holography, especially as it pertains to digital holographic microscopy. Furthermore I will concentrate on the special case of digital holography that creates holograms using incoherent light, called self-interference digital holography.

2.1 Mathematical and Physical Preliminaries

SPATIAL FREQUENCIES   While discussing the characteristics of an optical imaging systems, it is common to switch between real space (x, y, z) and frequency space (k_x, k_y, k_z), also commonly known as Fourier space or reciprocal space. The spatial frequencies representing an object are a measure of how often sinusoidal components (as determined by the Fourier transform) of the structure repeat per unit of distance. Similar to the concept of frequency when dealing with time, where the frequency is defined by the inverse of the period, the spatial frequency (k) of an object, (consider a 1D grating for simplicity) is defined by the inverse of the period of the gratings (d): $k \sim 1/d$. The diffraction limit of a microscope in terms of frequency then defines the maximum spatial frequency that can pass through the optical system.
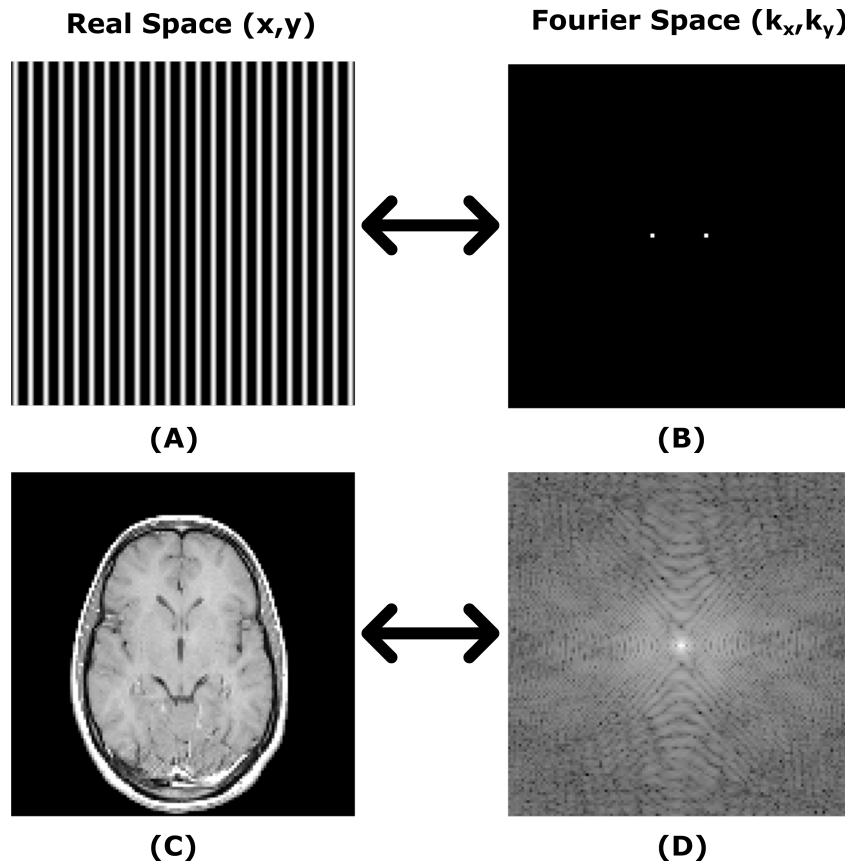
Figure 2.1: **Fourier transform**. (A) 2D sinusoidal pattern in the x-direction (B) The Fourier transform of a 2D sinusoidal pattern in Fourier space is represented as two peaks at the frequency ($+\omega_0$ and $-\omega_0$) of the sinusoidal pattern. (C) Single slice of MRI image of human brain. (D) A more complex signal will be represented as a sum of multiple sine functions, and will be represented in the Fourier space by their corresponding frequencies.

FOURIER TRANSFORM   In 1822, Joseph Fourier developed the Fourier transform (Fourier, 1822) as a mathematical tool to decompose any complicated signal into superpositions of pure sinusoidal waves of varying frequencies ($sin(k_x x)$ or $e^{-ik_x x}$ in a complex representation). The Fourier transform can be used to decompose a spatial signal (such as a function describing the density of fluorescent molecules that label a 3D biological sample) into sums of sine functions with different spatial frequencies. This can be visualized in Fig. 2.1, where Fig. 2.1 (A) shows a periodic 2D sinusoidal pattern in real space. The Fourier transform of the signal shown in Fig. 2.1 (A) is represented by two peaks corresponding to the frequency of the sinusoid. The Fourier transform takes an object/signal in real space (Fig. 2.1 (C)) (object of interest), where the coordinates are (x, y, z), and represents it in frequency space (Fig. 2.1 (D)) where the coordinates are (k_x, k_y, k_z) and the units of k_m are 1/length (i.e. $k_m \sim 1/m$, $m = x, y, z$. Mathematically, the two-dimensional (2D) Fourier transform of a function $g(x, y)$ is defined as

$$\mathcal{F}(k_x, k_y) = \frac{1}{\sqrt{2\pi}} \iint\limits_{-\infty}^{\infty} g(x, y) e^{-j(k_x x + k_y y)} dx dy \qquad (2.1)$$

where the transformed function $\mathcal{F}$ is a complex-valued function with two independent variables k_x and k_y (Goodman, 2005). The Fourier transform is reversible and applying the inverse transform returns the initial function without loss of information. The inverse Fourier transform of a function $G(k_x, k_y)$ is defined as

$$\mathcal{F}^{-1}(G) = \frac{1}{\sqrt{2\pi}} \iint\limits_{-\infty}^{\infty} G(k_x, k_y) e^{j(k_x x + k_y y)} dk_x dk_y \qquad (2.2)$$

The Fourier transform has many interesting mathematical properties that have proven to be very useful in the field of optical microscopy and digital holography. The *convolution theorem* is one such example that is heavily used in optical systems theory and also in the reconstruction process in digital holography. The 2D convolution of a two functions $f(x, y)$ and $g(x, y)$ is defined as (Goodman, 2005)

$$(f * g)(x, y) = \iint\limits_{-\infty}^{\infty} f(x', y') g(x - x', y - y') dx' dy' \qquad (2.3)$$

where $*$ denotes the convolution operator. The convolution theorem then states that the convolution as described in Eqn. 2.3 of two functions in real space is entirely equivalent to the simpler operation of multiplying their individual Fourier transforms and performing an inverse Fourier transform.

$$\mathscr{F}\{(f(x, y) * g(x, y)\} = \mathcal{F}(k_x, k_y)\mathcal{G}(k_x, k_y) \qquad (2.4)$$

where $\mathscr{F}$ indicates the Fourier transform operator and $\mathcal{F}$ and $\mathcal{G}$ denote the Fourier transformed functions with coordinates k_x and k_y in the Fourier (frequency) space.

MONOCHROMATIC WAVE PROPAGATION   Light is an electromagnetic wave whose behavior is governed by the well-known Maxwell's equations (Maxwell, 1861). In MKS units and in the absence of free charge, the equations are given by

$$\nabla \times \mathbf{H} \quad = \quad \epsilon \frac{\partial \mathbf{E}}{\partial t} \tag{2.5a}$$

$$\nabla \times \mathbf{E} \quad = \quad -\mu \frac{\partial \mathbf{H}}{\partial t} \tag{2.5b}$$

$$\nabla \cdot \epsilon \mathbf{E} \quad = \quad 0 \tag{2.5c}$$

$$\nabla \cdot \mu \mathbf{H} \quad = \quad 0 \tag{2.5d}$$

where $\mathbf{E} = (E_x(t), E_y(t), E_z(t))$ and $\mathbf{H} = (H_x(t), H_y(t), H_z(t))$ are, respectively, the vectorial representation of the electric and magnetic fields of the wave. They are both functions of position ($\mathbf{r} = (x,y,z)$) and time (t). μ and ϵ are the permeability and permittivity, respectively, of the medium in which the wave is propagating. The symbols $\times$ and $\cdot$ represent the vector cross product and vector dot product, respectively. The ∇ ('del') operator is a vector differential operator and is defined as

$$\nabla = \frac{\partial}{\partial x}\hat{i} + \frac{\partial}{\partial y}\hat{j} + \frac{\partial}{\partial z}\hat{k}$$

where $\hat{i}$, $\hat{j}$ and $\hat{k}$ are the unit vectors in x, y and z directions, respectively. This thesis will adopt the convention of z as the axis of wave propagation, or the 'optical axis'.

We assume that the wave is travelling in a medium that is linear, isotropic (independent of direction of polarization), homogeneous (constant permittivity), non-dispersive (i.e. permittivity is independent of wavelength over the wavelength region occupied by the propagating wave) and is non-magnetic ($\mu = \mu_0$, permeability of vaccum). Therefore, applying the $\nabla \times$ operation to both sides of Eqn.2.5b, we use the vector identity

$$\nabla \times (\nabla \times \mathbf{E}) = \nabla(\nabla \cdot \mathbf{E}) - \nabla^2 \mathbf{E} \tag{2.6}$$

Since the propagation medium is linear, isotropic, homogeneous and non-dispersive, substituting Eqns. 2.5b and 2.5c in Eqn. 2.6 gives

$$\left(\nabla^2 - \frac{n^2}{c^2}\frac{\partial^2}{\partial t^2}\right)\mathbf{E} = 0 \tag{2.7}$$

where ∇^2 is the Laplacian and n denotes the index of refraction of the medium and is given by

$$n = \sqrt{\frac{\epsilon}{\epsilon_0}} \tag{2.8}$$

ϵ_0 is the permittivity of vacuum, and c is the velocity of the electromagnetic wave in vacuum and is given by

$$c = \frac{1}{\sqrt{\mu_0 \epsilon_0}} \qquad (2.9)$$

Similarly, using the vector identity for Eqns. 2.5a and 2.5d gives

$$\left(\nabla^2 - \frac{n^2}{c^2}\frac{\partial^2}{\partial t^2}\right)\mathbf{H} = 0 \qquad (2.10)$$

Since both $\mathbf{E}$ and $\mathbf{H}$ obey the vector wave equation, all components of the two vectors must obey the vector wave equation which makes it possible to summarize the behavior of all the components of both $\mathbf{E}$ and $\mathbf{H}$ through a single scalar wave equation given by

$$\left(\nabla^2 - \frac{n^2}{c^2}\frac{\partial^2}{\partial t^2}\right)U(\mathbf{r}, t) = 0 \qquad (2.11)$$

where $U(\mathbf{r}, t)$ represents any scalar field component.

Detailed derivations of Eqn.2.11 can be found in Weber and Arfken, 2005.

THE HELMHOLTZ EQUATION   In the case of a purely monochromatic wave, the scalar field may be represented explicitly as

$$U(\mathbf{r}, t) = \text{Re}\{\tilde{U}(\mathbf{r})e^{-j\omega t}\} \qquad (2.12)$$

where 'Re' signifies the real part of a complex function. $\tilde{U}(\mathbf{r})$ is a complex function of position also known as a *phasor* and ω is the angular frequency of the wave and is related to its wavelength λ and velocity v by

$$\omega = \frac{2\pi v}{\lambda} \qquad (2.13)$$

$\tilde{U}(\mathbf{r})$ represents the amplitude $|\tilde{U}(\mathbf{r})|$ and phase $\psi(\mathbf{r})$ of the wave at a given position coordinate $\mathbf{r}$ and can be written as

$$\tilde{U}(\mathbf{r}) = |\tilde{U}(\mathbf{r})|e^{j\psi(\mathbf{r})} \qquad (2.14)$$

For the disturbance U(**r**,t) to be an optical wave, it must satisfy the scalar wave equation represented by Eqn. 2.11. By substituting Eqn. 2.12 in Eqn. 2.11, we arrive at the time-independent equation

$$(\nabla^2 + k^2)\tilde{U}(\mathbf{r}) = 0 \qquad (2.15)$$

where k is known as the *wavenumber* and is given by

$$k = \frac{n\omega}{c} = \frac{2\pi}{\lambda} \qquad (2.16)$$

and λ is the wavelength in the dielectric medium ($\lambda = c/nv$). Equation 2.15 is known as the *Helmholtz equation* and any optical disturbance propagating through vacuum ($n = 1$) or a homogeneous dielectric medium ($n > 1$) must obey the Helmholtz equation.

FREE-SPACE PROPAGATION   The most common imaging geometries involve the propagation for light from one plane ($z = 0$, $\tilde{U}(\mathbf{r_o})$) to another plane ($z > 0$, $\tilde{U}(\mathbf{r_1})$). There are two approaches that are generally taken to calculate the field at $z > 0$:

1. The field at $z > 0$ is calculated directly from the field originating from a light source at $z < 0$ using a Green's function formalism (Born & Wolf, 2013; Jackson, 2007).

2. The field at $z > 0$ is calculated based on the knowledge of the field at $z = 0$ using Kirchoff's boundary conditions (Kirchhoff, 1883). This method is discussed in detail in Goodman, 2005.

The problem of deriving the field $\tilde{U}(\mathbf{r_1})$ propagated from the aperture based on the field $\tilde{U}(\mathbf{r_o})$ inside the aperture (see Figure 2.2) is not trivial and is beyond the scope of this dissertation. Detailed derivations for scalar fields can be found in Goodman, 2005 and derivations involving a full vectorial treatment of light can be found in Born and Wolf, 2013 and Jackson, 2007. This dissertation only discusses the most relevant results.
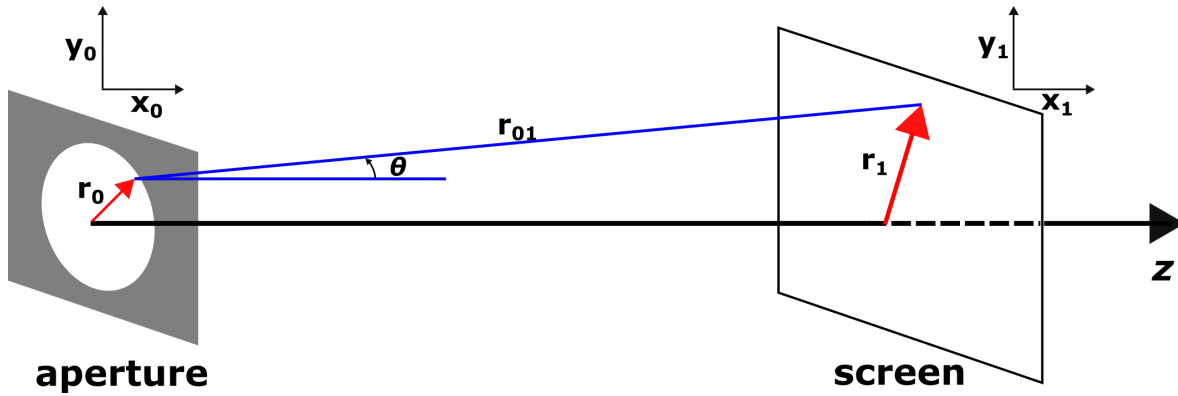
Figure 2.2: **Geometry for Free-space Propagation with Kirchoff boundary conditions**.

The relation between the scalar fields $\tilde{U}(\mathbf{r_o})$ and $\tilde{U}(\mathbf{r_1})$ is given by the Huygens-Fresnel principle and is stated as

$$\tilde{U}(\mathbf{r_1}) = \frac{1}{j\lambda} \iint\limits_{Aperture} \tilde{U}(\mathbf{r_o}) \frac{e^{jkr_{01}}}{r_{01}} \cos\theta \, d^2\mathbf{r_o} \qquad (2.17)$$

where θ is the angle between the optical axis and the vector r_{01} pointing from $\mathbf{r_o}$ to $\mathbf{r_1}$. If z is the distance along the optical axis between the aperture and the point of observation, we get

$$\cos\theta = \frac{z}{r_{01}}$$

and therefore Eqn. 2.17 can be rewritten as

$$\tilde{U}(x_1, y_1) = \frac{z}{j\lambda} \iint\limits_{Aperture} \tilde{U}(x_0, y_0)\frac{e^{jkr_{01}}}{r_{01}^2}dx_0\,dy_0 \qquad (2.18)$$

where r_{01} is given by

$$r_{01} = \sqrt{(x_1 - x_0)^2 + (y_1 - y_0)^2 + z^2} \qquad (2.19)$$

It should be noted that two approximations have been made in arriving at the expression described in Eqn. 2.18. One is the approximation inherent in the scalar theory that requires the diffracting structures (aperture in Fig. 2.2) to be large compared to the wavelength of light (λ). The second approximation is made by assuming that the field propagating through the medium is radiative, as opposed to an evanescent field (Mertz, 2019). This is made by assuming the observation distance to be many wavelengths away from the aperture, $r_{01} \gg \lambda$ (Marathay & McCalmont, 2004).

THE FRESNEL APPROXIMATION   In many applications the wavefronts associated with the fields propagating from the aperture to another plane vary slowly in the transverse direction (i.e., the path of light deviates only slightly from the axial propagation direction). In such cases, a small-angle approximation known as the *paraxial approximation* can be adopted, which amounts to setting: $\cos\theta \sim 1$ and $r_{01} \sim z$ in the denominator of Eqn. 2.18.

$$\tilde{U}(x_1, y_1) = \frac{1}{j\lambda z} \iint\limits_{Aperture} \tilde{U}(x_0, y_0)e^{jkr_{01}}\,dx_0\,dy_0 \qquad (2.20)$$

Despite the simplification, Eqn. 2.20 remains difficult to work with because of the variable r_{01} in the exponential. The error introduced by approximating $r_{01} \sim z$ for the r_{01}^2 term appearing in the denominator of Eqn. 2.18 is acceptably small. However, for the r_{01} term appearing in the exponent, the errors are much larger. Small changes in the phases in the order of a fraction of a radian can change the value of the exponent significantly. Therefore, it is important to restrain the approximation of r_{01} based on the binomial expansion of the expression described in Eqn. 2.19. By factoring z outside and applying the binomial expansion to Eqn. 2.19, an approximation of r_{01} by retaining on the first two terms of the expansion is given by

$$r_{01} \sim z\left[1 + \frac{1}{2}\left(\frac{x_1 - x_0}{z}\right)^2 + \frac{1}{2}\left(\frac{y_1 - y_0}{z}\right)^2\right] \qquad (2.21)$$

For approximating the r_{01}^2 term appearing in the denominator of Eqn. 2.18, only the first term in Eqn. 2.21 is used and all other terms are dropped. However, r_{01} in the exponent of Eqn. 2.18 is approximated using Eqn. 2.21. The resulting expression for the field at $\mathbf{r_1} = (x_1, y_1)$ therefore becomes

$$\tilde{U}(x_1, y_1) = \frac{e^{jkz}}{j\lambda z} \iint\limits_{-\infty}^{\infty} \tilde{U}(x_0, y_0) \exp\left\{ j\frac{k}{2z}\left[(x_1 - x_0)^2 + (y_1 - y_0)^2 \right] \right\} dx_0\, dy_0 \qquad (2.22)$$

Eqn. 2.22 is known as the *Fresnel diffraction integral* and can be seen as a convolution (Eqn. 2.3), expressed in the form

$$\tilde{U}(x_1, y_1) = \frac{e^{jkz}}{j\lambda z} \iint\limits_{-\infty}^{\infty} \tilde{U}(x_0, y_0) h(x_1 - x_0, y_1 - y_0)\, dx_0\, dy_0 \qquad (2.23)$$

where the convolution kernel, also known as the *Fresnel free-space propagator* is defined by

$$h(x, y) = \frac{e^{jkz}}{j\lambda z} \exp\left[\frac{jk}{2z}(x^2 + y^2) \right] \qquad (2.24)$$

Eqn. 2.24 is an important result as it is widely used in designing digital holographic microscopes as well as in the reconstruction process. Eqn. 2.23 can be re-written by factoring the quadratic phase term (also used to represent a diverging spherical wave, see chapter 4 in Goodman, 2005 for details)

$$exp\left[\frac{jk}{2z}(x^2 + y^2) \right]$$

outside the integral signs which gives us

$$\tilde{U}(x_1, y_1) = \frac{e^{jkz}}{j\lambda z} e^{j\frac{k}{2z}(x^2 + y^2)} \iint\limits_{-\infty}^{\infty} \left\{ \tilde{U}(x_0, y_0) e^{j\frac{k}{2z}(x_0^2 + y_0^2)} \right\} e^{-j\frac{2\pi}{\lambda z}(x_1 x_0 + y_1 y_0)}\, dx_0\, dy_0 \qquad (2.25)$$

where the terms inside the integral signs can be recognized as the Fourier transform of the product of the complex field just to the right of the aperture ($\tilde{U}(x_0, y_0)$) and a quadratic phase exponential ($e^{j\frac{k}{2z}(x_0^2 + y_0^2)}$). The approximation that leads to Eqn. 2.23 and Eqn. 2.25 is valid in the near-field (Mertz, 2019), which is to say

$$|\mathbf{r_1} - \mathbf{r_0}|^4 << \lambda z^3 \qquad (2.26)$$

which applies for most applications in optical microscopy.

THE FRAUNHOFER APPROXIMATION   The Fraunhofer approximation describes the behavior of the diffracting light when the plane of observation is sufficiently far from the aperture (i.e. the far-field). In such cases the diffracting light from the aperture can be thought to be parallel. Given the wavelength dependence of diffraction, this is tantamount to the small aperture approximation which is given by

$$z >> \frac{k}{2}(\mathbf{r_o})^2_{max} \tag{2.27}$$

If the approximation in Eqn. 2.27 is satisfied in addition to the Fresnel approximation, then the quadratic phase term inside the integral sign in Eqn. 2.25 is approximately 1 over the finite limits of the aperture and the the field observed at $\mathbf{r_1}$ (in the far-field) can now be written as

$$\tilde{U}(x_1, y_1) = \frac{e^{jkz}}{j\lambda z}e^{j\frac{k}{2z}(x^2+y^2)} \int\!\!\!\int\limits_{-\infty}^{\infty} \tilde{U}(x_0, y_0)e^{-j\frac{2\pi}{\lambda z}(x_1 x_0 + y_1 y_0)} \, dx_0 \, dy_0 \tag{2.28}$$

referred to as the *paraxial Fraunhofer diffraction integral* (Mertz, 2019).

OPERATOR NOTATION FOR HOLOGRAPHY   The previous section describes the methods used to calculate the field of an electromagnetic wave at different points in space when it is propagating over one region of free space. Optical systems used to study biological samples are more complex and typically involve multiple optical elements (i.e. lenses, phase modulating elements etc.) and multiple regions of free space. Although such systems can be analyzed using the methods described earlier, the complexity of the calculations increases as the number of optical elements grows. For this reason, an *operator* notation is used to analyze complex optical systems.

Several different operator notations have been developed for the simplification of the analysis of optical systems. In this dissertation, we follow the approach of Nazarathy and Shamir (Nazarathy & Shamir, 1980) to simplify our calculations.

The operator approach is based on several fundamental operations. The operators have parameters that are dependent on the geometry of the optical system being analyzed. The parameters of the optical system are included in square brackets [ ] and the operators act on the quantities contained in the curly brackets { }. The basic operators that will be used in this dissertation are as follows:

Quadratic Phase Exponential: The definition of the operator $\mathcal{Q}$ is

$$\mathcal{Q}[c]\{\tilde{U}(x)\} = e^{j\frac{k}{2}cx^2}\tilde{U}(x) \tag{2.29}$$

where $k = 2\pi/\lambda$ and c has units of inverse length. The inverse of $\mathcal{Q}[c]$ is $\mathcal{Q}[-c]$. This operator is usually used when the wavefront passes through a lens or to denote a diverging spherical wave. For a lens with focal length f, the operation on the wave is denoted by $\mathcal{Q}(-1/f)$ and when a diverging spherical wave passes a distance d, the operation on the wave is denoted by $\mathcal{Q}(1/d)$.

Linear Phase Factor: The transverse distribution of a tilted plane wave is described by the linear phase factor $\mathcal{L}$, which is defined by

$$\mathcal{L}[s]\{\tilde{U}(x)\} = e^{jksx}\tilde{U}(x) \tag{2.30}$$

where both the direction of the plane-wave propagation and the spatial frequency of the transverse complex amplitude distribution are specified by the vector s. The vector s has two related interpretations:

1. s is the tilt vector, i.e., the transverse-direction cosine vector obtained by taking a unit vector k in the direction of wave propagation and projecting it upon a transverse plane.

2. s is the normalized spatial frequency derived from the usual spatial frequency vector ν by $s = \lambda\nu$, where $\nu = k_x\hat{x} + k_y\hat{y}$.

This operator gives a compact mathematical notation for a tilted plane wave.

Free-Space Propagation: Free-space propagation (under the paraxial approximation) is represented by the operator $\mathcal{R}$, which is defined by the equation

$$\mathcal{R}[d]\{\tilde{U}(x_1)\} = \frac{1}{\sqrt{j\lambda d}} \int_{-\infty}^{\infty} \tilde{U}(x_1) e^{j\frac{k}{2d}(x_2-x_1)^2} dx_1 \tag{2.31}$$

where d is the distance of propagation ($d = x_2 - x_1$). The inverse of $\mathcal{R}[d]$ is $\mathcal{R}[-d]$.

In the previous section we saw, that free-space propagation using the Fresnel approximation leads to an integral which looks like the Fourier transform of the product of the complex field just to the right of the aperture and a quadratic phase exponential. This is represented in the operator notation by performing a convolution with a quadratic phase term and is given by

$$\mathcal{R}[d]\{\tilde{U}(x_1)\} = \tilde{U}(x_1) * \mathcal{Q}\{d^{-1}\} \tag{2.32}$$

where d is the distance between x_1 and x_2. Eqn. 2.32 will be used primarily in analyzing the optical systems described in this dissertation.

To learn about other operators that describe optical systems and their properties, the reader is encouraged to read chapter 5 in Goodman, 2005.

RAY-TRANSFER MATRICES Matrix optics is a technique for tracing paraxial rays. A ray is described by its position and its angle with respect to the optical axis. In the paraxial approximation, the position and angle of a ray at the input and output planes of an optical system can be described by two linear algebraic equations. This allows the optical system to be described by a 2 x 2 matrix called the *ray transfer matrix*. Matrix optics are convenient to calculate the position and angle of a ray at any plane in a complex optical system. The ray-transfer matrix of a complex optical system constituting of multiple of optical elements is the product of the ray-transfer matrices of the individual optical elements.

Consider a ray propagating in the y–z plane where the optical axis is in the z-direction. Let us specify a ray at position z_1 by two coordinates: the displacement from the axis y_1 and the orientation angle θ_1 (see Fig. 2.3). For a ray that enters an optical system from the plane z_1 with position and direction (y_1,θ_1), the ray is steered by the optical system so that it has a new position and direction (y_2,θ_2) at the output plane z_2.
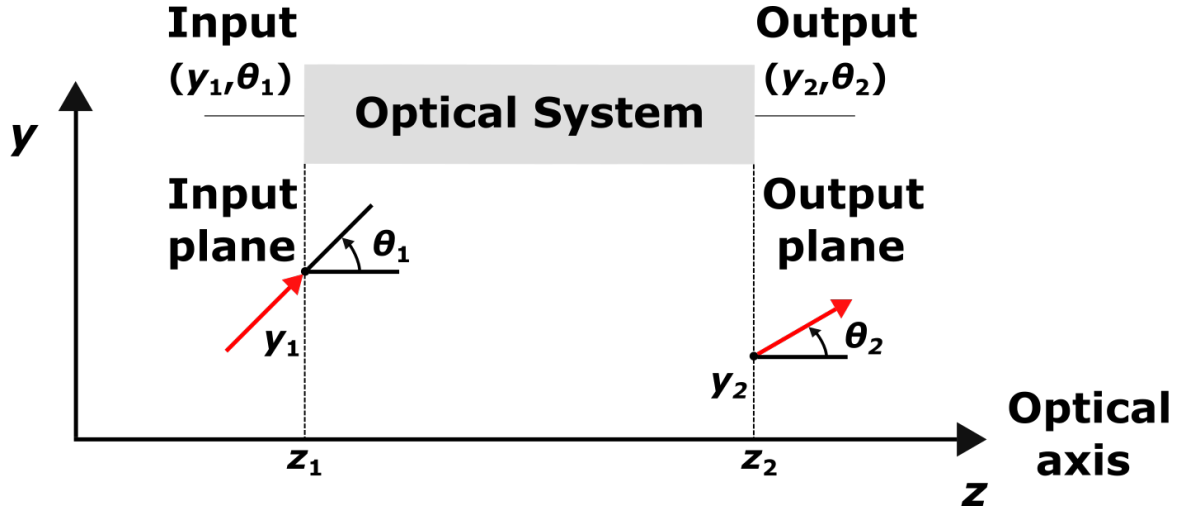
Figure 2.3: **Ray of light passing through an optical system**. A ray characterized by its coordinates y and θ, enters an optical system at the input plane z_1 at position y_1 with angle θ_1 and exits the optical system from the ouput plane z_2 at position y_2 with angle θ_2. Adapted from Saleh and Teich, 2019

In the paraxial approximation, when all angles are sufficiently small so that $\sin\theta \sim \theta$, the relationship between (y_2,θ_2) and (y_1,θ_1) is linear and can be written as

$$y_2 = \mathbf{A}y_1 + \mathbf{B}\theta_1 \tag{2.33a}$$

$$\theta_2 = \mathbf{C}y_1 + \mathbf{D}\theta_1 \tag{2.33b}$$

where $\mathbf{A}, \mathbf{B}, \mathbf{C}$ and $\mathbf{D}$ are real numbers (Peatross & Ware, 2011). Eqns. 2.33a and 2.33b can be rewritten in matrix form as

$$\begin{bmatrix} y_2 \\ \theta_2 \end{bmatrix} = \begin{bmatrix} \mathbf{A} & \mathbf{B} \\ \mathbf{C} & \mathbf{D} \end{bmatrix} \begin{bmatrix} y_1 \\ \theta_1 \end{bmatrix} \tag{2.34}$$

where the matrix with elements $\mathbf{A}$, $\mathbf{B}$, $\mathbf{C}$ and $\mathbf{D}$, characterizes the complete optical system and is called the ray-transfer matrix. The basic matrices that will be used in this dissertation to describe an optical system are as follows:

Free-space propagation: In a medium of uniform refractive index, rays travel along a straight path. Since the ray travels in the same direction $\theta_2 = \theta_1$. A ray traversing a distance d in free space is altered in accordance with $y_2 = y_1 + \theta_1 d$. The ray-transfer matrix is therefore given by

$$\mathbf{M} = \begin{bmatrix} 1 & d \\ 0 & 1 \end{bmatrix} \qquad (2.35)$$

Transmission through a thin lens: Paraxial rays enter and exit a thin lens at the same height, thus leaving $y_2 = y_1$. The relationship between θ_1 and θ_2 for paraxial rays transmitted through a thin lens of focal length f is given by $\theta_2 = -\frac{1}{f}y_1 + \theta_1$. Therfore, the ray-transfer matrix is

$$\mathbf{M} = \begin{bmatrix} 1 & 0 \\ -\frac{1}{f} & 1 \end{bmatrix} \qquad (2.36)$$

where $f > 0$ if the lens is convex and $f < 0$ if the lens is concave.

Matrices for multiple optical elements When analyzing optical systems that are made up of multiple regions of free space and thin lenses, the complete ray-transfer matrix of the entire optical system can be written as a product of the individual ray-transfer matrices (i.e., free-space or thin lens) in reverse chronological order. For an optical system with N optical components (each component must have its own ray-transfer matrix), the ray-transfer matrix of the entire optical system is givn by

$$\mathbf{M} = \mathbf{M}_N \dots \mathbf{M}_2 \mathbf{M}_1 \qquad (2.37)$$

INTERFERENCE OF LIGHT One of the important characteristics of electromagnetic waves is their ability, under certain circumstances, to interfere with one another. When two or more monochromatic waves are simultaneously present in the same space-time coordinates, the waves superpose to form a resultant wave of greater (*constructive interference*) or lower (*destructive interference*) amplitude.

Consider two monochromatic waves with the same angular frequency ω and complex amplitudes $\tilde{U}(\mathbf{r_1})$ and $\tilde{U}(\mathbf{r_2})$. The superposition of these two waves is then given by

$$\tilde{U}(\mathbf{r}) = \tilde{U}(\mathbf{r_1}) + \tilde{U}(\mathbf{r_2}) \qquad (2.38)$$

where $\tilde{U}(\mathbf{r_1}) = |\tilde{U}(\mathbf{r_1})|e^{j\psi_1}$, $\tilde{U}(\mathbf{r_2}) = |\tilde{U}(\mathbf{r_2})|e^{j\psi_2}$ and the intensities of the individual waves are $I_1 = |\tilde{U}(\mathbf{r_1})|^2$ and $I_2 = |\tilde{U}(\mathbf{r_2})|^2$. The intensity distribution of the wave resulting from the superposition can then be written as

$$\begin{aligned} I &= |\tilde{U}(\mathbf{r_1}) + \tilde{U}(\mathbf{r_2})|^2 \\ &= |\tilde{U}(\mathbf{r_1})|^2 + |\tilde{U}(\mathbf{r_2})|^2 + \tilde{U}(\mathbf{r_1})\tilde{U}^*(\mathbf{r_2}) + \tilde{U}^*(\mathbf{r_1})\tilde{U}(\mathbf{r_2}) \\ &= I_1 + I_2 + \sqrt{I_1 I_2}e^{j\psi_1}e^{-j\psi_2} + \sqrt{I_1 I_2}e^{-j\psi_1}e^{j\psi_2} \\ &= I_1 + I_2 + 2\sqrt{I_1 I_2}\cos(\psi_1 - \psi_2) \end{aligned} \qquad (2.39)$$

If the intensities of the two beams are equal i.e., $I_1 = I_2 = I_0$, we get

$$I = 2I_0[1 + \cos{(\psi_1 - \psi_2)}] = 4I_0 \cos^2{\left(\frac{\psi_1 - \psi_2}{2}\right)} \quad (2.40)$$

Eqn. 2.40 is the interference equation for two monochromatic waves with the same frequency. It must be noted, that temporal and spatial coherence are necessary conditions for interference to occur. Light emitted from a source is due to the emission of light from a large number of atoms or molecules independently. This introduces fluctuations in the light source because there is no fixed phase between two emissions occurring at two different times or locations in a random light source. Light emerging from a single ideal point source however has wavefronts that are spatially uniform in a lateral sense and such wavefronts are said to be *spatially coherent*. Young's double-slit experiment can be used to investigate the spatial coherence of quasi-monochromatic light and details pertaining to this experiment can be found in any physics textbook. Similarly, the *temporal coherence* is the measure of average correlation between the value of a wave and itself at any two instances separated by a time interval. The *degree of coherence* ($g(\tau)$) describes the visibility of the interference pattern and is given by

$$g(\tau) = \frac{G(\tau)}{G(0)} = \frac{\langle \tilde{U}^*(t)\tilde{U}(t+\tau)\rangle}{\langle \tilde{U}^*(t)\tilde{U}(t)\rangle} \quad (2.41)$$

where $G(\tau)$ is called the *coherence function* and is defined as

$$G(\tau) = \langle \tilde{U}^*(t)\tilde{U}(t+\tau)\rangle = \lim_{T\to\infty} \frac{1}{2T} \int_{-T}^{T} \tilde{U}^*(t)\tilde{U}(t+\tau)dt \quad (2.42)$$

Reconsidering the superposition of two waves shown previously in Eqn. 2.39, the equation can be rewritten as

$$I = I_1 + I_2 + 2\sqrt{I_1 I_2}|g_{12}|\cos{\psi_g} \quad (2.43)$$

where $|g_{12}|$ is the magnitude and $\cos{\psi_g}$ is the phase of the complex function g_{12} given by

$$g_{12} = \frac{\langle \tilde{U_1}^*(t)\tilde{U_2}(t)\rangle}{\sqrt{I_1 I_2}}$$

For two completely correlated waves, $|g_{12}| = 1$, and therefore we recover Eqn. 2.39. However for two completely uncorrelated waves, $|g_{12}| = 0$ and the intensity is just the sum of the intensities of the two individual waves, thus describing no interference. A Michelson interferometer (see. Fig. 2.4) is an experimental setup that can be used to investigate temporal coherence. A Michelson interferometer employs a 50:50 beamsplitter to divide an initial beam into two identical beams which travel different paths. The beams are then recombined using the same beamsplitter where they undergo superposition and create an interference pattern at the detector. For an interference pattern to be observed the relative path length difference between the two beams must be less than the coherence length of the

light source. The *coherence length* l_c of a light source is related to its spectral-width (i.e., range of frequencies) $\Delta\nu$ and is given by

$$l_c = \frac{c}{\Delta\nu} \tag{2.44}$$

where c is the speed of light in vacuum.
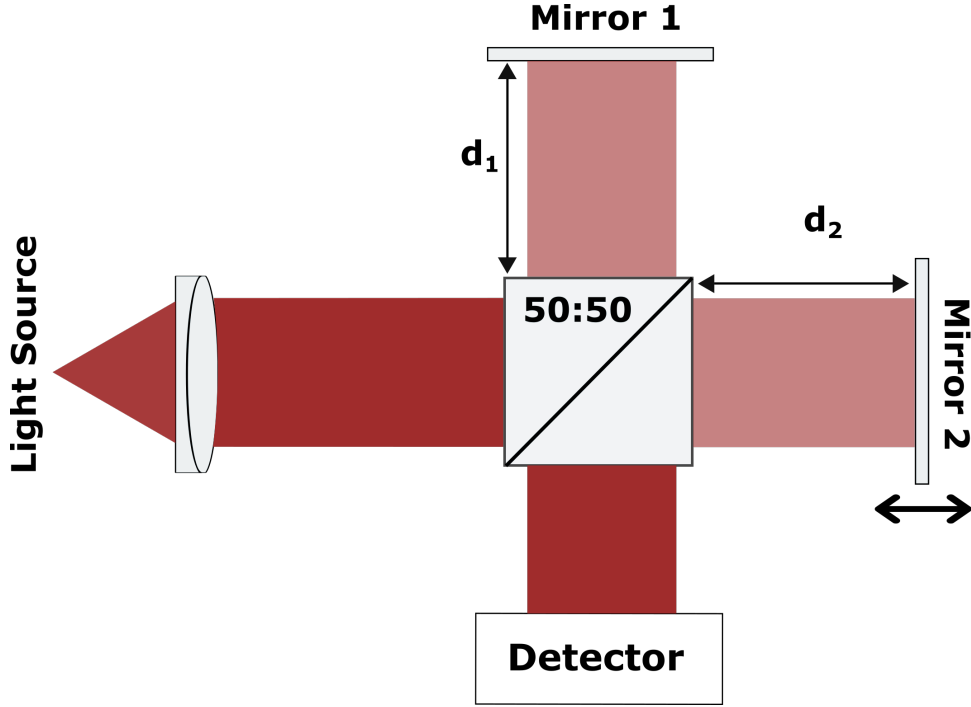
Figure 2.4: **Schematic of a Michelson interferometer**. An incoming beam is split into two by a 50:50 beam-splitter (BS). The two beams then reflect off mirrors 1 and 2 before recombining at the beam-splitter. Interference will be observed as long as the difference between d_1 and d_2 is no greater than half the coherence length of the light source.

Details on interference and the basics of coherence theory can be found in chapters 9 and 12 respectively in Hecht, 2017

2.2   Principles of Digital Holography

Holography is a two-part process which involves recording of the hologram by interference between the object wave and the reference wave. The resulting interferogram is recorded on an electronic camera, such as CCD or CMOS cameras and transferred to a computer in a digital form. The second part of digital holography involves numerically reconstructing (as opposed to optically reconstructing in conventional holography) the stored hologram to produce a 3D image of the object. The reader is

referred to classic textbooks (Collier et al., 1971; Goodman, 2005; Hariharan, 1996; Kim, 2011) for a detailed account of holography and its applications.
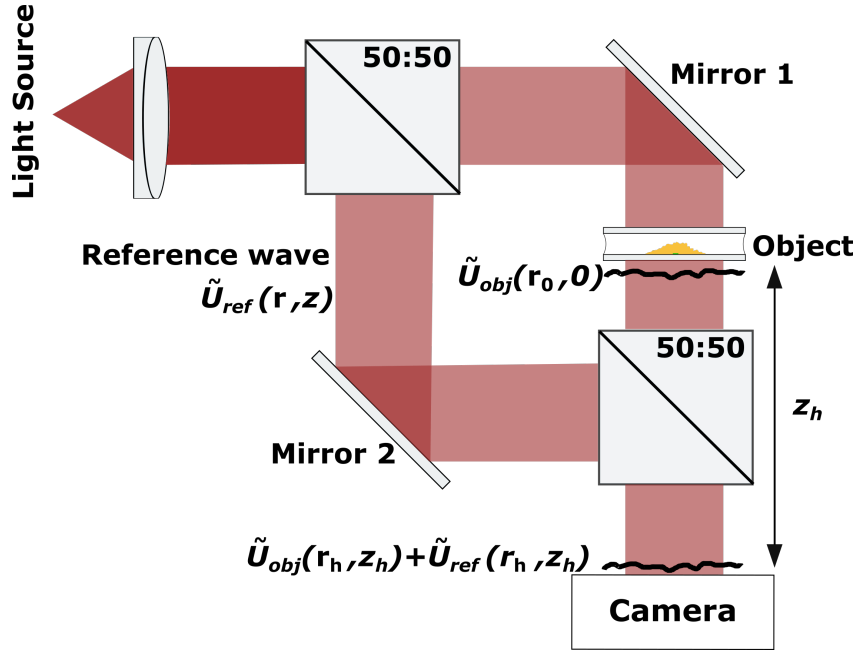
Figure 2.5: **Digital holography using a Mach-Zender interferometer**. The beam from the light source is split into two by a 50:50 beam-splitter. One of the beams reflects off Mirror 1 and passes through the object (object wave). The second beam (reference wave) reflects off Mirror 2 and recombines with the object wave at the second beamsplitter to form a hologram at the camera. For interference to occur, the distance travelled by the object wave and the reference wave to the beam-splitter must be the same. This experimental setup is known as a Mach-Zender interferometer.

HOLOGRAM FORMATION   Assuming that the light emanating from an object and the reference source obey the scalar theory of light and therefore satisy the time-independent Helmholtz equation (Eqn. 2.15), the object and reference waves can be defined, respectively as:

$$
\begin{aligned}
\tilde{U}_{obj}(\mathbf{r}, z) &= |U_{obj}(\mathbf{r}, z)|e^{j\phi(\mathbf{r},z)} \\
\tilde{U}_{ref}(\mathbf{r}, z) &= |U_{ref}(\mathbf{r}, z)|e^{j\psi(\mathbf{r},z)}
\end{aligned}
\tag{2.45}
$$

The complex field at the sample plane is denoted by $\tilde{U}_{obj}(\mathbf{r_o}, 0)$. This field propagates a distance z_h to the CCD camera (see Figure 2.5) which is also called the hologram plane. The field of the object wave at the hologram plane can be calculated using the Fresnel free-space propagator denoted by $h(\mathbf{r_h} - \mathbf{r_o}, z_h)$ and is therefore given by

$$\tilde{U}_{obj}(\mathbf{r_h}, z_h) = \iint\limits_{-\infty}^{\infty} \tilde{U}_{obj}(\mathbf{r_o}, 0) h(\mathbf{r_h} - \mathbf{r_o}, z_h) \, d^2\mathbf{r_o} \tag{2.46}$$

where the Fresnel propagator is given by Eqn. 2.24

$$h(\mathbf{r}, z) = \frac{e^{jkz}}{j\lambda z} \exp\left(\frac{jk}{2z} \|\mathbf{r}\|^2\right) \tag{2.47}$$

and is subject to the conditions outlined earlier (see *Monochromatic Wave Propagation*).

The primary goal in digital holography is to reconstruct the complex field $\tilde{U}_{obj}(\mathbf{r_o}, 0)$ at the sample plane based on a 2D intensity map recorded by the CCD camera at the hologram plane. The 2D intensity map $|U_{obj}(\mathbf{r_h}, z_h)|^2$ recorded by the CCD camera however is an intensity image and holds no information about the phase of the complex field (i.e., depth information of the object). In digital holography, the phase information is encoded into the intensity image by directing an additional reference wave $\tilde{U}_{ref}(\mathbf{r_h}, z_h)$ onto the CCD camera, which interferes with $\tilde{U}_{obj}(\mathbf{r_h}, z_h)$ to produce a 2D image with phase-dependent intensity variations (hologram). The requirements for the two waves to interfere are the same as discussed earlier (see *Interference of Light*). The total field incident on the CCD camera (hologram plane) as a result of the superposition of the object and reference wave is then given by

$$\tilde{U}_h(\mathbf{r_h}, z_h) = \tilde{U}_{obj}(\mathbf{r_h}, z_h) + \tilde{U}_{ref}(\mathbf{r_h}, z_h) \tag{2.48}$$

The intensity distribution recorded at the CCD camera due to the complex field resulting from the superposition of the object and reference wave is then given by

$$
\begin{aligned}
I_h(\mathbf{r_h}) &= |\tilde{U}_{obj}(\mathbf{r_h}) + \tilde{U}_{ref}(\mathbf{r_h})|^2 \\
&= |\tilde{U}_{obj}(\mathbf{r_h})|^2 + |\tilde{U}_{ref}(\mathbf{r_h})|^2 + \tilde{U}_{obj}(\mathbf{r_h})\tilde{U}^*_{ref}(\mathbf{r_h}) + \tilde{U}^*_{obj}(\mathbf{r_h})\tilde{U}_{ref}(\mathbf{r_h}) \\
&= I_{obj}(\mathbf{r_h}) + I_{ref}(\mathbf{r_h}) + \tilde{U}_{obj}(\mathbf{r_h})\tilde{U}^*_{ref}(\mathbf{r_h}) + \tilde{U}^*_{obj}(\mathbf{r_h})\tilde{U}_{ref}(\mathbf{r_h})
\end{aligned}
\tag{2.49}
$$

The axial parameter along the optical axis z_h has been dropped for representational simplicity. In Eqn. 2.49, the first and second terms are, respectively, the intensities of the object and reference waves. The third and fourth terms are created due to the interference between the two waves and are complex conjugates of one another. Together, they are responsible for creating the phase-dependent intensity variations and are called an interferogram. The third term in Eqn. 2.49 is of interest to us as it contains $\tilde{U}_{obj}(\mathbf{r_h}, z_h)$ which is related to $\tilde{U}_{obj}(\mathbf{r_o}, 0)$ as shown in Eqn. 2.46. Hence, the next step of the process involves extracting and isolating the third term from Eqn. 2.46.

PHASE-SHIFTING   Up until now, it was assumed that the relative phase between the object wave and reference wave is fixed and was therefore systematically omitted in our analysis. It is possible to extract the complex interference term from Eqn. 2.46, by introducing changes in the relative phase

between the two waves and varying it in a controlled manner. By introducing a change δ in the relative phase between the two waves Eqn. 2.48 can be rewritten as

$$\tilde{U}_h(\mathbf{r_h}, z_h) = \tilde{U}_{obj}(\mathbf{r_h}, z_h) + \tilde{U}_{ref}(\mathbf{r_h}, z_h)e^{j\delta} \tag{2.50}$$

Experimentally, δ is controlled by adjusting the optical path length of one of the interfering beams. This can be done by placing one of the mirrors of a Michelson interferometer on a piezoelectric transducer, therefore allowing electrical control over the path length of the beam. Introducing the phase term $e^{j\delta}$ in Eqn. 2.48 leads to

$$I_h^{\delta}(\mathbf{r_h}) = I_{obj}(\mathbf{r_h}) + I_{ref}(\mathbf{r_h}) + e^{-j\delta}\tilde{U}_{obj}(\mathbf{r_h})\tilde{U}_{ref}^*(\mathbf{r_h}) + e^{j\delta}\tilde{U}_{obj}^*(\mathbf{r_h})\tilde{U}_{ref}(\mathbf{r_h}) \tag{2.51}$$

which differs from Eqn. 2.49 in that it features a controllable parameter δ. By varying δ and capturing multiple holograms, it is possible to extract the complex interference term ($\tilde{U}_{obj}(\mathbf{r_h})\tilde{U}_{ref}^*(\mathbf{r_h})$). This method of isolating the complex interference term is known as *phase-shifting* (Yamaguchi & Zhang, 1997). In a K-step phase-shifting technique, the phase is shifted in a circular sequence $\delta_k = \frac{2\pi k}{K}$, where k is incremented from 0 to $K - 1$. The complex interference term in Eqn. 2.51 can then be isolated using the algorithm

$$\tilde{U}_{obj}(\mathbf{r_h})\tilde{U}_{ref}^*(\mathbf{r_h}) = \frac{1}{K} \sum_{k=0}^{K-1} e^{j\delta_k} I_h^{\delta_k}(\mathbf{r_h}) \tag{2.52}$$

In most applications, K typically ranges from 3 to 5. Further details on phase-shifting digital holography can be found in Chapter 8 in Kim, 2011.

FRESNEL HOLOGRAPHY As mentioned earlier, the second part of the process in digital holography involves the reconstruction of the complex field $\tilde{U}_{obj}(\mathbf{r_o}, 0)$ at the sample plane from Eqn. 2.49. There are various strategies developed to reconstruct the complex field $\tilde{U}_{obj}(\mathbf{r_o}, 0)$. Details pertaining to the different reconstruction strategies are beyond the scope of this dissertation and can be found in Mertz, 2019 and Kim, 2011. This dissertation will discuss one such reconstruction strategy known as *Fresnel holography* or *back-propagation* which has been heavily used in the work presented in this dissertation.

The complex interference term extracted using Eqn. 2.52 can be rewritten as

$$\tilde{U}_{obj}(\mathbf{r_h})\tilde{U}_{ref}^*(\mathbf{r_h}) = \tilde{U}_{ref}^*(\mathbf{r_h}) \int\!\!\!\int\limits_{-\infty}^{\infty} \tilde{U}_{obj}(\mathbf{r_o}, 0)h(\mathbf{r_h} - \mathbf{r_o}, z_h) \, d^2\mathbf{r_o} \tag{2.53}$$

In the simplest case where $\tilde{U}_{ref}^*(\mathbf{r_h})$ can be assumed to be a uniform plane wave and the relative phase between the two waves is fixed, $\tilde{U}_{ref}^*(\mathbf{r_h})$ can be taken to be real which leads to

$$\tilde{U}_{obj}(\mathbf{r_h})\tilde{U}_{ref}^*(\mathbf{r_h}) = \sqrt{I_{ref}} \iint\limits_{-\infty}^{\infty} \tilde{U}_{obj}(\mathbf{r_o}, 0)h(\mathbf{r_h} - \mathbf{r_o}, z_h) \, d^2\mathbf{r_o} \qquad (2.54)$$

By applying the Fresnel free-space propagator in the backward direction to both sides of Eqn. 2.54, we back-propagate the complex interference term to the sample plane to calculate the complex field of the object at the sample plane. The application of the Fresnel propagator in the backward direction to Eqn. 2.54 leads to

$$\iint\limits_{-\infty}^{\infty} \tilde{U}_{obj}(\mathbf{r_h})\tilde{U}_{ref}^*(\mathbf{r_h})h(\mathbf{r_o} - \mathbf{r_h}, -z_h) \, d^2\mathbf{r_h}$$
$$= \sqrt{I_{ref}} \iiiint\limits_{-\infty}^{\infty} \tilde{U}_{obj}(\mathbf{r_o}, 0)h(\mathbf{r_o} - \mathbf{r_h}, -z_h)h(\mathbf{r_h} - \mathbf{r_o}, z_h) \, d^2\mathbf{r_o}d^2\mathbf{r_h} \qquad (2.55)$$

where the term inside the integral in right hand side of Eqn. 2.55 describes the complex field $\tilde{U}_{obj}(\mathbf{r_o}, 0)$ travelling a roundtrip to the camera plane and back to the sample plane without any changes. Therefore, Eqn. 2.55 can be rewritten as

$$\tilde{U}_{obj}(\mathbf{r_o}, 0) = \frac{1}{\sqrt{I_{ref}}} \iint\limits_{-\infty}^{\infty} \tilde{U}_{obj}(\mathbf{r_h})\tilde{U}_{ref}^*(\mathbf{r_h})h(\mathbf{r_o} - \mathbf{r_h}, -z_h) \, d^2\mathbf{r_h} \qquad (2.56)$$

which describes a Fresnel back-propagation of the complex interference term $\tilde{U}_{obj}(\mathbf{r_h})\tilde{U}_{ref}^*(\mathbf{r_h})$ to the sample plane to calculate the complex field $\tilde{U}_{obj}(\mathbf{r_o}, 0)$ at the sample plane. Eqn. 2.56 is a numerically time consuming calculation as it involves a 2D convolution and it is usually simplified by using the convolution theorem which requires the application of two Fourier transforms instead

$$\tilde{U}_{obj}(\mathbf{r_o}, 0) = \frac{1}{\sqrt{I_{ref}}}\mathscr{F}^{-1}\{\mathscr{F}\{\tilde{U}_{obj}(\mathbf{r_h})\tilde{U}_{ref}^*(\mathbf{r_h})\}\mathscr{F}\{h(\mathbf{r_o} - \mathbf{r_h}, -z_h)\}\} \qquad (2.57)$$

2.3   Self-Interference Digital Holography

A crucial requirement for digital holographic microscopy (DHM) is the mutual coherence of the object and reference beams. If the two beams are not mutually coherent, they will not interfere thereby not creating a hologram at the CCD plane. However, fluorescence microscopy, which has become a mainstay in most biological and biomedical laboratories, uses fluorescence to create specificity and contrast in biological samples and fluorescent light is inherently incoherent. To overcome this limitation, the principle of self-interference has been used to develop DHM systems that allow the recording of holograms using fluorescent light. The self-interference principle dictates that any two, or more,

beams originating from the same point source are mutually coherent, and hence they can be mutually interfered. In the case of fluorescence, where any two different point sources on the sample are mutually incoherent, the self-interference property becomes the only way to obtain any interference pattern, and thus allows the recording of holograms. Although there exist other methods to create holograms using incoherent light such as optical scanning holography (Poon & Indebetouw, 2003; Schilling et al., 1997) and multiple view projection methods (Rivenson et al., 2011; Shaked et al., 2009), they do not use the principle of self-interference. An excellent review of different techniques for performing digital holography with incoherent light can be found in Rosen et al., 2009 and J.-P. Liu et al., 2018.

In this section, I will focus on incoherent digital holography (IDH) techniques that are based on the principle of self-interference (Kim, 2012a, 2013; Rosen & Brooker, 2007; Vijayakumar et al., 2016). Self-interference digital holography (SIDH) works on the principle of interfering incoherent light with itself. The incoherent light emitted from the object is split into two beams that are separately phase-modulated and recombined in a common plane to produce an interferogram. The density of the fringes on the interferogram depends on the distance between the object under investigation and the imaging lens. One or more holograms are acquired and stored in the computer. Most techniques based on SIDH require the acquisition of multiple holograms to extract the complex interference term (see 'Phase-Shifting' in Section 2.2). The isolation of the complex interference term eliminates the bias-image and the holographic 'twin-image' (virtual image due to $\tilde{U}_{obj}^*(\mathbf{r_h})\tilde{U}_{ref}(\mathbf{r_h})$ term in Eqn. 2.49 superimposed on the real image). Although single-shot SIDH techniques have been developed, most of them rely on performing optical tricks to acquire multiple holograms simultaneously (Liang et al., 2020; Nobukawa et al., 2018; Quan et al., 2017; Sakamaki et al., 2020) which are then combined to form a single digital hologram. Computational methods such as compressive sensing (Weng et al., 2016) and deep learning (Rivenson et al., 2018) have also been used to reconstruct the image of an object from a single hologram . Recently a single-shot SIDH technique using a modified reconstruction process has been developed that requires the acquisition of only one hologram to reconstruct the image of the object (Vijayakumar et al., 2020).

A comprehensive review of IDH using self-interference can be found in Rosen et al., 2019.

THERORETICAL ANALYSIS OF SIDH   In this section I will provide a theoretical analysis of SIDH following the convention in Rosen and Brooker, 2007. Referring to the generalized diagram in Fig. 2.6, consider a point source at $(\mathbf{r}_s, z_s)$ in front of the objective lens with focal length f_o. After light from the point source propagates through the objective lens to the diffractive optical element (DOE), it gets focused by the DOE displaying the phase components of two quadratic phase functions with focal lengths f_{d1} and f_{d2}. After further propagating a distance of z_h to the camera, the complex amplitude at the camera is given by

$$U_{CCD}(x_o, y_o) = \left(C_1(\mathbf{r_s}) L\left(\frac{-\mathbf{r_s}}{z_s} \right) Q\left(\frac{1}{z_s} \right) Q\left(\frac{-1}{f_o} \right) \otimes Q\left(\frac{1}{d} \right) \right)$$
$$\times \left(B_1 Q\left(\frac{-1}{f_{d1}} \right) + B_2 \exp(i\theta) Q\left(\frac{-1}{f_{d2}} \right) \right) \otimes Q\left(\frac{1}{z_h} \right) \tag{2.58}$$

where C_1 is a complex constant related to the complex amplitude of the point source, '$*$' denotes a 2D convolution, d is the distance between the objective lens and the DOE, B_1 and B_2 are constants that control the contribution of each lens to the hologram, θ is a constant phase term applied to the DOE to eliminate the bias term and the twin image, and z_h is the distance between the DOE and the camera.
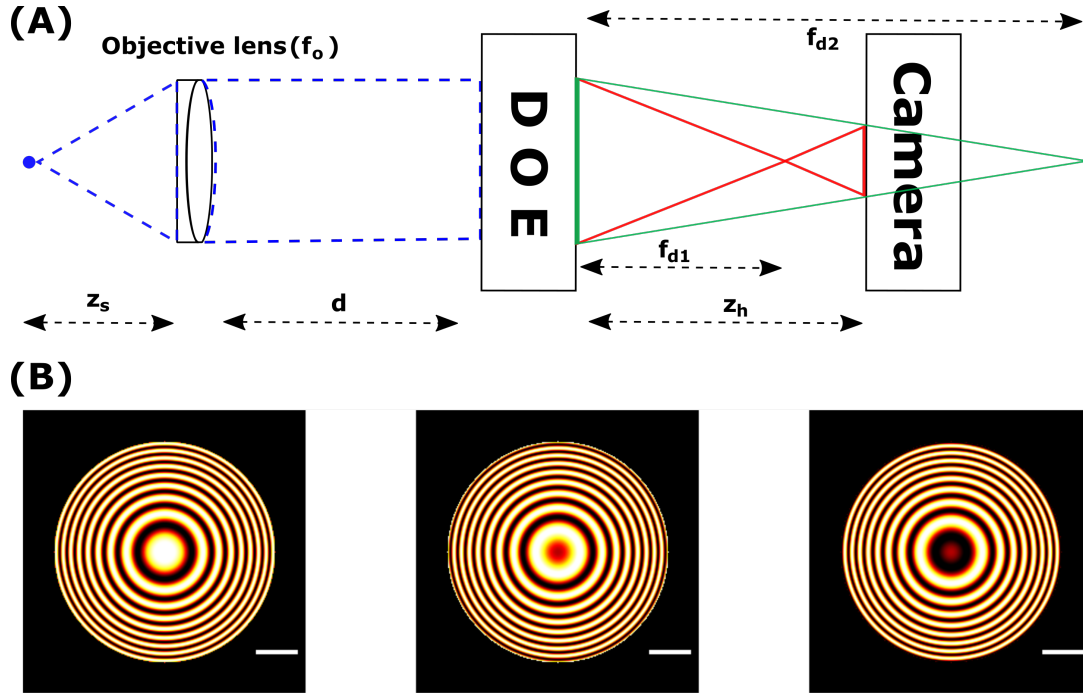
Figure 2.6: **Generalized Configuration for SIDH**. (A) Detection path for imaging using SIDH. SIDH creates holograms by a single-channel on axis incoherent interferometer process. (B) Simulated images of holograms of a single-emitter recorded using SIDH. We refer to these as the point spread holograms (PSH). Three holograms with different phases (0°, 120° and 240°) are required to reconstruct the final image. All scale bars are 5 μm.

After squaring and evaluating the complex amplitude given by Eqn. 2.58, the intensity of the recorded hologram of a point source can be calculated and is given by

$$I_{CCD}(x,y) = R_1 \left(2 + \exp\left\{ \frac{i\pi}{\lambda z_r}[(x - M_T x_s)^2 + (y - M_T y_s)^2] + i\theta \right\} \right.$$
$$\left. + \exp\left\{ \frac{-i\pi}{\lambda z_r}[(x - M_T x_s)^2 + (y - M_T y_s)^2] - i\theta \right\} \right)$$

(2.59)

where R_1 is a constant, λ is the wavelength of the emitted light, z_r is the reconstruction distance from the hologram plane, and M_T is the transverse magnification of the system. Besides the constant term, Eqn. 2.59 contains two terms that describe the correlation between the object and the z-dependent quadratic phase function. The constant term is the bias term and the third term is called the twin image. Both these terms need to be eliminated to reconstruct a clear image from the recorded hologram. Three holograms with phase shifts $\theta_1 = 0^o$, $\theta_2 = 120^o$, $\theta_3 = 240^o$ are recorded, which are then algebraically combined to form a final complex hologram that takes the form

$$I_{\text{final}}(x,y) = I_{CCD1}(x,y)[e^{-i\theta_3} - e^{-i\theta_2}]$$
$$+ I_{CCD2}(x,y)[e^{-i\theta_1} - e^{-i\theta_3}]$$
$$+ I_{CCD3}(x,y)[e^{-i\theta_2} - e^{-i\theta_1}]$$
$$= 6\sin(\frac{2\pi}{3}) \exp\left\{ \frac{i\pi}{\lambda z_r}[(x - M_T x_s)^2 + (y - M_T y_s)^2] \right\}$$

(2.60)

The final complex hologram $I_{\text{final}}(x,y)$ can be numerically back-propagated to produce a reconstructed 3D image $s(x,y,z)$ of the sample.

$$s(x,y,z) = I_{\text{final}}(x,y) * \exp\left[\frac{i\pi}{\lambda z_r}(x^2 + y^2) \right]$$

(2.61)

where z, which is a function of z_r, is the distance of the emitter from the objective focal plane.

SIDH WITH ONE PLANE WAVE AND ONE SPHERICAL WAVE   We first review the simplest case in SIDH, where the hologram is formed as a result of the interference between one spherical wave and one plane wave. Referring to Fig. 2.7, f_{d1} is responsible for the spherical wave and the plane wave is created when $f_{d2} \to \infty$. For the system shown in Fig. 2.7, the reconstruction distance (z_r) and the transverse magnification (M_T) are given by

$$z_r = \begin{cases} \pm(z_h - f_{d1}), & \text{for} \quad z_s = f_o \cap f_{d2} \to \infty \\ \\ \pm\left(\dfrac{(f_1 + z_h)(f_e + d + z_h)}{f_1 - f_e - d} \right), & \text{for} \quad z_s \neq f_o \cap f_{d2} \to \infty \end{cases}$$
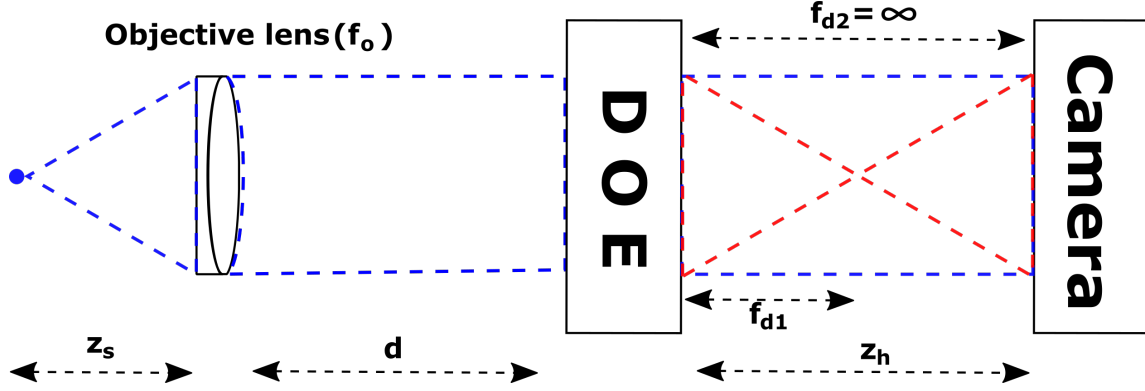
(2.62)

Figure 2.7: **SIDH with one plane wave and one spherical wave.** The interferogram formed at the camera is a result of a plane wave ($f_{d2} = \infty$) and a spherical wave (f_{d1}).

and

$$M_T = \left| \frac{\partial x_r}{\partial x_s} \right| = \begin{cases} \dfrac{z_h}{f_o}, & \text{for} \quad z_s = f_o \cap f_{d2} \to \infty \\[2ex] \dfrac{f_e z_h}{z_s(f_e + d)}, & \text{for} \quad z_s \neq f_o \cap f_{d2} \to \infty \end{cases} \tag{2.63}$$

where

$$f_1 = \frac{f_{d1}(f_e + d)}{f_{d1} - (f_e + d)}, \qquad \text{and} \qquad f_e = \frac{z_s f_o}{(f_o - z_s)}$$

The $\pm$ signs in Eqn. 2.62 show that the images can be reconstructed from either the real or the virtual image, depending on which is isolated using the phase-shifting process as described in Eqn. 2.60. The radius of the hologram at the CCD plane calculated using the ABCD ray transfer matrix framework. The framework for this analysis has been described earlier (see *Ray-transfer matrices*). The radii of the plane and spherical wave, for the optical system described by Fig. 2.7 at the CCD plane are given by

$$\begin{bmatrix} r_{plane} \\ \gamma_{plane} \end{bmatrix} = \begin{bmatrix} 1 & (z_h + d) \\ 0 & 1 \end{bmatrix} \begin{bmatrix} 1 & 0 \\ -1/f_o & 1 \end{bmatrix} \begin{bmatrix} 1 & z_s \\ 0 & 1 \end{bmatrix} \begin{bmatrix} h_{enter} \\ \gamma_{enter} \end{bmatrix} \tag{2.64}$$

and

$$\begin{bmatrix} r_{spherical} \\ \gamma_{spherical} \end{bmatrix} = \begin{bmatrix} 1 & z_h \\ 0 & 1 \end{bmatrix} \begin{bmatrix} 1 & 0 \\ -1/f_{d1} & 1 \end{bmatrix} \begin{bmatrix} 1 & d \\ 0 & 1 \end{bmatrix} \begin{bmatrix} 1 & 0 \\ -1/f_o & 1 \end{bmatrix} \begin{bmatrix} 1 & z_s \\ 0 & 1 \end{bmatrix} \begin{bmatrix} h_{enter} \\ \gamma_{enter} \end{bmatrix} \tag{2.65}$$

where r_{plane} and $r_{spherical}$ are the radii of the plane and spherical waves at the CCD plane and γ_{plane} and $\gamma_{spherical}$ are the maximum angles at which the rays from the plane and spherical waves meet

the CCD. $h_{enter} = 0$ is the distance from the optical axis at which the ray enters the system and $\gamma_{enter} = NA$ is the maximum angle at which the rays enters the system. Since the radius of the hologram is limited by the area of overlap between the radius of the plane and spherical waves the radius of the hologram (r_h) can be defined as

$$r_h = min(r_{plane}, r_{spherical})$$
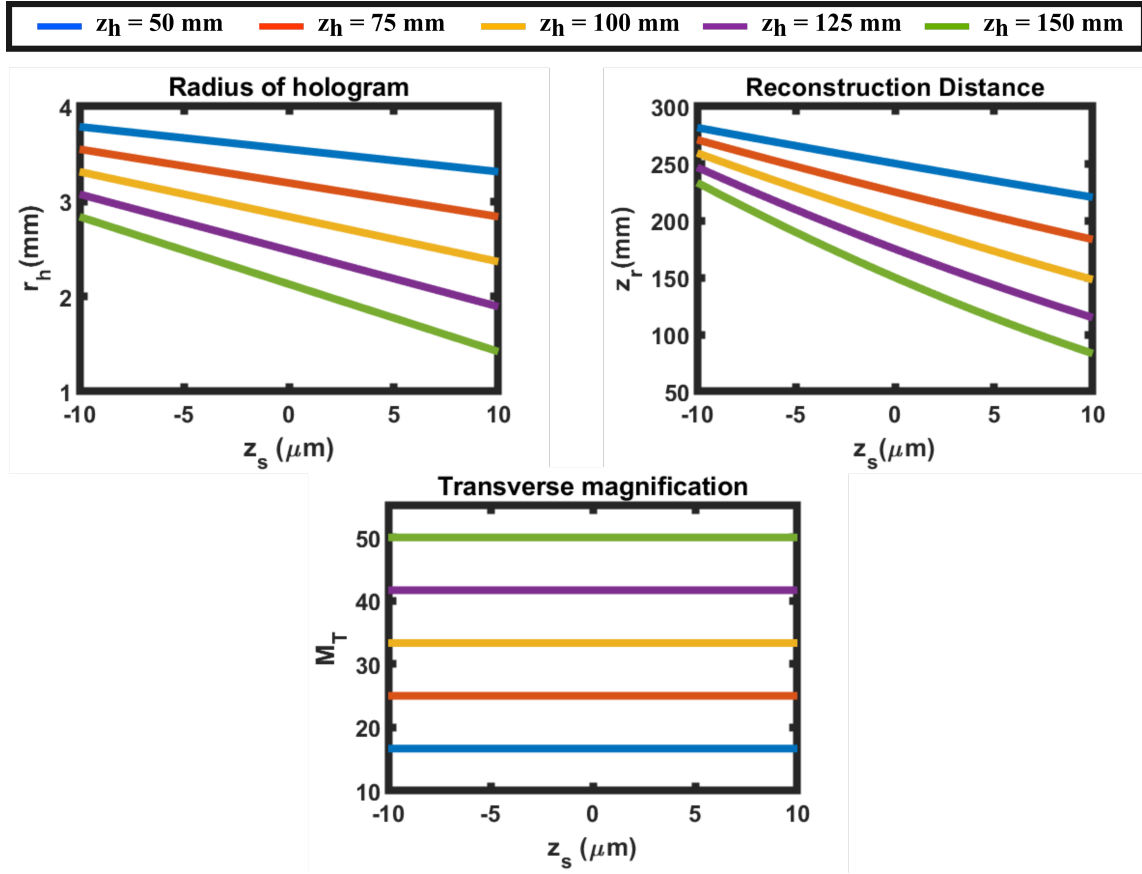
Figure 2.8: **Parameters of SIDH using configuration 1.** Hologram radius (r_h), reconstruction distance (z_r) and transverse magnification (M_T) of configuration 1 when the CCD is placed at different distances away from the DOE.

Using Eqns. 2.62-2.65 we can calculate various parameters of an SIDH system such as the radius of the hologram (r_h), transverse magnification of the system (M_T) and the reconstruction distance (z_r) for different DOE-CCD distances (z_h)(shown in Fig. 2.8). In order to simulate the SIDH system, a 60x, 1.42 numerical aperture (NA) objective is assumed $(f_o = 3$ mm), imaging into an index of 1.515. The wavelength of light is 670 nm. The distance between the objective lens and the DOE is $d = 3$ mm, the focal length of the quadratic phase pattern is $f_{d1} = 300$ mm and $f_{d2} = \infty$.

SIDH WITH TWO SPHERICAL WAVES SIDH has also been performed using two spherical waves with different focal lengths f_{d1} and f_{d2} to create the interferogram (Katz et al., 2012). This configuration shown in Fig. 2.9, offers the possibility of placing the camera closer to the DOE allowing greater light efficiency without adversely affecting the resolution in the reconstructed image. When SIDH is performed with this configuration, the reconstruction distance (z_r) is given by

$$z_r = \begin{cases} \pm \dfrac{(z_h - f_{d1})(z_h - f_{d2})}{f_{d1} - f_{d2}}, & \text{for} \quad z_s = f_o \cap f_{d2} \neq \infty \\[4mm] \pm \left(\dfrac{z_{f1} z_{f2}}{z_d^2 (f_{d1} - f_{d2})} \right), & \text{for} \quad z_s \neq f_o \cap f_{d2} \neq \infty \end{cases} \tag{2.66}$$

where

$$z_{fn} = z_h z_d - f_{dn}(z_d + z_h), \qquad \text{and} \qquad z_d = \frac{z_s(f_o - d) + f_o d}{(f_o - z_s)}$$
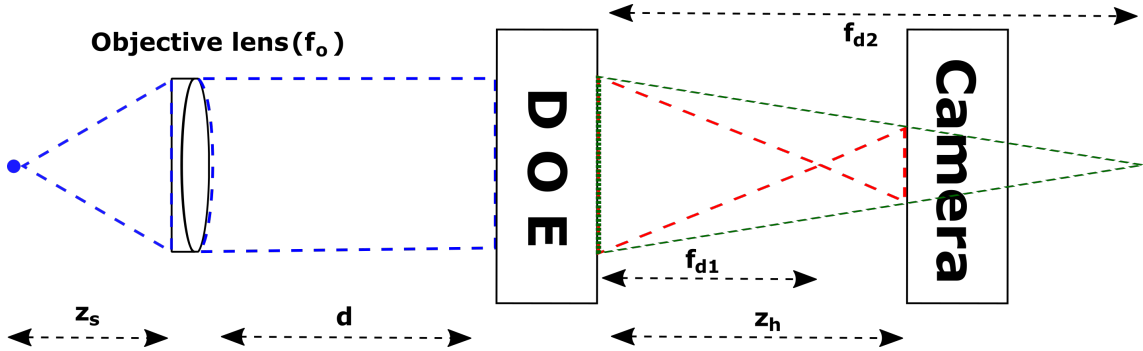
Figure 2.9: **SIDH with two spherical waves.** The interferogram formed at the camera is a result of two spherical waves (f_{d1} and f_{d2}).

The transverse magnification (M_T) for SIDH with two spherical waves is the same as that with one spherical and plane wave as described previously in Eqn. 2.63. The ABCD ray transfer matrices for the system shown in Fig. 2.9 are given by

$$\begin{bmatrix} r_{f_{d1}} \\ \gamma_{f_{d1}} \end{bmatrix} = \begin{bmatrix} 1 & z_h \\ 0 & 1 \end{bmatrix} \begin{bmatrix} 1 & 0 \\ -1/f_{d1} & 1 \end{bmatrix} \begin{bmatrix} 1 & d \\ 0 & 1 \end{bmatrix} \begin{bmatrix} 1 & 0 \\ -1/f_o & 1 \end{bmatrix} \begin{bmatrix} 1 & z_s \\ 0 & 1 \end{bmatrix} \begin{bmatrix} h_{enter} \\ \gamma_{enter} \end{bmatrix} \tag{2.67}$$

and

$$\begin{bmatrix} r_{f_{d2}} \\ \gamma_{f_{d2}} \end{bmatrix} = \begin{bmatrix} 1 & z_h \\ 0 & 1 \end{bmatrix} \begin{bmatrix} 1 & 0 \\ -1/f_{d2} & 1 \end{bmatrix} \begin{bmatrix} 1 & d \\ 0 & 1 \end{bmatrix} \begin{bmatrix} 1 & 0 \\ -1/f_o & 1 \end{bmatrix} \begin{bmatrix} 1 & z_s \\ 0 & 1 \end{bmatrix} \begin{bmatrix} h_{enter} \\ \gamma_{enter} \end{bmatrix} \tag{2.68}$$

where $r_{f_{d1}}$ and $r_{f_{d2}}$ are the radii of the spherical waves formed due to the two focal lengths f_{d1} and f_{d2} at the CCD plane. The radius of the hologram (r_h) is this configuration is defined by the area of overlap between the two spherical waves at the CCD plane as is similarly given by

$$r_h = min(r_{f_{d1}}, r_{f_{d2}})$$

The simulations for this configuration were performed using the same parameters as in the first configuration however the focal lengths of the two lenses were changed to $f_{d1} = 200$ mm and $f_{d2} = 400$ mm. Although this configuration allows the camera to be placed nearer to the CCD, in order to image across the entire axial range (~ 20 μm) it is necessary to place it not in the range $z_h = 200$ to 400 mm (f_{d1} to f_{d2}) to ensure that the values of the reconstruction distance (z_r) are not symmetric across the focal plane (Fig. 2.10)
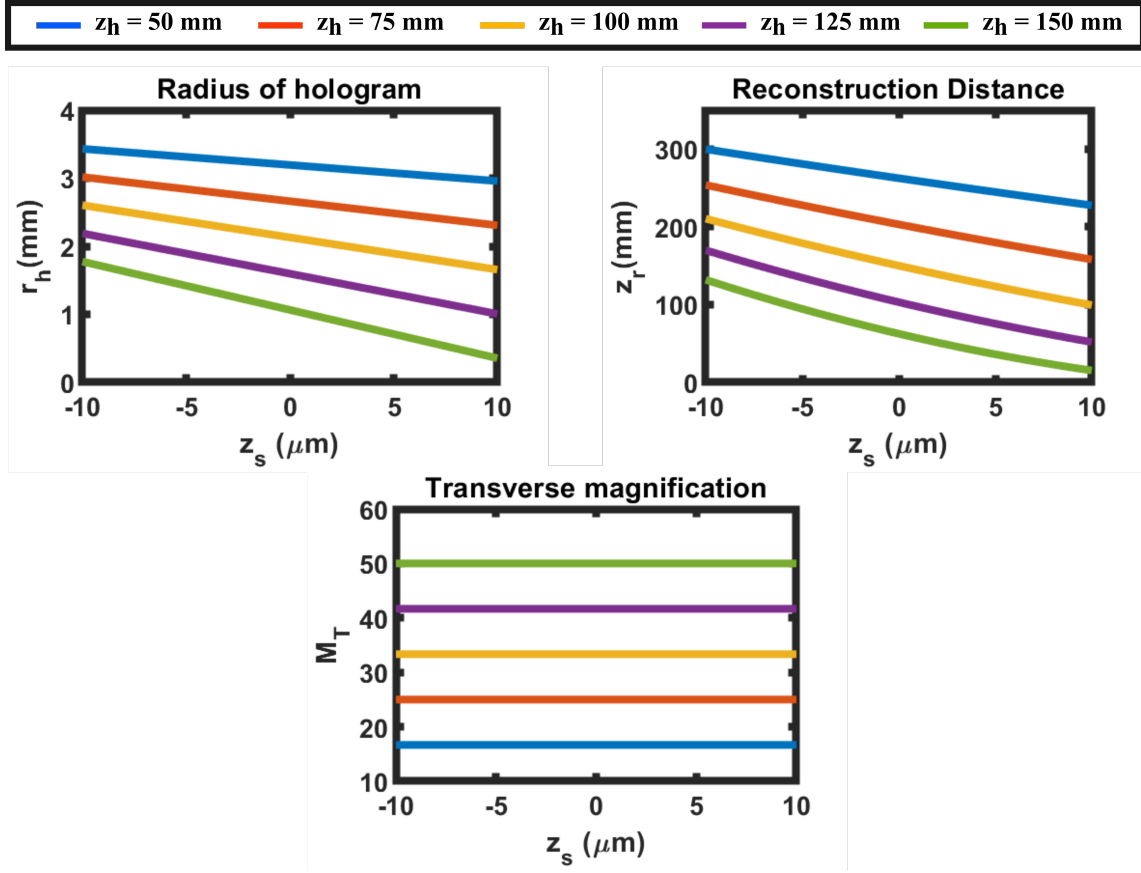
Figure 2.10: **Parameters of SIDH using configuration 2.** Hologram radius (r_h), reconstruction distance (z_r) and transverse magnification (M_T) of configuration 2 when the CCD is placed at different distances away from the DOE.

2.4 Conclusion

In this chapter I have introduced the mathematical and physical concepts required to understand the principles of self-interference digital holography. Furthermore, I have discussed the important param-

eters in an SIDH system and how they vary with changes in the optical system. The analysis provided in this chapter should be sufficient to understand the results provided in the next two chapters.

CHAPTER 3

3D PARTICLE LOCALIZATION USING SELF-INTERFERENCE DIGITAL HOLOGRAPHY

This Chapter focuses on the computational algorithms and instrument designs I developed and implemented along with my advisor Dr. Peter Kner to enable the imaging and localization of point-like emitters using self-interference digital holography (SIDH). Chapters 1 and 2 provide enough background to understand most of the instruments, experiments and calculations described throughout this chapter. I will briefly review the concept of localization and discuss the localization algorithm used in this dissertation for finding the sub-pixel positions of the emitters. Algorithms that I utilized but did not further refine will not be covered here.

First, I will present and describe an optical design used to image 0.2 μm fluorescent microspheres using SIDH with a diffractive optical element (DOE). Next, an optical design for implementing SIDH with a Michelson interferometer is shown. This design overcomes the problem of low light transmission faced when using a DOE to perform SIDH and allows us to image smaller particles (40 and 100 nm) that emit a significantly lower number of photons. Finally, I describe the design and operation of a light-sheet illumination pathway used in conjunction with the SIDH setup using a Michelson interferometer. The light-sheet illumination helps reduce the background noise thereby improving the Signal-to-background ratio (SBR) of the collected holograms.

Parts of the work described in this chapter have been published in:

- **Marar, A.**, & Kner, P. (2020). Three-dimensional nanoscale localization of point-like objects using self-interference digital holography. *Optics letters,45*(2), 591–594.

- **Marar, A.**, & Kner, P. (2019). Three-dimensional localization microscopy by incoherent holography. *Single Molecule Spectroscopy and Superresolution Imaging XII.*Vol. 10884. International Society for Optics and Photonics, 2019.

3.1 Simulations of SMLM using SIDH

In this section I present the results of a working simulation of the microscope that is in conformity with the theoretical principles upon which this technique relies. To demonstrate the working of the microscope, I programmed a computer model in Python that simulates the dynamics of fluorescent molecules placed on a synthetic helical structure (the object under study) that has a radius of 0.5 μm and extends 10 μm axially. The final output from the microscope undergoes two further steps of computational processing, before it delivers a result that is the super-resolved image. First, the raw hologram data is reconstructed that results in diffraction-limited images. The diffraction-limited images of the fluorescent molecules then undergo localization to provide a list of coordinates that result in a high-resolution image.
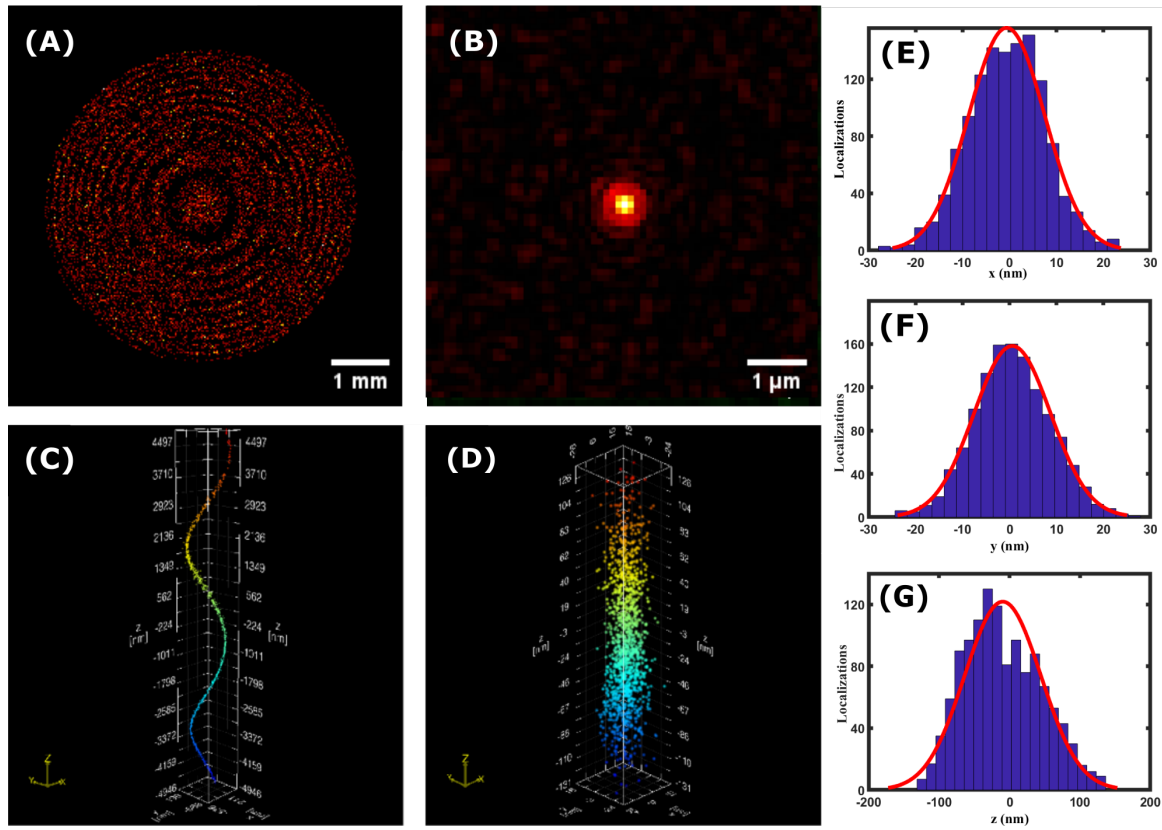
Figure 3.1: **SLM Reflectance function for SIDH**. Simulations of holographic imaging with 1000 phtons. (A) One of 3 raw images captured by the camera. (B) Reconstructed image of a fluorescent molecule at a single axial plane. (C) Reconstruction of helical structure of radius 500nm spanning an axial range of 10 μm. (D) Three-dimensional localization distribution of a single molecule placed at the center. (E,F,G) Histograms of localizations in x, y and z were fit to a Gaussian function, yielding standard deviations of $\sigma_x = \sigma_y = 8$ nm and $\sigma_x = 54$ nm.

A synthetic data series consisting of 3600 raw images was generated using 1000 expected photons per frame per fluorophore, and reconstructed using the first step to produce axial stacks of diffraction-limited images of the fluorescent molecules. Each diffraction-limited image is a result of three raw images, thus producing 1200 stacks of diffraction-limited images. Each stack comprises of 50 images at different axial planes, spanning a range of 10 μm with a step size of 200 nm. The 1200 stacks further undergo STORM reconstruction using parameter estimation algorithms (Smith et al., 2010) to provide a table with the localized coordinates of the fluorescent molecules.

To calculate the localization precision, a synthetic fluorescent molecule was programmed at the center of a 3D volume and 4500 raw images were generated. The standard deviations of the localized coordinates were found to calculate the spatial and axial localization precision.

3.2 SIDH of fluorescent nanoparticles using a Spatial Light Modulator

SIDH can be performed by having the light emitted from the sample interact with a DOE so that the light can interfere with itself to produce a hologram. In this dissertation, a spatial light modulator (SLM) was used as a DOE. The polarization sensitivity of an SLM leads to a 50% loss of the light emitted from the sample. The pixels of an SLM are in the form of a 2D grid like structure which results in higher diffraction orders when the light interacts with the SLM leading to a further loss of light. Furthermore the pixels of the SLM have poor reflection efficiency. Although the polarization requirements, poor reflection efficiency and the grid like structure of an SLM results in losses upward of 50% of the light emitted from the sample, we investigated the capability of such a system to produce holograms by imaging 0.2-μm fluorescent microspheres.

DESIGNING THE PHASE MASK   Since SIDH requires that the light emitted from the sample be interfered with itself (see Chapter 2) to create the holograms, the SLM is used to perform this task in such an experimental setup. To create an interference signal between a plane wave and a spherical wave, a reflectance function of the form

$$R(x, y) = \frac{1}{2} + \frac{1}{2}exp\left[- \frac{j\pi}{\lambda b}(x^2 + y^2) + j\theta \right],$$ (3.1)

is displayed on the SLM, where where λ is the central wavelength of the emitted light. The constant term $\frac{1}{2}$ in Eq. (3.1) represents the plane wave, and the quadratic phase term represents the spherical wave. To approximate Eq. 3.1 on a phase-only SLM, the phase values of the two waves are distributed randomly, uniformly and equally among all the pixels of the SLM. Although there exist two other ways to perform the multiplexing of the lenses:

- Phase sum method: The terms representing the two waves are summed and the phase distribution of the sum is displayed on all the pixels of the SLM
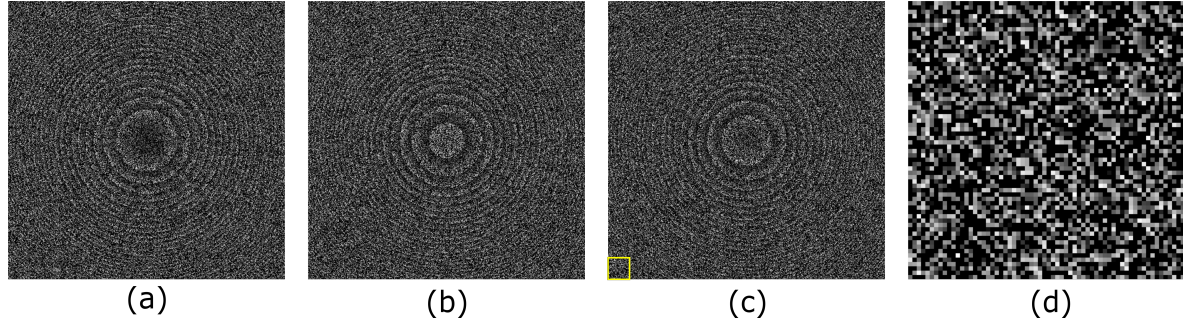
Figure 3.2: **SLM Reflectance function for SIDH**. (a) Phase distribution of the reflection masks displayed on the SLM using random-pixel method, with $\theta = 0^o$, (b) $\theta = 120^o$, (c) $\theta = 240^o$, (d) Enlarged section of (c) indicating that 50% of the SLM's pixels modulate light with a constant phase (black pixels, phase is 0). Reprinted with permission from Marar and Kner, 2019

- Random ring method: The phase values of the two waves are distributed randomly and uniformly among the SLM rings where each ring on the SLM contains the value of one of the waves.

Distributing the lenses randomly and uniformly proves to provide the best reconstruction results. The worse performance of the phase sum method and the random ring method are attributed to additional unwanted waves being generated which distort the interference between the two main waves related to the two images (Katz et al., 2012).

Optical Setup   Excitation light (647 nm, from a solid-state laser (OBIS 647 nm LX 120MW, Coherent) is passed through a 4-f system and magnified by the lens pair L1 = 100 mm and L2 = 300 mm. The magnified laser beam passes through lens L3 = 150 mm before being recollimated by an oil immersion objective lens (PLAPON 60XO, N.A. 1.42; Olympus) to produce a $1/e^2$ diameter of 42 μm at the sample plane. The sample is mounted on an xy piezo stage (SmarAct) and the objective is mounted on a z-axis piezo stage (SmarAct). Fluorescence emission light (shown as green) after passing through the objective is separated from the excitation light at the dichroic mirror (Di03-R660-t3-25x36, Semrock) as in a conventional fluorescence microscope. A 4f system is created using the tube lens (effective focal length = 180 mm, Olympus UTLU) and lens L4 = 120 mm to reduce the size of the back pupil-plane in order to match the active area of the reflective liquid-crystal SLM (1024 × 768 pixels. Boulder Nonlinear Systems). A linear polarizer (10LP-VIS-B, Newport) placed after L4 is used to block the horizontally polarized fluorescence light. The vertically polarized fluorescence light is then reflected off of the SLM onto which a phase mask was loaded as described above. The quadratic phase term in Eq. 3.1 that represents a converging spherical wave is set such that spherical wave produced after reflection off the SLM focused 300 mm away from the SLM. After reflecting off the SLM, the emission light is directed towards an EMCCD camera (iXon Life 897, Andor) after passing through

an emission filter (FF01-605/15-25, Semrock). The tube lens is placed d_1 = 100 mm away from the objective. In order to fill the SLM completely, the back-pupil plane of the objective is de-magnified by the tube lens and L4 which are placed d_2 = 222 mm apart. The SLM is placed, d_3 = 120 mm, away from L4 and the distance between the camera and the SLM is z_h = 600 mm.
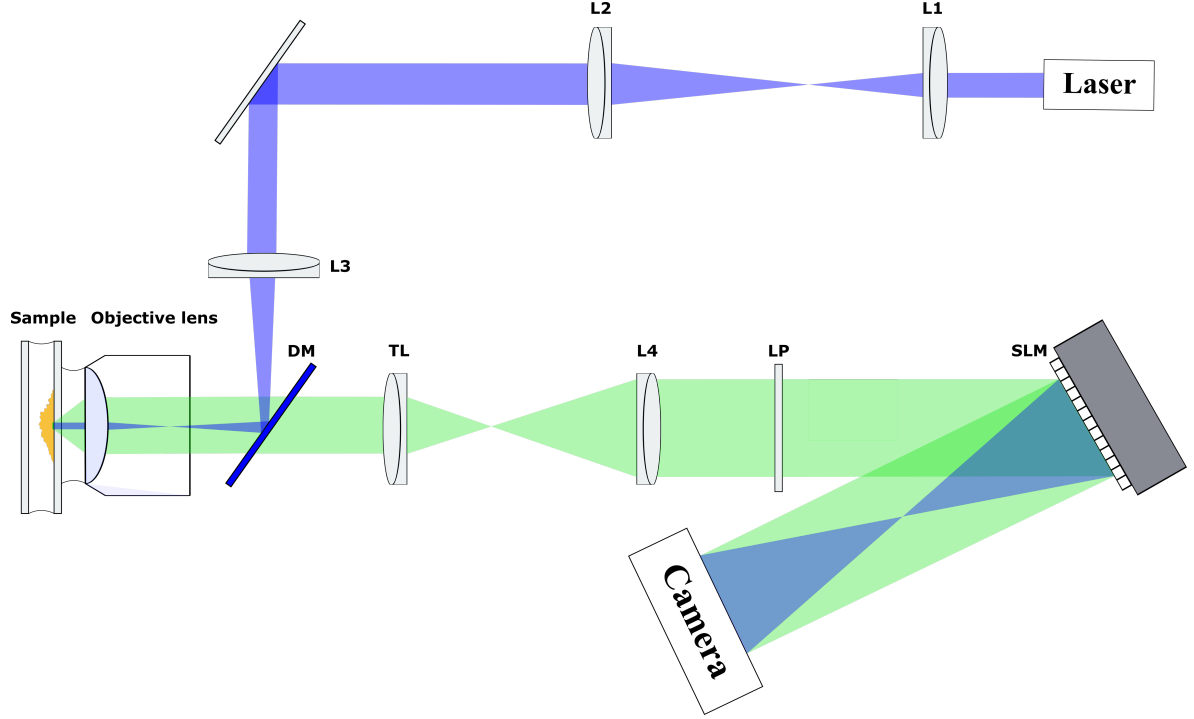
Figure 3.3: **Optical Setup for SIDH with SLM**. L1: 100 mm lens; L2: 300 mm lens; L3: 150 mm lens; DM: Dichoric Mirror; TL: Tube Lens with effective focal length (efl) = 180 mm; L4: 120 mm lens; LP: Linear polarizer. Reprinted with permission from Marar and Kner, 2019

CALCULATING THE RECONSTRUCTION DISTANCE AND MAGNIFICATION Both the reconstruction distance (z_r) and transverse magnification (M_T) are important parameters in the hologram reconstruction process as one needs to calculate them to reconstruct the hologram successfully. Both these parameters take different values with changes in the optical setup and therefore it is important to calculate these parameters accurately.

RECONSTRUCTION DISTANCE   The reconstruction distance is calculated by using the operator analysis discussed in the earlier chapter. For the system shown in Fig. 3.3, the electric field of the light emanating from a point source at the camera plane is given by

$$U_{CCD} = \left(\left(\left(C_1(\mathbf{r}_s) L\left(\frac{-\mathbf{r}_s}{z_s}\right) Q\left(\frac{1}{z_s}\right) Q\left(\frac{-1}{f_o}\right) * Q\left(\frac{1}{d_1}\right) \right) \right. \right.$$

$$\left. \times Q\left(\frac{-1}{f_{TL}}\right) * Q\left(\frac{1}{d_2}\right) \right) \times Q\left(\frac{-1}{f_2}\right) * Q\left(\frac{1}{d_3}\right) \right) \tag{3.2}$$

$$\left. \times \left(\frac{1}{2} + \frac{1}{2}e^{j\theta} Q\left(\frac{-1}{f_{SLM}}\right) \right) * Q\left(\frac{1}{z_h}\right) \right.$$

Upon simplifying Eqn. 3.2 we get

$$z_r = \pm \frac{(z_h + f^\dagger)(f'' + d_3 + z_h)}{f^\dagger - f'' - d_3} \tag{3.3}$$

where

$$f_e = \frac{f_o z_s}{f_o - z_s}, \quad f' = \frac{f_{TL}(d_1 + f_e)}{f_{TL} - (d_1 + f_e)}, \quad f'' = \frac{f_4(d_2 + f')}{f_4 - (d_2 + f')} \quad \text{and} \quad f^\dagger = \frac{f_{SLM}(d_3 + f'')}{f_{SLM} - (d_3 + f'')}$$

The $\pm$ symbol in Eqn. 3.3 denotes that one can reconstruct both the real and virtual image from the reconstruction process.

TRANSVERSE MAGNIFICATION The transverse magnification of the setup can be calculated using the imaging equation (see Chapter 1 in Saleh and Teich, 2019) for each lens in the system and taking the product of each of the magnifications. The magnification of the system shown in Fig. 3.3 is given by

$$M_T = \frac{z_h f_e f' f''}{z_s(d_1 + f_e)(d_2 + f')(d_3 + f'')} \tag{3.4}$$

where f_e, f' and f'' follow the same definitions as described above. It should be noted from Eq. 3.4 that the magnification of the system depends on the distance between the sample and the objective, z_s. This results in a variable magnification at different depths as seen in Figs. 3.4(d-f) and Figs 3.4(g-i). Numerical reconstruction techniques using Huygens convolution and angular spectrum methods as well as re-sampling the reconstructions can be used to produce reconstructions with constant transverse magnification (Kim, 2010; Siegel et al., 2012). Fixed transverse magnification in an SIDH system can can also be achieved by placing the DOE or the interferometer at the back-pupil plane of the objective lens (Imbe, 2018).

EXPERIMENTAL METHODS The experiments were carried out on the setup shown in Fig. 3.3. 0.2-μm dark red (660/680) fluorescent microspheres (Invitrogen) were first diluted in deionized water

(18.2 MΩ/cm) in the ratio of 1:10,000. They were then dried on 22 mm square gold seal cover slips (Electron Microscopy Sciences, 63786-01) which was mounted on a glass slide with glycerol. The fluorescent beads were placed in the focal plane of the objective (focal length f_o = 3 mm) and excited using a 647 nm laser (Coherent) with an irradiance of 1.2 kW/cm².
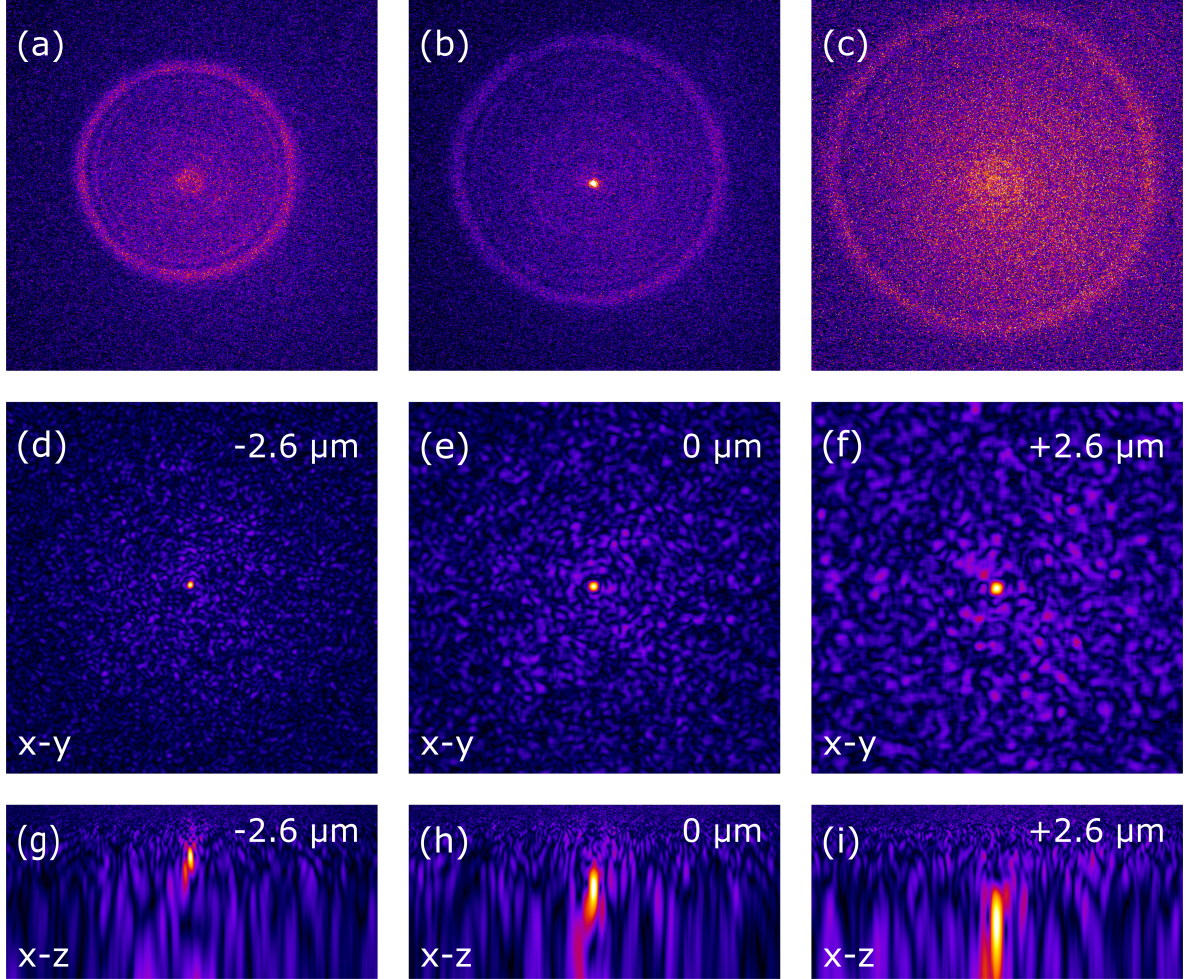
Figure 3.4: **Holograms of 0.2 μm fluorescent particle**. (a-c): One of the three holograms captured on the camera of a single 0.2 μm dark red (660/680) fluorescent microsphere at depths of (a) -2.6 μm, (b) focus and (c) +2.6 μm. (d-f): Reconstructions of the holograms (a)-(c) respectively using the method described in chapter 2. (g-i): The x-z cross-sections of the (d-f) showing that the plane of best focus is different for the three holograms (a-c). Reprinted with permission from Marar and Kner, 2019

A BeanShell script was written to run on Micromanager 2.0 which collected three images with the different phase patterns on the SLM. The SLM was loaded with three phase masks as shown in Fig. 3.2 with phases $\theta_1 = 0^o$, $\theta_2 = 120^o$ and $\theta_3 = 240^o$. 50% of the pixels were randomly selected to represent the spherical wave and the rest of the pixels were set to have a constant phase thus representing a plane

wave. A 6 μm stack was taken with the help of a piezo z-stage at steps of 200 nm. Fig. 3.4(a-c) show single holograms of the bead at three different depths relative to the focal plane of the objective. Three images of the bead were taken with the different phases at exposures of 50 ms. Each trio of images was then linearly combined to form a final complex hologram which was finally back-propagated using the free-space propagator to reconstruct the image of the fluorescent microsphere, Fig. 3.4(d-f).

SIDH of small fluorescent particles using an SLM poses challenges in terms of light efficiency. Since an SLM is polarization sensitive, only 50% of the light interacting the with the pixels of the SLM can be modulated using the reflective phase mask described in Eqn. 3.1. This results in more than 50% of the light being wasted. The loss of light due to the poor reflectance and polarization sensitivity of the SLM causes difficulties in capturing and reconstructing holograms because in a system such as the one shown in Fig. 3.3, the light from a single emitter is spread across $\sim$ 60,000 pixels as opposed to 9-16 pixels in a conventional widefield microscope. This significantly reduces the number of photons per pixel, thereby making it difficult to capture holograms if the signal per pixel in the system does not rise above the background per pixel, which can in turn decrease the axial range over which one can image using the SIDH system. The smallest particle imaged using SIDH with an SLM is a 0.2 μm fluorescent microsphere emitting $\sim$ 300,000 photons with an average background of β = 12 photons/pixel

In the next section, we describe the development and use of an alternative SIDH system which improves the SBR in the system and thereby increases the axial range over which a single emitter can be imaged and localized.

3.3   SIDH of fluorescent nanoparticles using a Michelson Interferometer

So far we have seen an optical setup that uses SIDH to image a 0.2 μm fluorescent nanoparticle. Superresolution fluorescence imaging with SMLM uses single molecules or fluorescent proteins to tag a biological sample. Commercially available single molecules are typically in the size range of $\sim$ 4-7 nm. Fluorescent microspheres are embedded with many single molecules which makes them very bright emitters. The number of photons emitted from a fluorescent microsphere is inversely proportional to its volume. The number of photons emitted from a single molecule is significantly lower than the number of photons emitted from a 0.2 μm fluorescent nanoparticle. Therefore, it is necessary to improve the light efficiency of the previously described SIDH system if it is to be used to image single molecules.

By replacing the SLM in Fig. 3.3 with a Michelson interferometer, the light efficiency of an SIDH system is tremendously improved. The additional losses in light caused due to the grid like arrangement of the pixels and their low reflection efficiency are no longer a concern in a Michelson interferometer. In addition to replacing the SLM with a Michelson interferometer, we also moved the camera closer to the Michelson interferometer to increase the signal-to-noise ratio (SNR) in the system. Although optimal resolution in an SIDH system demands that the camera be placed at a distance of twice the focal length of the diffractive lens (f_{SLM} in fig. 3.3) (Brooker et al., 2011), this is not a

serious concern if one plans to localize the images of the emitters after reconstructing the holograms. Using the modified optical setup we were able to accurately image smaller particles (0.1 and 0.04 μm) emitting lower numbers of photons (as low as 13,000 photons) over larger axial ranges (20 μm).

OPTICAL SETUP In the modified optical setup, the data was collected using a using a custom-built inverted wide-field microscope equipped with an oil-immersion objective (Olympus, PlanApoN 60x/1.42). Fig. 3.5 shows the schematic of the collection arm of the imaging system. Illumination lasers (561 nm, 50 mW; and 647 nm, 120 mW, all CW, from Coherent) were spectrally filtered (561 nm: LL02-561-12.5 excitation filter, 647 nm: LL02-647-12.5 excitation filter, both Semrock) and expanded and collimated using a custom-built beam expander. The fluorescence emitted by the sample was separated from the laser excitation light using a dichroic mirror (Omega, XF2054,485-555-650TBDR, USA) and a multi-band bandpass filter (Semrock, FF01-446/523/600/677-25, USA). We used a piezoelectric objective lens positioner (Smaract, Germany) to axially scan a sample of beads dried on a standard microscope cover-glass. The back-pupil plane of the objective was demagnified using a tube lens (f_{TL} = 180 mm, Olympus, UTLU, USA) and an achromat L1 (f_{L1} = 120 mm). The tube lens was placed d_1 = 75 mm fom the objective lens and the distance between the tube lens and L1 was d_2 = 222 mm. The size of the back-pupil plane controls the size of the hologram. It is necessary to have
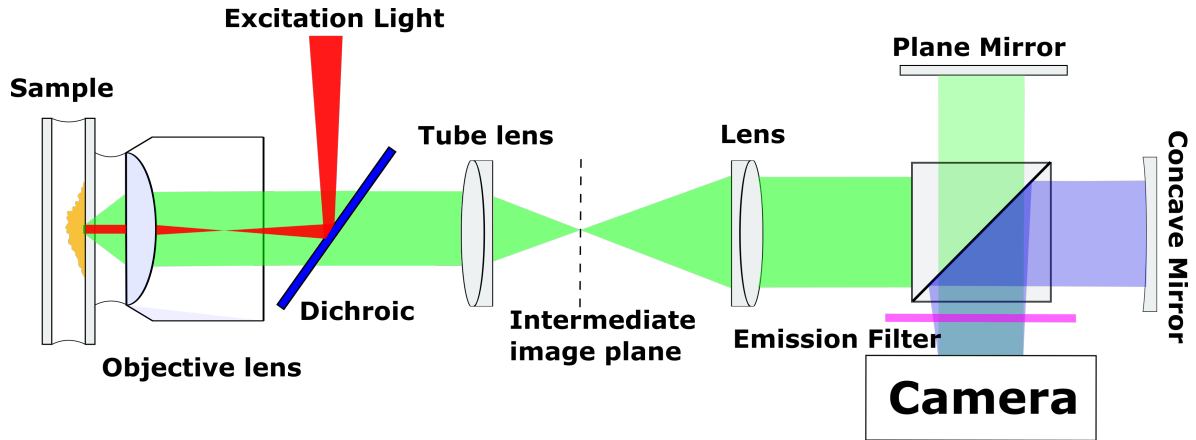
Figure 3.5: **Optical Setup for SIDH with Michelson interferometer**. Configuration for SIDH. Detection path for imaging using SIDH. Holograms are created using a Michelson interferometer. Adapted with permission from Marar and Kner, 2020b

an accurate control over the size of the hologram as it is related to the axial imaging range one can achieve using SIDH. A Michelson interferometer was constructed d_3 = 200 mm away from L1 with a concave mirror (f_d = 300mm) on one arm and a plane mirror on the other arm. The plane mirror was mounted on a piezoelectric translational stage (ThorLabs, NFL5DP20) to implement the phase-shift required to acquire three images. The fluorescence was detected with an electron-multiplying charge-coupled (EMCCD) camera (Andor iXon-897 Life,UK) which was placed z_h = 150 mm away from the interferometer.

3D IMAGING OF FLUORESCENT NANOPARTICLES To demonstrate 3D imaging, 0.1 μm diameter fluorescent beads emitting at 605 nm (Invitrogen, carboxylate modified,USA) were excited with a 561 nm laser light with an irradiance of 0.2 kW/cm².
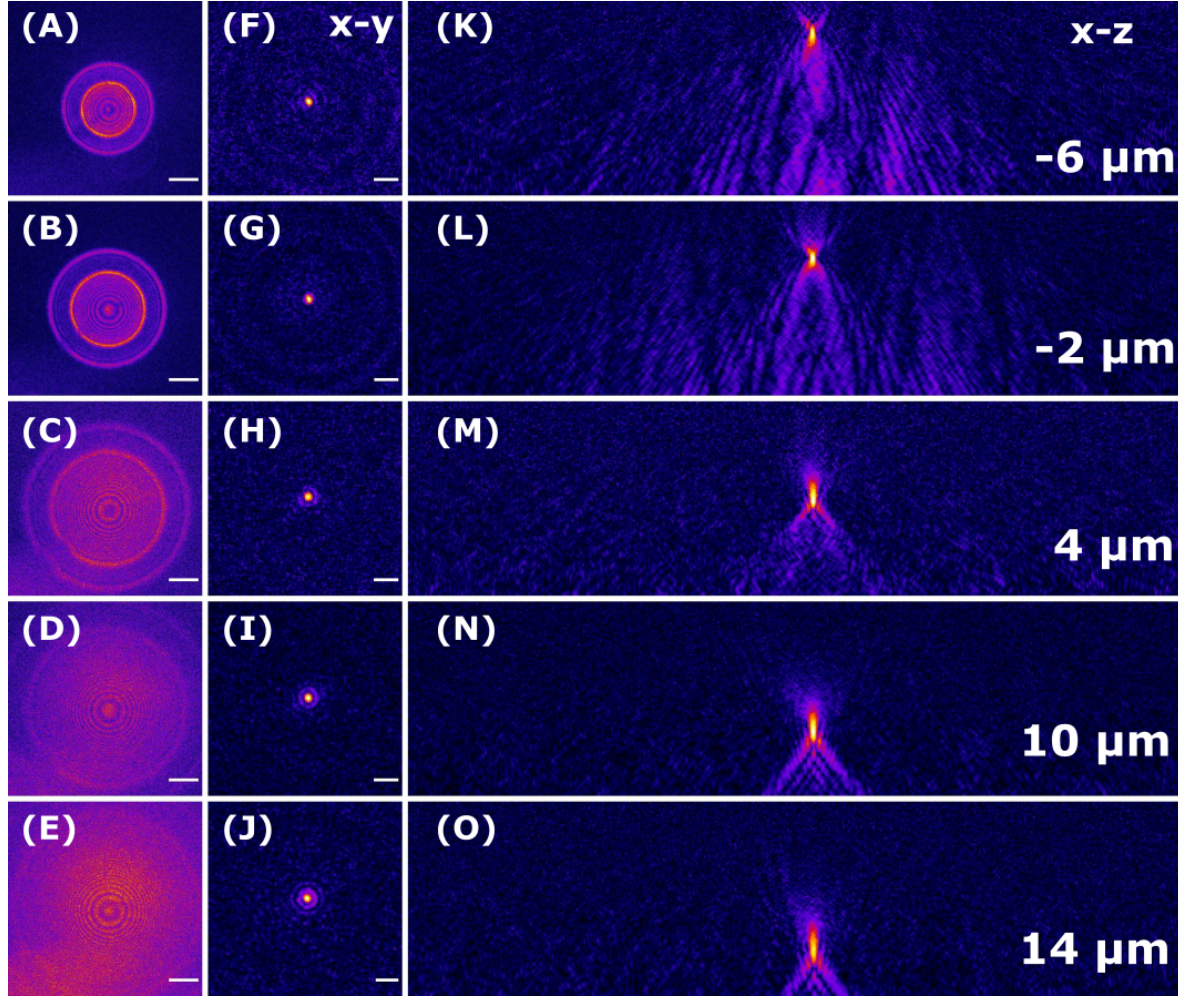
Figure 3.6: **3D imaging of a single 0.1 μm fluorescent bead using SIDH.** (A-E) Digital holograms of a fluorescent bead at different axial positions. Scale bars are 50 μm. (F-J) Lateral view of images reconstructed by back-propagating the holograms shown in (A-E). Scale bar of (F) is 2 μm, scale bar of (G) is 1.8 μm, scale bar of (H) is 1.6 μm, scale bar of (I) is 1.4 μm, scale bar of (J) is 1.2 μm. (K-0) Axial views of holograms reconstructed over the entire 20 μm axial range. Reprinted with permission from Marar and Kner, 2020b

A single bead was brought into focus and the three images were taken with the phase of one path shifted for each image. An average of 49,000 photons was detected per measurement with a background of β = 1.1 photons/pixel. The bead was then scanned along the optical axis using the piezoelectric objective lens positioner over an axial range of 20 μm, with three images collected at every axial position. Figs. 3.6 (A-E) shows how the density of the fringes in the hologram changes smoothly as a function of the

axial position of the emitter. In order to reconstruct the hologram to form an image of a single bead, three consecutive images with different phases are acquired which are then algebraically combined and reconstructed. Fig. 3.6 (F-J), shows the results of reconstructing the images by back-propagating the hologram to the appropriate reconstruction distance. It can be seen from Figs. 3.6 (A-E) that the size of the recorded hologram changes with depth, hence it is important to control the size of the hologram so that the distance between the interference fringes is resolvable by the camera. However, if the footprint of the recorded hologram is too large, the signal from the emitter may not rise above the noise making it impossible to reconstruct the hologram. This is due to the fact that the light from a single emitter that is usually spread across 9-16 pixels in a conventional microscope is now being spread across $\approx$ 60,000 pixels in the recorded hologram. In the system shown in Fig. 3.5, the optical elements are chosen such that the radius of the hologram at the camera is 2.33 mm when the emitter is in focus thus corresponding to a radius of $\approx$ 145 pixels on the camera.

LOCALIZATION PROCEDURE FOR SMLM USING SIDH   After the hologram of a single-emitter is reconstructed over the entire axial range, each stack of images undergoes a filtering step, where the single-emitter is identified in the reconstructed data by reducing the noise and enhancing the features we are interested in. Different types of low-pass (Gaussian, averaging) (Křížek et al., 2011) and band-pass (lowered Gaussian)(Holden et al., 2011) filters have been developed to achieve this goal. In this dissertation a filter based on wavelet transformation was used as it has been shown to achieve better results (Izeddin, Boulanger, et al., 2012). After filtering, the approximate position of the molecules in the input images are found. We do this by simply detecting the local intensity maxima in a 26-connected neighborhood and subject it to an intensity threshold. Various methods have been developed to calculate the intensity threshold based on an estimate of the background noise (Henriques et al., 2010; Izeddin, Boulanger, et al., 2012; Křížek et al., 2011). The intensity threshold was chosen to be a value between 0.5 and 2 times the standard deviation of the intensity values from the first wavelet level as recommended in Izeddin, Boulanger, et al., 2012. Details about wavelet levels can be found in section 3.1 in Ovesný, 2016. The approximate position of single-emitter in each stack is used to cut out a user-defined (7x7 pixels in this case) region of interest (ROI) surrounding the single-emitter. Each image in the ROI stack is then localized by fitting it to a Gaussian function (model in this case) using maximum-likelihood estimator (MLE) to find the emitter's sub-pixel position, the background and signal photons and the standard deviation of the Gaussian function (σ). To extract the axial position of the emitter, a curve is fit to the intensity values found in the previous step in each stack and the global maxima is found for the curve which provides us with the axial position of the emitter. The x and y positions determined using MLE are interpolated and using the position of the global minima found in the previous step, the sub-pixel 3D position of the nanosphere is determined. Reconstruction and fitting analysis of the captured holograms produced was performed using custom written Python code (see Appendix B). The localization code was based on an MLE algorithm that has been previously shown to compute and reach the Cramér-Rao Lower Bound (CRLB) (Smith et al., 2010).
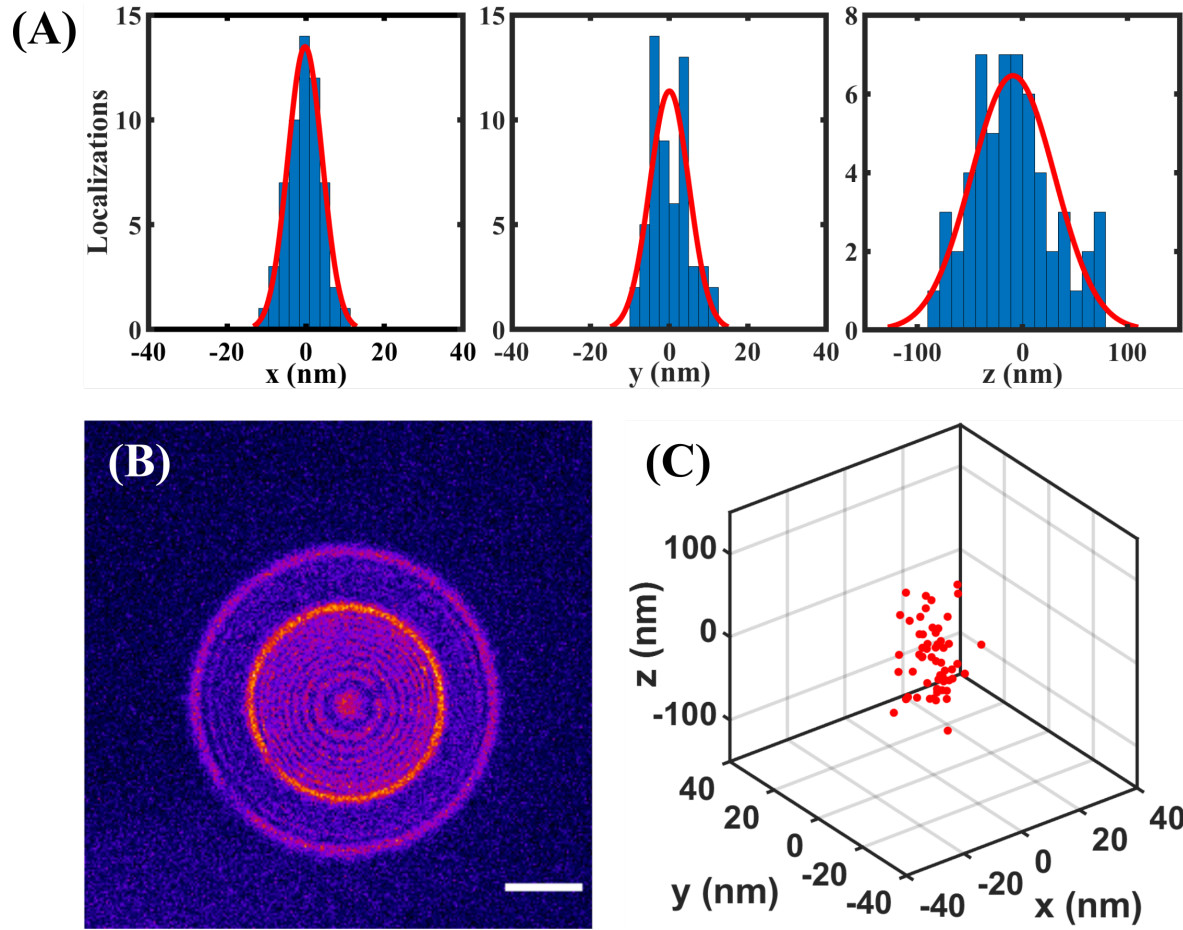
Figure 3.7: **3D localization of a single 0.1 μm fluorescent bead.** (A) Histograms of 68 localizations in x, y, and z of one single 0.1 μm red (580/605) fluorescent bead on a coverslip. The standard deviations of the measurements are $\sigma_x = \sigma_y = 5$ nm and $\sigma_z = 40$ nm. (B) Representative image of a single bead imaged with SIDH acquired in one 50-ms frame. Scale bar is 50 μm. (C) Localizations plotted in 3 dimensions. Reprinted with permission from Marar and Kner, 2020b

Figure 3.7 shows experimental localization results of a 100 nm nanosphere that was brought to focus using the axial piezo scanner. Over 68 measurements with a 50-ms exposure time, we achieved a localization precision of 5 nm in x and y and 40 nm in z for a bead with an average of 49,000 photons detected per measurement (each consisting of 3 images).

SIDH AT LOW LIGHT LEVELS   The localization precision and the reconstruction of a hologram depends on the SNR of the hologram. Figure 3.8 shows the dependence of SNR on the emitted number of photons. Each value in the figure was calculated from simulated holograms of a point like object emitting a constant number of photons. A constant background of 5 photons/pixel was added

to each of the simulated holograms and the hologram was subject to Poisson noise. It can be seen from Fig. 3.8 (A) that to achieve an SNR of 10 under the presumed imaging conditions, it is necessary to detect at least 5000 photons. The SNR was calculated as the ratio of mean signal to the mean of the standard deviation of the background.
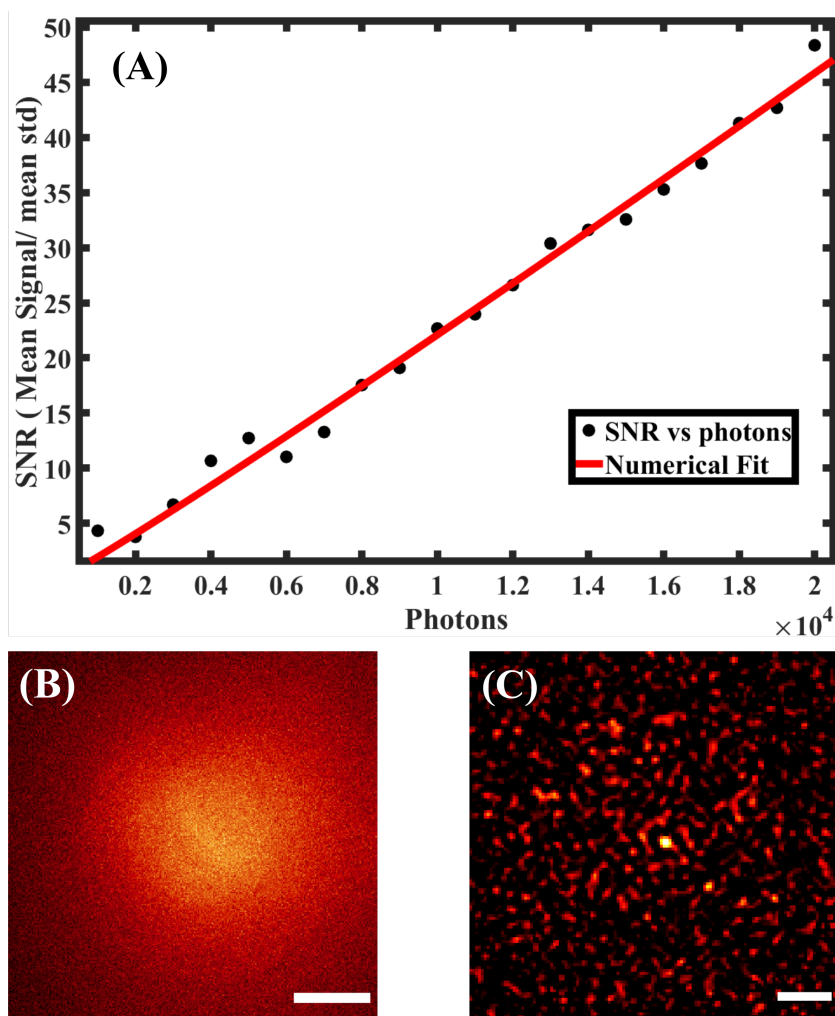
Figure 3.8: **SNR conditions for imaging using SIDH.**(A) SNR vs Photons for simulated image data with a constant background of 5 photons/pixel in the presence of Poisson noise. (B) PSH of 40 nm dark red (660/680) nanosphere. Scale bar is 1 mm in image space (C) Background subtracted reconstructed image of (B). Scale bar is 2 μm in sample space. Reprinted with permission from Marar and Kner, 2020b

The background (5 photons/pixel) dominates the number of signal photons (0.03-0.3 photons/pixel). Because SNR $\propto N_s/\sqrt{N_s + N_b}$, this explains the linear relationship between the SNR and the number of signal photons as seen in Fig. 3.8 (A). Fig. 3.8 (B) shows the PSH of a 40 nm dark red (660/680) fluorescence nanosphere (Invitrogen, carboxylate modified,USA). Even though the PSH is

not as clearly visible as in the case of the 100 nm bead, the hologram can be successfully reconstructed at the optimal reconstruction distance. When imaging with SIDH, it is not necessary for the PSH to be visible to the eye.
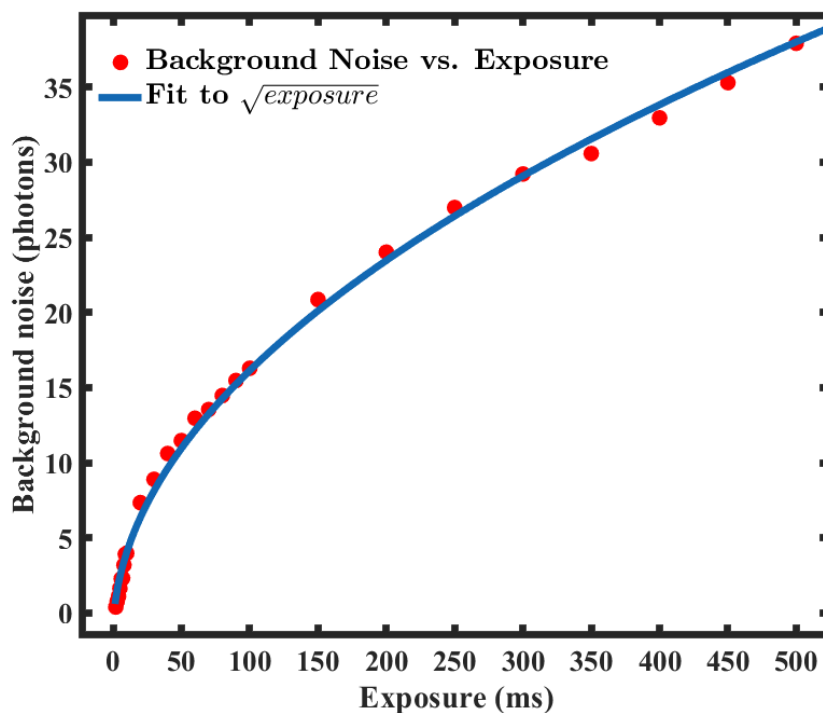
Figure 3.9: **Background noise vs Exposure for SIDH.** Background noise (in photons/pixel) in the optical setup in the presence of a clean glass slide placed at the focal plane of the objective lens. The background noise increases with the exposure time as expected, however the background in our system is currently too high for imaging a single molecule at exposure times conventionally used in SMLM. Reprinted with permission from Marar and Kner, 2020a

As long as the frequency of the rings obeys the Nyquist criterion, and the signal from the hologram rises above the background noise in the system, the hologram can be successfully reconstructed to provide an image of the emitter as shown in Fig. 3.8 (C). Simulating the optical setup described earlier, we measured the sampling frequency of the holograms at -6 μm (Fig. 3.6 (A)) and +14 μm (Fig. 3.6 (E)) to be 10 and 3 pixels/cycle respectively. The measurements were made at the edge of the hologram where the fringes are the closest to each other. The 40 nm bead was pumped with a 647 nm laser (Coherent, OBIS 647 nm LX 120 mW, USA) with an irradiance of 1.6 kW/cm² and each hologram was acquired in one 50-ms frame. The calibrated EM gain setting was 500 and an average of 13,000 photons were detected per estimation (each consisting of 3 images). The background from the reconstructed image was subtracted using the "Subtract Background" feature in ImageJ.

Light intensities suitable for SMLM produce high amounts of background noise ($\approx$ 20-50 background photons/pixel)(Gustavsson et al., 2018; Shechtman et al., 2015). Figure 3.9 shows the back-

ground noise in photons when just a clean slide without a coverslip, is placed at the focal plane of the objective lens. The glass slide was illuminated with 647 nm light at 1.6 kW/cm². It can be seen that as the exposure time increases so does the background noise. SMLM on biological samples is usually performed at exposure times $\leq$ 50 ms. At 50 ms the background noise in our system when only a slide is placed on the microscope is $\approx$ 11 photons/pixel. This background can be attributed to the autofluorescence inside the objective and the glass slide. Fig. 3.8 (A) shows us that for a background of 5 photons/pixel, to achieve an SNR of 10, one requires $\approx$ 5000 signal photons. Since, the single molecules commercially available have been reported to emit between 3000-5000 photons (Dempsey et al., 2011), to image a single molecule using SIDH it will be necessary to decrease the background noise in the system to allow the signal to rise above the noise.

IMAGING OVERLAPPING EMITTERS WITH SIDH   In SMLM, a critical requirement for resolving continuous structures is the labelling density. If the structure being imaged is sparsely labelled or if the number of emitters detected is too few, structural details are lost in the reconstructed image. The dense labelling of a sample however, makes it significantly challenging to extract the position of an emitter with high precision due to the existence of overlapping emitters.
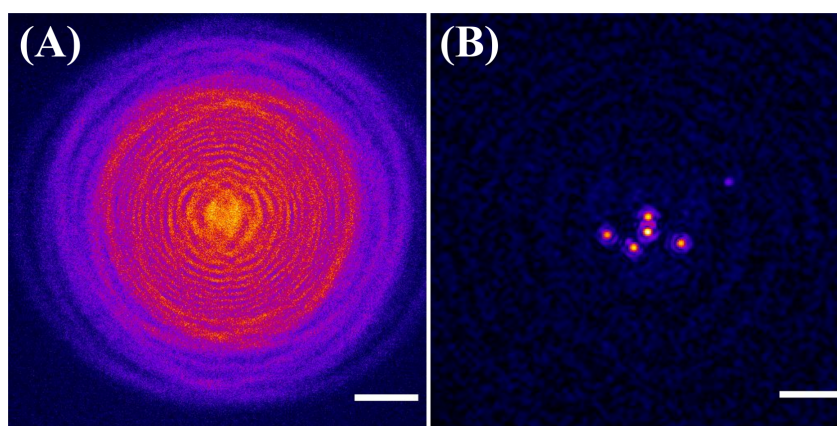
Figure 3.10: **Imaging overlapping emitters using SIDH.** (A) Digital hologram of 5 far red fluorescent beads (0.2 μm) in focus. Scale bar is 50 μm (B) Reconstructed image of (A). The laser intensity was 0.2 kW/cm^2 and the exposure time was 30 ms. Scale bar is 2 μm. Reprinted with permission from Marar and Kner, 2020b

One method to deal with this problem is to discard emitters that are within a user-defined distance, however this can lead to very few localizations points affecting the structural integrity of the reconstructed image. 2D multi-emitter fitting using the standard PSF has been addressed using various methods such as making a prior assumption of the sparsity of emitters in the region of interest (ROI) (Zhu et al., 2012), employing spatio-temporal statistical models of the blinking and overlap of the emitters (S. Cox et al., 2012; Wang et al., 2012) or MLE to find the most probable number of emitters (Holden et al., 2011; F. Huang et al., 2011).
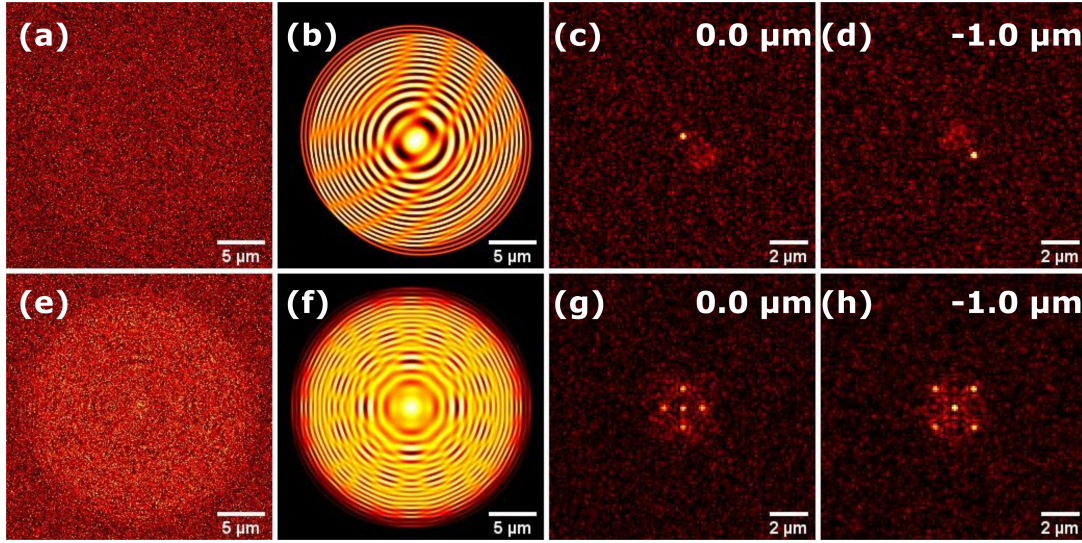
Figure 3.11: **Imaging and localizing overlapping emitters using SIDH.** Simulated image and reconstructions of two emitters separated by 1 μm in all three dimensions (a-d) and ten emitters separated 1 μm axially and a maximum distance of 2 μm spatially (e-h) imaged using IDH. (a) Numerically calculated raw image of two emitters separated by 1 μm corrupted by Poisson noise. (b) Numerically calculated model image of (a) without noise. (c-d) Reconstructed images of (a) at the appropriate reconstruction distances.(e) Numerically calculated raw image of two sets of 5 emitters separated by 1 μm axially and a maximum distance of 2 μm spatially corrupted by Poisson noise. (f) Numerically calculated model image of (e) without noise. (g-h) Reconstructed images of (e) at the appropriate reconstruction distances. Simulation parameters of 5000 signal photons in the presence of constant background of 3 photons/pixel.

In the case of SMLM using SIDH, a single complex hologram contains the entire 3D information about the three-dimensional scene thus containing information about all the emitters in a particular scene. Even if the PSH's from multiple emitters overlap in the case of SIDH, the final overlapped image of the complex hologram can be reconstructed at different distances to produce a wide-field image of the single-emitters at different axial distances. This in turn simplifies the problem of overlapping PSH's to that of the conventional wide-field case. Fig. 3.10 (A) shows overlapping PSH's of multiple 0.2 μm dark red (660/680) fluorescent nanospheres (Invitrogen). It can be seen from Fig. 3.10 (B), that even though the PSH's of multiple emitters overlap, the hologram can be reconstructed to produce a wide-field like image in which the emitters can then be localized with sub-pixel precision making SMLM using SIDH a suitable technique for high-resolution imaging with dense emitters.

Figs. 3.11(a) and (e) show simulations of overlapping PSH's of multiple emitters (2 in Fig. 3.11(a) and 10 in Fig. 3.11(e)) separated by a minimum distance of 1 μm in all three directions. Each emitter in both the cases was simulated to emit 5000 detected signal photons in the presence of constant background

noise of 3 photons/pixel. Figs. 3.11(b) and (f) show the model PSH's of their corresponding noisy holograms in the absence of noise. It can be seen that the overlap of the multiple emitters results in a complex hologram that contains the information of the entire 3-D scene, however when the complex
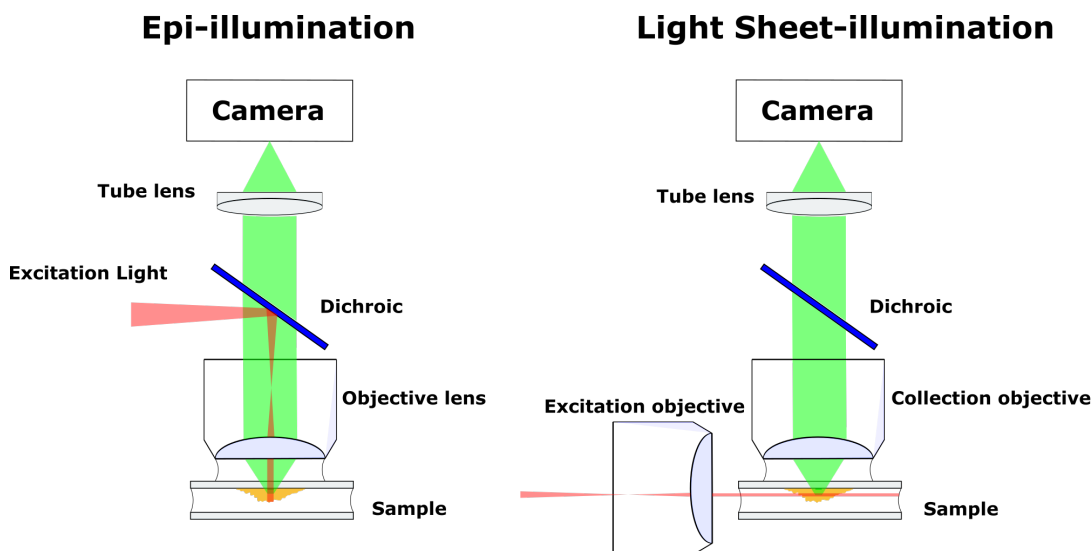
Figure 3.12: **Epi-illumination vs Light-sheet illumination** Light sheet illumination excites only a thin portion of the sample that is in the focal plane of the collection objective.

holograms shown in Figs. 3.11(a) and (e) are reconstructed at appropriate distances as shown in Fig. 3.11(c-d) and (g-h), SIDH presents a wide-field image of each emitter in the reconstructed plane. Hence single-molecule imaging with SIDH does not require the development of additional algorithms to deal with the problem of overlapping emitters. 50 images of two emitters separated by 1 μm were localized. The percentage of reliable localizations (3-D localization error<100nm) when imaging with SIDH was 100% with mean spatial localization precision of 20 nm and mean axial localization precision of 46 nm. In the case of 10 overlapping PSH's, the percentage of reliable localizations remained 100%. The mean spatial localization precision was 24 nm and the mean axial localization precision was 52 nm. The worsening of the localization precision can be attributed to higher background in the reconstructed images when two emitters are separated only in the axial dimension.

This is significantly better than the tetrapod PSF (Shechtman et al., 2014; Shechtman et al., 2015) where when two overlapping emitters were localized using the same conditions described above, the mean 3-D localization precision of the reliable localizations was 12 nm. Each emitter was localized 50 times to calculate the average localization precision. The mean 3-D localization error was 8 nm and the total percentage of reliable localizations was 80%. The localization performance worsens with increasing number of emitters and lower SNR's (Shechtman et al., 2016). Apart from the degradation of localization precision, the algorithm can result in false positives (fits made to non-existent localizations), false negatives (non-localized emitters) and model mismatch.

REDUCING BACKGROUND USING LIGHT-SHEET ILLUMINATION   Light sheet illumination as discussed in chapter 1 is a commonly used illumination scheme in SMLM that allows one to selectively illuminate a portion of the sample being imaged.
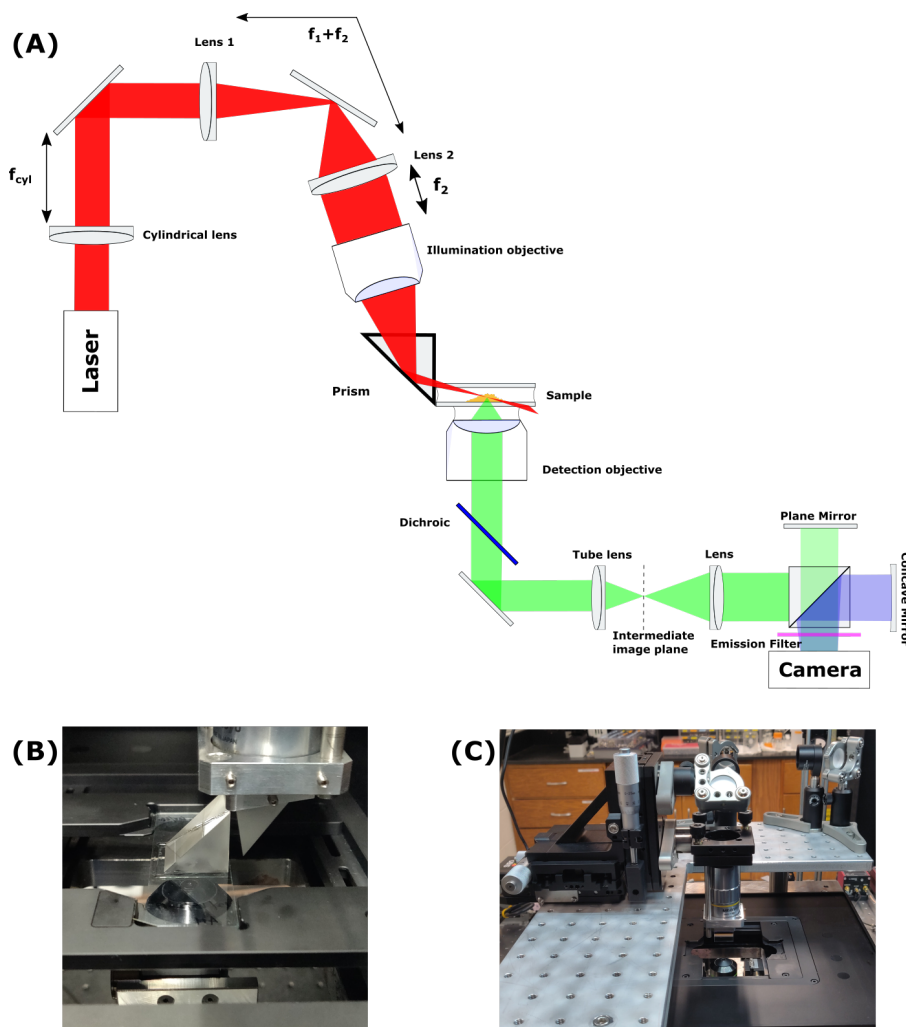
Figure 3.13: **Optical Setup for SIDH using light sheet illumination.** (A) Detailed schematic of the optical setup shown for a single-channel SIDH setup with a Michelson interferometer. f_{cyl}: 300 mm, f_1: 30 mm, f_2: 150 mm. (B) Photo of the light sheet setup being used with a glass slide. To reduce the refractive index mismatch, another prism is placed on the glass slide with a drop of immersion oil under it. (C) Photo of vertically mounted light sheet setup with prism holder.

This removes the out-of-focus light (thereby reducing the background) that passes through the collection objective in a epi-illumination scheme as can be seen in Fig. 3.12. Light sheet illumination has the added advantage that it also does not excite the fluorophores that are not in focal depth of the collection objective thereby preventing photo-bleaching of the biological sample.

OPTICAL SETUP   To reduce the background encountered when imaging single emitters using SIDH, we extended our illumination setup and added a light sheet illumination scheme similar to the one used in Gustavsson et al., 2018 to the SIDH setup with the Michelson interferometer. The light sheet is formed by a cylindrical lens, relayed to the back aperture of a long working distance illumination objective, and reflected at an angle into the sample using a glass prism on the outer side of the imaging chamber. When a sample is mounted on a glass slide, another prism is placed on the glass slide (see Fig.3.13(B)) to avoid the refractive index mismatch. The emission arm of the setup remained the same as described in section discussing SIDH with a Michelson interferometer. The excitation arm of the objective was modified such that the a flip-mirror could be used to flip between the epi-illumination pathway and the light-sheet illumination pathway. The light sheet illumination pathway consisted of a cylindrical lens (ACY254-200-A, f = 200 mm, Thorlabs), which focused the light in only one dimension onto a mirror. This mirror plane was imaged onto the back aperture of a long working distance illumination objective (378-803-3, x10, NA 0.28, Mitutoyo) by two lenses (f_1 = 30 mm and f_2 = 150 mm) in a 4f configuration. The illumination objective then focused the light sheet, which was directed into the sample at an angle of about 20° using a glass prism (PS908L-A, Thorlabs). The prism was held using a custom designed prism holder which was mounted using a cage system on a three axis translational stage (XRN-XZ, Thorlabs) (see Fig.3.13(C)).

IMAGING FLUORESCENT NANOSPHERES USING LIGHT SHEET ILLUMINATION
Using the light sheet excitation scheme, we imaged 0.04 and 0.2 μm fluorescent microspheres at extremely low light levels to compare the image quality between light sheet and epi-illumination when imaging with SIDH using a Michelson interferometer. Each hologram was acquired in one 50-ms frame and the calibrated EM gain setting was 500 when imaging with both the epi mode and the light sheet mode. In both case of the 40 nm bead was pumped with a 647 nm laser (Coherent, OBIS 647 nm LX 120 mW, USA). In the epi mode, the bead was pumped with an irradiance of 1.6 kW/cm² and in the light sheet mode, the bead was pumped with an irradiance of 0.14 kW/cm². It can be seen from Fig. 3.14 that the hologram formed using the light sheet illumination scheme (Fig. 3.14 (B)) has better SBR at lower levels of irradiance (1.6 kW/cm² vs 0.14 kW/cm²). Using light sheet illumination we were able to detect $\sim$ 10,000 photons with a background of β = 6 photons/pixel.

To further image using SIDH at lower light levels, we image a 0.2 μm fluorescent microsphere with the light sheet excitation scheme (see Fig.3.14(C)). The bead was pumped with a 561 nm laser (Coherent, OBIS 561 nm LS 50 mW, USA) with an irradiance of 0.02 kW/cm² and each hologram was acquired in one 1-ms frame. An average of 952 photons were detected per acquisition and the standard deviation of the background was measured to be 0.2 photons. With the hologram spread over $\sim$ 30000 pixels, we measured on average $\sim$ 0.036 photons/pixel. Fig. 3.14, shows that at very low background levels the fringes of the hologram might not be visible but can still be reconstructed to provide an image of the bead. This makes SIDH a promising tool for SMLM since commonly used organic dyes are known to emit between 1000-5000 photons (Dempsey et al., 2011).
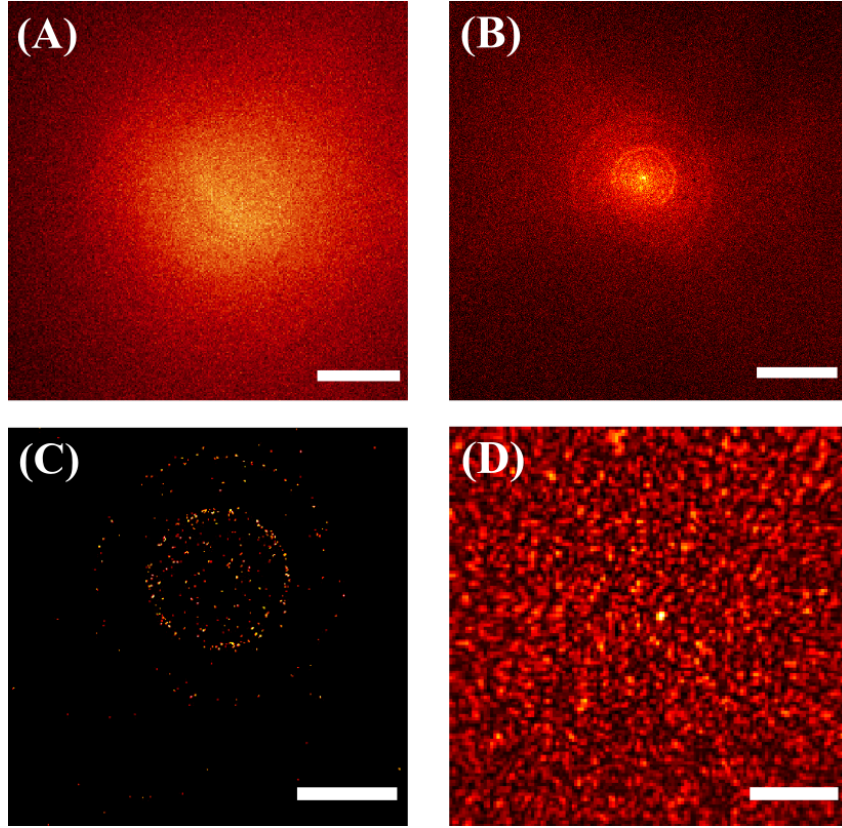
Figure 3.14: **Imaging using SIDH and light sheet illumination.** (A) PSH of a 40 nm bead using epi-illumination. The irradiance of the light exciting the bead was 1.6 kW/cm². (B) PSH of a 40 nm bead using light sheet illumination. The irradiance of the light exciting the bead was 0.14 kW/cm². Scale bar is 1 mm in image space. (C) PSH of a 200 nm bead using light sheet illumination. The irradiance of the light exciting the bead was 0.02 kW/cm². Scale bar is 1 mm in image space. (D) Background subtracted reconstructed image of (A). Scale bar is 2 μm in sample space.

3.4 Conclusion

In conclusion, we have demonstrated that SIDH can be used for imaging and localizing fluorescent nanoparticles at low light conditions. The use of a Michelson interferometer improves the light efficiency of the system which makes it possible to detect as low as 13000 photons using SIDH. SIDH with light sheet excitation can be used to reduce the background in the system to improve the SBR. We demonstrate that using light sheet excitation, as low as 952 photons can be detected in a hologram which can be successfully reconstructed to provide the image of the nanoparticle. Low number of photons emitted from organic dyes continues to be an obstacle when using SIDH to image single molecules. The development of brighter organic dyes for fluorescence imaging (Niekamp et al., 2020)

is one solution to this problem. The use of dual diffractive lenses to create holograms (Katz et al., 2012) could be another solution to this problem as it would allow one to reduce the size of the hologram thereby increasing the number of photons per pixel.

Here we have demonstrated that SIDH can provide 5 nm lateral precision and 40 nm axial precision and is a promising tool for single particle tracking over large axial ranges (> 20 μm) and might also be useful for SMLM. The ability to reconstruct a hologram depends on the ability to reduce the background in the system. As has been shown in Fig. 3.8, to image a single molecule emitting 5000 photons with a SNR of 10, it is necessary to reduce the background in the system to 3 photons/pixel. 3 photons/pixel is an extremely low level of background. Background levels in SMLM experiments lie usually between 20-50 photons/pixel. If this challenge of reducing the background to 3 photons/pixel can be achieved in a thick (10-20 μm) biological sample, then SIDH can be a promising technique for high resolution single molecule imaging.

CHAPTER 4

CRAMÉR-RAO LOWER BOUND FOR DIGITAL HOLOGRAPHIC MICROSCOPY

The ability of any particular 3D localization method to determine the position of a single emitter can be determined by calculating the Cramér-Rao lower bound (CRLB) from the Fisher information matrix (Cover & Thomas, 2012; Kay, 1993; Rao, 1973). This calculation yields the theoretically best precision that can be achieved for a given estimator and has been performed for most of the SMLM techniques. This quantity is useful because it (1) serves as a benchmark to which the precision provided by a particular estimator can be compared, thus indicating how much room there might be for improvement and (2) by calculating the quantity for a particular estimator under different experimental conditions, the lower bound helps in designing experiments where various parameters of the optical setup can be varied to achieve the desired level of precision. Calculation of the CRLB requires computation of the Fisher information matrix which provides a measure of the amount of information the data contains about the parameters being estimated. The precision with which a parameter can be estimated is directly proportional to the amount of information the collected data contains about the parameter. The amount of information in the data is determined by considering how the likelihood of obtaining a set of measurements in the presence of noise changes with the value of the parameter of interest. If the parameter of interest is the position of the emitter and the data collected is the response of the optical system, the Fisher information matrix calculates how the likelihood of the acquired data varies with changes in the position of the emitter. If the likelihood of the acquired data is very sensitive to changes in the position of the emitter, then the data contains a relatively large amount of information about the position and can be estimated with relatively high precision. The CRLB of a certain parameter (e.g., position) is obtained from the inverse of the Fisher information matrix, thus confirming the expectation that a large amount of information about the parameter should result in a smaller bound on the variance with which the parameter can be estimated (Chao et al., 2016). The CRLB has been calculated for many different PSF models to determine the precision with which a

single emitter can be localized (Chao et al., 2016; Holtzer et al., 2007; S. Liu et al., 2013; Ober et al., 2004a; Ram et al., 2006; Stallinga & Rieger, 2012; M. A. Thompson et al., 2010). Saddle point and tetrapod PSFs were developed by optimizing the Fisher information matrix in an engineered PSF over a certain axial range, thereby generating a PSF that contains the maximum amount of information with regard to the position of the emitter (Shechtman et al., 2015). On-axis digital holographic microscopy (DHM) and SIDH have become popular tools for 3D particle tracking over large volumes, however the CRLB for SIDH has not been calculated yet. A closed form expression for on-axis digital holography has been calculated (Fournier et al., 2010) using a different imaging model and has not yet been compared to other 3D microscopy techniques.

In this chapter I will calculate the CRLB for SIDH. Furthermore I will compare the CRLB of SIDH with that of the Gaussian and astigmatic PSF and discuss their results over different signal-to-background ratios (SBR).

4.1 Calculating the CRLB for the Gaussian and the Astigmatic Imaging Model

The CRLB is the limiting lower bound of the variance for any unbiased estimator and is given by the inverse of the Fisher information matrix

$$S_\theta \geq \frac{1}{\sqrt{F(\theta)}} \tag{4.1}$$

where S_θ is the standard deviation of the estimator and $F(\theta)$ is the Fisher information matrix. The equal sign is the minimum value of the estimation and is referred to as the CRLB. The elements of the Fisher information matrix are given by (Kay, 1993; Rao, 1973)

$$F_{\theta\theta} = \int \frac{1}{q} \frac{\partial q}{\partial \theta} \frac{\partial q}{\partial \theta} dx dy \tag{4.2}$$

where q describes the imaging model. Using Eqns. 4.1 & 4.2 we calculate the fundamental limit of the localization precision for the PSF approximated by a Gaussian profile given by

$$q(x, y) = \frac{1}{2\pi\sigma_o^2} exp\left(\frac{-(x^2 + y^2)}{2\sigma_o^2}\right) \tag{4.3}$$

where $(x,y) \in \mathbb{R}^2$. Due to symmetry, the off-diagonal elements of the Fisher information matrix are zero. For a particle emitting N photons the elements of the Fisher information matrix describing the x amd y localization precisions can be given by

$$F_{xx} = F_{yy} = N \int_{\mathbb{R}^2} \frac{1}{q(x,y)} \frac{\partial q(x,y)}{\partial x} \frac{\partial q(x,y)}{\partial x} dxdy$$

$$= \frac{N}{\sigma_o^4} \left(\frac{1}{\sqrt{2\pi}\sigma_o} \int_{\mathbb{R}} x^2 e^{-\frac{x^2}{2\sigma_o^2}} dx \right) \left(\frac{1}{\sqrt{2\pi}\sigma_o} \int_{\mathbb{R}} e^{-\frac{y^2}{2\sigma_o^2}} dy \right) \qquad (4.4)$$

$$= \frac{N}{\sigma_o^2}$$

Eqn. 4.4 is the Fisher information matrix for a Poisson process. In order to calculate the CRLB of the z estimation for a Gaussian profile, we described the PSF with a 2D Gaussian with a z-dependent standard deviation (Holtzer et al., 2007) given by

$$\sigma(z) = \sigma_o \sqrt{1 + \frac{z^2}{d^2}} \qquad (4.5)$$

where σ_o is the standard deviation of the in-focus PSF and d is the depth of focus of the objective lens. The element of the Fisher information matrix F_{zz} can now be calculated similar to Eqn. 4.4

$$F_{zz} = N \int_{\mathbb{R}^2} \frac{1}{q(x,y)} \frac{\partial q(x,y)}{\partial z} \frac{\partial q(x,y)}{\partial z} dxdy$$

$$= N \left[\frac{\partial \sigma(z)}{\partial z} \right]^2 \int_{\mathbb{R}^2} \left(\frac{1}{2\pi\sigma(z)^2} \right) \left(\exp \left(\frac{-(x^2+y^2)}{2\sigma(z)^2} \right) \right) \left(\frac{(x^2+y^2-2\sigma(z)^2)^2}{\sigma(z)^6} \right) dxdy$$

$$= \frac{N4z^2}{(d^2+z^2)^2}$$

$$(4.6)$$

Therefore, using Eqn. 4.1 the calculated limit of localization precision for a Gaussian profile is given by $S_x = S_y = \dfrac{\sigma_o}{\sqrt{N}}$ and $S_z = \dfrac{1}{\sqrt{N}} \left(\dfrac{d^2}{2z} + \dfrac{z}{2} \right)$.

In the case of the astigmatic PSF, a weak cylindrical lens is introduced in the imaging pathway which splits the focal plane into two perpendicular focal planes at different depths giving an asymmetric PSF. The form of the astigmatic PSF on the detector can be approximated by Holtzer et al., 2007

$$q(x,y) = \frac{1}{2\pi\sigma_x(z)\sigma_y(z)} exp \left(-\frac{x^2}{2\sigma_x(z)^2} - \frac{y^2}{2\sigma_y(z)^2} \right) \qquad (4.7)$$

σ_x and σ_y are the full-width half maximums (FWHMs) of the intensity distributions in x and y directions. $\sigma_x = \sigma_y$ only half way between the two focal planes; we define this plane as $z = 0$. Assuming the y-direction is focused above the focal plane and using Eqn. 4.5, $z \to z - \gamma$ for the y-direction and $z \to z + \gamma$ for the x-direction.

$$\sigma_x(z) = \sigma_o\sqrt{1 + \frac{(z + \gamma)^2}{d^2}} \tag{4.8a}$$

$$\sigma_y(z) = \sigma_o\sqrt{1 + \frac{(z - \gamma)^2}{d^2}} \tag{4.8b}$$

where γ is the amount of astigmatism introduced by the cylindrical lens. The CRLB for the astigmatic PSF is calculated in a similar manner to that of the Gaussian PSF as described by Eqns. 4.1 & 4.2 and is given by

$$S_x = \frac{\sigma_x}{\sqrt{N}}, \qquad S_y = \frac{\sigma_y}{\sqrt{N}} \tag{4.9a}$$

$$S_z = \begin{cases} \dfrac{1}{\sqrt{N}}\left(\dfrac{\sqrt{5}d^2}{4(z + \gamma)} + \dfrac{\sqrt{5}(z + \gamma)}{4}\right), & \epsilon < 1 \\[3ex] \dfrac{1}{\sqrt{N}}\left(\dfrac{\sqrt{5}d^2}{4(z - \gamma)} + \dfrac{\sqrt{5}(z - \gamma)}{4}\right), & \epsilon > 1 \end{cases} \tag{4.9b}$$

where $\epsilon = \sqrt{\sigma_y/\sigma_x}$ and d is the focal depth of the objective lens.

4.2   Calculating the CRLB for SIDH imaging model

For a first calculation of the Cramér-Rao limits for lateral and axial precision for SIDH, we follow the approach in Ober et al., 2004a and calculate the limits for a photon distribution given by the point spread hologram (PSH)

$$q(\rho, \phi) = A(1 + \cos\alpha\rho^2)\, P(\rho) \tag{4.10}$$

where $\alpha = k/2z_r$, $k = 2\pi/\lambda$, and the normalization constant, A, is given by

$$A = \frac{1}{\pi\left(r_h^2 + \frac{2z_r}{k}\sin\frac{k}{2z_r}r_h^2\right)} \tag{4.11}$$

where r_h is the radius of the hologram at the CCD plane and

$$P(\rho) = \begin{cases} 1, & \rho < r_h \\ 0, & \rho > r_h \end{cases} \tag{4.12}$$

Upon calculating the terms of the Fisher information matrix using Eqns. 4.1 & 4.2 we find that (see the appendix A for the derivation)

$$F_{xx} = F_{yy} = 2A\alpha^2 M_T^2 \pi \left(\frac{r_h^4}{2} + \frac{1}{\alpha^2}(1 - \cos \alpha r_h^2) - \frac{r_h^2}{\alpha} \sin \alpha r_h^2 \right) \tag{4.13}$$

and

$$F_{zz} = \frac{\pi k^2 A}{2z_r^4} \left(\frac{r_h^6}{3} - \frac{2r_h^2}{\alpha^2} \cos \alpha r_h^2 - \frac{\alpha^2 r_h^4 - 2}{\alpha^3} \sin \alpha r_h^2 \right) \left[\frac{\partial z_r}{\partial z} \right]^2 \tag{4.14}$$

In the equation for F_{zz} above, we have simplified the derivation by ignoring the z_r dependence of the constant A and the PSH radius r_h. Because the radial fringes change more rapidly with the axial position than the PSH radius, we believe this is a valid approximation (See Figs. 4.3 & 4.7 for the results)

4.3   Effects of background noise

The calculated fundamental limits of localization precision assume the best case scenario for the acquisition system. These expressions derived above present the best possible localization precision in the absence of deteriorating factors such as background noise. The elements of the Fisher information matrix in the case where the PSF is corrupted by noise were calculated analogously to the ideal case and are given by

$$F_{\theta\theta} = \int \frac{1}{(q + bg)} \frac{\partial q}{\partial \theta} \frac{\partial q}{\partial \theta} dxdy \tag{4.15}$$

where bg is the background signal (photons/mm^2) corrupting the PSF/PSH in each of the cases. Since the integral in Eqn. 4.15 cannot be calculated analytically, it was calculated numerically using custom written MATLAB code (see Appendix C).

4.4   CRLB for SIDH with one plane wave and one spherical wave

We revisit the analysis done in chapter 2 where the hologram is formed as a result of the interference between one spherical wave and one plane wave. Referring to Fig. 4.1, f_{d1} is responsible for the spherical wave and the plane wave is created when $f_{d2} \to \infty$. In this case the reconstruction distance (z_r) and the transverse magnification (M_T) are given by
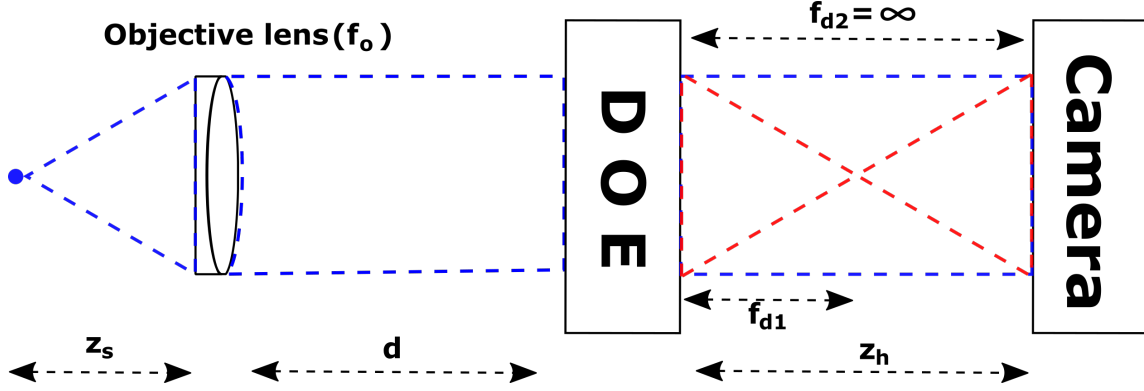
Figure 4.1: **SIDH with one plane wave and one spherical wave.** The interferogram formed at the camera is a result of a plane wave ($f_{d2} = \infty$) and a spherical wave (f_{d1}).

$$z_r = \begin{cases} \pm(z_h - f_{d1}), & \text{for} \quad z_s = f_o \cap f_{d2} \to \infty \\[2ex] \pm\left(\dfrac{(f_1 + z_h)(f_e + d + z_h)}{f_1 - f_e - d}\right), & \text{for} \quad z_s \neq f_o \cap f_{d2} \to \infty \end{cases} \tag{4.16}$$

and

$$M_T = \left|\frac{\partial x_r}{\partial x_s}\right| = \begin{cases} \dfrac{z_h}{f_o}, & \text{for} \quad z_s = f_o \cap f_{d2} \to \infty \\[2ex] \dfrac{f_e z_h}{z_s(f_e + d)}, & \text{for} \quad z_s \neq f_o \cap f_{d2} \to \infty \end{cases} \tag{4.17}$$

where

$$f_1 = \frac{f_{d1}(f_e + d)}{f_{d1} - (f_e + d)}, \qquad \text{and} \qquad f_e = \frac{z_s f_o}{(f_o - z_s)}$$

The radius of the hologram at the CCD plane is calculated using the ray transfer matrix framework described in chapter 2. The radii of the plane and spherical wave, for the optical system described by Fig. 4.1 at the CCD plane are given by

$$\begin{bmatrix} r_{plane} \\ \gamma_{plane} \end{bmatrix} = \begin{bmatrix} 1 & (z_h + d) \\ 0 & 1 \end{bmatrix} \begin{bmatrix} 1 & 0 \\ -1/f_o & 1 \end{bmatrix} \begin{bmatrix} 1 & z_s \\ 0 & 1 \end{bmatrix} \begin{bmatrix} h_{enter} \\ \gamma_{enter} \end{bmatrix} \tag{4.18}$$

and

$$\begin{bmatrix} r_{spherical} \\ \gamma_{spherical} \end{bmatrix} = \begin{bmatrix} 1 & z_h \\ 0 & 1 \end{bmatrix} \begin{bmatrix} 1 & 0 \\ -1/f_{d1} & 1 \end{bmatrix} \begin{bmatrix} 1 & d \\ 0 & 1 \end{bmatrix} \begin{bmatrix} 1 & 0 \\ -1/f_o & 1 \end{bmatrix} \begin{bmatrix} 1 & z_s \\ 0 & 1 \end{bmatrix} \begin{bmatrix} h_{enter} \\ \gamma_{enter} \end{bmatrix} \tag{4.19}$$

where r_{plane} and $r_{spherical}$ are the radii of the plane and spherical waves at the CCD plane and γ_{plane} and $\gamma_{spherical}$ are the maximum angles at which the rays from the plane and spherical waves meet the CCD. $h_{enter} = 0$ is the distance from the optical axis at which the ray enters the system and $\gamma_{enter} = NA$ is the maximum angle at which the rays enters the system. Since the radius of the hologram is limited by the area of overlap between the radius of the plane and spherical waves the radius of the hologram (r_h) can be defined as

$$r_h = min(r_{plane}, r_{spherical})$$

Using Eqns. 4.16-4.19 we calculate various parameters of an SIDH system such as the radius of the hologram (r_h), transverse magnification of the system (M_T) and the reconstruction distance (z_r) for different Diffractive Optical Element (DOE) to CCD distances (z_h)(shown in Fig. 4.2). In order to simulate the SIDH system, a 60x, 1.42 numerical aperture (NA) objective is assumed (f_o = 3 mm), imaging into an index of 1.515.

Figure 4.2: **Parameters of SIDH using configuration 1.** Hologram radius (r_h), reconstruction distance (z_r) and transverse magnification (M_T) of configuration 1 when the CCD is placed at different distances away from the DOE.

The wavelength of light is 670 nm. The distance between the objective lens and the DOE is $d = 3$ mm, the focal length of the quadratic phase pattern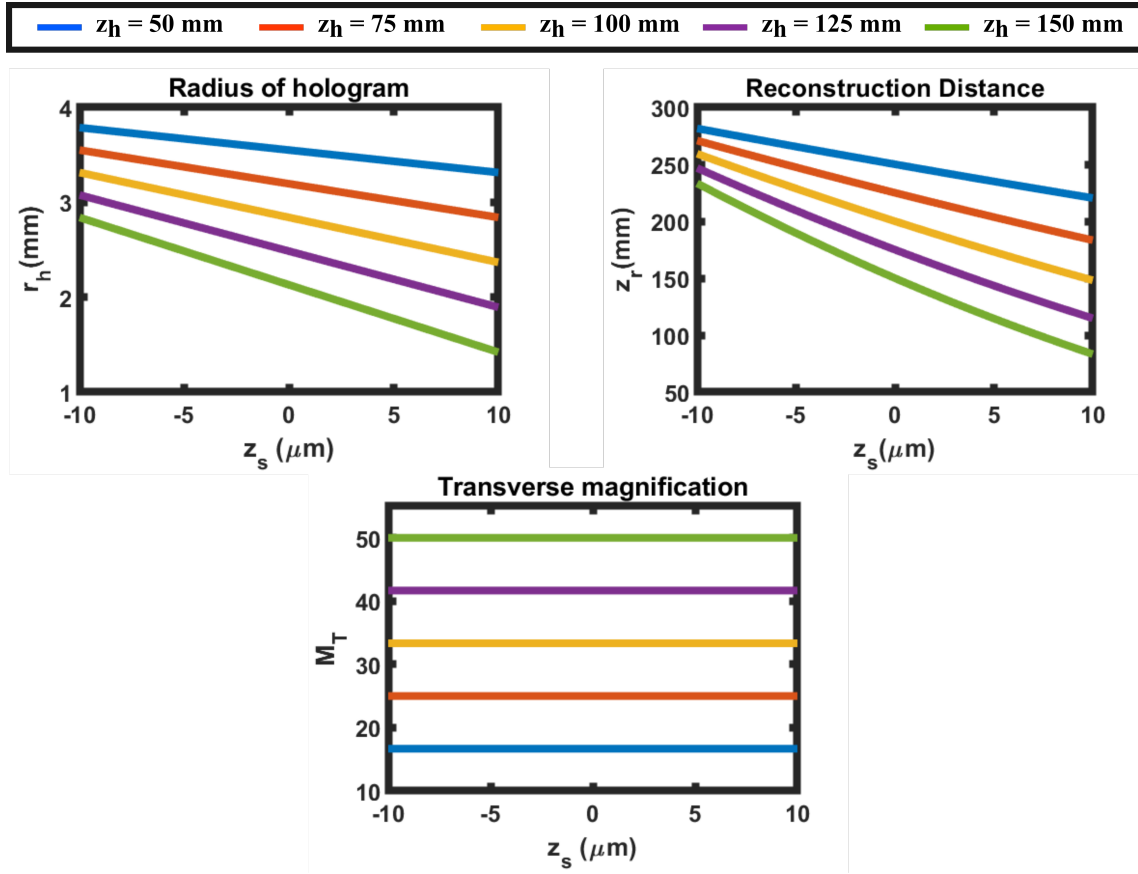 is $f_{d1} = 300$ mm and $f_{d2} = \infty$. The CRLB for SIDH was calculated for $z_h = 150$ mm. When the camera is placed at $z_h \geq 150$ mm, the hologram comes to focus within the 20 μm axial range thereby reducing the achievable axial range. For the numerical simulation of the Gaussian PSF, we use the approximations to the "true" PSF that can be calculated quickly and are frequently used in SPT and SMLM to localize the PSF (Ober et al., 2004a). The focal depth for a high-NA imaging system is given by $d = \lambda/(n(1-(1- NA^2/n^2)^{1/2})) \approx 679$ nm (Gao, 2015) and the spot size $\sigma_0 \approx \lambda/(4NA\sqrt{2 \ ln \ 2}) \approx 122$ nm (at $z = 0$). For simulating the astigmatic PSF, the amount of astigmatism introduced in the system was assumed to be $\gamma = 400$ nm. The focal depth and the spot size are the same as assumed in the Gaussian case. Both the Gaussian and the astigmatic setups were assumed to have a magnification equal to $M_T = 50$.

Figure 4.3 compares x,y, and z localization precision of SIDH with the Gaussian PSF and the astigmatic PSF as a function of the axial position z_s with respect to focus. The first row of the figure [(A)-(C)] corresponds to $N=6000$ photons in the absence of background noise ($\beta = 0$ photons/mm^2), the second row [(D)-(F)] shows the localization precision for typical single molecule imaging when $N=6000$ photons in the presence of background noise $\beta = 60,000$ photons/mm^2 (≈ 10 photons/pixel) in the image space and the third row [(G)-(I)] shows the localization precision, typical for imaging a fluorescent bead, when $N=50,000$ photons in the presence of background noise $\beta = 60,000$ photons/mm^2 (≈ 10 photons/pixel) in the image space.

In the absence of noise, SIDH provides <20 nm precision and has more uniform localization precision than the other two PSF models in all three dimensions throughout the entire 20 μm depth of field. This is a direct result of the constant spatial variation rate in all three dimensions, which makes it more suitable for 3D localization based microscopy. In the low SBR case ($N=6000$, $\beta=10$ photons/pixel in Fig. 4.3(F)), SIDH does not perform as well as the Gaussian and the astigmatic PSF over the 20 μm range, thus making SIDH less suitable for 3D imaging at low SBR conditions. In the case of high SBR ($N=50,000$, $\beta= 10$ photons/pixel in Fig. 4.3(I)), the axial localization precision provided by SIDH outperforms the astigmatic and the Gaussian PSF when imaging away from focus thus making it suitable for single particle tracking applications.

It can be seen from Fig. 4.2, that the parameters of an SIDH system change with different DOE-CCD distances (z_h). The changes in the parameters result in changes in the CRLB of the SIDH system. Fig. 4.4 shows the CRLB of an SIDH system that uses one plane wave and one spherical wave (configuration 1) for different distances of z_h.

4.5 CRLB for SIDH with two spherical waves

When SIDH is performed using two spherical waves with different focal lengths f_{d1} and f_{d2}, the reconstruction distance (z_r) is given by
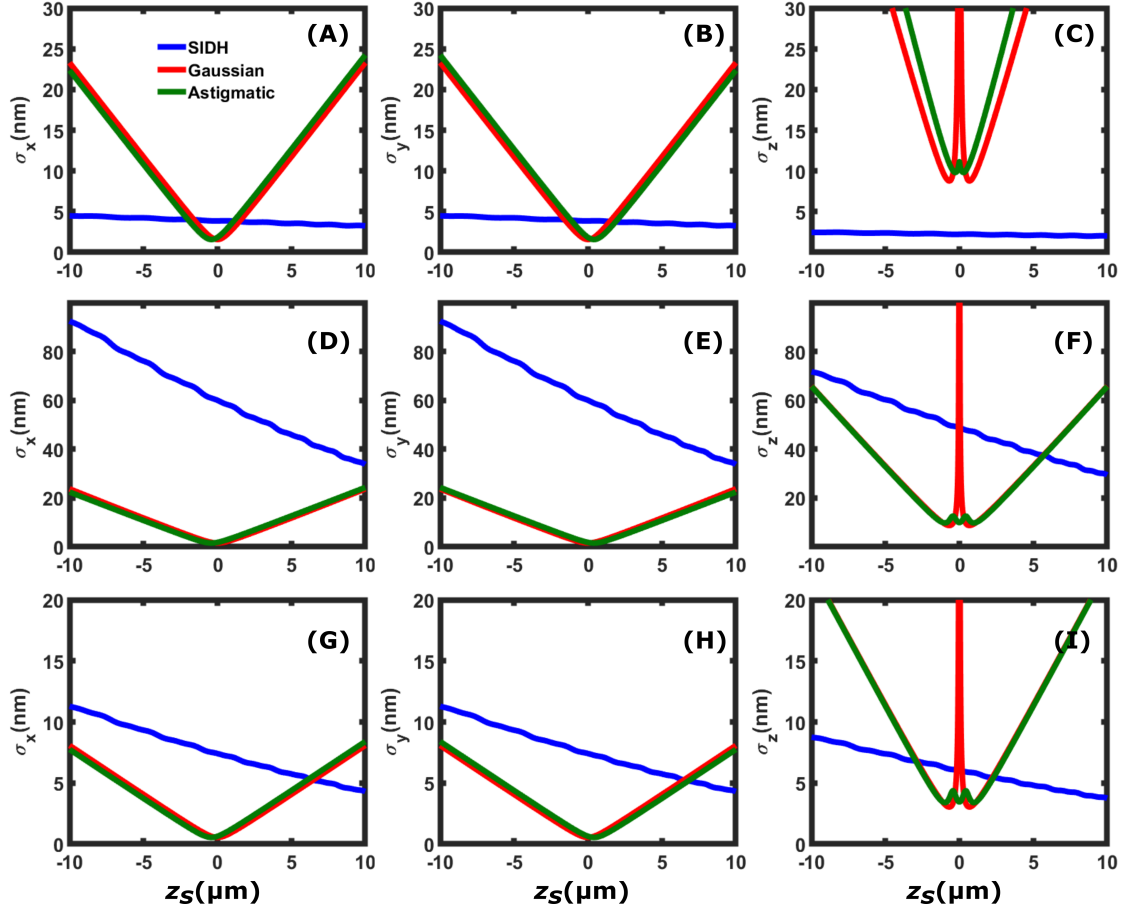
Figure 4.3: **Comparison of CRLB for SIDH with configuration 1, Gaussian and Astigmatic imaging models.** Comparison of the x [(A), (D) and (G)], y [(B), (E) and (H)], and z [(C), (F) and (I)] localization precision among SIDH with configuration 1, the astigmatic PSF, and the Gaussian PSF. The first row [(A)-(C)] shows the localization precisions when the single emitter is emitting N=6000 photons in the absence of background (β = 0 photons/mm^2), (D)-(F) when N=6000 photons and β = 60,000 photons/mm^2 ($\approx$ 10 photons/pixel) and (G)-(I) when N=50,000 photons and β = 60,000 photons/mm^2.

$$z_r = \begin{cases} \pm \dfrac{(z_h - f_{d1})(z_h - f_{d2})}{f_{d1} - f_{d2}}, & \text{for} \quad z_s = f_o \cap f_{d2} \neq \infty \\[3ex] \pm \left(\dfrac{z_{f1} z_{f2}}{z_d^2 (f_{d1} - f_{d2})} \right), & \text{for} \quad z_s \neq f_o \cap f_{d2} \neq \infty \end{cases} \tag{4.20}$$

86
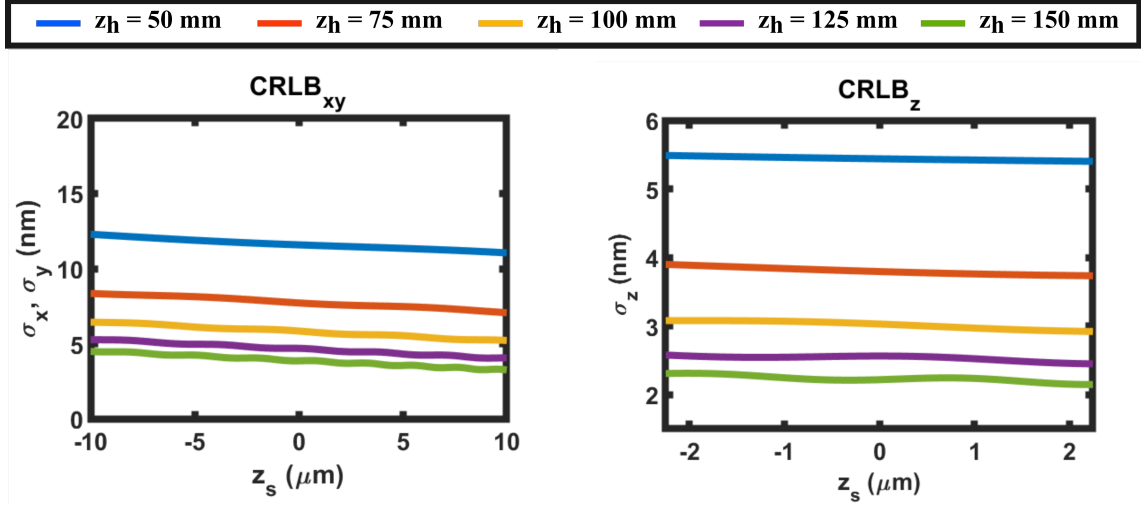
Figure 4.4: **CRLB for configuration 1 with different DOE-CCD distances.** σ_x, σ_y and σ_z calculations for SIDH with configuration 1 when the CCD is placed at different distances away from the DOE. N=6000 photons and β = 0 photons/mm^2.

where

$$z_{fn} = z_h z_d - f_{dn}(z_d + z_h), \qquad \text{and} \qquad z_d = \frac{z_s(f_o - d) + f_o d}{(f_o - z_s)}$$
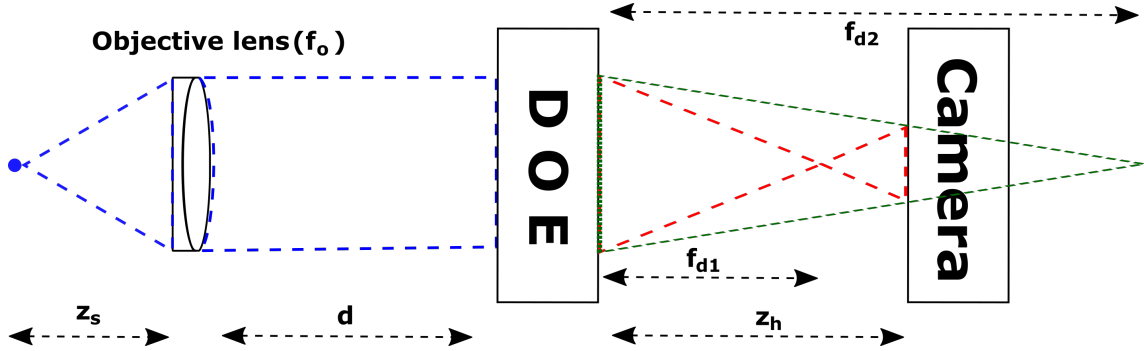
Figure 4.5: **SIDH with two spherical waves.** The interferogram formed at the camera is a result of two spherical waves (f_{d1} and f_{d2}).

The transverse magnification (M_T) for SIDH with two spherical waves is the same as that with one spherical and plane wave as described previously in Eqn. 4.17. The ABCD ray transfer matrices for

the system shown in Fig. 4.5 are given by

$$\begin{bmatrix} r_{f_{d1}} \\ \gamma_{f_{d1}} \end{bmatrix} = \begin{bmatrix} 1 & z_h \\ 0 & 1 \end{bmatrix} \begin{bmatrix} 1 & 0 \\ -1/f_{d1} & 1 \end{bmatrix} \begin{bmatrix} 1 & d \\ 0 & 1 \end{bmatrix} \begin{bmatrix} 1 & 0 \\ -1/f_o & 1 \end{bmatrix} \begin{bmatrix} 1 & z_s \\ 0 & 1 \end{bmatrix} \begin{bmatrix} h_{enter} \\ \gamma_{enter} \end{bmatrix} \qquad (4.21)$$

and

$$\begin{bmatrix} r_{f_{d2}} \\ \gamma_{f_{d2}} \end{bmatrix} = \begin{bmatrix} 1 & z_h \\ 0 & 1 \end{bmatrix} \begin{bmatrix} 1 & 0 \\ -1/f_{d2} & 1 \end{bmatrix} \begin{bmatrix} 1 & d \\ 0 & 1 \end{bmatrix} \begin{bmatrix} 1 & 0 \\ -1/f_o & 1 \end{bmatrix} \begin{bmatrix} 1 & z_s \\ 0 & 1 \end{bmatrix} \begin{bmatrix} h_{enter} \\ \gamma_{enter} \end{bmatrix} \qquad (4.22)$$

where $r_{f_{d1}}$ and $r_{f_{d2}}$ are the radii of the spherical waves formed due to the two focal lengths f_{d1} and f_{d2} at the CCD plane. The radius of the hologram (r_h) is this configuration is defined by the area of overlap between the two spherical waves at the CCD plane as is similarly given by

$$r_h = min(r_{f_{d1}}, r_{f_{d2}})$$

Although this configuration allows the camera to be placed nearer to the CCD, in order to image across the entire axial range ($\sim$ 20 μm) it is necessary to place it not in the range $z_h = 200$ to 400 mm (f_{d1} to f_{d2}) to ensure that the values of the reconstruction distance (z_r) are not symmetric across the focal plane (Fig. 4.6) Therefore, simulations for calculating the CRLB for SIDH using the configuration shown in Fig. 4.5 were performed by placing the camera at $z_h = 150$ mm.

The simulations to calculate the CRLB using this configuration are the same as those described in the previous section. the focal lengths of the quadratic phase patterns are f_{d1} = 200 mm and f_{d2} = 400 mm. Fig. 4.7 compares x, y, and z localization precision of SIDH using the second configuration with the Gaussian PSF and the astigmatic PSF as a function of the axial position z_s with respect to focus. The top row (Fig. 4.7 [(A)-(C)]) shows the CRLB comparisons for N=6000 photons in the absence for background noise, the middle row (Fig. 4.7 [(D)-(F)]) shows the CRLB comparisons for N=6000 photons in the presence of background noise β = 60,000 photons/mm^2 ($\approx$ 10 photons/pixel) and the third row (Fig. 4.7 [(G)-(I)]) shows the CRLB comparisons for N=50,000 photons in the presence of background noise β = 60,000 photons/mm^2.

The precision bounds for SIDH using this configuration are similar to the first configuration (with one plane wave and one spherical wave), however in the high SBR case, Fig. 4.7(I), this configuration provides better
axial localization precision than the astigmatic and the Gaussian PSF over the entire axial range. In general it can be seen from Fig. 4.7 that SIDH with configuration 2 performs better than SIDH with configuration 1. This can be attributed to the smaller hologram size throughout the axial range in configuration 2 which can be seen in Figs. 4.2 and 4.6. Since the number of photons contained in each of the holograms is the same, the larger size of the hologram in configuration 1 leads to more background noise in the hologram thereby degrading the localization precision.

Similar to configuration 1, the parameters of an SIDH system that uses two spherical waves to create holograms also changes with changes in the DOE-CCD distance (z_h). Fig. 4.8 shows the CRLB of an SIDH system that uses two spherical waves (configuration 2) for different distances of z_h.
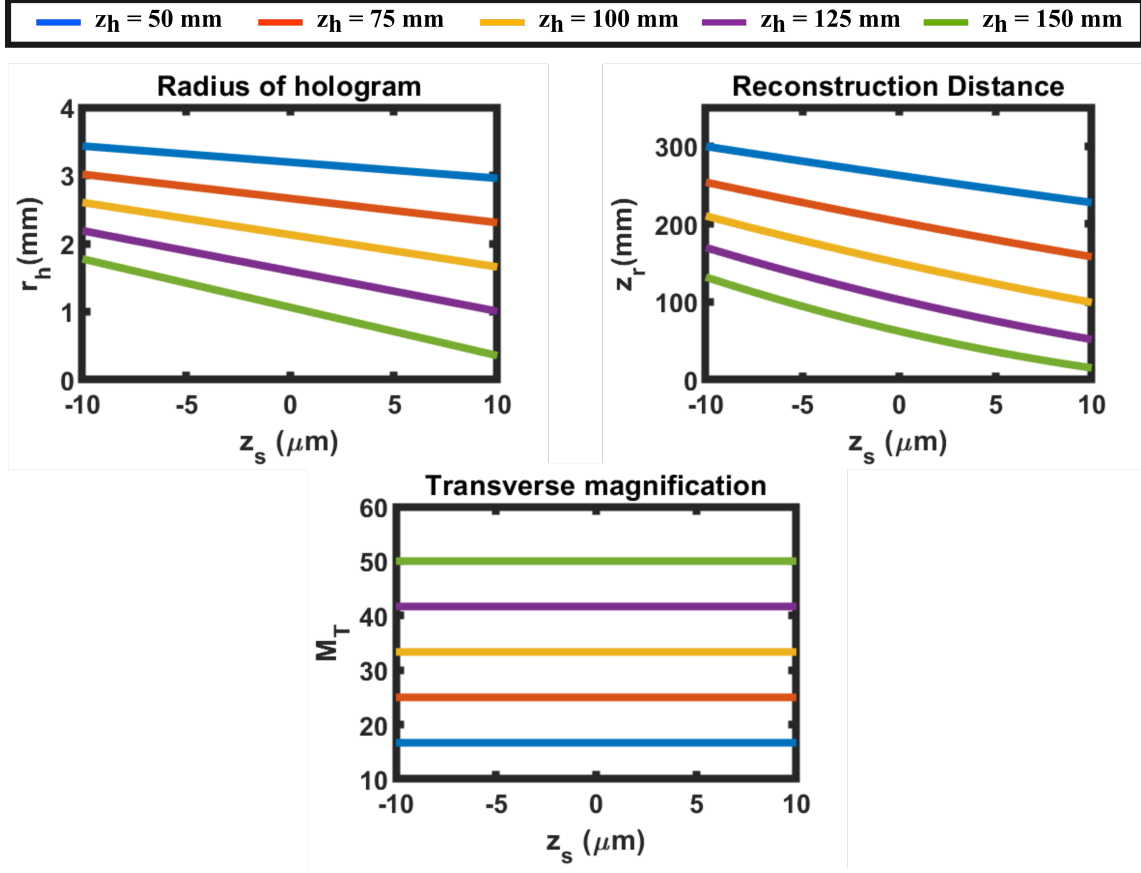
Figure 4.6: **Parameters of SIDH using configuration 2.** Hologram radius (r_h), reconstruction distance (z_r) and transverse magnification (M_T) of configuration 2 when the CCD is placed at different distances away from the DOE.

4.6 Comparing CRLB with simulated SIDH data

In this section we perform single molecule fitting of simulated incoherent holograms produced by a single particle emitting N = 6000 photons over three images in the presence of background noise β = 1000 photons/mm^2. We measure the precision of the localization by performing the localization 50 times for each axial position and comparing the standard deviation of the measurements to the CRLB values calculated above for configuration 1. The synthetic data was produced using the equations described in section 2.3 and the fitting of the reconstructed images was performed using custom written Python code described in Chapter 3 although here we localize in the z coordinate by finding the maximum intensity along the z direction rather than the minimum spot width.
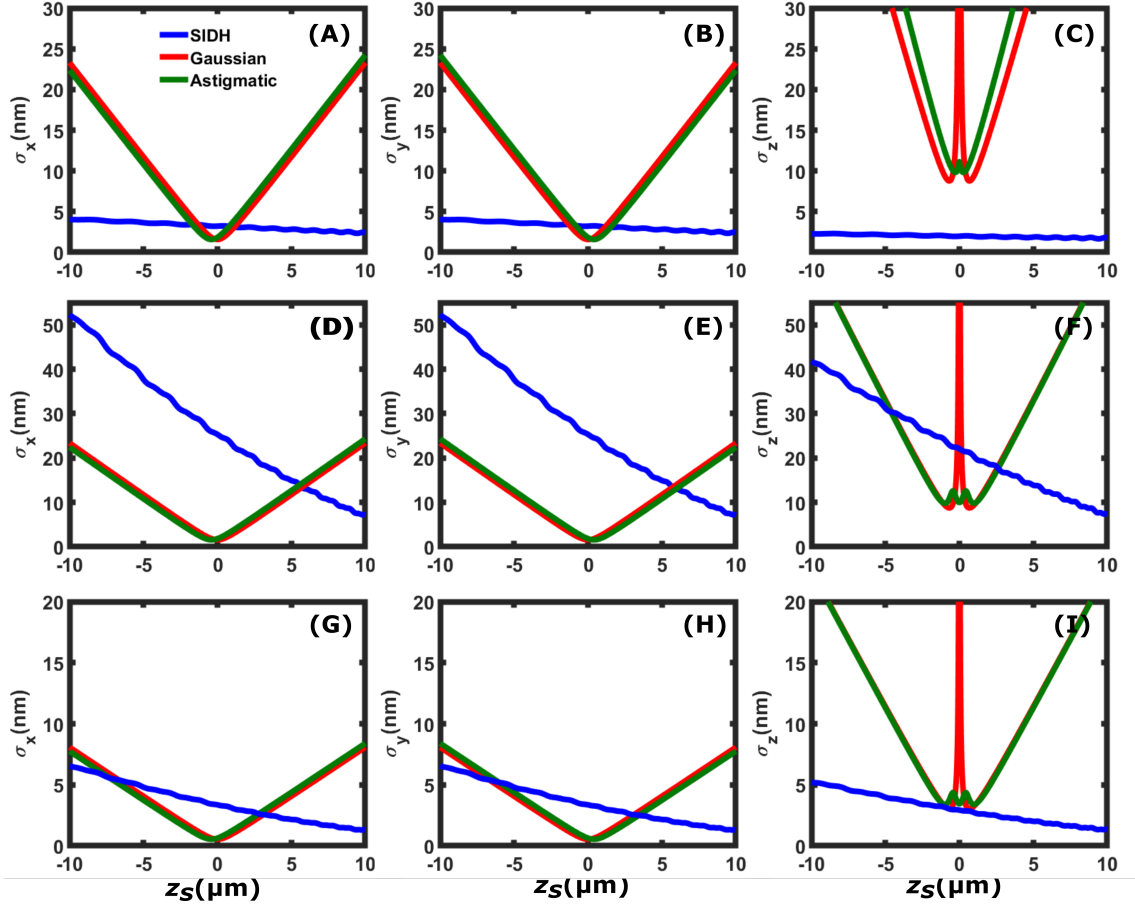
Figure 4.7: **Comparison of CRLB for SIDH with configuration 2, Gaussian and Astigmatic imaging models.** Comparison of the x [(A), (D) and (G)], y [(B), (E) and (H)], and z [(C), (F) and (I)] localization precision among SIDH with configuration 2, the astigmatic PSF, and the Gaussian PSF. The first row [(A)-(C)] shows the localization precisions when the single emitter is emitting N=6000 photons in the absence of background (β = 0 photons/mm^2), (D)-(F) when N=6000 photons and β = 60,000 photons/mm^2 ($\approx$ 10 photons/pixel) and (G)-(I) when N=50,000 photons and β = 60,000 photons/mm^2.

Figure. 4.9 shows that our code for fitting the data is close to the CRLB in the lateral dimensions (x-y). In the axial dimension (z), the measured standard deviations are roughly twice the calculated CRLB values. The spatial (x-y) localized coordinates are found by fitting a 2D Gaussian function to the images formed by reconstructing the holograms. Since the algorithm used to find the spatial coordinates converges to the maximum likelihood estimate (MLE) of the position, they reach the CRLB (Chao et al., 2016), however the reported axial (z) localized coordinates are found by fitting a curve to the intensity values in the axial direction and finding the maximum intensity value. We
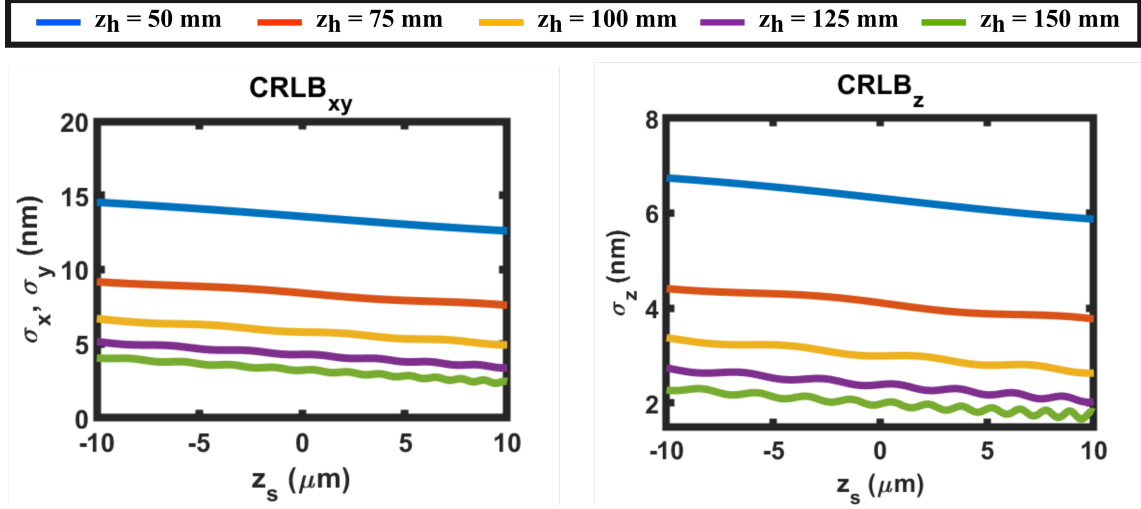
Figure 4.8: **CRLB for configuration 1 with different DOE-CCD distances.** σ_x, σ_y and σ_z calculations for SIDH with configuration 2 when the CCD is placed at different distances away from the DOE. N=6000 photons and β = 0 photons/mm^2.

speculate that this is the reason the reported axial localization precision does not reach the CRLB and that if we used a better model to fit the axial PSF of the images reconstructed from the holograms, the observed axial localization precision would reach the CRLB.
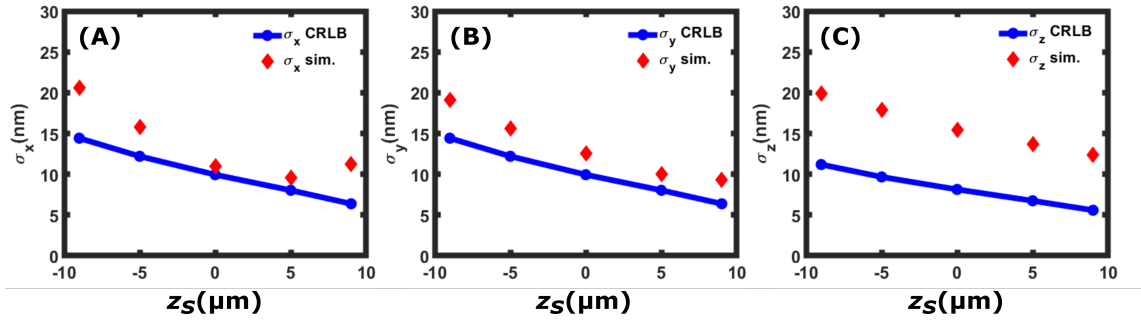
Figure 4.9: **Simultaneous fits to x, y, z, intensity and background for simulated data.** Shown are the reported σ_x, σ_y and σ_z values from 50 measurements of the simulated data. The calculated CRLB values are shown in solid blue lines and circles whereas the standard deviations from the simulations are labeled as red diamonds. The simulated dataset was created assuming a single particle emitting N = 6000 photons in the presence of background noise of β = 1000 photons/mm^2.

In Chapter 3 we have shown that SIDH can be used for localizing single particles by imaging a 100 nm fluorescent microsphere at $z_s = 0$ μm using SIDH and localizing it to produce a spatial precision

(σ_{xy}) of 5 nm and axial precision (σ_z) of 40 nm (Marar & Kner, 2020b). The number of photons emitted by the fluorescent particle was measured to be N = 49,000 photons and the background was β = 6 photons/pixel. We calculate the CRLB using the same number of photons and background as measured from the 100 nm fluorescent particle and calculated the lateral precision to be $\sigma_{xy} = 5.4$ nm and the axial precision to be σ_z = 4.4 nm.

4.7   Comparing the CRLB for SIDH with COSA

In this section we compare the CRLB for SIDH with that of the Cropped Oblique Secondary Astigmatism (COSA) PSF (Zhou & Carles, 2020). The COSA PSF is similar to the tetrapod PSF (Shechtman et al., 2015) and provides high axial localization precision over an adjustable axial range (6-20 μm). For simulating the COSA PSF we use a Numerical Aperture (NA) of 1.4, an emission wavelength of 670 nm, and a refractive index of 1.515. The imaging setup was designed to have an overall magnification of M_T = 50. The COSA PSF can be calculated using Fourier optics theory and can be written as

$$q(x, y) = |\mathcal{F}\{P(\rho) \exp\left(2\pi j \left(\psi(\rho, \phi) + D(\rho, z)\right)\right)\}|^2 \tag{4.23}$$

where $P(\rho) = \text{circ}(\rho)$ is the pupil function, $D(\rho, z) = z\lambda^{-1}\sqrt{n^2 + (\text{NA}\rho)^2}$ is the phase that results from a defocus, z and $\psi(\rho, \phi) = \alpha(\rho^4 - \rho^2)\sin(2\phi)$ is the COSA phase function (Zhou & Carles, 2020). The parameter α can be calculated for a desired axial range and system parameters using Eq. (5) from (Zhou & Carles, 2020). In these simulations, the adjustable parameter, α, is set to 11.46 which corresponds to a 15 μm axial range for our parameters.

To calculate the matrix elements quickly, we use a purely numeric approach and calculate the PSF from the FFT of the back pupil plane. We calculate the PSF over 2048 $\times$ 2048 pixels with a pixel size of 60 nm. dq/dx is calculated from the finite difference along the x axis from the PSF image, and dq/dz is calculated as the finite difference along the axial direction from the images, $q(x, y; z \pm \Delta z)$. $\Delta z = 2.5$nm.

Fig. 4.10 shows comparisons for the case of no background and for the case of a background of 60,000 photons/mm^2 ($\approx$ 10 photons / pixel) in the image plane. Again, we see that SIDH compares favorably in the case of no background, but does not perform as well with background.

4.8   Effect of background noise on CRLB for SIDH

As mentioned in section 4.3, background noise can have a deteriorating affect on the measured precision in SMLM. In Fig. 4.11, we calculate the CRLB for SIDH using configurations 1 and 2 as a function of background (up to $\approx$ 20 photons/pixel). For each configuration, we plot the best and worst precision over the range. We plot the maximum CRLB value with increasing background photon values up to β = 10^5 photons/mm^2 ($\approx$ 20 photons/pixel). Fig. 4.11 shows that while SIDH is successful at providing nm-scale precision across large axial ranges, the technique is highly sensitive
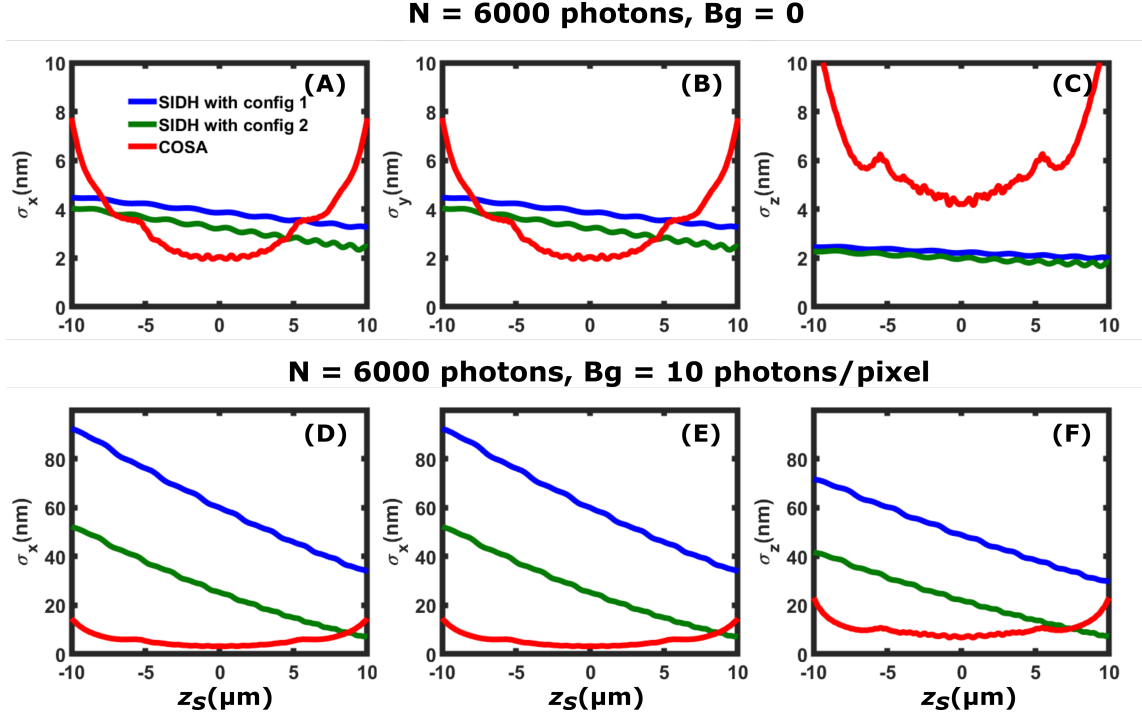
Figure 4.10: **CRLB for SIDH vs COSA.** Comparison of the x [(A) and (D)], y [(B) and (E)], and z [(C) and (F)] localization precision between SIDH with configurations 1 (blue plot), 2 (green plot) and the COSA PSF (red plot). The first row [(A)-(C)] shows the localization precision when the single emitter is emitting N=6000 photons in the absence of background (β = 0 photons/mm²) and (D)-(F) when N=6000 photons and β = 60,000 photons/mm².

to noise. As shown in Fig. 4.3 (D-F), the SIDH CRLB has a negative slope with respect to the axial position. This is due to the change in the size of the hologram as one moves across the entire axial range. The shape of the hologram is largest when the emitter is -10 μm away from the focal plane. Therefore the worst precision occurs at -10μm, and the best occurs at +10μm.

4.9   Conclusion

We have introduced a simple calculation for the fundamental limit to precision when using SIDH to perform localization based microscopy using the Fisher information matrix. The results introduced in this paper can be used to design SIDH systems to obtain a desired localization precision. Furthermore, these expressions can be used as a benchmark against which algorithms can be evaluated that are used to estimate the location of emitters. These results show that high precision localization in all three dimensions can be achieved over a 20 μm axial range using SIDH with high SBR. We have neglected

SIDH using Configuration 1

SIDH using Configuration 2
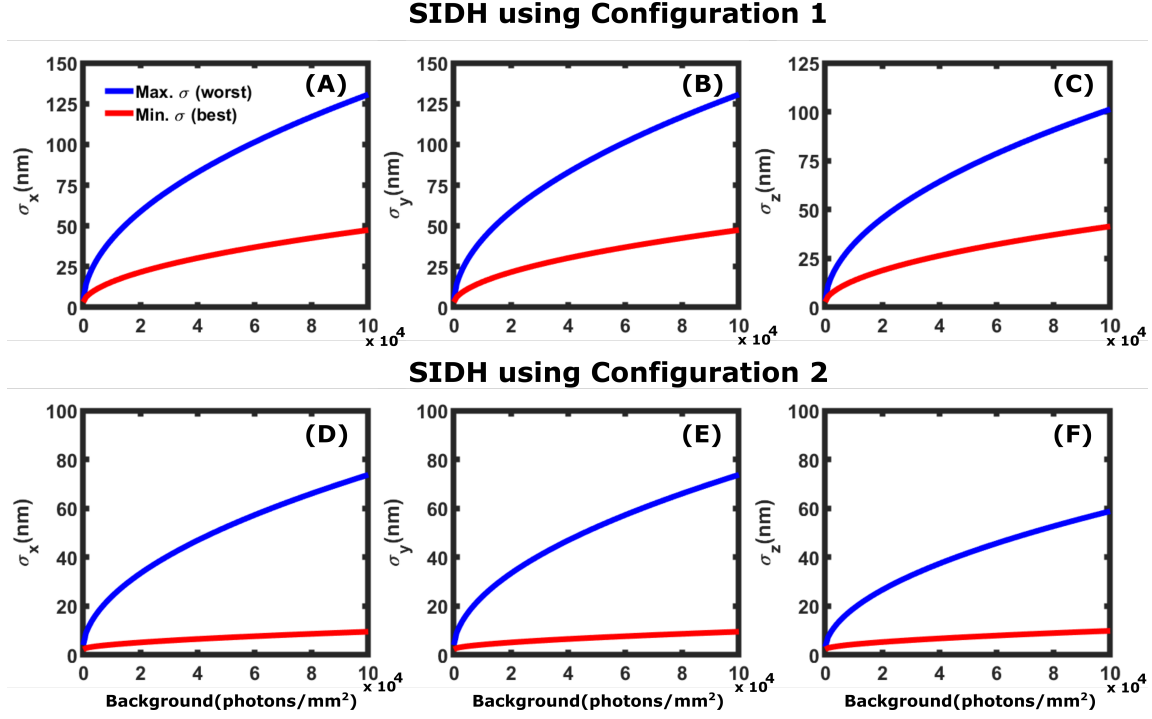
Figure 4.11: **Effect of background noise on CRLB.** Maximum (worst) and minimum (best) localization precision for SIDH using configuration 1 [(A)-(C)] and configuration 2 [(D)-(F)] for a particle emitting N = 6000 photons in the presence of background noise β = 0 - 10^5 photons/mm^2 ($\approx$ 0-20 photons/pixel). The CRLB plots shown in the figures are when the particle is at z_s = -10 μm (blue plot) and z_s = +10 μm (red plot). These are the highest (worst) and lowest (best) values of precision across the entire axial range due to size of the hologram being the largest and smallest at these points.

the effect of pixelation on the precision in our calculations because this does not relate directly to the effectiveness of SIDH as a localization technique, but including pixelation would be a next step in this work.

We also compare the localization precision of SIDH using two different configurations with localization precision from different PSF models including the astigmatic and the Gaussian PSF using parameters matched as closely as possible to their actual implementations. SIDH using both the configurations results in a small and almost constant localization precision over a large axial range of $\sim$ 20 μm for lower SBR conditions. In the presence of higher background noise (β > 5000 photons/mm^2, N = 6000 photons), SIDH continues to provide <50 nm precision in all three dimensions over the entire axial range. However, under such conditions, the astigmatic PSF provides better precision near the focal plane making it more suitable for imaging thinner samples ($\sim$1 μm thick). The high sensitivity to

background noise in SIDH is primarily due to the large size of the hologram compared to a Gaussian or astigmatic PSF. Since the hologram is spread over $\sim$ 2-4 mm^2, for β = 60000 photons/mm^2, the SBR for SIDH is significantly lower than the SBR for the astigmatic and the Gaussian PSF's thereby degrading the precision of the system. Localization over a large axial range can also be achieved with the tetrapod PSF for which the CRLB is $\approx$ 60 nm over 20 microns with 3500 signal photons and 50 background photons per pixel (Shechtman et al., 2015). With a background of 20 photons per pixel, SIDH achieves a precision of 125 nm. While the tetrapod PSF performs better than SIDH, understanding the performance of SIDH is of interest due to the analytical reconstruction process (Marar & Kner, 2020b) which allows reliable imaging of overlapping PSFs as discussed in chapter 3 and the ability to correct for optical aberrations in SIDH (Kim, 2012b). In SIDH, the reconstruction process provides the phase as well as the amplitude on the wavefront. Access to the phase information allows for the correction of the phase in the reconstruction process (Adie et al., 2012; Man et al., 2018) thereby reducing optical aberrations and improving the localization precision.

CHAPTER 5

MULTI-COLOR IMAGING USING DIRECT STOCHASIC OPTICAL RECONSTRUCTION MICROSCOPY

One of the primary advantages of fluorescence microscopy is the capacity to image specimens labeled with multiple fluorophores of distinct color to generate images featuring two or more channels to help unravel the relative organization and interactions between the biological structures or molecules of interest. In cases where multiple fluorescent probes are present within the same 3D volume, they can be subjected to co-localization analysis to determine their relative overlap, yielding information about potential in vivo molecular interactions. The higher resolution and quantitative nature of SMLM makes co-localization analysis of single molecule data more accurate than that performed on diffraction-limited data. Although multi-color fluorescence microscopy is well-established, additional demands have to be met in the context of multi-color SMLM.

Multi-color SMLM imaging with organic dyes was first demonstrated with probes that contained both an activator and a reporter fluorophore referred to as an activator-reporter pair or "dye pair". By combining different optically distinguishable fluorescent probes as activator-reporter pairs, multi-color imaging was realized by spectrally selective activation of the reporter fluorophore (Bates et al., 2007). A key advantage of using the same reporter with different activators (eg. Alexa 405-Cy5, Cy2-Cy5 and Cy3-Cy5) in multi-color stochastic optical reconstruction microscopy (STORM) is that chromatic aberrations are minimized because the same reporter fluorophore is detected. Although dye-pairs have been successfully used to perform multi-color STORM, they are not commercially available and have to be synthesized. Additionally, while synthesizing activator-reporter pairs is trivial in the case of antibodies, it is more challenging for smaller probes such as phalloidin and taxol, or in combination with chemical tags, such as SNAP-tag, and click chemistry (Boyce & Bertozzi, 2011; Keppler et al., 2003). Since, Alexa 647 has been evaluated to be one of the best organic dyes for SMLM (Dempsey et al., 2011), many multi-color STORM experiments use Alexa 647 dye as the reporter dye. However when using an activator-reporter pair such as Cy5-Alexa 647, the red-imaging

laser can directly activate the reporter dye and can also activate the dark state of the dye pair in an activator independent manner. Although these localizations can be filtered out assuming a constant non-specific activation probability, it reduces the number of single-molecule localizations which has negative affects, especially when trying to obtain statistical information from the localization table.

The commercial availability of antibodies that are readily tagged with photoswtichable fluorescent dyes makes *direct* STORM (*d*STORM) a promising option for multi-color SMLM (van de Linde et al., 2009). For multi-color SMLM using activator-free fluorophores, the most critical step is identifying a suitable set of fluorophores that can be used in the same experiment such that there is minimal spectral overlap between the reporter dyes and they must have compatible blinking conditions (i.e. organic fluorophores of different chemical classes require different "switching buffers", experimental conditions for blinking for the two dyes must be similar to be used in the same biological sample). Two-color *d*STORM using organic fluorophores has been successfully demonstrated using Alexa 532 - Alexa 647 (Flottmann et al., 2013) and ATTO 520 - Alexa 647 (Löschberger et al., 2012).

In this chapter, I first discuss the different techniques used for multi-color SMLM. Finally, I will discuss the experimental details of several conventional as well as multi-color *d*STORM experiments I performed with collaborators during my PhD.

5.1 Multi-color SMLM

In addition to the careful selection of photoswitchable fluorophores, the experimental protocol followed during imaging is of crucial importance in multi-color SMLM. Multi-color SMLM can be performed using different protocols and the choice of protocol is dependent on the the choice of fluorophores and vice-versa. In this section I will discuss the different methods that have been developed and used in this dissertation to perform multi-color SMLM.

ALTERNATING AND SEQUENTIAL IMAGING   In multi-color STORM imaging using the original cyanine dyes (Bates et al., 2007), different activator dyes paired with the same reporter fluorophore can be activated independently using lasers emitting different wavelengths. Different dye pairs are activated alternatively and the detected localizations form a two-color composite image with minimal cross-talk. Two color SMLM has also been performed using a photo-switchable protein and an organic dye (Bock et al., 2007). Two-color images of microtubules were recorded sequentially (completely imaging one dye and then imaging the second dye) and the reconstructed images from each dataset were then manually aligned to form a two-color composite image. Photoactivatable and photoswitchable proteins have also been used together to obtain two-color images of adhesion proteins and the actin cytoskeleton with sequential acquisitions (Shroff et al., 2007). The recording of the photoactivatable protein signal first was a key element of the method as both proteins were activated at the same wavelength but the photoswitchable probe could be reversed to a dark state in between the two acquisitions. Image registration was realized by localization of fiducials emitting in both channels, however registration in such a manner leads to errors on the order of tens of nanometers (Churchman & Spudich, 2012). Multi-color SMLM has also been achieved while imaging two photoswitchable

proteins (Andresen et al., 2008), two photoactivatable proteins (Subach et al., 2009) and multiple organic dyes without pairing (van de Linde et al., 2009).
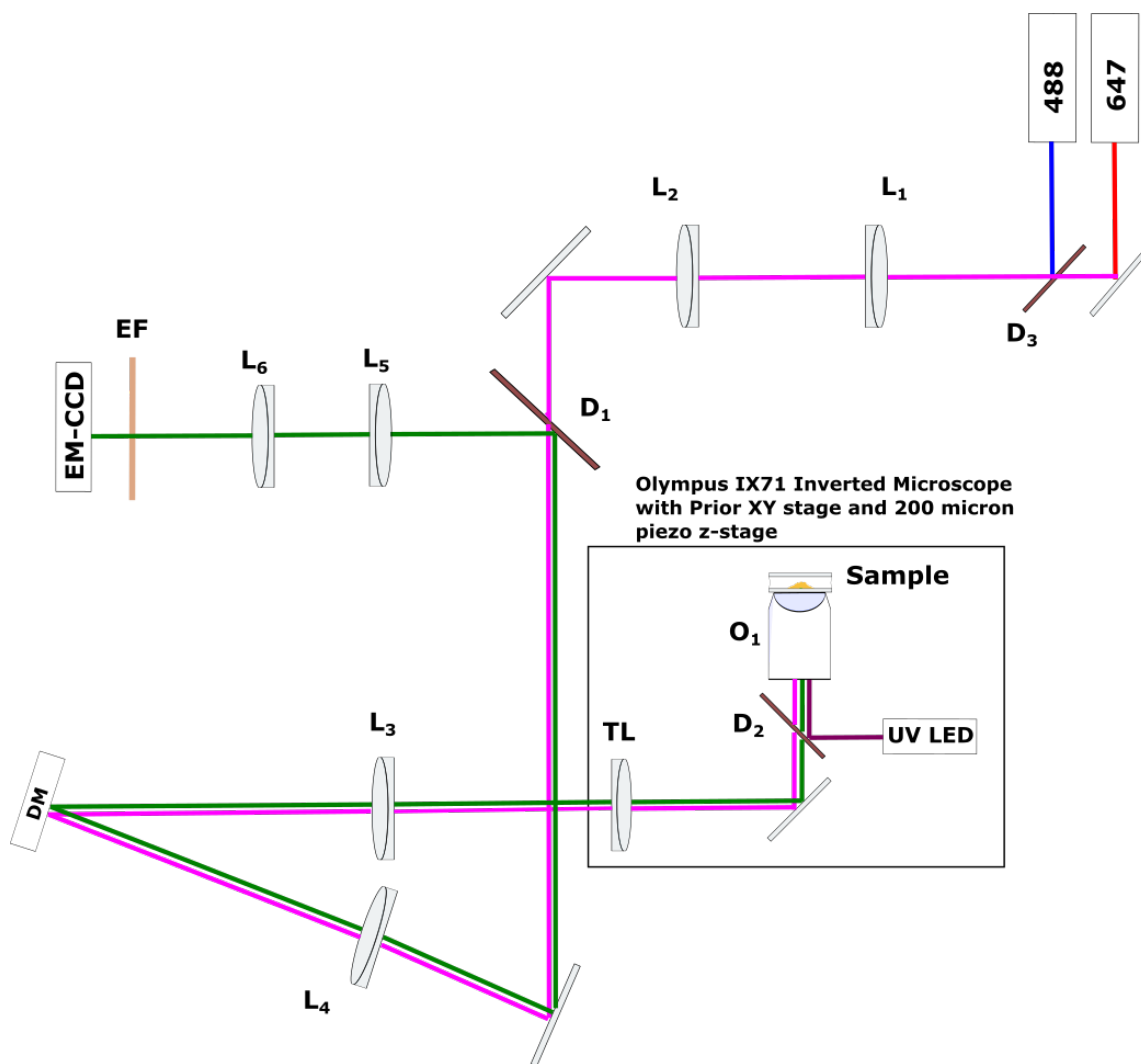
Figure 5.1: **Optical setup for two-color imaging of Meiotic Chromosomes** L_1: 100 mm, L_2: 300 mm, $L_3 = L_4$: 350 mm, DM: Deformable mirror, TL:Tube lens, 180 mm effective focal length (efl), L_5: 100 mm, L_6: 300 mm, O_1: Objective lens, $D_1 = D_2$: Dichroic Mirrors, EF: Emission Filter.

TWO-COLOR IMAGING OF MEIOTIC CHROMOSOMES   In this dissertation multi-color sequential imaging of meiotic chromosomes was done using organic dyes Alexa 488 and Alexa 647. Super-resolution imaging of chromosomes was performed on a STORM microscope system (see Fig. 5.1) that has been previously described (Tehrani et al., 2015). In these experiments, a 488nm laser (Cyan 488, Newport) and a 647nm laser (OBIS 647 LX, Coherent, Inc.) were used. The 488 nm laser beam is reflected off of a long-pass dichroic (DMLP567T, Thorlabs) so that excitation in both blue

and red channels can be combined. The emission and excitation paths are separated by a multiband dichroic (XF2054 485-555-650 TBDR, Omega Optical) and a multiband emission filter is placed before the CCD camera (BrightLine triple-band bandpass filter; FF01-515/588/700-25; Semrock). The objective is a 60x oil immersion objective (1.42 N.A., 60x oil immersion, Plan Apo N, Olympus) and the image is magnified by an additional factor of 3 before the CCD camera so that the effective pixel size at the sample plane is 89nm. The CCD camera is a 14-bit EMCCD that was used in emgain mode for these experiments (iXon DV887DCS-BV, Andor).
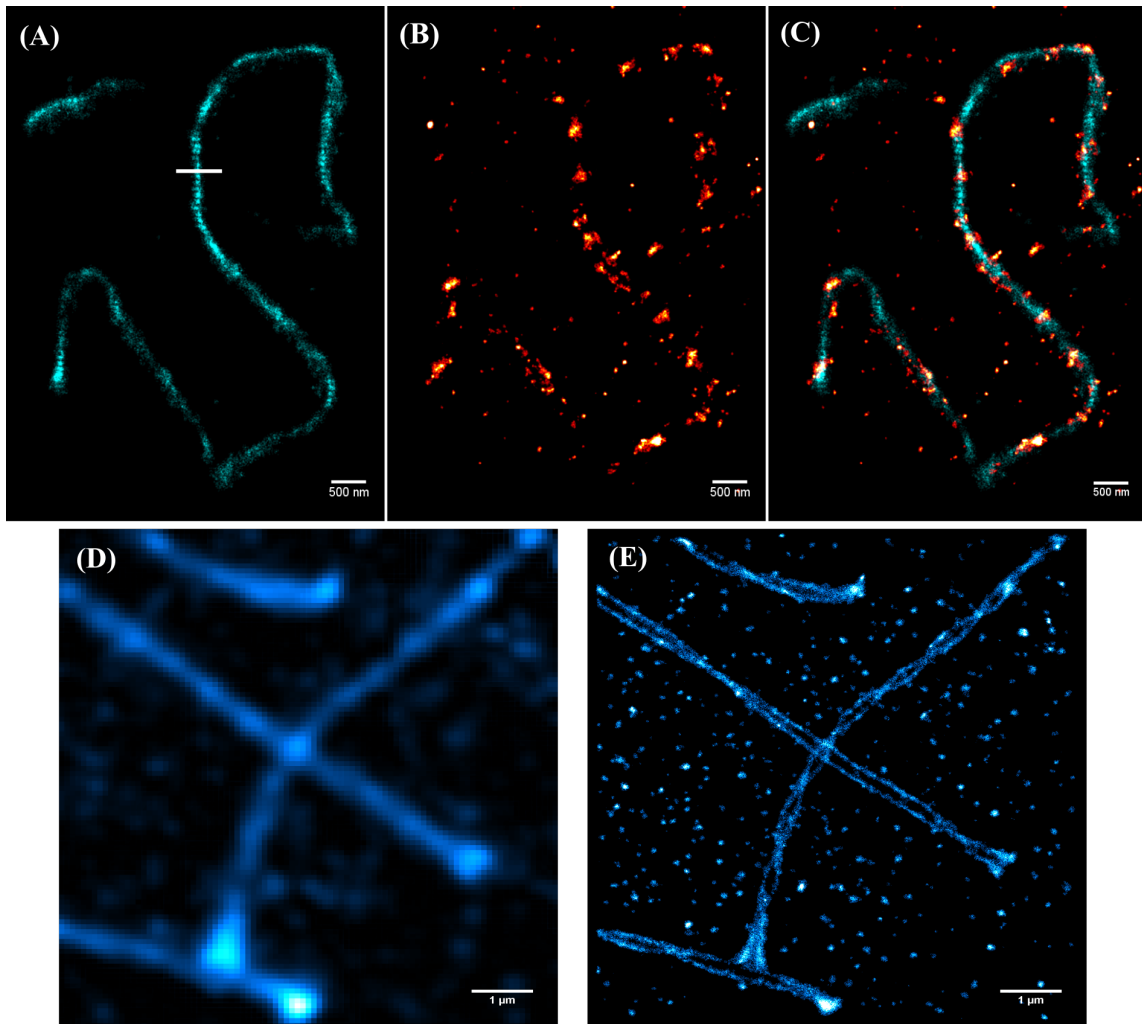
Figure 5.2: *d***STORM imaging of Meiotic Chromosomes.** *d*STORM images of (A) Alexa 488 conjugated with anti-SYCP3 (B) H3T11 with Alexa 647 (C) Composite two color image of (A) and (B). (A)-(C) show *d*STORM images of an x-y chromosome pair (D) Wide-field image of Alexa 488 conjugated with anti-SYCP3. (E) *d*STORM image of (D). Scale bars are 500 nm for (A-C) and 1 μm for (D) and (E).

The synaptonemal complex (SC) is an important structural component of meiosis that is used to localise pachytene chromosomes in routine experiments (Baudat et al., 2013). Chromosome spreads from mouse oocytes were obtained from the De La Fuente lab at the University of Georgia. Samples were immunostained using Alexa 488 conjugated anti-SYCP3 (Synaptonemal Complex Proteins) and H3T11 (Histone 3 at Threonine 11) with Alexa 647. An MEA switching buffer was prepared using the protocol listed in Dempsey et al., 2011. We first imaged Alexa 647 (in the case of H3T11) and then imaged Alexa 488 (in the case of SYCP3). 10,000 frames were acquired while collecting data for both the channels under continuous UV illumination using a 405 nm LED. In the case of the Alexa 488, the images were acquired at an integration time of 30 ms, whereas in the case of Alexa 647 the images were acquired at an integration time of 20 ms. The sample was irradiated with 5 kW/cm^2 using both 488 and 647 lasers in epi-illumination mode. The data sets were analyzed with the ThunderSTORM analysis module (Ovesný et al., 2014). The sub-pixel positions of the single molecules were determined by fitting a PSF model to the images of single molecules. An integrated form of a 2D Gaussian function was used as the PSF model for fitting and maximum likelihood estimation (MLE) was used as the parameter estimation algorithm to perform the fitting. The single-molecule positions further underwent uncertainty correction and a super-resolution image reconstructed with a pixel size of 8.9 nm. The visualization algorithm used a density estimation approach based on average shifted histograms (Scott, 1985). Four histograms were averaged in total, i.e., for two shifts in each dimension. The origin of each histogram was shifted by 8.9 nm from the previous histogram and the width of the histogram bin was set to be 17.8 nm. A two-color image was generated after manually aligning the two channels that revealed periodic clusters of chromatin. Fig. 5.2 shows the two-color *d*STORM image of SYCP3 (Blue) and H3T11 (red).

TWO-COLOR IMAGING OF SYNAPTIC PROTEINS   Synaptic proteins play a role in the regulation of neurotransmitter release in neurons as well as their development. Throughout neuronal development, the cytoskeletal organization and the molecular organization changes. It has been previously reported that synapsins, a type of synaptic protein, play a role in tethering synaptic vesicles to the cytoskeleton to regulate release of neurotransmitters at the mature synapse (Cesca et al., 2010). In addition to looking at the morphology of the growth cone to assess the development of the synapse, we can also evaluate its maturation by looking at localization of synaptic vesicle proteins. Synapsins are one the most abundant group of proteins associated with synaptic vesicles (Greengard et al., 1993). By evaluating the localization of synapsin we can assess the relative size of the synaptic vesicles throughout development that can be released from mature synapses and study different functions of these proteins during the developmental processes.

We performed multi-color *d*STORM imaging of protein interaction on a neuronal filopodia using the optical setup shown in Fig. 5.3. The data was collected using a custom-built inverted wide-field microscope. Illumination lasers (OBIS 405 nm LX 100 mW; OBIS 561 LS 50 mW; and OBIS 647 LX 120 mW, all continuous wave (CW), from Coherent) were spectrally filtered (561 nm: LL02-561-12.5 excitation filter, 647 nm: LL02-647-12.5 excitation filter, both Semrock) and expanded and collimated using a custom-built beam expander. The light emitted from the sample was collected using a high NA
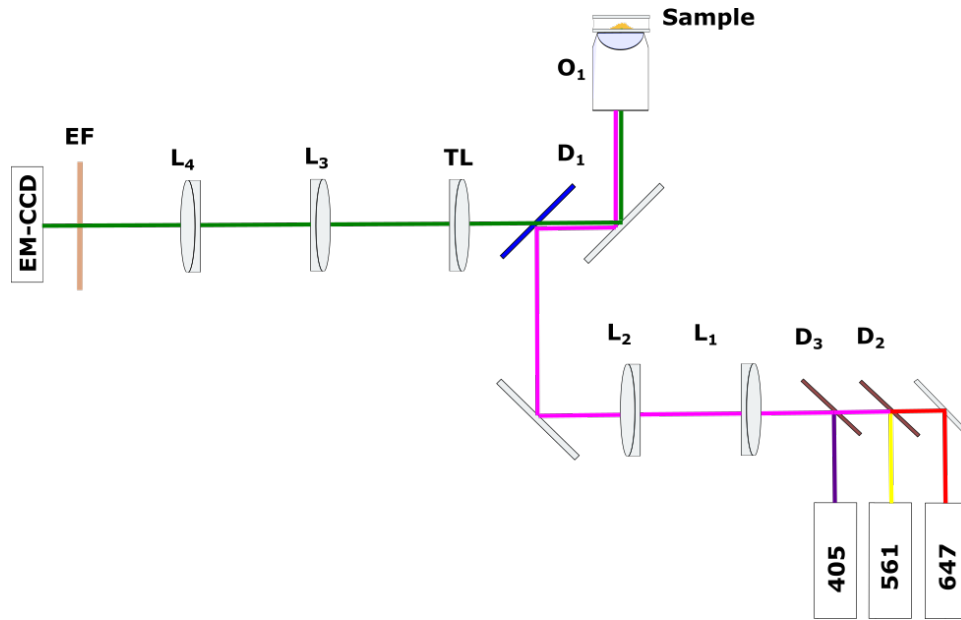
Figure 5.3: **Optical setup for two-color imaging of neuronal filopodia.** L_1: 100 mm, L_2: 120 mm, L_3: 120 mm, L_4: 300 mm, TL:Tube lens, 180 mm effective focal length (efl), O_1: Objective lens, D_1: Dichoric Mirror, EF: Emission Filter.

oil-immersion objective (Olympus, PlanApoN 60x/1.42) mounted on a piezoelectric objective lens positioner (Smaract, Germany). The emitted light was spectrally filtered (Omega, XF2054,485-555-650TBDR dichroic, Semrock, FF01-446/523/600/677-25 multi-bandpass filter, for far red detection: Semrock, FF01-680/42 bandpass filter, Semrock, NF01-488/647 notch filter and for red detection: Semrock, FF01-605/15 bandpass filter and Chroma, ZET561NF notch filter) and focused by the tube lens (efl = 180 mm, Olympus, UTLU). The intermediate image plane formed by the tube lens was further magnified and imaged using a 4f system onto an electron-multiplying charge-coupled device (EMCCD) camera (Andor, iXon-897 Life).

Filleted *Drosophila* embryos were obtained from the Kamiyama lab at the University of Georgia. The growth cone was labelled with anti-HRP conjugated with Alexa 647 and the synapsin protein was labelled with CF 568 (Biotium). We first imaged Alexa 647 (Growth Cone) and then imaged CF 568 (Synapsin). 60,000 frames were acquired while collecting data for Alexa 647 under continuous UV illumination using a 405 nm laser. In the case of the CF 568, only 10,000 images were acquired at which point the the sample stopped blinking. Images in both channels were acquired at an integration time of 20 ms and the data was reconstructed using the ThunderSTORM analysis module (Ovesný et al., 2014) with similar parameters as described previously (see "Two-color imaging of meiotic chromosomes"). Fig. 5.4 shows two-color *d*STORM imaging of localization of synaptic proteins on the growth cone.
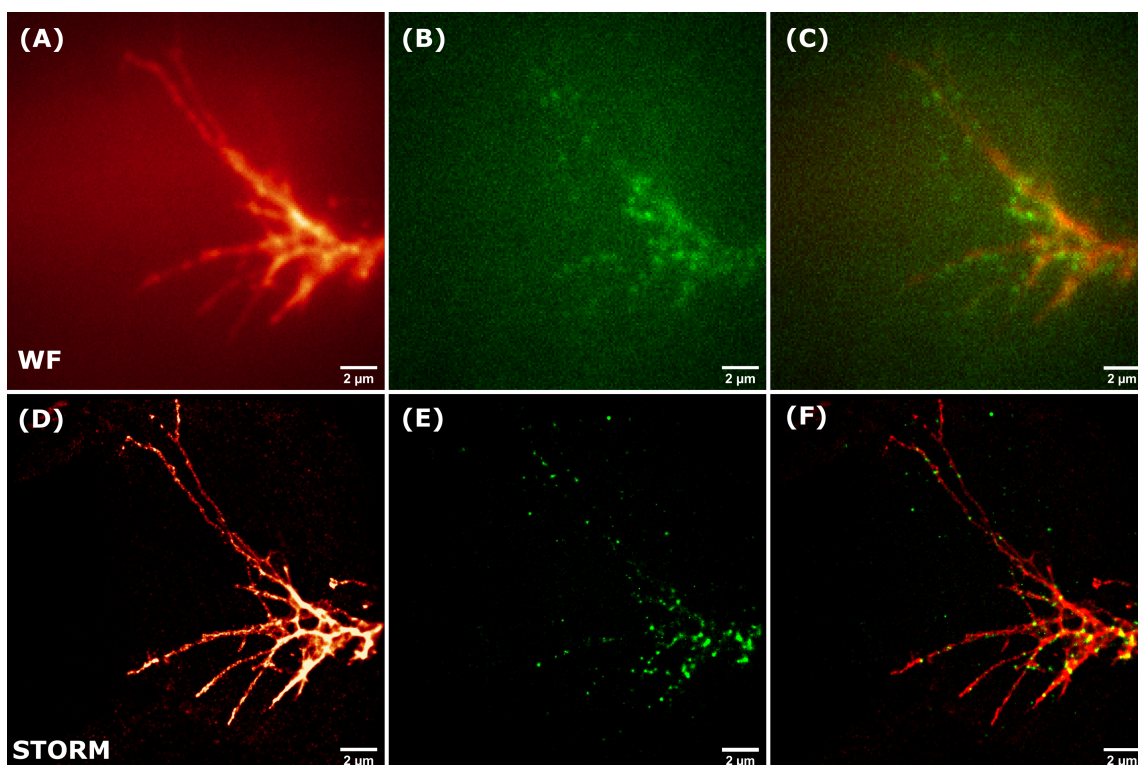
Figure 5.4: **Two-color *d*STORM image of synaptic proteins.** Diffraction limited images of (A) Alexa 647 conjugated with HRP tagging neuronal filopodia (B) Synapsin tagged with CF 568 (C) Composite two color diffraction limited image of (A) and (B). (D-F) *d*STORM images of (A-C) respectively. Scale bars are 2 μm.

Data was acquired in both channels (561 and 647) using 5 kW/cm^2 of laser power. The experiment starts with the 405 nm laser turned off and is turned on when the number of blinking events starts to decrease ($\sim$ 10,000 frames for Alexa 647). The laser power of the 405 channel is gradually increased (start from 1 mW coming out of the laser and go till 100 mW) till the sample stops blinking.

Registration of the two channels was performed using the NanoJ-Core (Laine et al., 2019) plugin in Fiji. To calculate a chromatic shift map across the entire field of view (FOV), a calibration data set was obtained by imaging 200 nm TetraSpeck beads in the far-red channel (Fig. 5.5 (D)) and the red channel (Fig. 5.5 (E)). The calibration dataset was acquired using the exact same optical system (same objective, additional magnification, filter sets etc.) that was used for imaging the synaptic proteins. Fig. 5.5 (F) shows the composite image of the two channels in the calibration dataset where we can clearly see the chromatic misalignment. Figures 5.5(A) and (B) were used to calculate the chromatic shift map using the dark-red channel (Fig. 5.5 (A)) as the reference channel. The shift map is presented as two images which are the same size of the entire camera chip (512x512 in this case). Fig. 5.6(A) shows
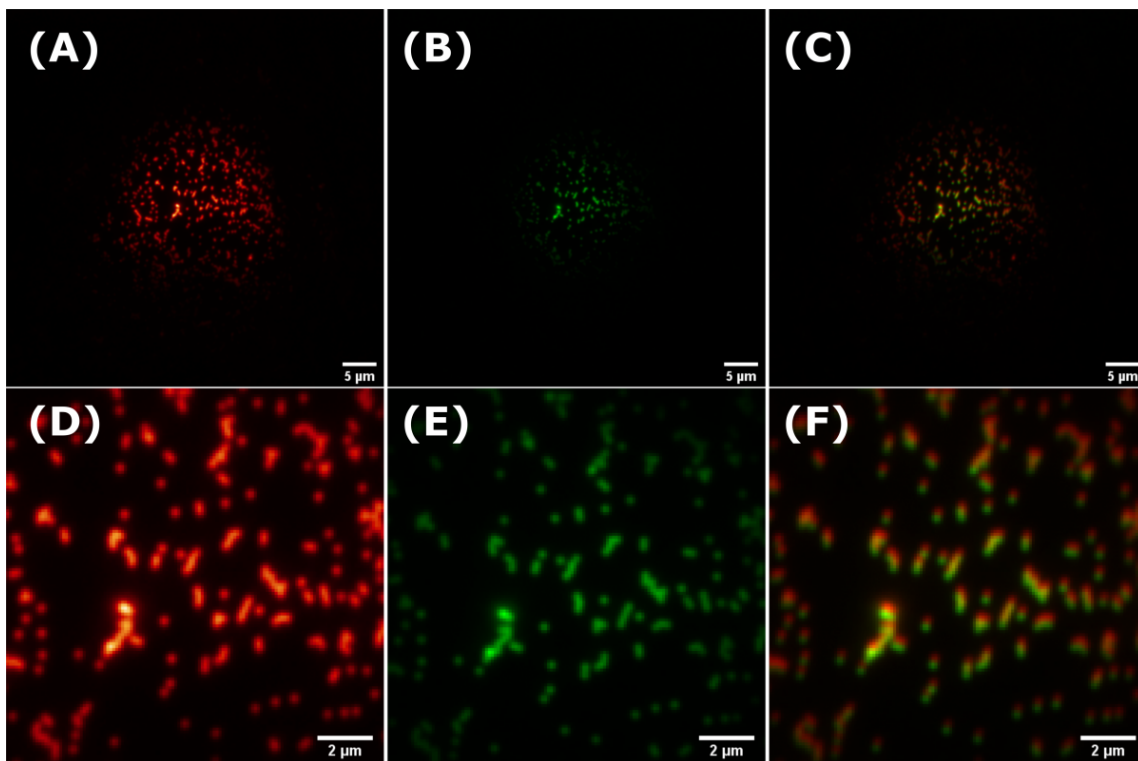
Figure 5.5: **Calibration dataset for two-color image registration.** Chromatic shift seen when imaging 200 nm tetrapeck beads using laser light of 647 nm and 561 nm. (A) Image of 200 nm tetraspeck beads seeing using 647 nm laser (B) Image of 200 nm tetraspeck beads seeing using 561 nm laser (C) Composite of (A) and (B) showing two-color data (D, E, F) Magnified images of the central 128 X 128 pixels of (A), (B) and (C).

the chromatic shift map in the x-direction and Fig. 5.6(B) shows the shift map in the y-direction. For a given channel, each pixel value within the horizontal/vertical shift map indicates the horizontal/vertical displacement that needs to be applied to that pixel to align it with the reference channel.

Default parameters in the NanoJ-Core plugin were used to calculate the shift map. The channel registration performed by NanoJ-Core creates new images for each channel where the intensity value for each pixel coordinate corresponds to the intensity value from the original image at the equivalent coordinate corrected for local chromatic shift given by the chromatic shift masks. For cases in which these coordinates are not discrete (sub-pixel shift), a bicubic spline interpolation is used to recover pixel values in continuous space. Because the shift map can be extrapolated to continuous space, the registration procedure obtained from diffraction-limited images can also easily be used to correct super-resolved images obtained using the same optical configuration. The chromatic shift mask obtained by aligning the calibration dataset was scaled to the size of the super-resolution image
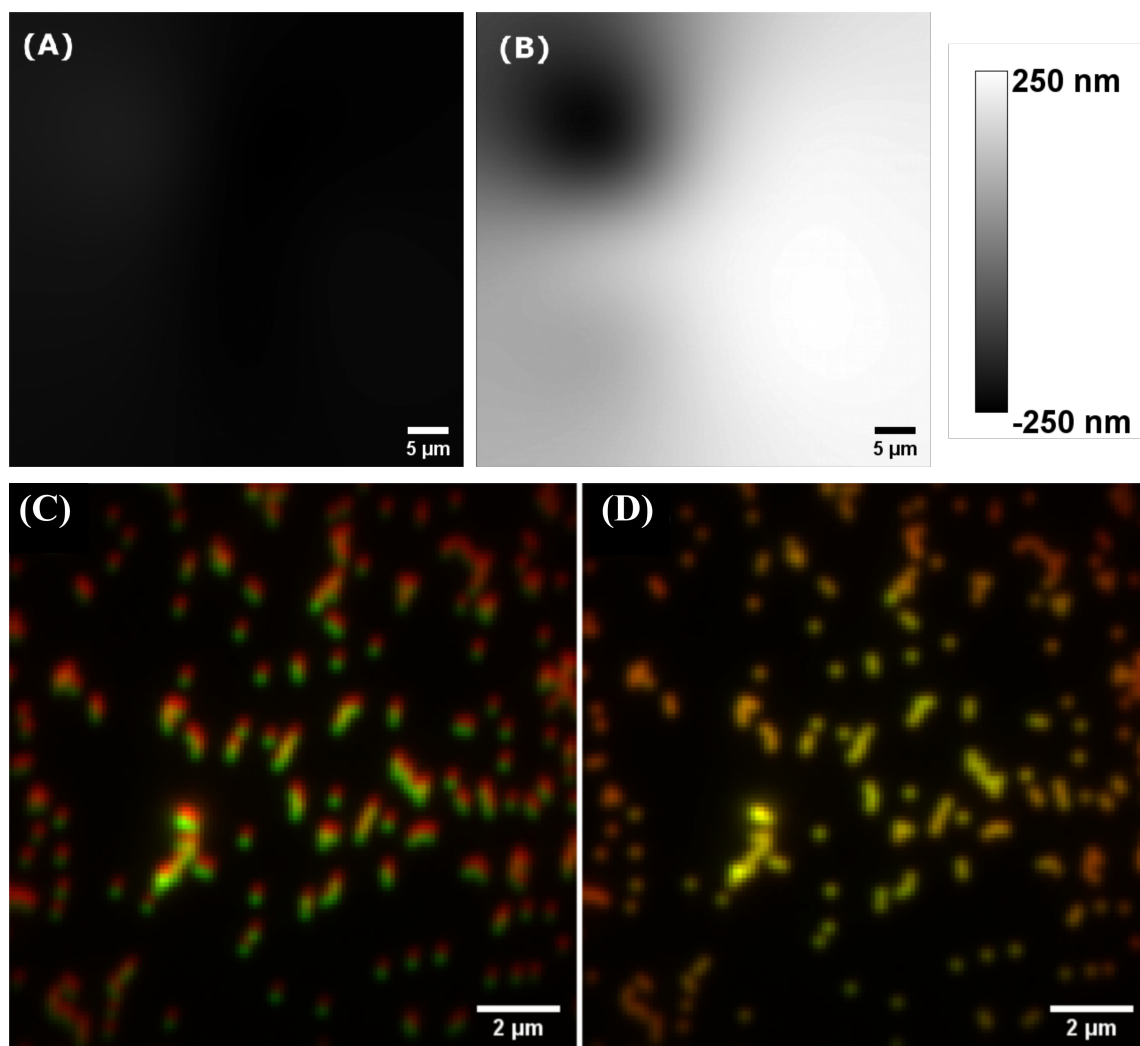
Figure 5.6: **Chromatic shift map and calibration data realignment.** (A) Estimated chromatic shift in x across the 512x512 field of view (B) Estimated chromatic shift in y across the 512x512 field of view (C) Two-color image of beads acquired using the two channels before registration (D) Two-color image of beads acquired using the two channels after registration

and the corresponding ROI was cut out of the chromatic shift mask to realign the composite image of the growth cone and the synaptic protein (Fig. 5.7).

SIMULTANEOUS IMAGING   Instead of alternating or sequential imaging, chromatically separated fluorescence can be acquired simultaneously and split using dichroic mirrors. The spectrally separated fluorescence can then be imaged using separate cameras or on the same camera by dividing the camera chip into multiple portions. The collected data is divided into the regions representing
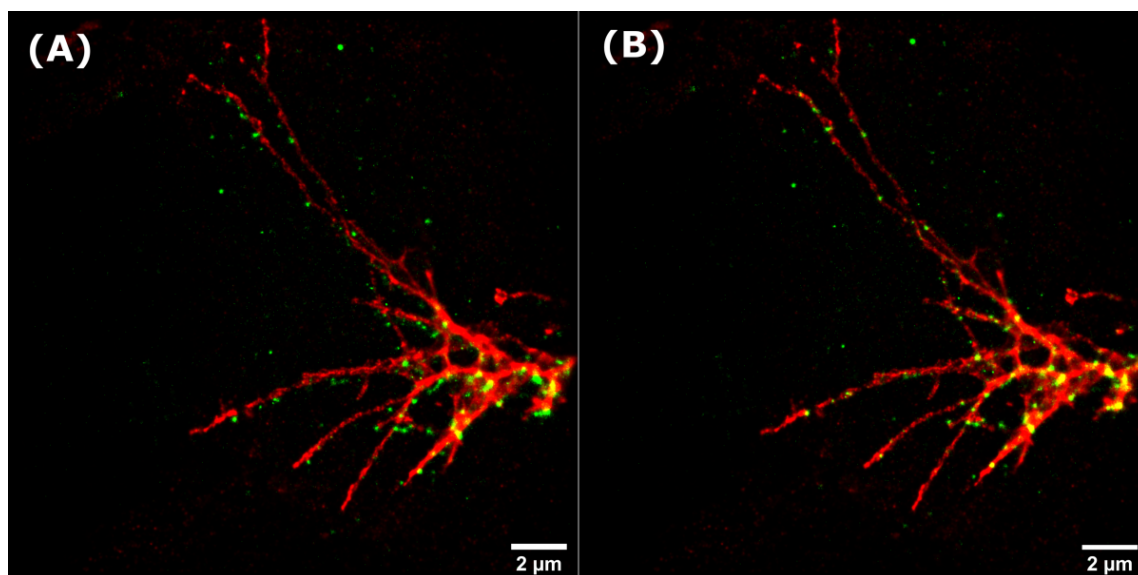
Figure 5.7: **Chromatic shift correction on super-resolution data.** *d*STORM image of the growth cone tagging HRP (red) and synapsin (green) (A) before chromatic shift correction (B) after chromatic shift correction.

the different channels and then manually aligned. As in the case of sequential imaging, such methods are susceptible to registration errors. An interesting alternative that circumvents the need for registration involves imaging fluorescent molecules with close but slightly shifted emission spectra (Bossi et al., 2008). In this case, the fluorescence is split using a dichroic mirror and imaged on multiple channels, however since the spectra are very similar and the localizations appear on both the channels, the individual fluorescent probes are identified by plotting the number of detected photons in each channel. The small difference in the fluorescence spectrum of each channel means that the ratio of transmitted to reflected photons from the dichroic will be different for each of the fluorescent probes. Each population forms a cluster defined by the photon ratio thereby making it easy to assign each localization to a specific fluorescent marker. Once, localizations have been classified, the final image can be rendered in a single channel thereby avoiding the need for registration. Furthermore, since the emission spectra of the fluorescent markers are close to each other, chromatic aberrations observed in such systems are minimal. Multi-color imaging using ratiometric analysis has been shown using organic dyes (Baddeley, Crossman, et al., 2011; Bossi et al., 2008; Testa et al., 2010; Winterflood et al., 2015) and fluorescent proteins (Gunewardene et al., 2011).

5.2   Experimental Methods

This Section describes the sources, optics, and detectors necessary for quantitative single molecule imaging. It also details how to augment a conventional fluorescence microscope with the necessary optical components for implementing light sheet illumination and self-interference digital holography. Several optical designs are presented, depending upon whether conventional fluorescence microscopy, self-interference digital holography, or simultaneous two-color imaging is desired.

EXCITATION SOURCES AND OPTICS   In this section I summarize the functions of the components depicted in the excitation path in Figure 5.8 (red path). Single molecules are typically excited by a coherent laser source tuned near their peak absorption wavelength, although sufficiently bright arc lamps and light emitting diodes (LED) also can be used. The bandwidth of some light sources may be broad enough to leak into the fluorescence detection channel, and thus, a narrow bandpass excitation filter is usually used to reject long wavelength photons that could contribute to unwanted background.

The excitation light can be coupled into the microscope in several different ways depending upon the sample of interest (Hu et al., 2014). The most straight-forward geometry is conventional widefield epifluorescence excitation (dotted red path in Fig. 5.8), in which the excitation beam is focused onto the pupil of the objective lens by a widefield lens (also known as a Köhler lens). This arrangement produces a collimated excitation beam in the sample parallel with the optical axis of the objective lens. However, when imaging a thick sample, conventional widefield excitation can produce a large amount of background autofluorescence. A simple way of reducing background is to tilt the pumping beam in the sample, referred to as pseudo- or quasi-total internal reflection (TIR) or a highly inclined and laminated optical (HILO) sheet (Tokunaga et al., 2008), so that the thickness of the excitation region is reduced. Due to the Fourier transform relationship between pupil and sample planes, tilting of the beam in the sample is produced by translation of the beam at the pupil. Finally, in total internal reflection fluorescence (TIRF) microscopy (Axelrod et al., 1984), the excitation beam is tilted beyond the critical angle such that it is confined within the microscope coverglass. The penetration depth of the evanescent field is very thin ($\sim$ 200 nm), and thus, TIRF microscopes exhibit a great ability to image single molecules in thick, highly autofluorescent cells. The drawback of this method also arises from the extremely thin excitation region; 2D or 3D imaging beyond the surface of the cell at the coverslip is impossible. Another way to decrease the background autofluorescence in single molecule imaging involves exciting the sample with light sheet illumination (solid red path in Fig. 5.8) which uses a cylindrical lens to create a sheet of light which is coupled into another objective (O_2) and excites the sample in a way that is perpendicular (or at a small angle) to the emission objective (O_1) thereby exciting only a thin layer of the sample. The sheet can then be moved in the axial direction using a motorized mirror placed in the back pupil plane of the excitation objective (O_2 in fig. 5.8). Details about the light sheet excitation pathway have been described in chapter 3.
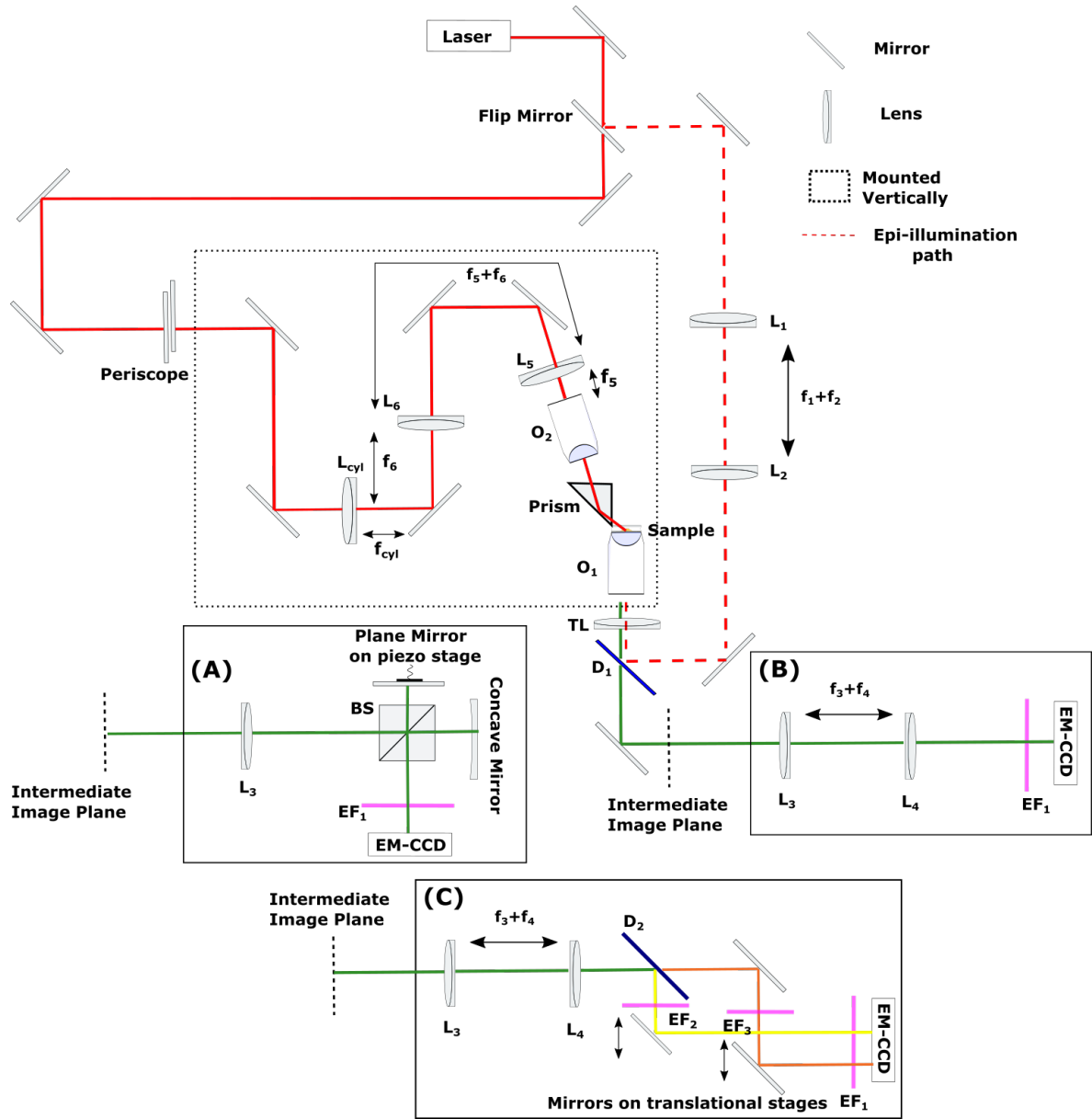
Figure 5.8: **Optical system used for SMLM and SIDH.** The optical system used in this dissertation allowed for epi-illumination (dotted red path) and light sheet ilumination (solid red path). Details of the light sheet setup can be found in chapter 3. In the epi-illumination pathway the light from the laser is passed through a telescope (L_1: 100 mm and L_2: 120 mm) to expand the beam. Emission pathways are shown in green for the (A) SIDH setup (B) conventional SMLM setup and (C) simultaneous two-color SMLM setup. L_3: 120 mm, L_4: 300 mm, TL: 180 mm.

COLLECTION OPTICS AND DETECTORS In this section I summarize the functions of the components depicted in the collection path in Figure 5.8 (green pathway). The objective lens defines the imaging performance of modern optical microscopes, which are mostly differentiated by NA and aberration-correction performance. The light-collection capability of an objective lens is characterized by its NA, where the solid angle of collection is proportional to NA^2. Since localization precision improves with the square root of the number of detected photons (See chapter 1), the NA should be as large as possible. The image plane of the microscope is formed by the tube lens of a focal length that depends upon the microscope manufacturer. Olympus microscopes use a focal length of 180 mm, while Nikon microscopes use a focal length of 200 mm, for example. Note that the matching of a manufacturer's objective and tube lenses together create the specified magnification factor printed on the objective lens. Finally, the fluorescence photons are captured by a highly-sensitive 2D array detector, typically an EMCCD or scientific complimentary metal-oxide-semiconductor (sCMOS) (F. Huang et al., 2013) camera. These detectors have high quantum efficiency (>90% for EMCCD, >60% for sCMOS), low read noise, and low dark counts (via sensor cooling), enabling them to be excellent for photon-limited single molecule imaging. Depending upon the pixel size of these detectors and the magnification of the microscope, an additional imaging telescope may be needed to optimize the number of pixels used to sample each diffraction-limited PSF.

EMISSION PATHWAY FOR ALTERNATING SMLM The fluorescence emitted by the sample was separated from the laser excitation light using a dichroic mirror (Omega, XF2054,485-555-650TBDR, USA) and a multi-band bandpass filter (Semrock, FF01-446/523/600/677-25, USA). The objective lens and the tube lens (f_{TL} = 180 mm, Olympus, UTLU, USA) formed an intermediate image plane which was further magnified using achromats L_3 = 120 mm and L_4 = 300 mm before being imaged onto the EMCCD camera (Andor iXon-897 Life,UK).

EMISSION PATHWAY FOR SIDH The fluorescence emitted by the sample was separated from the laser excitation light using a dichroic mirror (Omega, XF2054,485-555-650TBDR, USA) and a multi-band bandpass filter (Semrock, FF01-446/523/600/677-25, USA). We used a piezoelectric objective lens positioner (Smaract, Germany) to axially scan a sample of beads dried on a standard microscope cover-glass. The back-pupil plane of the objective was demagnified using a tube lens (f_{TL} = 180 mm, Olympus, UTLU, USA) and an achromat L_3 (f_{L_3} = 120 mm). The tube lens was placed 75 mm away fom the objective lens and the distance between the tube lens and L_3 was 222 mm. A Michelson interferometer was constructed 200 mm away from L_3 with a concave mirror (f_d = 300mm) on one arm and a plane mirror on the other arm. The plane mirror was mounted on a piezoelectric translational stage (ThorLabs, NFL5DP20) to implement the phase-shift required to acquire three images. The fluorescence was detected with an electron-multiplying charge-coupled (EMCCD) camera (Andor iXon-897 Life,UK) which was placed 150 mm away from the interferometer.

EMISSION PATHWAY FOR TWO-COLOR IMAGING USING A SPLITTER To facilitate simultaneous two-color single molecule imaging (see Fig. 5.8 (C)) with Alexa 647 (emission peak: 670 nm) and CF 568 (emission peak: 583 nm), we built an optical splitter that spectrally separated

the emission light using a dichroic mirror (D_2, Semrock, FF640-Di02-t3-25X36). The spectrally separated light is further filtered using the respective notch (ZET561NF notch filter for red detection and NF01-488/647 for far red detection) and emission filters (Semrock, FF01-605/15 for red detection and Semrock, FF01-680/42 for far red detection) to remove unwanted background light before being reflected off two mirrors placed on translational stages (ThorLabs, MT1) and imaged on the EMCCD (Andor iXon-897 Life,UK).

Figure 5.9: **Parameters used for SMLM reconstruction using ThunderSTORM.**

APPENDIX A

A.1 Derivation of CRLB for Self-Interference Digital Holography

Assuming that the emitter emits N photons and that the counting process is a Poisson process. We first consider the PSH given by

$$q(x, y) = A(1 + \cos[\alpha((x - M_T x_s)^2 + (y - M_T y_s)^2)])$$ (A.1)

where $\alpha = k/2z_r$, $k = 2\pi/\lambda$ and the normalization constant, A, is given by

$$A = \frac{1}{\pi \left(r_h^2 + \frac{2z_r}{k} \sin \frac{k}{2z_r} r_h^2 \right)}$$ (A.2)

where r_h is the radius of the hologram at the CCD plane. The derivative of q with respect to x_s is given by

$$\frac{\partial q(x, y)}{\partial x_s} = 2\alpha A M_T (x - M_T x_s) \sin[\alpha((x - M_T x_s)^2 + (y - M_T y_s)^2)]$$ (A.3)

Since the PSH is symmetric, the non-diagonal elements of the Fisher information matrix are zero and $F_{xx} = F_{yy}$. Thus we have

$$F_{xx} = F_{yy} = N \int_{\mathbb{R}^2} \frac{1}{q(x_s, y_s)} \frac{\partial q(x_s, y_s)}{\partial x_s} \frac{\partial q(x_s, y_s)}{\partial x_s} dx_s dy_s$$

$$= \int_{\mathbb{R}^2} \frac{4NA^2 M_T^2 \alpha^2 (x - M_T x_s)^2 \sin^2[\alpha((x - M_T x_s)^2 + (y - M_T y_s)^2)]}{A(1 + \cos[\alpha((x - M_T x_s)^2 + (y - M_T y_s)^2)])} dx_s dy_s$$

<div align="right">(A.4)</div>

$$= 4NAM_T^2 \alpha^2 \int_0^{2\pi} \cos^2 \phi \, d\phi \int_0^{r_h} \frac{\rho^3 \sin^2(\alpha \rho^2)}{1 + \cos(\alpha \rho^2)} d\rho$$

$$= 2NAM_T^2 \alpha^2 \pi \left(\frac{r_h^4}{2} + \frac{1}{\alpha^2}(1 - \cos \alpha r_h^2) - \frac{r_h^2}{\alpha} \sin \alpha r_h^2 \right)$$

where $x - M_T x_s = \rho \cos \phi$ and $y - M_T y_s = \rho \sin \phi$. We similarly calculate F_{zz}, however note that in these calculations we ignore the dependence of z_s on A and r_h. The derivative of $q(x, y)$ with respect to z_s is given by

$$\frac{\partial q(x, y)}{\partial z_s} = \frac{A\alpha}{z_r} \sin[\alpha(x - M_T x_s)^2 + (y - M_T y_s)^2] \frac{\partial z_r}{\partial z_s} \tag{A.5}$$

and

$$F_{zz} = \frac{N\pi k^2 A}{2z_r^4} \left(\frac{r_h^6}{3} - \frac{2r_h^2}{\alpha^2} \cos \alpha r_h^2 - \frac{\alpha^2 r_h^4 - 2}{\alpha^3} \sin \alpha r_h^2 \right) \left[\frac{\partial z_r}{\partial z_s} \right]^2 \tag{A.6}$$

Appendix B

B.1 storm_holographic.py

```python
import os, sys, time
sys.path.append('..\\simsxy')

import scipy.ndimage as nd
import Utility as U
import zernike as Z
import glob

import numpy as N
import numpy.random as rd
import numpy.fft as ft
import tifffile as tf
import scipy.ndimage as nd
from scipy.special import erf
from scipy import interpolate
import gausslib as G
from collections import defaultdict

orig_path = "Z:/pythonfiles/storm/STORMholographic_postdec"

import pylab

pi = N.pi
fft2 = N.fft.fft2
ifft2 = N.fft.ifft2
fftshift = N.fft.fftshift

class sim(object):

    def __init__(self):
```

```python
        self.nnp = 5                    # avg # of fluorophores per image
        self.iip =6000                  # avg # of photons per fluorophore
        self.avg_no = 32
        self.nx = 1024
        self.dx = 13.
        self.na = 1.42
        self.wl = 0.670
        self.nzarr = 15
        self.zarr = 0.0*rd.randn(15)
        self.zarr[4] = 0.0
        self.zarr[11] = 0.0
        self.f_doe = 300.e+3        #focal length of SLM
        self.f_obj = 3.e+3           #focal length of objective
        self.d1 = 3.e+3            #distance between objective and SLM
        self.z_h = 150.e+3          #distance between SLM and CCD
aperture
        #self.mask = N.zeros((self.nx,self.nx),dtype=N.float32)
        self.img = N.zeros((self.nx,self.nx),dtype=N.float32)
        self.z_r = 0.                    #reconstruction distance
        self.trans_mag = 0.        #transverse magnification
        self.Nangs = 3
        self.angles = N.array([0.0,2*pi/3,4*pi/3])
        self.mult = N.zeros((self.nx,self.nx),dtype=N.float32)
        self.r = 163.0


    def __del__(self):
        pass


    def getoneptcr(self):
        ''' one flurophore at the center'''
        dx = self.dx
        #nxh = int(self.nx/2)
        self.xcntr = 0.0
        self.ycntr = 0.0
        self.exth = int(1.0/dx) # half extent in pixels

    def getobj(self):
        ''' put fluorophores in circle '''
        dx = self.dx
        nxh = int(self.nx/2)
        Np = 1000
        rad = 0.5
        phi = N.linspace(0,2.0*pi,Np)
        self.xps = rad*N.cos(phi)
        self.yps = rad*N.sin(phi)
```

```python
77          self.exth = int(1.0/dx) # half extent in pixels
78
79      def getobj3d(self):
80          '''put fluorophores on a helix'''
81          dx = self.dx
82          Np = 1000
83          rad = 0.500
84          phi = N.linspace(0,4*pi,Np)
85          z = N.linspace(-5,5,Np)
86          self.xps = rad*N.cos(phi)
87          self.yps = rad*N.sin(phi)
88          self.zps = z + self.f_obj
89          self.exth = int(1.0/dx) # half extent in pixels
90
91      def getobj3d_line(self):
92          '''put fluorophores on a straight Line'''
93          dx = self.dx
94          Np = 5000
95          self.xcntr = 0.0
96          self.ycntr = 0.0
97          z = N.linspace(-10,10,Np)
98          self.zps = z + self.f_obj
99          self.exth = int(1.0/dx) # half extent in pixels
100
101     def getonept(self):
102         ''' one fluorophore '''
103         Np = 2
104         dx = self.dx
105         nxh = int(self.nx/2)
106         self.xps = N.array([nxh*dx,0.75*nxh*dx])
107         self.yps = N.array([nxh*dx,nxh*dx])
108         self.exth = int(1.0/dx) # half extent in pixels
109
110     def getaberr(self):
111         wl = self.wl
112         na = self.na
113         n2 = 1.512
114         dp = 1/(self.nx*self.dx)
115         radius = (na/wl)/dp
116         ## prepare for focus mode
117         x = N.arange(-self.nx/2,self.nx/2,1)
118         X,Y = N.meshgrid(x,x)
119         rho = N.sqrt(X**2 + Y**2)/radius
120         msk = (rho<=1.0).astype(N.float64)
121         self.defoc = msk*(2*pi)*(n2/wl)*N.sqrt(1-(na*msk*rho/n2)**2)
122         #######################
```

```
123          #msk = U.shift(U.discArray((self.nx,self.nx),radius))/(pi*
     radius**2)
124          msk = U.shift(U.discArray((self.nx,self.nx),radius))/N.sqrt(pi*
     radius**2)/self.nx
125          phi = N.zeros((self.nx,self.nx))
126          for m in range(1,self.nzarr):
127              phi = phi + self.zarr[m]*Z.Zm(m,radius,[0,0],self.nx)
128          self.wf = msk*N.exp(1j*phi).astype(N.complex64)
129
130      def addpsf(self,x,y,z,I):
131          # create phase
132          nx = self.nx
133          alpha = 2*pi/nx/self.dx
134          g = lambda m, n: N.exp(1j*alpha*(m*x+n*y)).astype(N.complex64)
135          defoc = N.exp(1j*z*self.defoc)
136          ph = N.fromfunction(g, (nx,nx), dtype=N.float32)
137          ph = U.shift(ph*defoc)
138          wfp = N.sqrt(I)*ph*self.wf
139          #wfp = wfp
140          self.img = self.img + abs(fft2(wfp))**2
141
142      def gethgrams(self):
143          focus = self.f_obj
144          self.img[:,:] = 0.0
145          #self.den[:,:] = 20.0
146          nxh = int(self.nx/2)
147          self.hstack =  N.zeros((3,self.nx,self.nx),dtype=N.float32)
148          angles = self.angles
149          # get points
150          self.Np = rd.poisson(self.nnp)
151          pti = rd.randint(0,5000,self.Np)
152          #self.xp = self.xps[pti]
153          #self.yp = self.yps[pti]
154          #self.zp = self.zps[pti]
155          self.zp = N.array([3000.0])
156          '''For flurophore in center'''
157          self.Np_sng = 1
158          self.xp = N.array([self.xcntr])
159          self.yp = N.array([self.ycntr])
160          self.Ip = 2000.
161          #self.getfzpimg(xp,yp,3.e+3,0.0,Ip)
162          #self.Ip = rd.poisson(self.iip,self.Np)
163          print self.xp
164          print self.yp
165          print self.zp #print focus/self.zp
166          print self.Ip
167          # create psfs
```

```python
168            for n in range(self.Nangs):
169                for m in range(self.Np_sng):
170                    '''usually in range(self.Np)'''
171                    self.hol_1angle = self.getfzpimg_nonoise(self.xp[m],
        self.yp[m],self.zp[m],angles[n],self.Ip)
172                #self.hstack[n,:,:] = rd.poisson(self.img.copy())
173                self.hstack[n,:,:] = self.hol_1angle
174                self.img[:,:] = 0.0
175            #done!
176
177     def gethgrams_oneangle(self):
178         focus = self.f_obj
179         self.img[:,:] = 0.0
180         #self.den[:,:] = 20.0
181         nxh = int(self.nx/2)
182         self.frame =  N.zeros((self.nx,self.nx),dtype=N.float32)
183         #angles = self.angles
184         '''get points'''
185         self.Np = rd.poisson(self.nnp)
186         pti = rd.randint(0,1000,self.Np)
187         self.xp = self.xps[pti]
188         self.yp = self.yps[pti]
189         self.zp = self.zps[pti]
190         #self.zp = focus
191         '''For flurophore in center'''
192         #self.Np_sng = 1
193         #self.xp = self.xcntr
194         #self.yp = self.ycntr
195         #self.Ip = 4000.
196         #self.getfzpimg(xp,yp,3.e+3,0.0,Ip)
197         self.Ip = rd.poisson(self.iip,self.Np)
198         print self.xp
199         print self.yp
200         print self.zp #print focus/self.zp
201         print self.Ip
202         # create psfs
203         for m in range(self.Np):
204             self.hol_1angle = self.getfzpimg_nonoise(self.xp[m],self.yp
        [m],self.zp[m],0.0,self.Ip[m])
205         #self.hstack[n,:,:] = rd.poisson(self.img.copy())
206         self.frame = rd.poisson(self.hol_1angle)
207         self.img[:,:] = 0.0
208         #done!
209
210
211
212     def getfzpimg(self,x,y,z,theta,Ip):
```

```
213     #create Fresnel Zone Plates for individual single emitters
214         self.indivdual = N.zeros((self.nx,self.nx),dtype=N.float32)
215         nx = self.nx
216         wl = self.wl
217         f_o = self.f_obj
218         f_d = self.f_doe
219         z_h = self.z_h
220         d1 = self.d1
221         dx = self.dx
222         nxh = int(nx/2)
223         if(abs(z)) == f_o:
224             self.z_r = (z_h-f_d)
225             self.trans_mag = z_h/f_d
226         else:
227             f_e = (z*f_o)/(f_o-z)
228             f_1 = (f_d*(f_e+d1))/(f_d-(f_e+d1));
229             self.z_r = -(((f_1+z_h)*(f_e+d1+z_h))/(f_1-f_e-d1))
230             self.trans_mag = (z_h*f_e)/(z*(f_e+d1));
231         #the intensity function
232         g = lambda m, n: N.exp((1j*pi/wl/self.z_r)*(((dx*(m-nxh)) -
    self.trans_mag*x)**2 + ((dx*(n-nxh)) - self.trans_mag*y)**2)+1j*
    theta).astype(N.complex64)
233         self.amp = N.fromfunction(g, (nx,nx), dtype=N.complex64)
234         self.individual = (2 + self.amp + N.conjugate(self.amp)).real
235         #self.mult = Ip/N.sum(self.individual)
236         #self.img += self.individual*self.mult
237         self.img += self.individual
238         return(self.img)
239         #td = '%d' % time.time()
240         #tf.imsave('fzp_single' + td[-5:] + '.tif',self.img.astype(N.
    float32))
241         #done!
242
243  def getfzpimg_nonoise(self,x,y,z,theta,Ip):
244         '''create Fresnel Zone Plates for individual single emitters'''
245         #self.img = 300*N.ones((self.nx,self.nx),dtype=N.float32)
246         #self.img = rd.poisson(self.img)
247         self.individual = N.zeros((self.nx,self.nx),dtype=N.float32)
248         nx = self.nx
249         wl = self.wl
250         f_o = self.f_obj
251         f_d = self.f_doe
252         z_h = self.z_h
253         d1 = self.d1
254         dx = self.dx
255         nxh = int(nx/2)
256         r = self.r
```

```
257            if(abs(z)) == f_o:
258                self.z_r = (z_h-f_d)
259                self.trans_mag = z_h/f_d
260            else:
261                f_e = (z*f_o)/(f_o-z)
262                f_1 = (f_d*(f_e+d1))/(f_d-(f_e+d1));
263                self.z_r = -(((f_1+z_h)*(f_e+d1+z_h))/(f_1-f_e-d1))
264                self.trans_mag = (z_h*f_e)/(z*(f_e+d1));
265            #the intensity function
266            g = lambda m, n: N.exp((1j*pi/wl/self.z_r)*(((dx*(m-nxh)) -
       self.trans_mag*x)**2 + ((dx*(n-nxh)) - self.trans_mag*y)**2)+1j*
       theta).astype(N.complex64)
267            self.amp = N.fromfunction(g, (nx,nx), dtype=N.complex64)
268            self.individual = N.abs(2+ self.amp + N.conjugate(self.amp))
269            #self.individual = 300*rd.poisson(self.individual)
270            x_coord, y_coord = (((self.trans_mag*x)/dx)+nxh), (((self.
       trans_mag*y)/dx)+nxh)
271            '''artificial BPP'''
272            a,b = N.ogrid[-x_coord:nx-x_coord, -y_coord:nx-y_coord]
273            self.mask = a*a + b*b <= r*r
274            self.individual = self.individual*self.mask
275            self.mult = Ip/N.sum(self.individual)
276            self.img += self.individual*self.mult
277            return self.img
278            #td = '%d' % time.time()
279            #tf.imsave('fzp_single' + td[-5:] + '.tif',self.img.astype(N.
       float32))
280            #done!
281
282     def getoneimg(self):
283            self.img[:,:] = 20.0
284            # get points
285            Np = rd.poisson(self.nnp)
286            pti = rd.randint(0,1000,Np)
287            #xp = self.xps[pti]
288            #yp = self.yps[pti]
289            xp = self.xcntr
290            yp = self.ycntr
291            zp = self.zps[pti]
292            #Ip = rd.poisson(self.iip,Np) #[self.iip]
293            Ip = rd.exponential(self.iip,Np)
294            # create psfs
295            for m in range(Np):
296                self.addpsf(xp,yp,zp[m],Ip[m])
297            # noise
298            self.img = rd.poisson(self.img)
299            # done!
```

```
300
301     def runseq(self,Ns):
302         ''' create sequence of raw storm data
303             the data is saved to storm1.tif and
304             can be analyzed with QuickPalm or RapidStorm '''
305         #os.mkdir('temp')
306         nxh = int(self.nx/2)
307         self.stack = N.zeros((3*Ns,512,512),dtype=N.float32)
308         self.stack_bg = N.zeros((3*Ns,512,512),dtype=N.float32)
309         self.stack_noisy = N.zeros((3*Ns,512,512),dtype=N.uint32)
310         #nxh = int(self.nx/2)
311         beg = nxh-int(nxh/2)
312         edd = nxh+int(nxh/2)
313         # get some stats
314         #rpk = N.zeros((Ns))
315         #rm = N.zeros((Ns))
316         for m in range(Ns):
317             #self.getoneimgdrift(m)
318             #self.getoneimgcoma()
319             self.gethgrams()
320             self.stack[3*m:3*m+3,:,:] = self.hstack[:,beg:edd,beg:edd]
321             #self.stack[m,:,:] = self.frame
322             #if self.img.max()>0:
323             #    rpk[m] = self.img.max()
324             #    rm[m] = self.getmetric()
325         # save file
326         self.stack_bg = self.stack + 0.000667
327         self.stack_noisy = rd.poisson(self.stack_bg)
328         td = '%d' % time.time()
329         tf.imsave('fzp_' + td[-5:] + '.tif',self.stack_noisy.astype(N.
    uint32),photometric = 'minisblack')
330         # plot stats
331         #pylab.figure(1)
332         #pylab.plot(rpk,'b-o')
333         #pylab.hist(rpk)
334         #pylab.figure(2)
335         #pylab.plot(rm,'b-o')
336         #pylab.hist(rm)
337         #print rpk.mean()/rpk.std()
338         #print rm.mean()/rm.std()
339         return td
```

B.2 finch_recon.py

```
1  import os, sys, time
```

```python
sys.path.append('..\\simsxy')

import scipy.ndimage as nd
import Utility as U
import zernike as Z
import glob

import numpy as N
import numpy.random as rd
import numpy.fft as ft
import tifffile as tf
import scipy.ndimage as nd
from scipy.special import erf
from scipy import interpolate
import gausslib as G
from collections import defaultdict

orig_path = "F:\FINCH\Code\Python"

import pylab

pi = N.pi
fft2 = N.fft.fft2
ifft2 = N.fft.ifft2
fftshift = N.fft.fftshift

class finch(object):


    def __init__(self,img_stack=None):
        self.nz, self.ny, self.nx = img_stack.shape
        self.img = img_stack
        self.dx = 13.0
        self.dx_mag = 0.120
        #self.nx_recon,self.ny_recon = 64
        self.N = N.linspace(-3.840,3.720,64)
        self.xx,self.yy = N.meshgrid(self.N,self.N)
        self.wl = 0.670
        self.recon_z = -150.e+3
        self.angles = N.array([0.0,2*pi/3,4*pi/3])
        self.f_doe = 300.e+3        #focal length of SLM
        self.f_obj = 3.e+3        #focal length of objective
        #Wself.f2 = 400.e+3
        self.d1 = 3.e+3        #distance between objective and SLM
        self.z_h = 150.e+3         #distance between SLM and CCD aperture
        #self.Np = 20
        self.z_r = 0.
```

```python
        self.z_rel_gen = N.linspace(-10.,10.,51)
        self.z_abs_gen = self.z_rel_gen + self.f_obj


    def __del__(self):
        pass

    def finch_recon(self,recon_dist):
        realsz = int(self.nz/3)
        wl = self.wl
        nx = self.nx
        'changes for BFLY camera'
        ny = self.ny
        nxh = int(nx/2)
        nyh = int(ny/2)
        dx = self.dx
        beg_y = nyh-int(nyh/12)
        edd_y = nyh+int(nyh/12)
        beg_x = nxh-int(nxh/12)
        edd_x = nxh+int(nxh/12)
        self.intensity_stack = N.zeros((realsz,ny,nx),dtype=N.complex64
    )
        self.strm_stack = N.zeros((realsz,ny,nx),dtype=N.float64)
        angles = self.angles
        img = self.img.astype(N.float64)
        for m in range(realsz):
            #self.final_intensity = img[m]
            self.final_intensity = (img[3*m]*(N.exp(1j*angles[2])-N.exp
    (1j*angles[1])) +
                                    img[3*m+1]*(N.exp(1j*angles[0])-N.exp(1j
    *angles[2])) +
                                    img[3*m+2]*(N.exp(1j*angles[1])-N.exp(1j
    *angles[0])))
            self.intensity_stack[m,:,:] = self.final_intensity
            g = lambda m, n: fftshift(ifft2(fft2(fftshift(self.
    final_intensity))*fft2(fftshift(N.exp((1j*pi/wl/recon_dist)*((dx*(m-
    nyh))**2+(dx*(n-nxh))**2))))))).astype(N.complex128)
            self.recond = N.fromfunction(g, (ny,nx), dtype=N.complex64)
            'Entire FOV'
            self.strm_stack[m,:,:] = abs(self.recond)
            #self.strm_stack[m,:,:] = (abs(self.recond)-abs(self.recond
    ).min())*(2**16-1)/(abs(self.recond).max()-abs(self.recond).min())
            #self.strm_stack[m,:,:] = abs(self.recond[beg_y:edd_y,beg_x
    :edd_x])
        #td = '%d' % time.time()
        #tf.imsave('storm_' + td[-7:] + '.tif',self.strm_stack.astype(N
    .float32), photometric = 'minisblack')
```

```
87              #done!

88

89          def recon_dist_calc(self,zpos_abs,Np):
90              self.zr_stack = N.zeros((Np,1),dtype=N.float32)
91              self.mag = N.zeros((Np,1),dtype=N.float32)
92              f_o = self.f_obj
93              f_d = self.f_doe
94              z_h = self.z_h
95              d1 = self.d1
96              self.z_abs = zpos_abs
97              for m in range(Np):
98                  if(abs(self.z_abs[m])) == f_o:
99                      self.z_r = (z_h-f_d)
100                     self.trans_mag = z_h/f_d
101                 else:
102                     f_e = (self.z_abs[m]*f_o)/(f_o-self.z_abs[m])
103                     f_1 = (f_d*(f_e+d1))/(f_d-(f_e+d1));
104                     self.z_r = -(((f_1+z_h)*(f_e+d1+z_h))/(f_1-f_e-d1))
105                     self.trans_mag = (z_h*f_e)/(self.z_abs[m]*(f_e+d1))
106                 self.zr_stack[m,:] = self.z_r
107                 self.mag[m,:] = self.trans_mag
108             return(self.zr_stack)
109             #done!

110

111         def recon_dist_calc2(self,zpos_abs,Np):
112             self.zr_stack = N.zeros((Np,1),dtype=N.float32)
113             f_o = self.f_obj
114             f_d = self.f_doe
115             z_h = self.z_h
116             f_tl = 180.e+3
117             d1 = 183.e+3
118             f_4 = 120.e+3
119             d2 = 300.e+3
120             d3 = 240.e+3
121             #f2 = self.f2/1.e+3
122             self.z_abs = zpos_abs
123             for m in range(Np):
124                 if(abs(self.z_abs[m])) == f_o:
125                     self.z_r = -(z_h-f_d)
126                     #self.trans_mag = z_h/f_o
127                 else:
128                     f_e = (self.z_abs[m]*f_o)/(f_o-self.z_abs[m])
129                     f_g = (f_tl*(f_e+d1))/(f_tl-(f_e+d1))
130                     f_h = (f_4*(f_g+d2))/(f_4-(f_g+d2))
131                     f_k = (f_d*(f_h+d3))/(f_d-(f_h+d3))
132                     self.z_r = ((f_k+z_h)*(z_h+d3+f_h))/(f_k-f_h-d3)
133                     #self.trans_mag = (z_h*f_e)/(self.z_abs[m]*(f_e+d1))
```

```
134            self.zr_stack[m,:] = self.z_r
135        return(self.zr_stack)
136        #done!
137
138    def finch_recon3D(self,recon_dist,img,Np):
139        self.imsz = img.shape
140        self.zpos = recon_dist
141        realsz = int(self.nz/3)
142        wl = self.wl
143        nx = self.nx
144        ny = self.ny
145        #sz = 128 # kernel size
146        #szh = 64
147        nyh = int(ny/2)
148        nxh = int(nx/2)
149        dx = self.dx
150        beg = nxh-int(nxh/16)
151        edd = nxh+int(nxh/16)
152        #Np = self.Np
153        #z = self.z
154        self.intensity_stack = N.zeros((Np,ny,nx),dtype=N.complex64)
155        self.strm_stack = N.zeros((Np,32,32),dtype=N.float32)
156        angles = self.angles
157        #img = self.img
158        for l in  range(realsz):
159            for m in range(Np):
160                #self.final_intensity = img[l]
161                self.final_intensity = (img[3*l]*(N.exp(1j*angles[2])-N
    .exp(1j*angles[1])) +
162                                        img[3*l+1]*(N.exp(1j*angles[0])-N.exp(1j
    *angles[2])) +
163                                        img[3*l+2]*(N.exp(1j*angles[1])-N.exp(1j
    *angles[0])))
164                self.intensity_stack[m,:,:] = self.final_intensity
165                self.z_test = self.zpos[m]
166                g = lambda m, n: ft.fftshift(ft.ifft2(ft.fft2(ft.
    fftshift(self.final_intensity))*ft.fft2(ft.fftshift(N.exp((1j*pi/wl/
    self.z_test)*((dx*(m-nxh))**2+(dx*(n-nyh))**2)))))).astype(N.
    complex64)
167                self.recond = N.fromfunction(g, (ny,nx), dtype=N.
    complex64)
168                #self.strm_stack[m,:,:] = (abs(self.recond)-abs(self.
    recond).min())*(2**16-1)/(abs(self.recond).max()-abs(self.recond).
    min())
169                self.strm_stack[m,:,:] = abs(self.recond)[beg:edd,beg:
    edd]
170            td = '%d' % time.time()
```

```python
            tf.imsave('storm_' + td[-5:] + '.tif',self.strm_stack.
    astype(N.float32))
            self.strm_stack[:,:,:] = 0.0
        #done!


    def finch_recon3D_oneangle(self,recon_dist,img,Np):
        self.imsz = img.shape
        self.zpos = recon_dist
        realsz = self.nz
        wl = self.wl
        nx = self.nx
        ny = self.ny
        #sz = self.nz # kernel size
        #szh = int(sz/2.0)
        nyh = int(ny/2)
        nxh = int(nx/2)
        dx = self.dx
        beg = nxh-int(nxh/16)
        edd = nxh+int(nxh/16)
        #Np = self.Np
        #z = self.z
        self.intensity_stack = N.zeros((Np,nx/16,nx/16),dtype=N.
    complex64)
        self.strm_stack = N.zeros((Np,nx/32,nx/32),dtype=N.float32)
        angles = self.angles
        #img = self.img
        for l in  range(realsz):
            for m in range(Np):
                self.final_intensity = img[l]
                #self.final_intensity = (img[3*l]*(N.exp(1j*angles[2])-
    N.exp(1j*angles[1])) +
                #                    img[3*l+1]*(N.exp(1j*angles[0])-N.exp(1j
    *angles[2])) +
                #                     img[3*l+2]*(N.exp(1j*angles[1])-N.exp(1
    j*angles[0])))
                #self.intensity_stack[m,:,:] = self.final_intensity
                self.z_test = self.zpos[m]
                g = lambda m, n: ft.fftshift(ft.ifft2(ft.fft2(ft.
    fftshift(self.final_intensity))*ft.fft2(ft.fftshift(N.exp((1j*pi/wl/
    self.z_test)*((dx*(m-nxh))**2+(dx*(n-nxh))**2)))))).astype(N.
    complex64)
                self.recond = N.fromfunction(g, (ny,nx), dtype=N.
    complex64)
                #self.strm_stack[m,:,:] = (abs(self.recond)-abs(self.
    recond).min())*(2**16-1)/(abs(self.recond).max()-abs(self.recond).
    min())
```

```
207            self.strm_stack[m,:,:] = abs(self.recond[beg:edd,beg:
     edd])
208         td = '%d' % time.time()
209         tf.imsave('storm_' + td[-5:] + '.tif',self.strm_stack.
     astype(N.float32))
210         self.strm_stack[:,:,:] = 0.0
211      #done!
212
213
214  def finch_recon3D_finer(self,recon_dist,img,Np):
215      '''reconstructing the holograms to finer slices'''
216      self.imsz = img.shape
217      self.zpos = recon_dist
218      realsz = int(self.imsz[0]/3)
219      wl = self.wl
220      nx = self.nx
221      ny = self.ny
222      nxh = int(nx/2)
223      dx = self.dx
224      beg = nxh-int(nxh/2)
225      edd = nxh+int(nxh/2)
226      #Np = self.Np
227      #z = self.z
228      self.intensity_stack = N.zeros((Np,nx,nx),dtype=N.complex64)
229      self.strm_stack = N.zeros((Np,nx,nx),dtype=N.float32)
230      angles = self.angles
231      #img = self.img
232      for l in  range(realsz):
233          for m in range(Np):
234              #self.final_intensity = img
235              self.final_intensity = (img[3*l]*(N.exp(1j*angles[2])-N
     .exp(1j*angles[1])) +
236                              img[3*l+1]*(N.exp(1j*angles[0])
     -N.exp(1j*angles[2])) +
237                              img[3*l+2]*(N.exp(1j*angles[1])
     -N.exp(1j*angles[0])))
238              self.intensity_stack[m,:,:] = self.final_intensity
239              self.z_test = self.zpos[m]
240              g = lambda m, n: ft.fftshift(ft.ifft2(ft.fft2(ft.
     fftshift(self.final_intensity))*ft.fft2(ft.fftshift(N.exp((1j*pi/wl/
     self.z_test)*((dx*(m-nxh))**2+(dx*(n-nxh))**2)))))).astype(N.
     complex64)
241              self.recond = N.fromfunction(g, (nx,nx), dtype=N.
     complex64)
242              #self.strm_stack[m,:,:] = abs(self.recond[beg:edd,beg:
     edd])
243              self.strm_stack[m,:,:] = abs(self.recond)
```

```
244        i,j,k = N.unravel_index(self.strm_stack.argmax(),self.
       strm_stack.shape)
245        self.strm_stack = self.strm_stack[:,j-16:j+16,k-16:k+16]
246        return(self.strm_stack)
247         #done!!!
248
249    def wavelet(self,path):
250        '''Wavelet filtering with kernel using B-Spline Basis
251        function of the 3rd order with a scaling factor of 2'''
252        self.k1 = N.array([0.0625,0.250,0.375,0.250,0.0625],dtype=N.
       float32)
253        self.k2 = N.array([0.0625,0.0,0.250,0,0.375,0,0.250,0,0.0625],
       dtype=N.float32)
254        #path_in = "Z:\\pythonfiles\\storm\\STORMholographic_postdec\\3
       D\\Helix\\5000photons_noise_1angle\\Reconstructions"
255        path_in = path
256        os.chdir(path_in)
257        for filename in glob.glob('*.tif'):
258            self.img = tf.imread(filename)
259            self.img = self.img +20.0
260            self.V0 = self.img
261            self.nz,self.ny,self.nx = self.img.shape
262            self.fltrd_img = N.zeros((self.nz,self.ny,self.nx),dtype=N.
       float32)
263            '''kernels'''
264            for m in range(self.nz):
265                '''first wavelet level'''
266                self.V1_inner = nd.filters.convolve1d(self.V0[m],self.
       k1,axis=1,mode='reflect')
267                self.V1 = nd.filters.convolve1d(self.V1_inner,self.k1,
       axis=0,mode='reflect')
268                '''second wavelet level'''
269                self.V2_inner = nd.filters.convolve1d(self.V1,self.k2,
       axis=1,mode='reflect')
270                self.V2 = nd.filters.convolve1d(self.V2_inner,self.k2,
       axis=0,mode='reflect')
271                '''Watershed'''
272                self.W = self.V1 - self.V2
273                self.fltrd_img[m,:,:] = self.W
274            outname = 'Filtered_' + filename[6:11] + '.tif'
275            print(outname)
276            tf.imsave(outname, self.fltrd_img.astype(N.float32),
       photometric = 'minisblack')
277        os.chdir(orig_path)
278
279
280    def crop_sm(self,path):
```

```python
        '''Crop smaller region aroung single molecule'''
        path_in = path
        os.chdir(path_in)
        self.crpd_imgs = N.zeros((80,32,32),dtype=N.float32)
        for frame,filename in enumerate(glob.glob('*.tif')):
            self.img_init = tf.imread(filename)
            i,j,k = N.unravel_index(self.img_init.argmax(),self.
    img_init.shape)
            self.img_crpd = self.img_init[:,j-16:j+16,k-16:k+16]
            tf.imsave(filename[6:11] + '_crpd_recon.tif', self.img_crpd
    .astype(N.float32),photometric = 'minisblack')
            print(frame)
        os.chdir(orig_path)

    def max_pos(self,path,coords):
        path_in = path
        os.chdir(path_in)
        self.max_stack_fltrd = N.zeros((100,32,32),dtype=N.float32)
        for frame,filename in enumerate(glob.glob('*.tif')):
            self.img3D_fltrd_crpd = tf.imread(filename)
            self.max_stack_fltrd[frame,:,:] = self.img3D_fltrd_crpd[
    coords[frame,1],:,:]
        tf.imsave('3D_fltrd_max_stack'+'.tif',self.max_stack_fltrd.
    astype(N.float32),photometric='minisblack')
        os.chdir(orig_path)



    def approx_pos(self,thrsh,path):
        '''Finding approximate positions of molecules using local
    intensity maximum
        and 26-connected neighborhood'''
        path_in = path
        os.chdir(path_in)
        self.coords = [[0,0,0,0]]
        self.coords_a = [[0,0,0,0]]
        self.coords_b = [[0,0,0,0]]
        for frame,filename in enumerate(glob.glob('*.tif')):
            print(frame)
            self.fltrd = tf.imread(filename)
            for l in range(1,self.fltrd.shape[0]-1):
                for m in range(1,self.fltrd.shape[1]-1):
                    for n in range(1,self.fltrd.shape[2]-1):
                        cube = self.fltrd[l-1:l+2,m-1:m+2,n-1:n+2]
                        i,j,k = N.unravel_index(cube.argmax(),cube.
    shape)
```

```python
                              if (self.fltrd[l,m,n] >= thrsh) & ([i,j,k] ==
    [1,1,1]):
                                  self.coords = N.append(self.coords,[[frame,
    l,m,n]],axis=0)
        self.coords = self.coords[1:,:]
        self.fin_coords_approx = self.frame_del(self.coords,self.coords
    [:,0])
        os.chdir(orig_path)

    def approx_pos_2D(self,thrsh,img):
        '''Finding approximate positions of molecules using local
    intensity maximum
        and 8-connected neighborhood'''
        #path_in = "C:\\Users\\Abhijit Marar\\Desktop\\Code\\
    STORMholographic_postdec\\3D\\Helix\\Filtered"
        #path_in = "C:\\Users\\abhij\\Desktop\\Code\\Code\\
    STORMholographic_postdec\\3D\\Helix\\Filtered"
        #path_in = "Z:/pythonfiles/storm/STORMholographic_postdec/500ph
    /450 holograms/Filtered"
        #os.chdir(path_in)
        self.coords = [[0,0,0]]
        self.coords_a = [[0,0,0,0]]
        self.coords_b = [[0,0,0,0]]
        for frame in range(img.shape[0]):
            for m in range(1,img.shape[1]-1):
                for n in range(1,img.shape[2]-1):
                    self.square = img[frame][m-1:m+2,n-1:n+2]
                    i,j = N.unravel_index(self.square.argmax(),self.
    square.shape)
                    if (img[frame][m,n] >= thrsh) & ([i,j] == [1,1]):
                        self.coords = N.append(self.coords,[[frame,m,n
    ]],axis=0)
        self.coords = self.coords[1:,:]
        #self.fin_coords_approx = self.frame_del(self.coords,self.
    coords[:,0])
        #os.chdir(orig_path)

    def list_duplicates(self,seq):
        tally = defaultdict(list)
        for i,item in enumerate(seq):
            tally[item].append(i)
        return ((key,locs) for key,locs in tally.items()
                            if len(locs)>1)

    def frame_del(self,coords,frame_list):
        '''find fluorophores too close to each other in z and delete
    them'''
```

```python
        self.coords_bad = [[0,0,0,0]]
        self.indices = [0]
        for dup in sorted(self.list_duplicates(frame_list)):
            self.test = dup[0]
            self.dup_indices = dup[1]
            self.dup_coords = coords[self.dup_indices]
            if ((N.abs(N.diff(self.dup_coords[:,1]))).min() <= 4):
                #or (N.abs(N.diff(self.dup_coords[:,3]))).min() <= 4
                self.coords_bad = N.append(self.coords_bad,self.
    dup_coords,axis=0)
                self.indices = N.append(self.indices,self.dup_indices,
    axis=0)
                continue
        self.coords_bad = self.coords_bad[1:,:]
        self.indices = self.indices[1:]
        self.reduced_coords_list = N.delete(coords,self.indices,axis=0)
        return(self.reduced_coords_list)

    def finer_z(self,coord,slices):
        '''creates finer slice distances'''
        #Change linspace to arange to ensure constant distances between
     slices
        self.zfine_stack = N.zeros((slices,1),dtype=N.float32)
        f_o = self.f_obj
        '''Reconstruction distance corresponding to given above frames
    '''
        self.zpt = self.z_rel_gen[coord]
        if (coord == 1 or coord == 49):
            nslices = 2*slices
            self.zpt_above = self.z_rel_gen[coord-1]
            self.zpt_below = self.z_rel_gen[coord+1]
            self.finer_zstack = N.linspace(self.zpt_above,self.
    zpt_below,nslices)
            self.z_abs_finer = self.finer_zstack + f_o
            self.zfine_stack = self.recon_dist_calc(self.z_abs_finer,
    nslices)
        else:
            nslices = 2*slices
            self.zpt_above = self.z_rel_gen[coord-2]
            self.zpt_below = self.z_rel_gen[coord+2]
            self.finer_zstack = N.linspace(self.zpt_above,self.
    zpt_below,nslices)
            self.z_abs_finer = self.finer_zstack + f_o
            self.zfine_stack = self.recon_dist_calc(self.z_abs_finer,
    nslices)
        return(self.zfine_stack, self.finer_zstack, nslices)
```

```python
396     def sub_region(self,sz,img,xcoord,ycoord):
397         ''' cut out subregions from original image'''
398         self.img_finer = img
399         self.xpos = xcoord
400         self.ypos = ycoord
401         '''frame of interest'''
402         self.ROI_finer = self.img_finer[:,self.xpos-int(N.floor(sz/2)):
    self.xpos+int(N.floor(sz/2)+1),self.ypos-int(N.floor(sz/2)):self.
    ypos+int(N.floor(sz/2)+1)]
403         self.xx_roi = self.xx[:,self.xpos-int(N.floor(sz/2)):self.xpos+
    int(N.floor(sz/2)+1)]
404         self.yy_roi = self.yy[self.ypos-int(N.floor(sz/2)):self.ypos+
    int(N.floor(sz/2)+1),:]
405         return(self.ROI_finer,self.xx_roi,self.yy_roi)
406
407     def finer_stack(self,slices):
408         '''creates stack based on the above finer slices'''
409         coords = self.coords
410         for i in range(len(coords)):
411             self.frame = coords[i,0]
412             self.z_approx = coords[i,1]
413             self.img_set = self.img[3*self.frame:3*self.frame+3]
414             self.dist = self.finer_z(self.z_approx,slices)
415             self.finer_img_stck = self.finch_recon3D_finer(self.dist,
    self.img_set,slices)
416             td = '%d' % time.time()
417             tf.imsave('finer_' + td[-5:] + '.tif',self.finer_img_stck.
    astype(N.float32))
418     #done!
419
420     def loc_coords(self,sz,slices,Sigma,iterations):
421         '''Main function to call after approx positions have been found
    '''
422         coords = self.fin_coords_approx
423         self.final_res = [[0,0,0,0,0,0,0]]
424         #self.CRLB_final = [[0,0,0,0,0,0,0]]
425         for i in range(len(coords)):
426             print i
427             self.mid_res = [[0,0,0,0,0]]
428             self.frame = coords[i,0]
429             self.z_approx = coords[i,1]
430             self.img_set = self.img[3*self.frame:3*self.frame+3]
431             self.dist = self.finer_z(self.z_approx,slices)
432             self.finer_img_stck = self.finch_recon3D_finer(self.dist
    [0],self.img_set,self.dist[2])
433             td = '%d' % time.time()
```

```
434            tf.imsave('finer_' + td[-5:] + '.tif',self.finer_img_stck.
       astype(N.float32))
435            '''Cut out ROI's for each finer stack'''
436            self.x_approx = coords[i,2]
437            self.y_approx = coords[i,3]
438            self.finer_subrgn = self.sub_region(sz,self.finer_img_stck,
       self.x_approx,self.y_approx)
439            self.real_spacex = self.finer_subrgn[1]
440            self.real_spacey = self.finer_subrgn[2]
441            tf.imsave('roits_' + str(i) + '.tif',self.finer_subrgn[0].
       astype(N.float32))
442            '''Localize each frame in the ROI'''
443            for num in range(len(self.finer_subrgn[0])):
444                self.loc_single = self.MLEfit_sigma(self.finer_subrgn
       [0][num,:,:],Sigma,sz,iterations)
445                self.mid_res = N.append(self.mid_res,self.loc_single,
       axis = 0)
446            self.mid_res = self.mid_res[1:,:]
447            self.max_intensity_pixel = N.array(N.where(self.
       finer_subrgn[0] == self.finer_subrgn[0].max()))
448            self.z_intensity_line_profile = self.finer_subrgn[0][:,self
       .max_intensity_pixel[1],self.max_intensity_pixel[2]]
449            self.z_intensity_line_profile = N.reshape(self.
       z_intensity_line_profile,[len(self.z_intensity_line_profile)])
450            #self.z_fit_res = self.z_fit(self.dist[1],self.mid_res
       [:,2])
451            self.z_fit_res = self.z_fit(self.dist[1],self.
       z_intensity_line_profile)
452            self.z_loc_um = self.z_fit_res[0]
453            #self.sgm = self.z_fit_res[1]
454            self.I = self.z_fit_res[1]
455            self.intrpltd_res = self.x_y_pos(self.dist[1],self.mid_res
       [:,0],
456                                              self.mid_res[:,1],
       self.mid_res[:,4],
457                                              self.mid_res[:,3],
       self.z_loc_um)
458            self.x_loc_roi = self.intrpltd_res[0]
459            self.y_loc_roi = self.intrpltd_res[1]
460            #self.final_coords_roi = N.append(self.final_coords_roi,[[
       self.x_loc_roi,self.y_loc_roi]],axis =0)
461            #self.x_loc = (self.real_spacex[0,0]+(self.dx_mag*self.
       intrpltd_res[0]))*1.e+3
462            #self.y_loc = (self.real_spacey[0,0]+(self.dx_mag*self.
       intrpltd_res[1]))*1.e+3
463            self.z_loc_nm = 1.e+3*(self.z_fit_res[0])
464            self.I_loc = self.intrpltd_res[2]
```

```python
            self.bg_loc = self.intrpltd_res[3]
            '''***************I_loc is sigma************************
'''
            self.final_res = N.append(self.final_res,[[self.frame,self.
    x_loc_roi,self.y_loc_roi,self.z_loc_nm[0],self.I_loc[0],self.I[0],
    self.bg_loc[0]]],axis=0)
        self.final_res = self.final_res[1:,:]
        #self.final_coords_roi = self.final_coords_roi[1:,:]


    def loc_coords2(self,sz,slices,Sigma,iterations):
        '''find fluorophore position by gaussian fitting'''
        coords = self.fin_coords_approx
        self.final_res = [[0,0,0,0,0,0,0]]
        for i in range(len(coords)):
            print i
            self.mid_res = [[0,0,0,0,0]]
            self.frame = coords[i,0]
            self.z_approx = coords[i,1]
            self.img_set = self.img[3*self.frame:3*self.frame+3]
            self.dist = self.finer_z(self.z_approx,slices)
            self.finer_img_stck = self.finch_recon3D_finer(self.dist
    [0],self.img_set,self.dist[2])
            td = '%d' % time.time()
            tf.imsave('finer_' + td[-5:] + '.tif',self.finer_img_stck.
    astype(N.float32))
            '''Cut out ROI's for each finer stack'''
            self.x_approx = coords[i,2]
            self.y_approx = coords[i,3]


    def x_y_pos(self,z_array,x_array,y_array,I_array,bg_array,zpos):
        ''' interpolate x,y,I and bg to find result corresponding to
    z_loc'''
        '''z_array: dist[1],x_array = inter_res[:,0],y_array =
    inter_res[:,1]'''
        '''zpos = z_loc, I_array = inter_res[:,2], bg_array = inter_res
    [:3]'''
        self.min_dist = N.abs(z_array[0]-z_array[1])
        self.idx = N.where(N.abs(z_array-zpos) < self.min_dist)
        if (self.idx[0].size == 0):
            return(N.array([0]),N.array([0]),N.array([0]),N.array([0]))
        self.idx_l = self.idx[0][0]
        if (self.idx_l == 0 or self.idx_l == 39):
            self.x_loc_interp = N.array([x_array[self.idx_l]])
            self.y_loc_interp = N.array([y_array[self.idx_l]])
            self.I_loc_interp = N.array([I_array[self.idx_l]])
            self.bg_loc_interp = N.array([bg_array[self.idx_l]])
```

```
        else:
            self.idx_r = self.idx[0][1]
            self.x_loc_l = x_array[self.idx_l]
            self.x_loc_r = x_array[self.idx_r]
            self.y_loc_l = y_array[self.idx_l]
            self.y_loc_r = y_array[self.idx_r]
            self.I_loc_l = I_array[self.idx_l]
            self.I_loc_r = I_array[self.idx_r]
            self.bg_loc_l = bg_array[self.idx_l]
            self.bg_loc_r = bg_array[self.idx_r]
            self.abscissa =  N.array([z_array[self.idx_l],z_array[self.
    idx_r]])
            self.ord_x = N.array([self.x_loc_l,self.x_loc_r])
            self.ord_y = N.array([self.y_loc_l,self.y_loc_r])
            self.ord_I = N.array([self.I_loc_l,self.I_loc_r])
            self.ord_bg = N.array([self.bg_loc_l,self.bg_loc_r])
            f_x = interpolate.interp1d(self.abscissa,self.ord_x)
            f_y = interpolate.interp1d(self.abscissa,self.ord_y)
            f_I = interpolate.interp1d(self.abscissa,self.ord_I)
            f_bg = interpolate.interp1d(self.abscissa,self.ord_bg)
            self.x_loc_interp = f_x(zpos)
            self.y_loc_interp = f_y(zpos)
            self.I_loc_interp = f_I(zpos)
            self.bg_loc_interp = f_bg(zpos)
        return(self.x_loc_interp,self.y_loc_interp,self.I_loc_interp,
    self.bg_loc_interp)


    def z_fit(self,x,y):
        '''Performs polynomial fit of distance vs sigma/intensity and
    finds minimum'''
        print(x)
        print(y)
        self.coeff = N.polyfit(x,y,2)
        self.pol = N.poly1d(self.coeff)
        self.crit = self.pol.deriv().r
        self.r_crit = self.crit[self.crit.imag==0].real
        #self.bst_sgm = self.pol(self.r_crit)
        self.bst_I = self.pol(self.r_crit)
        #return(self.r_crit,self.bst_sgm)
        return(self.r_crit,self.bst_I)

    def sub_region_2D(self,sz,img,xcoord,ycoord):
        ''' cut out subregions from original image'''
        self.img = img
        self.xpos = xcoord
```

```
548        self.ypos = ycoord
549        '''frame of interest'''
550        self.ROI_finer = self.img[self.xpos-int(N.floor(sz/2)):self.
     xpos+int(N.floor(sz/2))+1,self.ypos-int(N.floor(sz/2)):self.ypos+int
     (N.floor(sz/2)+1)]
551        self.xx_roi = self.xx[:,self.xpos-int(N.floor(sz/2)):self.xpos+
     int(N.floor(sz/2))+1]
552        self.yy_roi = self.yy[self.ypos-int(N.floor(sz/2)):self.ypos+
     int(N.floor(sz/2))+1,:]
553        return(self.ROI_finer,self.xx_roi,self.yy_roi)
554
555    def loc_coords_2D(self,img,sz,Sigma,iterations):
556        '''Main function to call after approx positions have been found
     '''
557        coords = self.coords
558        '''deleting first column for 2D lolcalization after 3D approx
     pos'''
559        coords = N.delete(coords,1,1)
560        image = img
561        self.final_res = [[0,0,0,0,0,0]]
562        for i in range(len(coords)):
563            print i
564            #self.mid_res = [[0,0,0,0,0]]
565            self.frame = coords[i,0]
566            self.x_approx = coords[i,1]
567            self.y_approx = coords[i,2]
568            self.roi = self.sub_region_2D(sz,image[self.frame],self.
     x_approx,self.y_approx)
569            self.real_spacex = self.roi[1]
570            self.real_spacey = self.roi[2]
571            '''Localize each frame in the ROI'''
572            self.loc_single = self.MLEfit_sigma(self.roi[0],Sigma,sz,
     iterations)
573            self.x_loc = self.loc_single[0,0]
574            self.y_loc = self.loc_single[0,1]
575            #self.x_loc = (self.real_spacex[0,0]+(self.dx_mag*self.
     loc_single[0,0]))*1.e+3
576            #self.y_loc = (self.real_spacey[0,0]+(self.dx_mag*self.
     loc_single[0,1]))*1.e+3
577            self.final_res = N.append(self.final_res,[[self.frame,self.
     x_loc,self.y_loc,self.loc_single[0,2],self.loc_single[0,3],self.
     loc_single[0,4]]],axis = 0)
578        self.final_res = self.final_res[1:,:]
579
580    def MLEfit_sigma(self,data,PSFsigma,sz,iterations):
581        params = 5
582        self.M = N.zeros((params,params),dtype=N.float)
```

```
583        self.Minv = N.zeros((params,params),dtype=N.float)
584        self.CRLB = N.zeros((params,1),dtype=N.float)
585        self.dudt = N.zeros((params,1),dtype=N.float)
586        self.d2udt2 = N.zeros((params,1),dtype=N.float)
587        self.theta = N.zeros((params,1),dtype=N.float)
588        self.maxjump = N.array([1.0, 1.0, 100.0, 2.0, 0.5])
589        self.gamma = N.array([1.0,1.0,0.5,1.0,1.0])
590        ''' Calculating Center of Mass'''
591        self.init_coords = nd.measurements.center_of_mass(data)
592        #self.init_coords = G.com_2d(data,sz)
593        ''' Initializing fitting parameters, theta = {x,y,I,bg,sigma}
    '''
594        self.theta[0] = self.init_coords[0]
595        self.theta[1] = self.init_coords[1]
596        #self.theta[3] = N.minimum(10.0e+10,N.min(data))
597        self.int_bg = G.GaussFMaxMin2D(sz,PSFsigma,data)
598        self.theta[3] = self.int_bg[1]
599        self.theta[2] = N.maximum(0.0, (self.int_bg[0]-self.theta[3])
    *2*N.pi*pow(PSFsigma,2))
600        #self.theta[3] = 10.
601        #self.theta[2] = 500.
602        self.theta[4] = PSFsigma
603        '''main iterative loop'''
604        for itr in range(iterations):
605            self.num = N.zeros((params,1),dtype=N.float)
606            self.den = N.zeros((params,1),dtype=N.float)
607            for i in range(sz):
608                for j in range(sz):
609                    self.PSFx = G.IntGauss1D(i,self.theta[0],self.theta
    [4])
610                    self.PSFy = G.IntGauss1D(j,self.theta[1],self.theta
    [4])
611                    self.model = self.theta[3]+self.theta[2]*self.PSFx*
    self.PSFy
612                    '''Calculating the Derivatives'''
613                    self.x_derivative = G.DerivativeIntGauss1D(i,self.
    theta[0],PSFsigma,self.theta[2],self.PSFy)
614                    self.dudt[0] = self.x_derivative[0]
615                    self.d2udt2[0] = self.x_derivative[1]
616                    self.y_derivative = G.DerivativeIntGauss1D(j,self.
    theta[1],PSFsigma,self.theta[2],self.PSFx)
617                    self.dudt[1] = self.y_derivative[0]
618                    self.d2udt2[1] = self.y_derivative[1]
619                    self.sigma_derivative = G.DerivativeIntGauss2DSigma(
    i,j,self.theta[0],self.theta[1],self.theta[4],self.theta[2],self.
    PSFx,self.PSFy)
620                    self.dudt[4] = self.sigma_derivative[0]
```

```
621                    self.d2udt2[4] = self.sigma_derivative[1]
622                    self.dudt[2] = self.PSFx*self.PSFy
623                    self.d2udt2[2] = 0.0
624                    self.dudt[3] = 1.0
625                    self.d2udt2[3] = 0.0
626                    '''Newton-Raphson Iteration'''
627                    self.cf = 0.0
628                    self.df = 0.0
629                    if (self.model>10.0e-3):
630                        self.cf = data[i,j]/self.model-1
631                        self.df = data[i,j]/pow(self.model,2)
632                    self.cf = N.minimum(self.cf,10.0e4)
633                    self.df = N.minimum(self.df,10.0e4)
634                    for ll in range(params):
635                        self.num[ll]+=self.dudt[ll]*self.cf
636                        self.den[ll]+=self.d2udt2[ll]*self.cf-pow(self.
    dudt[ll],2)*self.df
637            '''The update'''
638            if(itr<5):
639                for ll in range(params):
640                    self.theta[ll]-=self.gamma[ll]*N.minimum(N.maximum(
    self.num[ll]/self.den[ll], -self.maxjump[ll]), self.maxjump[ll])
641                    print self.theta[0]
642                    print self.theta[1]
643            else:
644                for ll in range(params):
645                    self.theta[ll]-=N.minimum(N.maximum(self.num[ll]/
    self.den[ll], -self.maxjump[ll]), self.maxjump[ll])
646                    print self.theta[0]
647                    print self.theta[1]
648            '''Any other constraints'''
649            self.theta[2]=N.maximum(self.theta[2], 1.0)
650            self.theta[3]=N.maximum(self.theta[3], 0.01)
651            self.theta[4]=N.maximum(self.theta[4], 0.5)
652            self.theta[4]=N.minimum(self.theta[4], sz/2.0)
653        return(N.transpose(self.theta))
```

B.3   gausslib.py

```
1  import os, sys, time
2  sys.path.append('..\\simsxy')
3  import glob
4  orig_path = "Z:/pythonfiles/storm/STORMholographic_postdec"
5
6  import scipy.ndimage as nd
```

```python
7  from scipy.special import erf
8  #import Utility as U
9  #import zernike as Z
10
11 import numpy as N
12 #import numpy.random as rd
13 #import numpy.fft as ft
14 import tifffile as tf
15
16 def IntGauss1D(ii,x,sigma):
17     '''Calculating PSF model using Error functions'''
18     norm = 0.5/pow(sigma,2)
19     return 0.5*(erf((ii-x+0.5)*N.sqrt(norm))-erf((ii-x-0.5)*N.sqrt(norm
       )))
20
21 def DerivativeIntGauss1D(ii,x,sigma,ph,PSFy):
22   '''Calculating the Derivative of 1D Gaussian'''
23   a = N.exp(-0.5*pow(((ii+0.5-x)/sigma), 2.0))
24   b = N.exp(-0.5*pow(((ii-0.5-x)/sigma), 2.0))
25   dudt =  -ph*(a-b)*PSFy/(N.sqrt(2.0*N.pi)*sigma)
26   d2udt2 = -ph*((ii+0.5-x)*a-(ii-0.5-x)*b)*PSFy/(N.sqrt(2.0*N.pi)*pow(
       sigma, 3))
27   return(dudt,d2udt2)
28
29 def DerivativeIntGauss1DSigma(ii,x,Sx,ph,PSFy):
30   '''Calculating derivative of 1D Gaussian'''
31   ax = N.exp(-0.5*pow(((ii+0.5-x)/Sx), 2.0))
32   bx = N.exp(-0.5*pow(((ii-0.5-x)/Sx), 2.0))
33   dudt = -ph*(ax*(ii-x+0.5)-bx*(ii-x-0.5))*PSFy/(N.sqrt(2.0*N.pi)*pow(
       Sx,2))
34   d2udt2 = -2.0*dudt/Sx-ph*(ax*pow((ii-x+0.5),3)-bx*pow((ii-x-0.5),3))*
       PSFy/(N.sqrt(2.0*N.pi)*pow(Sx,5))
35   return(dudt,d2udt2)
36
37 def DerivativeIntGauss2DSigma(ii,jj,x,y,S,ph,PSFx,PSFy):
38   '''Calculating derivative of 2D Gaussian'''
39   doublederivative_x = DerivativeIntGauss1DSigma(ii,x,S,ph,PSFy)
40   dSx = doublederivative_x[0]
41   ddSx = doublederivative_x[1]
42   doublederivative_y = DerivativeIntGauss1DSigma(jj,y,S,ph,PSFx)
43   dSy = doublederivative_y[0]
44   ddSy = doublederivative_y[1]
45   dudt = dSx+dSy
46   d2udt2 = ddSx+ddSy
47   return(dudt,d2udt2)
48
49 def GaussFMaxMin2D(sz,sigma,data):
```

```python
50      MaxN = 0.0
51      MinBG = 10.0e+10
52      norm = 0.5/pow(sigma,2)
53      '''loop over all pixels'''
54      for kk in range(sz):
55          for ll in range(sz):
56              filteredpixel = 0.0
57              Sum = 0.0
58              for ii in range(sz):
59                  for jj in range(sz):
60                      filteredpixel+=N.exp(-pow((ii-kk-2),2)*norm)*N.exp
    (-pow((ll-jj-2),2)*norm)*data[ii,jj]
61                      Sum+=N.exp(-pow((ii-kk-2),2)*norm)*N.exp(-pow((ll-
    jj-2),2)*norm)
62              filteredpixel/=Sum
63              MaxN = N.maximum(MaxN,filteredpixel)
64              MinBG = N.minimum(MinBG,filteredpixel)
65      return(MaxN,MinBG)
66
67  def com_2d(self,data,sz):
68      '''Finds 2D center of mass'''
69      self.tmpx = 0.0
70      self.tmpy = 0.0
71      self.tmpsum = 0.0
72      for a in range(sz):
73          for b in range(sz):
74              self.tmpx += data[a,b]*a
75              self.tmpy += data[a,b]*b
76              self.tmpsum += data[a,b]
77      self.x = self.tmpx/self.tmpsum
78      self.y = self.tmpy/self.tmpsum
79      return(self.x,self.y)
```

Appendix C

C.1   Code for calculating CRLB for SIDH

C.2   Basic_config_single_spherical_lens.m

```matlab
clear all
%%%%%%%%%%%%%%%%%%%%%%%%%%%%%%%%%%%%%%%%%%%%
% SIDH characterization
% 01/14/2020
% Abhijit Marar
%%%%%%%%%%%%%%%%%%%%%%%%%%%%%%%%%%%%%%%%%%%%
% SIDH with 1 spherical wave, Simple configuration
%%%%%%%%%%%%%%%%%%%%%%%%%%%%%%%%%%%%%%%%%%%%
%DEFINE CONSTANTS
%%%%%%%%%%%%%%%%%%%%%%%%%%%%%%%%%%%%%%%%%%%%
f_o = 3;                                % Focal length of objective (mm)
NA = 1.42;                              % Numerical aperture of objective
D_bpp = (2*f_o*NA);                     % Diameter of back pupil plane
wave = 670e-6;                          % Wavelength of light (mm)
delta_c = 16e-3;                        % Pixel size of camera (mm)
z_s = 2.990:50e-6:3.010;                 % Distance between sample and
    objective
d_slm = 3;                              % Distance between objective and
    SLM
f_slm = 300;                            % Focal length of diffractive lens
z_h = 150;
%z_h = [50,75,100,125,150];             % Distance between SLM and camera
%z_h = [450,475,500,525,550];           % Distance between SLM and camera
defocus = (z_s*1e+3-3e+3);
%%%%%%%%%%%%%%%%%%%%%%%%%%%%%%%%%%%%%%%%%%%%
%RADIUS OF SPHERICAL WAVE AT CAMERA
%%%%%%%%%%%%%%%%%%%%%%%%%%%%%%%%%%%%%%%%%%%%
```

```matlab
syms d_SLM f_O z_S z_H f_SLM
mat_spherical_wave = simplify([1 z_H;0 1]*[1 0; -1/f_SLM 1]*[1 d_SLM;0
    1]*[1 0; -1/f_O 1]*[1 z_S;0 1]);
radius_spherical_wave = zeros(length(z_h),length(z_s));
figure;
h(1) = subplot(3,2,1);
for j = 1:length(z_h)
    for i = 1:length(z_s)
        mat_spherical_wave_const = subs(mat_spherical_wave,[d_SLM,f_O,
    z_S,z_H,f_SLM],[d_slm,f_o,z_s(i),z_h(j),f_slm]);
        radius_spherical_wave(j,i) = abs(mat_spherical_wave_const(1,2)*
    NA);
    end
    plot(defocus,radius_spherical_wave(j,:),'LineWidth',3);
    hold on
end
title('Radius of spherical wave');
xlabel('Distance between sample and objective (\mum)');
ylabel('Radius(mm)');
hold off
%%%%%%%%%%%%%%%%%%%%%%%%%%%%%%%%%%%%%%%%%%%
%RADIUS OF PLANE WAVE AT CAMERA
%%%%%%%%%%%%%%%%%%%%%%%%%%%%%%%%%%%%%%%%%%%
mat_plane_wave = simplify([1 (d_SLM+z_H);0 1]*[1 0; -1/f_O 1]*[1 z_S;0
    1]);
radius_plane_wave = zeros(length(z_h),length(z_s));
h(2) = subplot(3,2,2);
for j = 1:length(z_h)
    for i = 1:length(z_s)
        mat_plane_wave_const = subs(mat_plane_wave,[d_SLM,f_O,z_S,z_H
    ],[d_slm,f_o,z_s(i),z_h(j)]);
        radius_plane_wave(j,i) = abs(mat_plane_wave_const(1,2)*NA);
    end
    plot(defocus,radius_plane_wave(j,:),'LineWidth',3);
    hold on
end
title('Radius of plane wave')
xlabel('Distance between sample and objective (\mum)')
ylabel('Radius(mm)')
hold off
%%%%%%%%%%%%%%%%%%%%%%%%%%%%%%%%%%%%%%%%%%%%%%%
%RADIUS OF HOLOGRAM AT CAMERA
%%%%%%%%%%%%%%%%%%%%%%%%%%%%%%%%%%%%%%%%%%%%%%%
radius_hologram = zeros(length(z_h),length(z_s));
h(3) = subplot(3,2,3);
for j = 1:length(z_h)
    for i = 1:length(z_s)
```

```matlab
68        mat_spherical_wave_const = subs(mat_spherical_wave,[d_SLM,f_O,
   z_S,z_H,f_SLM],[d_slm,f_o,z_s(i),z_h(j),f_slm]);
69        radius_spherical_wave(j,i) = abs(mat_spherical_wave_const(1,2)*
   NA);
70        mat_plane_wave_const = subs(mat_plane_wave,[d_SLM,f_O,z_S,z_H
   ],[d_slm,f_o,z_s(i),z_h(j)]);
71        radius_plane_wave(j,i) = abs(mat_plane_wave_const(1,2)*NA);
72        radius_hologram(j,i) = min(radius_plane_wave(j,i),
   radius_spherical_wave(j,i));
73     end
74     plot(defocus,radius_hologram(j,:),'LineWidth',3);
75     hold on
76 end
77 title('Radius of hologram')
78 xlabel('Distance between sample and objective (\mum)')
79 ylabel('Radius(mm)')
80 hold off
81 %%%%%%%%%%%%%%%%%%%%%%%%%%%%%%%%%%%%%%%%%%%%%
82 %CALCULATION OF RECONSTRUCTION DISTANCE (Z_R)
83 %Siegel, Nisan, Joseph Rosen, and Gary Brooker. Optics express 20.18
    (2012): 19822-19835.
84 %%%%%%%%%%%%%%%%%%%%%%%%%%%%%%%%%%%%%%%%%%%%%%
85 f_e = simplify((z_S*f_O)/(f_O-z_S));
86 f1 = simplify((f_SLM*(f_e+d_SLM))/(f_SLM-(f_e+d_SLM)));
87 z_r_focus = simplify((f_SLM-z_H));
88 num2 = (f1+z_H)*(f_e+d_SLM+z_H);
89 den2 = f1-f_e-d_SLM;
90 z_r_out_of_focus = num2/den2;
91 z_r = zeros(length(z_h),length(z_s));
92 h(4) = subplot(3,2,4);
93 for j = 1:length(z_h)
94    for i = 1:length(z_s)
95        if (z_s(i) == f_o)
96            z_r(j,i) = double(subs(z_r_focus, [f_SLM,z_H],[f_slm,z_h(j)
   ]));
97        else
98            fe_const = subs(f_e, [f_O,z_S],[f_o,z_s(i)]);
99            f1_const = subs(f1, [f_SLM,f_e,d_SLM],[f_slm,fe_const,d_slm
   ]);
100            num2_const = subs(num2, [f1,z_H,f_e,d_SLM],[f1_const,z_h(j)
   ,fe_const,d_slm]);
101            den2_const = subs(den2, [f1,f_e,d_SLM],[f1_const,fe_const,
   d_slm]);
102            z_r(j,i) = double(subs(z_r_out_of_focus, [num2,den2],[
   num2_const,den2_const]));
103        end
104    end
```

```
105     plot(defocus,z_r(j,:),'LineWidth',3);
106     hold on
107 end
108 title('Reconstruction Distance')
109 xlabel('Distance between sample and objective (\mum)')
110 ylabel('z_{r}(mm)')
111 hold off
112 %%%%%%%%%%%%%%%%%%%%%%%%%%%%%%%%%%%%%%%%%%%%%%%%
113 %CALCULATION OF TRANSVERSE MAGNIFICATION
114 %%%%%%%%%%%%%%%%%%%%%%%%%%%%%%%%%%%%%%%%%%%%%%%%
115 trans_mag = zeros(length(z_h),length(z_s));
116 mag_out_of_focus_num = (f_e*z_H);
117 mag_out_of_focus_den = (f_e+d_SLM);
118 h(5) = subplot(3,2,5);
119 for j = 1:length(z_h)
120     for i = 1:length(z_s)
121         if (z_s(i) == f_o)
122             trans_mag(j,i) = z_h(j)/f_o;
123         else
124             fe_const = subs(f_e, [f_O,z_S],[f_o,z_s(i)]);
125             mag_num_cnst = double(subs(mag_out_of_focus_num,[f_e,z_H],[
    fe_const,z_h(j)]));
126             mag_den_cnst = z_s(i)*double(subs(mag_out_of_focus_den,[f_e
    ,d_SLM],[fe_const,d_slm]));
127             trans_mag(j,i) = mag_num_cnst/mag_den_cnst;
128         end
129     end
130     plot(defocus,trans_mag(j,:),'LineWidth',3);
131     hold on
132 end
133 title('Transverse magnification')
134 legend(strcat('z_h =',num2str(z_h),' mm'),'Location','bestoutside','
    FontWeight','bold')
135 xlabel('Distance between sample and objective (\mum)')
136 ylabel('M_{T}')
137 pos = get(h,'Position');
138 new = mean(cellfun(@(v)v(1),pos(1:2)));
139 set(h(5),'Position',[new,pos{end}(2:end)])
```

C.3   Basic_config_dual_spherical_lens.m

```
1 %%%%%%%%%%%%%%%%%%%%%%%%%%%%%%%%%%%%%%%%%%%%%%%
2 % SIDH characterization
3 % 02/1/2020
4 % Abhijit Marar
```

```matlab
%%%%%%%%%%%%%%%%%%%%%%%%%%%%%%%%%%%%%%%%%%%%%%
% SIDH with 2 spherical waves, Simple configuration
%%%%%%%%%%%%%%%%%%%%%%%%%%%%%%%%%%%%%%%%%%%%%%
%DEFINE CONSTANTS
%%%%%%%%%%%%%%%%%%%%%%%%%%%%%%%%%%%%%%%%%%%%%%
f_o = 3;                                    % Focal length of objective
    (mm)
NA = 1.42;                                  % Numerical aperture of
    objective
D_bpp = (2*f_o*NA);                         % Diameter of back pupil
    plane
R_o = f_o*NA;                               % Radius of beam at
    interferometer
wave = 670e-6;                              % Wavelength of light (mm)
delta_c = 16e-3;                            % Pixel size of camera (mm)
z_s = 2.990:5e-6:3.010;                     % Distance between sample
    and objective
d_slm = 3;                                  % Distance between
    objective and SLM
f_slm1 = 200;                               % Focal length of shorter
    focal length mirror
f_slm2 = 400;                               % Focal length of longer
    focal length mirror
s_fac = (f_slm2-f_slm1)/(f_slm2+f_slm1);    % s-factor
%z_h = (2*f_slm1*f_slm2)/(f_slm1+f_slm2);   % Distance between
    interferometer and camera (maximum overlap)
%z_h = [500,525,550,575,600];
z_h = 150;
zh_min = (4*R_o*delta_c)/wave;              % Min distance between
    interferometer and camera
defocus = (z_s*1e+3-3e+3);
%%%%%%%%%%%%%%%%%%%%%%%%%%%%%%%%%%%%%%%%%%%%%%%%%%
%RADIUS OF SHORTER FOCAL LENGTH SPHERICAL WAVE AT CAMERA
%%%%%%%%%%%%%%%%%%%%%%%%%%%%%%%%%%%%%%%%%%%%%%%%%%%
syms d_SLM f_O z_S z_H f_SLM1 f_SLM2
mat_shorter_wave = simplify([1 z_H;0 1]*[1 0; -1/f_SLM1 1]*[1 d_SLM;0
    1]*[1 0; -1/f_O 1]*[1 z_S;0 1]);
rad_shorter_wave = zeros(length(z_h),length(z_s));
figure;
for j = 1:length(z_h)
    for i = 1:length(z_s)
        mat_shorter_wave_const = subs(mat_shorter_wave,[d_SLM,f_O,z_S,
    z_H,f_SLM1],[d_slm,f_o,z_s(i),z_h(j),f_slm1]);
        rad_shorter_wave(j,i) = abs(mat_shorter_wave_const(1,2)*NA);
    end
    plot(defocus,rad_shorter_wave(j,:),'LineWidth',6);
    hold on
```

```matlab
40  end
41  title('Radius of f_{d1}');
42  xlabel('Distance between sample and objective (\mum)');
43  ylabel('Radius(mm)');
44  hold off
45  %%%%%%%%%%%%%%%%%%%%%%%%%%%%%%%%%%%%%%%%%%%%%%%%%%%%
46  %RADIUS OF LONGER FOCAL LENGTH SPHERICAL WAVE AT CAMERA
47  %%%%%%%%%%%%%%%%%%%%%%%%%%%%%%%%%%%%%%%%%%%%%%%%%%%%
48  mat_longer_wave = simplify([1 z_H;0 1]*[1 0; -1/f_SLM2 1]*[1 d_SLM;0
        1]*[1 0; -1/f_O 1]*[1 z_S;0 1]);
49  rad_longer_wave = zeros(length(z_h),length(z_s));
50  figure;
51  for j = 1:length(z_h)
52      for i = 1:length(z_s)
53          mat_longer_wave_const = subs(mat_longer_wave,[d_SLM,f_O,z_S,z_H
        ,f_SLM2],[d_slm,f_o,z_s(i),z_h(j),f_slm2]);
54          rad_longer_wave(j,i) = abs(mat_longer_wave_const(1,2)*NA);
55      end
56      plot(defocus,rad_longer_wave(j,:),'LineWidth',6);
57      hold on
58  end
59  title('Radius of f_{d2}');
60  xlabel('Distance between sample and objective (\mum)');
61  ylabel('Radius(mm)');
62  hold off
63  %%%%%%%%%%%%%%%%%%%%%%%%%%%%%%%%%%%%%%%%%%%%%%%%%%%%
64  %RADIUS OF HOLOGRAM AT CAMERA
65  %%%%%%%%%%%%%%%%%%%%%%%%%%%%%%%%%%%%%%%%%%%%%%%%%%%%
66  radius_hologram = zeros(length(z_h),length(z_s));
67  figure;
68  for j = 1:length(z_h)
69      for i = 1:length(z_s)
70          radius_hologram(j,i) = min(rad_shorter_wave(j,i),
        rad_longer_wave(j,i));
71      end
72      plot(defocus,radius_hologram(j,:),'LineWidth',6);
73      hold on
74  end
75  title('Radius of Hologram');
76  xlabel('Distance between sample and objective (\mum)');
77  ylabel('Radius(mm)');
78  hold off
79  %%%%%%%%%%%%%%%%%%%%%%%%%%%%%%%%%%%%%%%%%%%%%%%%
80  %CALCULATION OF RECONSTRUCTION DISTANCE (Z_R)
81  %Siegel, Nisan, Joseph Rosen, and Gary Brooker. Optics express 20.18
        (2012): 19822-19835.
82  %%%%%%%%%%%%%%%%%%%%%%%%%%%%%%%%%%%%%%%%%%%%%%%
```

```
83  syms z_d
84  zr_focus = simplify(abs(((z_H-f_SLM1)*(z_H-f_SLM2))/(f_SLM1-f_SLM2)));
85  z_D = simplify((z_S*(f_O-d_SLM)+f_O*d_SLM)/(f_O-z_S));
86  z_f1 = simplify((z_H*z_D)-f_SLM1*(z_D+z_H));
87  z_f2 = simplify((z_H*z_D)-f_SLM2*(z_D+z_H));
88  zr_out_of_focus = simplify(abs((z_f1*z_f2)/(z_d^2*(f_SLM1-f_SLM2))));
89  z_r = zeros(length(z_h),length(z_s));
90  figure;
91  for j = 1:length(z_h)
92      for i = 1:length(z_s)
93          if (z_s(i) == f_o)
94              z_r(j,i) = double(subs(zr_focus, [z_H,f_SLM1,f_SLM2],[z_h(j
    ),f_slm1,f_slm2]));
95          else
96              z_D_const = subs(z_D,[z_S,f_O,d_SLM],[z_s(i),f_o,d_slm]);
97              z_f1_const = subs(z_f1,[z_H,z_D,f_SLM1],[z_h(j),z_D_const,
    f_slm1]);
98              z_f2_const = subs(z_f2,[z_H,z_D,f_SLM2],[z_h(j),z_D_const,
    f_slm2]);
99              z_r(j,i) = double(subs(zr_out_of_focus,[z_f1,z_f2,z_d,
    f_SLM1,f_SLM2],[z_f1_const,z_f2_const,z_D_const,f_slm1,f_slm2]));
100          end
101      end
102      plot(defocus,z_r(j,:),'LineWidth',6);
103      hold on
104  end
105  title('Reconstruction Distance');
106  xlabel('Distance between sample and objective (\mum)');
107  ylabel('Radius(mm)');
108  hold off
109  %%%%%%%%%%%%%%%%%%%%%%%%%%%%%%%%%%%%%%%%%%%%%%
110  %CALCULATION OF TRANSVERSE MAGNIFICATION
111  %%%%%%%%%%%%%%%%%%%%%%%%%%%%%%%%%%%%%%%%%%%%%%%
112  f_e = simplify((z_S*f_O)/(f_O-z_S));
113  trans_mag = zeros(length(z_h),length(z_s));
114  mag_out_of_focus_num = (f_e*z_H);
115  mag_out_of_focus_den = (f_e+d_SLM);
116  figure;
117  for j = 1:length(z_h)
118      for i = 1:length(z_s)
119          if (z_s(i) == f_o)
120              trans_mag(j,i) = z_h(j)/f_o;
121          else
122              fe_const = subs(f_e, [f_O,z_S],[f_o,z_s(i)]);
123              mag_num_cnst = double(subs(mag_out_of_focus_num,[f_e,z_H],[
    fe_const,z_h(j)]));
```

```
124            mag_den_cnst = z_s(i)*double(subs(mag_out_of_focus_den,[f_e
       ,d_SLM],[fe_const,d_slm]));
125            trans_mag(j,i) = mag_num_cnst/mag_den_cnst;
126        end
127    end
128    plot(defocus,trans_mag(j,:),'LineWidth',6);
129    hold on
130 end
131 title('Transverse Magnification');
132 legend(strcat('z_h =',num2str(z_h'),' mm'),'Location','best','
       FontWeight','bold');
133 xlabel('Distance between sample and objective (\mum)');
134 ylabel('Radius(mm)');
135 hold off
```

C.4 z_r_derivative.m

```
1 %Derivative of z_r w.r.t z_s
2
3 f_o = 3;
4 dist = 2.990:50e-6:3.010;
5 d_slm = 3;                              % Distance between objective and
       SLM
6 f_slm = 300;                            % Focal length of diffractive lens
7 %camera_dist = [500,525,550,575,600];
8 camera_dist = 150;
9 defocus = (dist*1e+3-3e+3);
10
11 syms fo z fslm dslm z_h z_s
12
13 fe = (fo*z_s)/(fo-z_s);
14 f1 = (fslm*(fe+dslm))/(fslm-fe-dslm);
15 zr = ((f1+z_h)*(fe+dslm+z_h))/(f1-fe-dslm);
16
17 fe_prime = simplify(diff(fe,z_s));
18 f1_prime = simplify(diff(f1,z_s));
19 zr_prime = simplify(diff(zr,z_s));
20
21 df_zr = zeros(length(z_h),length(z_s));
22 figure;
23 for j = 1: length(camera_dist)
24     for i = 1:length(dist)
25         zr_prime_cnst = simplify(subs(zr_prime,[fo,z_h,dslm,fslm,z_s],[
       f_o,camera_dist(j),d_slm,f_slm,dist(i)]));
26         df_zr(j,i) = double(abs(zr_prime_cnst));
```

```
27        end
28        plot(defocus,df_zr(j,:),'LineWidth',3);
29        hold on
30 end
31 hold off
```

C.5   z_r_derivative_dual_spherical_wave.m

```
1  %Derivative of z_r w.r.t z_s for SIDH with dual spherical waves
2
3  f_o = 3;
4  dist = 2.990:5e-6:3.010;
5
6  d_slm = 3;                                      % Distance between
       objective and SLM
7  f_slm1 = 200;                                   % Focal length of shorter
       focal length mirror
8  f_slm2 = 400;                                   % Focal length of longer
       focal length mirror
9
10
11 %camera_dist = (2*f_slm1*f_slm2)/(f_slm1+f_slm2);
12 %camera_dist = [500,525,550,575,600];
13 camera_dist = 150;
14 defocus = (dist*1e+3-3e+3);
15
16 syms fo z fslm1 fslm2 dslm z_h z_s
17
18 z_d = simplify((z_s*(fo-dslm)+fo*dslm)/(fo-z_s));
19 z_f1 = simplify((z_h*z_d)-fslm1*(z_d+z_h));
20 z_f2 = simplify((z_h*z_d)-fslm2*(z_d+z_h));
21
22 zr_out_of_focus = simplify((z_f1*z_f2)/(z_d^2*(fslm1-fslm2)));
23
24 zd_prime = simplify(diff(z_d,z_s));
25 zf1_prime = simplify(diff(z_f1,z_s));
26 zf2_prime = simplify(diff(z_f2,z_s));
27 zr_prime = simplify(diff(zr_out_of_focus,z_s));
28
29 df_zr = zeros(length(camera_dist),length(dist));
30 figure;
31 for j = 1:length(camera_dist)
32     for i = 1:length(dist)
33         zr_prime_cnst = simplify(subs(zr_prime,[fo,z_h,dslm,fslm1,fslm2
       ,z_s],[f_o,camera_dist(j),d_slm,f_slm1,f_slm2,dist(i)]));
```

```
34         df_zr(j,i) = double(abs(zr_prime_cnst));
35     end
36     plot(defocus,df_zr(j,:),'LineWidth',3);
37     hold on
38 end
39 hold off
```

C.6   SIDH_CRLB_withnoise.m

```
1  %%%%%%%%%%%%%%%%%%%%%%%%%%%%%%%%%%%%%%%%%%%%%
2  % CRLB calculation for SIDH with Poisson noise
3  % 02/12/2020
4  % Abhijit Marar
5  %%%%%%%%%%%%%%%%%%%%%%%%%%%%%%%%%%%%%%%%%%%%%
6  %DEFINE CONSTANTS
7  %%%%%%%%%%%%%%%%%%%%%%%%%%%%%%%%%%%%%%%%%%%%%
8  f_o = 3;                              % Focal length of objective (mm)
9  NA = 1.42;                            % Numerical aperture of objective
10 D_bpp = (2*f_o*NA);                   % Diameter of back pupil plane
11 wave = 670e-6;                        % Wavelength of light (mm)
12 k = 2*pi/wave;                        % Wavenumber
13 z_s = 2.990:50e-6:3.010;              % Distance between sample and
       objective
14 d_slm = 3;                            % Distance between objective and
       SLM
15 f_slm = 300;                          % Focal length of diffractive lens
16 z_h = 150;
17 %z_h = [50,75,100,125,150];           % Distance between SLM and camera
       before focus
18 %z_h = [450,475,500,525,550];         % Distance between SLM and camera
       after focus
19 r_h = radius_hologram;
20 r_h(r_h == 0) = eps;
21 z_r(z_r == 0) = eps;
22 N = 6000;                             % No. of photons in hologram
23 bg = 1000;                            % Bg photons
24 defocus = (z_s*1e+3-3e+3);
25 %%%%%%%%%%%%%%%%%%%%%%%%%%%%%%%%%%%%%%%%%%%%%
26 A = zeros(length(z_h),length(z_s));
27 fisher_x = zeros(length(z_h),length(z_s));
28 fisher_z = zeros(length(z_h),length(z_s));
29 CRLB_x_SIDH = zeros(length(z_h),length(z_s));
30 CRLB_z_SIDH = zeros(length(z_h),length(z_s));
31 %%%%%%%%%%%%%%%%%%%%%%%%%%%%%%%%%%%%%%%%%%%%%
32 %CRLB_x
```

```matlab
%%%%%%%%%%%%%%%%%%%%%%%%%%%%%%%%%%%%%%%%%%%%
figure
p_noise(1) = subplot(1,2,1);
for j = 1:length(z_h)
    for i = 1:length(z_s)
        A(j,i) = 1/(pi*(r_h(j,i)^2+2*(z_r(j,i)/k)*sin((k/(2*z_r(j,i)))*
r_h(j,i)^2)));
        q_sidh = @(a,b) A(j,i).*(1+cos((k/(2*z_r(j,i))).*(a.^2+b.^2)));
        dq_dxs = @(a,b) 2.*A(j,i).*trans_mag(j,i).*(k/(2*z_r(j,i))).*
sin((k/(2*z_r(j,i))).*(a.^2+b.^2)).*a;
        F_xx = @(a,b) ((N./(q_sidh(a,b)+(bg/N))).*dq_dxs(a,b).*dq_dxs(a
,b));
        polar_Fxx = @(theta,r) F_xx(r.*cos(theta),r.*sin(theta)).*r;
        fisher_x(j,i) = integral2(polar_Fxx,0,2*pi,0,r_h(j,i),'method',
'iterated');
        CRLB_x_SIDH(j,i) = 1.e+6/sqrt(fisher_x(j,i));
    end
    plot(defocus,CRLB_x_SIDH(j,:),'LineWidth',3);
    hold on
end
axis([-10 10 0 50]);
title('CRLB_{xy}');
legend(strcat('z_h =',num2str(z_h'),' mm'),'Location','northwest','
FontWeight','bold');
xlabel('Distance between sample and objective (\mum)');
ylabel('\sigma_{x}, \sigma_{y} (nm)');
hold off
%%%%%%%%%%%%%%%%%%%%%%%%%%%%%%%%%%%%%%%%%%%%
%CRLB_z
%%%%%%%%%%%%%%%%%%%%%%%%%%%%%%%%%%%%%%%%%%%%
p_noise(2) = subplot(1,2,2);
for j = 1: length(z_h)
    for i = 1:length(z_s)
        A(j,i) = 1/(pi*(r_h(j,i)^2+2*(z_r(j,i)/k)*sin((k/(2*z_r(j,i)))*
r_h(j,i)^2)));
        q_sidh = @(a,b) A(j,i).*(1+cos((k/(2*z_r(j,i))).*(a.^2+b.^2)));
        dq_dzr = @(a,b) ((A(j,i).*(a.^2+b.^2).*k)./(2.*z_r(j,i).^2)).*
sin((k/(2*z_r(j,i))).*(a.^2+b.^2));
        F_zz = @(a,b) ((N./(q_sidh(a,b)+(bg/N))).*dq_dzr(a,b).*dq_dzr(a
,b).*df_zr(j,i).*df_zr(j,i));
        polar_Fzz = @(theta,r) F_zz(r.*cos(theta),r.*sin(theta)).*r;
        fisher_z(j,i) = integral2(polar_Fzz,0,2*pi,0,r_h(j,i),'method',
'iterated');
        CRLB_z_SIDH(j,i) = 1.e+6/sqrt(fisher_z(j,i));
    end
    plot(defocus,CRLB_z_SIDH(j,:),'LineWidth',3)
    hold on
```

```
71  end
72  axis([-10 10 0 50]);
73  title('CRLB_{z}');
74  legend(strcat('z_h =',num2str(z_h'),' mm'),'Location','northwest','
        FontWeight','bold');
75  xlabel('Distance between sample and objective (\mum)');
76  ylabel('\sigma_{z}(nm)');
77  hold off
```

C.7 Astigmatic_PSF_CRLB_withnoise.m

```
1   %%%%%%%%%%%%%%%%%%%%%%%%%%%%%%%%%%%%%%%%%%%
2   % CRLB calculation for Astigmatic PSF with noise
3   % 02/07/2020
4   % Abhijit Marar
5   %%%%%%%%%%%%%%%%%%%%%%%%%%%%%%%%%%%%%%%%%%%
6   %clear all
7
8   f_o = 3;                                % Focal length of objective (mm
                                                )
9   NA = 1.42;                              % Numerical aperture of
        objective
10  wave = 670e-6;                          % Wavelength of light (mm)
11  n = 1.515;                              %Refractive index
12  FWHM = (0.61*wave)/NA;                  % FWHM
13  sigma_o = FWHM/(2*sqrt(2*log(2)));      % standard deviation of
        Gaussian
14  z = 2.990:50e-6:3.010;                  % Distance between sample and
        objective
15  z_s = (z-3.000);
16  N = 6000;                               % No. of photons
17  %d = (2*wave)/NA^2;                      % Depth of focus (mm)
18  d = wave/(n*(1-(1-(NA/n)^2)^(1/2)));
19  gamma = 405e-6;                         % Amount of astigmatism (mm)
20  bg = 1000;                              % No. of bg photons/area
21
22  sigma_x = zeros(1,length(z_s));
23  sigma_y = zeros(1,length(z_s));
24  dsigmax_dz = zeros(1,length(z_s));
25  dsigmay_dz = zeros(1,length(z_s));
26  CRLB_x = zeros(1,length(z_s));
27  CRLB_y = zeros(1,length(z_s));
28  CRLB_z = zeros(1,length(z_s));
29  epsilon = zeros(1,length(z_s));
30  fisher_x = zeros(1,length(z_s));
```

```matlab
fisher_y = zeros(1,length(z_s));
fisher_z = zeros(1,length(z_s));

for i = 1:length(z_s)
    sigma_x(i) = sigma_o*sqrt(1+((z_s(i)+gamma)/d)^2);
    sigma_y(i) = sigma_o*sqrt(1+((z_s(i)-gamma)/d)^2);
    epsilon(i) = sqrt(sigma_y(i)/sigma_x(i));
    q_astigmatic = @(x,y) (1./(2*pi*sigma_x(i).*sigma_y(i))).*exp(-(((x
    .^2)/(2*sigma_x(i).^2))+((y.^2)/(2*sigma_y(i).^2)))));
    dq_dx = @(x,y) (-x./(2.*pi.*sigma_y(i).*sigma_x(i).^3)).*exp(-(((x
    .^2)/(2*sigma_x(i).^2))+((y.^2)/(2*sigma_y(i).^2)))));
    dq_dy = @(x,y) (-y./(2.*pi.*sigma_x(i).*sigma_y(i).^3)).*exp(-(((x
    .^2)/(2*sigma_x(i).^2))+((y.^2)/(2*sigma_y(i).^2)))));
    dq_dsigmax = @(x,y) q_astigmatic(x,y).*((x.^2/sigma_x(i).^3)-(1/
    sigma_x(i)));
    dq_dsigmay = @(x,y) q_astigmatic(x,y).*((y.^2/sigma_y(i).^3)-(1/
    sigma_y(i)));
    dsigmax_dz(i) = ((sigma_o*(z_s(i)+gamma))/d^2)*(1+((z_s(i)+gamma)/d
    )^2)^(-1/2);
    dsigmay_dz(i) = ((sigma_o*(z_s(i)-gamma))/d^2)*(1+((z_s(i)-gamma)/d
    )^2)^(-1/2);
    dq_dz = @(x,y) (dq_dsigmax(x,y).*dsigmax_dz(i)) + (dq_dsigmay(x,y)
    .*dsigmay_dz(i));
    F_xx =  @(x,y) ((N./((bg/N)+q_astigmatic(x,y))).*dq_dx(x,y).*dq_dx(
    x,y));
    F_yy =  @(x,y) ((N./((bg/N)+q_astigmatic(x,y))).*dq_dy(x,y).*dq_dy(
    x,y));
    F_zz =  @(x,y) ((N./((bg/N)+q_astigmatic(x,y))).*dq_dz(x,y).*dq_dz(
    x,y));
    fisher_x(i) = integral2(F_xx,-6*sigma_x(i),6*sigma_x(i),-6*sigma_y(
    i),6*sigma_y(i));
    fisher_y(i) = integral2(F_yy,-6*sigma_x(i),6*sigma_x(i),-6*sigma_y(
    i),6*sigma_y(i));
    fisher_z(i) = integral2(F_zz,-6*sigma_x(i),6*sigma_x(i),-6*sigma_y(
    i),6*sigma_y(i));
    CRLB_x(i) = 1/sqrt(fisher_x(i));
    CRLB_y(i) = 1/sqrt(fisher_y(i));
    CRLB_z(i) = 1/sqrt(fisher_z(i));
end

defocus = z_s*1.e+3;
%{
figure
subplot(1,2,1)
plot(defocus,CRLB_x.*1e+6,'LineWidth',3)
hold on
plot(defocus,CRLB_y.*1e+6,'LineWidth',3)
```

```
64 axis([-2 2 0 30])
65 title('CRLB_{xy}')
66 xlabel('Distance between sample and objective (\mum)')
67 ylabel('\sigma_{x}, \sigma_{y} (nm)')
68 legend('\sigma_{x}', '\sigma_{y}')
69 hold off
70 subplot(1,2,2)
71 plot(defocus,CRLB_z*1e+6,'LineWidth',3)
72 axis([-2 2 0 100])
73 title('CRLB_{z}')
74 xlabel('Distance between sample and objective (\mum)')
75 ylabel('\sigma_{z}(nm)')
76 %}
```

C.8   Gaussian_PSF_CRLB_withnoise.m

```
1  %%%%%%%%%%%%%%%%%%%%%%%%%%%%%%%%%%%%%%%%%%%%
2  % CRLB calculation for a Gaussian PSF with noise
3  % 02/07/2020
4  % Abhijit Marar
5  %%%%%%%%%%%%%%%%%%%%%%%%%%%%%%%%%%%%%%%%%%%%
6  %clear all
7
8  f_o = 3;                              % Focal length of objective (mm
                                            )
9  NA = 1.42;                            % Numerical aperture of
                                            objective
10 wave = 670e-6;                        % Wavelength of light (mm)
11 n = 1.515;                            % Refractive index
12 FWHM = (0.61*wave)/NA;                % FWHM
13 sigma_o = FWHM/(2*sqrt(2*log(2)));    % standard deviation of
                                            Gaussian
14 z = 2.990:50e-6:3.010;                % Distance between sample and
                                            objective
15 z_s = (z-3.000);
16 N = 6000;                             % No. of photons
17 %d = (2*wave)/NA^2;                   % Depth of focus (mm)
18 d = wave/(n*(1-sqrt(1-(NA^2/n^2))));
19 bg = 1000;                            % No. of bg photons/area
20
21
22 sigma_g = zeros(1,length(z_s));
23 fisher_x = zeros(1,length(z_s));
24 fisher_z = zeros(1,length(z_s));
25 sigma_xy = zeros(1,length(z_s));
```

```matlab
26  sigma_z = zeros(1,length(z_s));
27  dzg_dz = zeros(1,length(z_s));
28
29  for i = 1:length(z_s)
30      sigma_g(i) = sigma_o*sqrt(1+(z_s(i)/d)^2);
31      q_gauss = @(x,y) (1./(2*pi*sigma_g(i).^2)).*exp(-(x.^2+y.^2)/(2*
        sigma_g(i).^2));
32      dq_dx = @(x,y) (-x./(2.*pi.*sigma_g(i).^4)).*exp(-(x.^2+y.^2)/(2.*
        sigma_g(i).^2));
33      dq_dzg = @(x,y) q_gauss(x,y).*((x.^2+y.^2-2.*sigma_g(i).^2)./(
        sigma_g(i).^3));
34      dzg_dz(i) = ((sigma_o*z_s(i))/d^2)*(1+(z_s(i)/d)^2)^(-1/2);
35      F_xx =   @(x,y) ((N./((bg/N)+q_gauss(x,y))).*dq_dx(x,y).*dq_dx(x,y))
        ;
36      F_zz = @(x,y) ((N./((bg/N)+q_gauss(x,y))).*dq_dzg(x,y).*dq_dzg(x,y)
        .*dzg_dz(i).*dzg_dz(i));
37      fisher_x(i) = integral2(F_xx,-6*sigma_g(i),6*sigma_g(i),-6*sigma_g(
        i),6*sigma_g(i));
38      fisher_z(i) = integral2(F_zz,-6*sigma_g(i),6*sigma_g(i),-6*sigma_g(
        i),6*sigma_g(i));
39      sigma_xy(i) = 1/sqrt(fisher_x(i));
40      sigma_z(i) = 1/sqrt(fisher_z(i));
41  end
42
43
44  defocus = z_s*1.e+3;
45  %{
46  figure
47  subplot(1,2,1)
48  plot(defocus,CRLB_x.*1e+6,'LineWidth',3)
49  axis([-1 1 0 30])
50  title('CRLB_{xy}')
51  xlabel('Distance between sample and objective (\mum)')
52  ylabel('\sigma_{x}, \sigma_{y} (nm)')
53  subplot(1,2,2)
54  plot(defocus,CRLB_z*1e+6,'LineWidth',3)
55  axis([-1 1 0 100])
56  title('CRLB_{z}')
57  xlabel('Distance between sample and objective (\mum)')
58  ylabel('\sigma_{z}(nm)')
59  %}
```

Appendix D
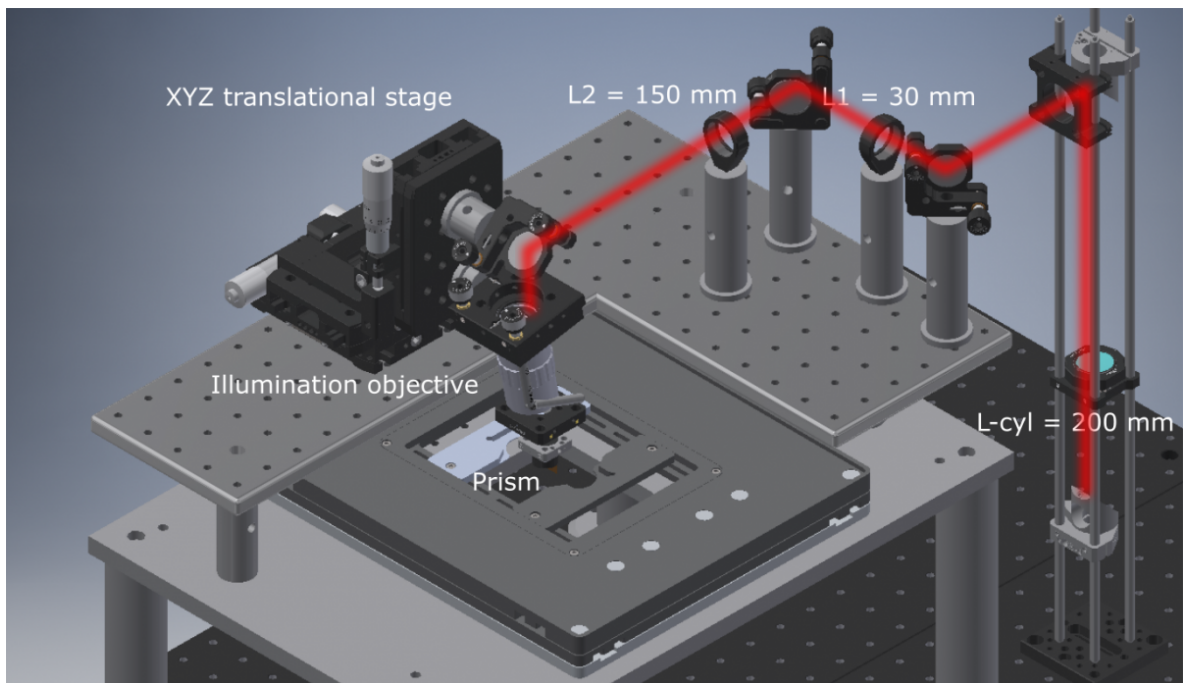
D.1 Drawing of Light sheet system

Figure D.1: **Autodesk drawing of light sheet setup**

Bibliography

Abbe, E. (1873). Beiträge zur theorie des mikroskops und der mikroskopischen wahrnehmung. *Arch. Mikrosk. Anat*, *9*, 413–68.

Abbe, E. (1880). Ueber die grenzen der geometrischen optik. *Jenaische Zeitschrift f ür Naturwissenschaft. Sitzungsberichte*, *14*, 71–109.

Abrahamsson, S., Chen, J., Hajj, B., Stallinga, S., Katsov, A. Y., Wisniewski, J., Mizuguchi, G., Soule, P., Mueller, F., Darzacq, C. D., et al. (2013). Fast multicolor 3d imaging using aberration-corrected multifocus microscopy. *Nature methods*, *10*(1), 60–63.

Abrahamsson, S., Ilic, R., Wisniewski, J., Mehl, B., Yu, L., Chen, L., Davanco, M., Oudjedi, L., Fiche, J.-B., Hajj, B., et al. (2016). Multifocus microscopy with precise color multi-phase diffractive optics applied in functional neuronal imaging. *Biomedical optics express*, *7*(3), 855–869.

Adie, S. G., Graf, B. W., Ahmad, A., Carney, P. S., & Boppart, S. A. (2012). Computational adaptive optics for broadband optical interferometric tomography of biological tissue. *Proceedings of the National Academy of Sciences*, *109*(19), 7175–7180.

Airy, G. B. (1835). On the diffraction of an object-glass with circular aperture. *Transactions of the Cambridge Philosophical Society*, *5*, 283.

Amidror, I. (2009). *The theory of the moiré phenomenon: Volume i: Periodic layers* (Vol. 38). Springer Science & Business Media.

Andresen, M., Stiel, A. C., Fölling, J., Wenzel, D., Schönle, A., Egner, A., Eggeling, C., Hell, S. W., & Jakobs, S. (2008). Photoswitchable fluorescent proteins enable monochromatic multilabel imaging and dual color fluorescence nanoscopy. *Nature biotechnology*, *26*(9), 1035–1040.

Aquino, D., Schönle, A., Geisler, C., v Middendorff, C., Wurm, C. A., Okamura, Y., Lang, T., Hell, S. W., & Egner, A. (2011). Two-color nanoscopy of three-dimensional volumes by 4pi detection of stochastically switched fluorophores. *Nature methods*, *8*(4), 353–359.

Ash, E., & Nicholls, G. (1972). Super-resolution aperture scanning microscope. *Nature*, *237*(5357), 510.

Axelrod, D., Burghardt, T. P., & Thompson, N. L. (1984). Total internal reflection fluorescence. *Annual review of biophysics and bioengineering*, *13*(1), 247–268.

Babcock, H., Sigal, Y. M., & Zhuang, X. (2012). A high-density 3d localization algorithm for stochastic optical reconstruction microscopy. *Optical Nanoscopy*, *1*(1), 6.

Babcock, H. P., & Zhuang, X. (2017). Analyzing single molecule localization microscopy data using cubic splines. *Scientific reports*, *7*(1), 552.

Backlund, M. P., Arbabi, A., Petrov, P. N., Arbabi, E., Saurabh, S., Faraon, A., & Moerner, W. (2016). Removing orientation-induced localization biases in single-molecule microscopy using a broadband metasurface mask. *Nature photonics*, *10*(7), 459.

Backlund, M. P., Lew, M. D., Backer, A. S., Sahl, S. J., & Moerner, W. (2013). The role of molecular dipole orientation in single-molecule fluorescence microscopy and implications for super-resolution imaging. *ChemPhysChem*, *15*(4), 587–599.

Baddeley, D., & Bewersdorf, J. (2018). Biological insight from super-resolution microscopy: What we can learn from localization-based images. *Annual review of biochemistry*, *87*, 965–989.

Baddeley, D., Cannell, M. B., & Soeller, C. (2010). Visualization of localization microscopy data. *Microscopy and Microanalysis*, *16*(1), 64–72.

Baddeley, D., Cannell, M. B., & Soeller, C. (2011). Three-dimensional sub-100 nm super-resolution imaging of biological samples using a phase ramp in the objective pupil. *Nano Research*, *4*(6), 589–598.

Baddeley, D., Crossman, D., Rossberger, S., Cheyne, J. E., Montgomery, J. M., Jayasinghe, I. D., Cremer, C., Cannell, M. B., & Soeller, C. (2011). 4d super-resolution microscopy with conventional fluorophores and single wavelength excitation in optically thick cells and tissues. *PloS one*, *6*(5), e20645.

Badieirostami, M., Lew, M. D., Thompson, M. A., & Moerner, W. (2010). Three-dimensional localization precision of the double-helix point spread function versus astigmatism and biplane. *Applied physics letters*, *97*(16), 161103.

Bailey, B., Farkas, D. L., Taylor, D. L., & Lanni, F. (1993). Enhancement of axial resolution in fluorescence microscopy by standing-wave excitation. *Nature*, *366*(6450), 44.

Bailey, B., Krishnamurthi, V., Farkas, D. L., Taylor, D. L., & Lanni, F. (1994). Three-dimensional imaging of biological specimens with standing wave fluorescence microscopy. *Three-Dimensional Microscopy: Image Acquisition and Processing*, *2184*, 208–213.

Banterle, N., Bui, K. H., Lemke, E. A., & Beck, M. (2013). Fourier ring correlation as a resolution criterion for super-resolution microscopy. *Journal of structural biology*, *183*(3), 363–367.

Basov, N., & Prokhorov, A. (1954). Application of molecular clusters to radiospectroscopic study of rotational spectra of molecules. *Zh. Eksperimental. Teor. Fiz.*, *27*, 431–438.

Bates, M., Huang, B., Dempsey, G. T., & Zhuang, X. (2007). Multicolor super-resolution imaging with photo-switchable fluorescent probes. *Science*, *317*(5845), 1749–1753.

Baudat, F., Imai, Y., & De Massy, B. (2013). Meiotic recombination in mammals: Localization and regulation. *Nature Reviews Genetics*, *14*(11), 794–806.

Bellve, K., Standley, C., Lifshitz, L., & Fogarty, K. (2014). Design and implementation of 3d focus stabilization for fluorescence microscopy. *Biophysical Journal*, *106*(2), 606a.

Betzig, E. (1995). Proposed method for molecular optical imaging. *Optics letters*, *20*(3), 237–239.

Betzig, E., & Chichester, R. J. (1993). Single molecules observed by near-field scanning optical microscopy. *Science*, *262*(5138), 1422–1425.

Betzig, E., Patterson, G. H., Sougrat, R., Lindwasser, O. W., Olenych, S., Bonifacino, J. S., Davidson, M. W., Lippincott-Schwartz, J., & Hess, H. F. (2006). Imaging intracellular fluorescent proteins at nanometer resolution. *Science*, *313*(5793), 1642–1645.

Binnig, G., Quate, C. F., & Gerber, C. (1986). Atomic force microscope. *Physical review letters*, *56*(9), 930.

Binnig, G., & Rohrer, H. (1983). Scanning tunneling microscopy. *Surface science*, *126*(1-3), 236–244.

Blanchard, P. M., & Greenaway, A. H. (1999). Simultaneous multiplane imaging with a distorted diffraction grating. *Applied optics*, *38*(32), 6692–6699.

Blom, H., & Widengren, J. (2017). Stimulated emission depletion microscopy. *Chemical reviews*, *117*(11), 7377–7427.

Bock, H., Geisler, C., Wurm, C. A., Von Middendorff, C., Jakobs, S., Schönle, A., Egner, A., Hell, S. W., & Eggeling, C. (2007). Two-color far-field fluorescence nanoscopy based on photo-switchable emitters. *Applied Physics B*, *88*(2), 161–165.

Booth, M. J. (2007). Adaptive optics in microscopy. *Philosophical Transactions of the Royal Society A: Mathematical, Physical and Engineering Sciences*, *365*(1861), 2829–2843.

Born, M., & Wolf, E. (2013). *Principles of optics: Electromagnetic theory of propagation, interference and diffraction of light*. Elsevier.

Bossi, M., Fölling, J., Belov, V. N., Boyarskiy, V. P., Medda, R., Egner, A., Eggeling, C., Schönle, A., & Hell, S. W. (2008). Multicolor far-field fluorescence nanoscopy through isolated detection of distinct molecular species. *Nano letters*, *8*(8), 2463–2468.

Botcherby, E. J., Juskaitis, R., Booth, M. J., & Wilson, T. (2007). Aberration-free optical refocusing in high numerical aperture microscopy. *Optics letters*, *32*(14).

Bourg, N., Mayet, C., Dupuis, G., Barroca, T., Bon, P., Lécart, S., Fort, E., & Lévêque-Fort, S. (2015). Direct optical nanoscopy with axially localized detection. *Nature Photonics*, *9*(9), 587.

Boyce, M., & Bertozzi, C. R. (2011). Bringing chemistry to life. *Nature methods*, *8*(8), 638–642.

Brand, L., Eggeling, C., Zander, C., Drexhage, K., & Seidel, C. (1997). Single-molecule identification of coumarin-120 by time-resolved fluorescence detection: Comparison of one-and two-photon excitation in solution. *The Journal of Physical Chemistry A*, *101*(24), 4313–4321.

Bretschneider, S., Eggeling, C., & Hell, S. W. (2007). Breaking the diffraction barrier in fluorescence microscopy by optical shelving. *Physical review letters*, *98*(21), 218103.

Brooker, G., Siegel, N., Wang, V., & Rosen, J. (2011). Optimal resolution in fresnel incoherent correlation holographic fluorescence microscopy. *Optics express*, *19*(6), 5047–5062.

Brumberg, E. M. (1959). Fluorescence microscopy of biological objects using light from above. *Biophysics*, *4*, 97–104.

Burgert, A., Letschert, S., Doose, S., & Sauer, M. (2015). Artifacts in single-molecule localization microscopy. *Histochemistry and cell biology*, *144*(2), 123–131.

Burke, D., Patton, B., Huang, F., Bewersdorf, J., & Booth, M. J. (2015). Adaptive optics correction of specimen-induced aberrations in single-molecule switching microscopy. *Optica*, *2*(2), 177–185.

Burns, D. H., Callis, J. B., Christian, G. D., & Davidson, E. R. (1985). Strategies for attaining super-resolution using spectroscopic data as constraints. *Applied Optics*, *24*(2), 154–161.

Castiglioni, A. (1947). *A history of medicine*. Knopf.

Cesca, F., Baldelli, P., Valtorta, F., & Benfenati, F. (2010). The synapsins: Key actors of synapse function and plasticity. *Progress in neurobiology*, *91*(4), 313–348.

Chalfie, M., Tu, Y., Euskirchen, G., Ward, W. W., & Prasher, D. C. (1994). Green fluorescent protein as a marker for gene expression. *Science*, *263*(5148), 802–805.

Chandler, T., Shroff, H., Oldenbourg, R., & La Rivière, P. (2019a). Spatio-angular fluorescence microscopy i. basic theory. *J. Opt. Soc. Am. A*, *36*(8), 1334–1345.

Chandler, T., Shroff, H., Oldenbourg, R., & La Rivière, P. (2019b). Spatio-angular fluorescence microscopy ii. paraxial 4f imaging. *J. Opt. Soc. Am. A*, *36*(8), 1346–1360.

Chao, J., Ward, E. S., & Ober, R. J. (2016). Fisher information theory for parameter estimation in single molecule microscopy: Tutorial. *JOSA A*, *33*(7), B36–B57.

Churchman, L. S., & Spudich, J. A. (2012). Colocalization of fluorescent probes: Accurate and precise registration with nanometer resolution. *Cold Spring Harbor Protocols*, *2012*(2), pdb–top067918.

Coles, B. C., Webb, S. E., Schwartz, N., Rolfe, D. J., Martin-Fernandez, M., & Schiavo, V. L. (2016). Characterisation of the effects of optical aberrations in single molecule techniques. *Biomedical optics express*, *7*(5), 1755–1767.

Collier, R., Burckhardt, C., & Lin, L. (1971). Optical holography.

Coons, A. H., Creech, H. J., & Jones, R. N. (1941). Immunological properties of an antibody containing a fluorescent group. *Proceedings of the Society for Experimental Biology and Medicine*, *47*(2), 200–202.

Coons, A. H., & Kaplan, M. H. (1950). Localization of antigen in tissue cells: Ii. improvements in a method for the detection of antigen by means of fluorescent antibody. *Journal of Experimental Medicine*, *91*(1), 1–13.

Copeland, C. R., McGray, C. D., Ilic, B. R., Geist, J., & Stavis, S. M. (2020). Accurate localization microscopy in six degrees of freedom by intrinsic aberration calibration. *arXiv preprint arXiv:2009.01170*.

Cordes, T., Strackharn, M., Stahl, S. W., Summerer, W., Steinhauer, C., Forthmann, C., Puchner, E. M., Vogelsang, J., Gaub, H. E., & Tinnefeld, P. (2009). Resolving single-molecule assembled patterns with superresolution blink-microscopy. *Nano letters*, *10*(2), 645–651.

Cover, T. M., & Thomas, J. A. (2012). *Elements of information theory*. John Wiley & Sons.

Cox, G., & Sheppard, C. J. (2004). Practical limits of resolution in confocal and non-linear microscopy. *Microscopy research and technique*, *63*(1), 18–22.

Cox, S., Rosten, E., Monypenny, J., Jovanovic-Talisman, T., Burnette, D. T., Lippincott-Schwartz, J., Jones, G. E., & Heintzmann, R. (2012). Bayesian localization microscopy reveals nanoscale podosome dynamics. *Nature methods*, *9*(2), 195.

Dalgarno, P. A., Dalgarno, H. I., Putoud, A., Lambert, R., Paterson, L., Logan, D. C., Towers, D. P., Warburton, R. J., & Greenaway, A. H. (2010). Multiplane imaging and three dimensional nanoscale particle tracking in biological microscopy. *Optics express*, *18*(2), 877–884.

Dasgupta, A., Deschamps, J., Matti, U., Huebner, U., Becker, J., Strauss, S., Jungmann, R., Heintzmann, R., & Ries, J. (2020). Direct supercritical angle localization microscopy for nanometer 3d superresolution. *bioRxiv*.

Davidovits, P., & Egger, M. D. (1969). Scanning laser microscope. *Nature*, *223*(5208), 831.

Demmerle, J., Wegel, E., Schermelleh, L., & Dobbie, I. M. (2015). Assessing resolution in super-resolution imaging. *Methods*, *88*, 3–10.

Dempsey, G. T., Bates, M., Kowtoniuk, W. E., Liu, D. R., Tsien, R. Y., & Zhuang, X. (2009). Photoswitching mechanism of cyanine dyes. *Journal of the American Chemical Society*, *131*(51), 18192–18193.

Dempsey, G. T., Vaughan, J. C., Chen, K. H., Bates, M., & Zhuang, X. (2011). Evaluation of fluorophores for optimal performance in localization-based super-resolution imaging. *Nature methods*, *8*(12), 1027.

Deng, Y., Sun, M., Lin, P.-H., Ma, J., & Shaevitz, J. W. (2014). Spatial covariance reconstructive (score) super-resolution fluorescence microscopy. *PloS one*, *9*(4), e94807.

Denk, W., Strickler, J. H., & Webb, W. W. (1990). Two-photon laser scanning fluorescence microscopy. *Science*, *248*(4951), 73–76.

Dertinger, T., Colyer, R., Iyer, G., Weiss, S., & Enderlein, J. (2009). Fast, background-free, 3d super-resolution optical fluctuation imaging (sofi). *Proceedings of the National Academy of Sciences*, *106*(52), 22287–22292.

Deschamps, J., Mund, M., & Ries, J. (2014). 3d superresolution microscopy by supercritical angle detection. *Optics express*, *22*(23), 29081–29091.

Deschout, H. (2017). *Quantifying the Localization Precision of Single Fluorescent Emitters* [https://www.imaging-git.com/science/light-microscopy/quantifying-localization-precision-single-fluorescent-emitters [Last checked on Sep 23, 2019.]].

Deschout, H., Zanacchi, F. C., Mlodzianoski, M., Diaspro, A., Bewersdorf, J., Hess, S. T., & Braeckmans, K. (2014). Precisely and accurately localizing single emitters in fluorescence microscopy. *Nature methods*, *11*(3), 253.

Duim, W. C., Chen, B., Frydman, J., & Moerner, W. (2011). Sub-diffraction imaging of huntingtin protein aggregates by fluorescence blink-microscopy and atomic force microscopy. *ChemPhysChem*, *12*(13), 2387–2390.

Durisic, N., Cuervo, L. L., & Lakadamyali, M. (2014). Quantitative super-resolution microscopy: Pitfalls and strategies for image analysis. *Current opinion in chemical biology*, *20*, 22–28.

Dyba, M., & Hell, S. W. (2002). Focal spots of size $\lambda/23$ open up far-field florescence microscopy at 33 nm axial resolution. *Physical review letters*, *88*(16), 163901.

Einstein, A. (1917). Zur quantentheorie der strahlung. *Phys. Z.*, *18*, 121–128.

Erdélyi, M., Sinkó, J., Kákonyi, R., Kelemen, A., Rees, E., Varga, D., & Szabó, G. (2015). Origin and compensation of imaging artefacts in localization-based super-resolution microscopy. *Methods*, *88*, 122–132.

Flottmann, B., Gunkel, M., Lisauskas, T., Heilemann, M., Starkuviene, V., Reymann, J., & Erfle, H. (2013). Correlative light microscopy for high-content screening. *Biotechniques*, *55*(5), 243–252.

Fourier, J. (1822). *Théorie analytique de la chaleur*.

Fournier, C., Denis, L., & Fournel, T. (2010). On the single point resolution of on-axis digital holography. *JOSA A*, *27*(8), 1856–1862.

Frohn, J. T., Knapp, H. F., & Stemmer, A. (2000). True optical resolution beyond the rayleigh limit achieved by standing wave illumination. *Proceedings of the National Academy of Sciences*, *97*(13), 7232–7236.

Fu, Y., Winter, P. W., Rojas, R., Wang, V., McAuliffe, M., & Patterson, G. H. (2016). Axial superresolution via multiangle tirf microscopy with sequential imaging and photobleaching. *Proceedings of the National Academy of Sciences*, *113*(16), 4368–4373.

Gabor, D. (1948). A new microscopic principle.

Gao, L. (2015). Optimization of the excitation light sheet in selective plane illumination microscopy. *Biomedical optics express*, *6*(3), 881–890.

Gebhardt, J. C. M., Suter, D. M., Roy, R., Zhao, Z. W., Chapman, A. R., Basu, S., Maniatis, T., & Xie, X. S. (2013). Single-molecule imaging of transcription factor binding to dna in live mammalian cells. *Nature methods*, *10*(5), 421.

Gibson, S. F., & Lanni, F. (1992). Experimental test of an analytical model of aberration in an oil-immersion objective lens used in three-dimensional light microscopy. *JOSA A*, *9*(1), 154–166.

Goodman, J. W. (2005). *Introduction to fourier optics*. Roberts; Company Publishers.

Greengard, P., Valtorta, F., Czernik, A. J., & Benfenati, F. (1993). Synaptic vesicle phosphoproteins and regulation of synaptic function. *Science*, *259*(5096), 780–785.

Greiss, F., Deligiannaki, M., Jung, C., Gaul, U., & Braun, D. (2016). Single-molecule imaging in living drosophila embryos with reflected light-sheet microscopy. *Biophysical journal*, *110*(4), 939–946.

Grover, G., Mohrman, W., & Piestun, R. (2015). Real-time adaptive drift correction for super-resolution localization microscopy. *Optics express*, *23*(18), 23887–23898.

Gu, M., & Sheppard, C. (1995). Comparison of three-dimensional imaging properties between two-photon and single-photon fluorescence microscopy. *Journal of microscopy*, *177*(2), 128–137.

Gunewardene, M. S., Subach, F. V., Gould, T. J., Penoncello, G. P., Gudheti, M. V., Verkhusha, V. V., & Hess, S. T. (2011). Superresolution imaging of multiple fluorescent proteins with highly overlapping emission spectra in living cells. *Biophysical journal*, *101*(6), 1522–1528.

Gur, A., Zalevsky, Z., Micó, V., García, J., & Fixler, D. (2011). The limitations of nonlinear fluorescence effect in super resolution saturated structured illumination microscopy system. *Journal of fluorescence*, *21*(3), 1075–1082.

Gustafsson, M. G. (2000). Surpassing the lateral resolution limit by a factor of two using structured illumination microscopy. *Journal of microscopy*, *198*(2), 82–87.

Gustafsson, M. G. (2005). Nonlinear structured-illumination microscopy: Wide-field fluorescence imaging with theoretically unlimited resolution. *Proceedings of the National Academy of Sciences*, *102*(37), 13081–13086.

Gustafsson, M. G., Agard, D. A., & Sedat, J. W. (1995). Sevenfold improvement of axial resolution in 3d wide-field microscopy using two objective-lenses. *Three-Dimensional Microscopy: Image Acquisition and Processing II*, *2412*, 147–156.

Gustafsson, M. G., Agard, D. A., & Sedat, J. W. (1996). 3d widefield microscopy with two objective lenses: Experimental verification of improved axial resolution. *Three-Dimensional Microscopy: Image Acquisition and Processing III*, *2655*, 62–66.

Gustafsson, M. G., Agard, D. A., & Sedat, J. W. (1999). I5m: 3d widefield light microscopy with better than 100nm axial resolution. *Journal of microscopy*, *195*(1), 10–16.

Gustafsson, M. G., Shao, L., Carlton, P. M., Wang, C. R., Golubovskaya, I. N., Cande, W. Z., Agard, D. A., & Sedat, J. W. (2008). Three-dimensional resolution doubling in wide-field fluorescence microscopy by structured illumination. *Biophysical journal*, *94*(12), 4957–4970.

Gustavsson, A.-K., Petrov, P. N., Lee, M. Y., Shechtman, Y., & Moerner, W. (2018). 3d single-molecule super-resolution microscopy with a tilted light sheet. *Nature communications*, *9*(1), 123.

Hajj, B., El Beheiry, M., & Dahan, M. (2016). Psf engineering in multifocus microscopy for increased depth volumetric imaging. *Biomedical optics express*, *7*(3), 726–731.

Hajj, B., Wisniewski, J., El Beheiry, M., Chen, J., Revyakin, A., Wu, C., & Dahan, M. (2014). Whole-cell, multicolor superresolution imaging using volumetric multifocus microscopy. *Proceedings of the National Academy of Sciences*, *111*(49), 17480–17485.

Hansma, P., Drake, B., Marti, O., Gould, S., & Prater, C. (1989). The scanning ion-conductance microscope. *Science*, *243*(4891), 641–643.

Hariharan, P. (1996). *Optical holography: Principles, techniques and applications*. Cambridge University Press.

Hayazawa, N., Inouye, Y., Sekkat, Z., & Kawata, S. (2000). Metallized tip amplification of near-field raman scattering. *Optics Communications*, *183*(1-4), 333–336.

Hecht, E. (2017). *Optics*. Pearson Education.

Heim, R., & Tsien, R. Y. (1996). Engineering green fluorescent protein for improved brightness, longer wavelengths and fluorescence resonance energy transfer. *Current biology*, *6*(2), 178–182.

Heintzmann, R., & Cremer, C. G. (1999). Laterally modulated excitation microscopy: Improvement of resolution by using a diffraction grating. *Optical Biopsies and Microscopic Techniques III*, *3568*, 185–196.

Heintzmann, R., Jovin, T. M., & Cremer, C. (2002). Saturated patterned excitation microscopy—a concept for optical resolution improvement. *JOSA A*, *19*(8), 1599–1609.

Hell, S., Reiner, G., Cremer, C., & Stelzer, E. H. (1993). Aberrations in confocal fluorescence microscopy induced by mismatches in refractive index. *Journal of microscopy*, *169*(3), 391–405.

Hell, S., & Stelzer, E. H. (1992). Fundamental improvement of resolution with a 4pi-confocal fluorescence microscope using two-photon excitation. *Optics Communications*, *93*(5-6), 277–282.

Hell, S. W. (2003). Toward fluorescence nanoscopy. *Nature biotechnology*, *21*(11), 1347.

Hell, S. W. (2007). Far-field optical nanoscopy. *Science*, *316*(5828), 1153–1158.

Hell, S. W., & Kroug, M. (1995). Ground-state-depletion fluorscence microscopy: A concept for breaking the diffraction resolution limit. *Applied Physics B*, *60*(5), 495–497.

Hell, S. W., Schmidt, R., & Egner, A. (2009). Diffraction-unlimited three-dimensional optical nanoscopy with opposing lenses. *Nature Photonics*, *3*(7), 381.

Hell, S. W., & Wichmann, J. (1994). Breaking the diffraction resolution limit by stimulated emission: Stimulated-emission-depletion fluorescence microscopy. *Optics letters*, *19*(11), 780–782.

Henriques, R., Lelek, M., Fornasiero, E. F., Valtorta, F., Zimmer, C., & Mhlanga, M. M. (2010). Quickpalm: 3d real-time photoactivation nanoscopy image processing in imagej. *Nature methods*, *7*(5), 339.

Herschel, J. W. (1828). *Treatises on physical astronomy, light and sound contributed to the encyclopaedia metropolitana*. R. Griffin.

Herschel, J. W. (1845). On a case of superficial colour presented by a homogeneous liquid internally colourless. *Philosophical Transactions of the Royal Society of London*, (135), 143–145.

Hess, S. T., Girirajan, T. P., & Mason, M. D. (2006). Ultra-high resolution imaging by fluorescence photoactivation localization microscopy. *Biophysical journal*, *91*(11), 4258–4272.

Hiraoka, Y., Sedat, J. W., & Agard, D. A. (1990). Determination of three-dimensional imaging properties of a light microscope system. partial confocal behavior in epifluorescence microscopy. *Biophysical journal*, *57*(2), 325–333.

Hofmann, M., Eggeling, C., Jakobs, S., & Hell, S. W. (2005). Breaking the diffraction barrier in fluorescence microscopy at low light intensities by using reversibly photoswitchable proteins. *Proceedings of the National Academy of Sciences*, *102*(49), 17565–17569.

Holden, S. J., Uphoff, S., & Kapanidis, A. N. (2011). Daostorm: An algorithm for high-density super-resolution microscopy. *Nature methods*, *8*(4), 279.

Holtzer, L., Meckel, T., & Schmidt, T. (2007). Nanometric three-dimensional tracking of individual quantum dots in cells. *Applied Physics Letters*, *90*(5), 053902.

Hooke, R. (1665). *Micrographia: Or, some physiological descriptions of minute bodies made by magnifying glasses, with observations and inquiries thereupon*. London: Martyn; Allestry.

Hu, Y. S., Nan, X., Sengupta, P., Lippincott-Schwartz, J., & Cang, H. (2013). Accelerating 3b single-molecule super-resolution microscopy with cloud computing. *Nature methods*, *10*(2), 96.

Hu, Y. S., Zimmerley, M., Li, Y., Watters, R., & Cang, H. (2014). Single-molecule super-resolution light-sheet microscopy. *ChemPhysChem*, *15*(4), 577–586.

Huang, B., Babcock, H., & Zhuang, X. (2010). Breaking the diffraction barrier: Super-resolution imaging of cells. *Cell*, *143*(7), 1047–1058.

Huang, B., Bates, M., & Zhuang, X. (2009). Super-resolution fluorescence microscopy. *Annual review of biochemistry*, *78*, 993–1016.

Huang, B., Wang, W., Bates, M., & Zhuang, X. (2008). Three-dimensional super-resolution imaging by stochastic optical reconstruction microscopy. *Science*, *319*(5864), 810–813.

Huang, F., Hartwich, T. M., Rivera-Molina, F. E., Lin, Y., Duim, W. C., Long, J. J., Uchil, P. D., Myers, J. R., Baird, M. A., Mothes, W., et al. (2013). Video-rate nanoscopy using scmos camera–specific single-molecule localization algorithms. *Nature methods*, *10*(7), 653.

Huang, F., Schwartz, S. L., Byars, J. M., & Lidke, K. A. (2011). Simultaneous multiple-emitter fitting for single molecule super-resolution imaging. *Biomedical optics express*, *2*(5), 1377–1393.

Huang, F., Sirinakis, G., Allgeyer, E. S., Schroeder, L. K., Duim, W. C., Kromann, E. B., Phan, T., Rivera-Molina, F. E., Myers, J. R., Irnov, I., et al. (2016). Ultra-high resolution 3d imaging of whole cells. *Cell*, *166*(4), 1028–1040.

Huisken, J., Swoger, J., Del Bene, F., Wittbrodt, J., & Stelzer, E. H. (2004). Optical sectioning deep inside live embryos by selective plane illumination microscopy. *Science*, *305*(5686), 1007–1009.

Imbe, M. (2018). Optical configuration with fixed transverse magnification for self-interference incoherent digital holography. *Applied optics*, *57*(9), 2268–2276.

Izeddin, I., Boulanger, J., Racine, V., Specht, C., Kechkar, A., Nair, D., Triller, A., Choquet, D., Dahan, M., & Sibarita, J. (2012). Wavelet analysis for single molecule localization microscopy. *Optics express*, *20*(3), 2081–2095.

Izeddin, I., El Beheiry, M., Andilla, J., Ciepielewski, D., Darzacq, X., & Dahan, M. (2012). Psf shaping using adaptive optics for three-dimensional single-molecule super-resolution imaging and tracking. *Optics express*, *20*(5), 4957–4967.

Jabłoński, A. (1935). Über den mechanismus der photolumineszenz von farbstoffphosphoren. *Zeitschrift für Physik*, *94*(1-2), 38–46.

Jackson, J. D. (2007). *Classical electrodynamics*. John Wiley & Sons.

Jia, S., Vaughan, J. C., & Zhuang, X. (2014). Isotropic three-dimensional super-resolution imaging with a self-bending point spread function. *Nature photonics*, *8*(4), 302.

Jimenez, A., Friedl, K., & Leterrier, C. (2019). About samples, giving examples: Optimized single molecule localization microscopy. *bioRxiv*, 568295.

Jones, S. A., Shim, S.-H., He, J., & Zhuang, X. (2011). Fast, three-dimensional super-resolution imaging of live cells. *Nature methods*, *8*(6), 499.

Juette, M. F., Gould, T. J., Lessard, M. D., Mlodzianoski, M. J., Nagpure, B. S., Bennett, B. T., Hess, S. T., & Bewersdorf, J. (2008). Three-dimensional sub–100 nm resolution fluorescence microscopy of thick samples. *Nature methods*, *5*(6), 527–529.

Kao, H. P., & Verkman, A. (1994). Tracking of single fluorescent particles in three dimensions: Use of cylindrical optics to encode particle position. *Biophysical journal*, *67*(3), 1291–1300.

Katz, B., Rosen, J., Kelner, R., & Brooker, G. (2012). Enhanced resolution and throughput of fresnel incoherent correlation holography (finch) using dual diffractive lenses on a spatial light modulator (slm). *Optics express*, *20*(8), 9109–9121.

Kay, S. M. (1993). *Fundamentals of statistical signal processing*. Prentice Hall PTR.

Keppler, A., Gendreizig, S., Gronemeyer, T., Pick, H., Vogel, H., & Johnsson, K. (2003). A general method for the covalent labeling of fusion proteins with small molecules in vivo. *Nature biotechnology*, *21*(1), 86–89.

Kim, M. K. (2010). Principles and techniques of digital holographic microscopy. *SPIE reviews*, *1*(1), 018005.

Kim, M. K. (2011). Digital holographic microscopy. *Digital holographic microscopy* (pp. 149–190). Springer.

Kim, M. K. (2012a). Adaptive optics by incoherent digital holography. *Optics letters*, *37*(13), 2694–2696.

Kim, M. K. (2012b). Adaptive optics by incoherent digital holography. *Optics Letters*, *37*(13), 2694–2696. https://doi.org/10.1364/OL.37.002694

Kim, M. K. (2013). Full color natural light holographic camera. *Optics Express*, *21*(8), 9636–9642.

Kirchhoff, G. (1883). Zur theorie der lichtstrahlen. *Annalen der Physik*, *254*(4), 663–695.

Kirz, J., Jacobsen, C., & Howells, M. (1995). Soft x-ray microscopes and their biological applications. *Quarterly reviews of biophysics*, *28*(1), 33–130.

Klar, T. A., & Hell, S. W. (1999). Subdiffraction resolution in far-field fluorescence microscopy. *Optics letters*, *24*(14), 954–956.

Klar, T. A., Jakobs, S., Dyba, M., Egner, A., & Hell, S. W. (2000). Fluorescence microscopy with diffraction resolution barrier broken by stimulated emission. *Proceedings of the National Academy of Sciences*, *97*(15), 8206–8210.

Kopfermann, H., & Ladenburg, R. (1928). Experimental proof of 'negative dispersion.' *Nature*, *122*(3073), 438.

Köthe, U., Herrmannsdörfer, F., Kats, I., & Hamprecht, F. A. (2014). Simplestorm: A fast, self-calibrating reconstruction algorithm for localization microscopy. *Histochemistry and cell biology*, *141*(6), 613–627.

Křížek, P., Raška, I., & Hagen, G. M. (2011). Minimizing detection errors in single molecule localization microscopy. *Optics express*, *19*(4), 3226–3235.

Lagrue, K. (2014). *The power of STED microscopy, Part 1: How does it work?* [https://bitesizebio.com/21988/the-power-of-sted-microscopy-part-1-how-does-it-work/ [Last checked on Sep 24, 2019.]].

Laine, R. F., Tosheva, K. L., Gustafsson, N., Gray, R. D., Almada, P., Albrecht, D., Risa, G. T., Hurtig, F., Lindås, A.-C., Baum, B., et al. (2019). Nanoj: A high-performance open-source super-resolution microscopy toolbox. *Journal of Physics D: Applied Physics*, *52*(16), 163001.

Legant, W. R., Shao, L., Grimm, J. B., Brown, T. A., Milkie, D. E., Avants, B. B., Lavis, L. D., & Betzig, E. (2016). High-density three-dimensional localization microscopy across large volumes. *Nature methods*, *13*(4), 359.

Leith, E. N., & Upatnieks, J. (1962). Reconstructed wavefronts and communication theory. *JOSA*, *52*(10), 1123–1130.

Leith, E. N., & Upatnieks, J. (1963). Wavefront reconstruction with continuous-tone objects. *JOSA*, *53*(12), 1377–1381.

Leith, E. N., & Upatnieks, J. (1964). Wavefront reconstruction with diffused illumination and three-dimensional objects. *Josa*, *54*(11), 1295–1301.

Lew, M. D., Backlund, M. P., & Moerner, W. (2013). Rotational mobility of single molecules affects localization accuracy in super-resolution fluorescence microscopy. *Nano letters*, *13*(9), 3967–3972.

Lew, M. D., Lee, S. F., Badieirostami, M., & Moerner, W. (2011). Corkscrew point spread function for far-field three-dimensional nanoscale localization of pointlike objects. *Optics letters*, *36*(2), 202–204.

Lew, M. D., Lee, S. F., Thompson, M. A., Hsiao-lu, D. L., & Moerner, W. (2012). Single-molecule photocontrol and nanoscopy. *Far-field optical nanoscopy* (pp. 87–110). Springer.

Lew, M. D., & Moerner, W. (2014). Azimuthal polarization filtering for accurate, precise, and robust single-molecule localization microscopy. *Nano letters*, *14*(11), 6407–6413.

Lewis, A., Isaacson, M., Harootunian, A., & Muray, A. (1984). Development of a 500 Å spatial resolution light microscope: I. light is efficiently transmitted through $\lambda/16$ diameter apertures. *Ultramicroscopy*, *13*(3), 227–231.

Li, D., Shao, L., Chen, B.-C., Zhang, X., Zhang, M., Moses, B., Milkie, D. E., Beach, J. R., Hammer, J. A., Pasham, M., Kirchhausen, T., Baird, M. A., Davidson, M. W., Xu, P., & Betzig, E. (2015). Extended-resolution structured illumination imaging of endocytic and cytoskeletal dynamics. *Science*, *349*(6251), aab3500.

Liang, D., Zhang, Q., Wang, J., & Liu, J. (2020). Single-shot fresnel incoherent digital holography based on geometric phase lens. *Journal of Modern Optics*, *67*(2), 92–98.

Liu, J.-P., Tahara, T., Hayasaki, Y., & Poon, T.-C. (2018). Incoherent digital holography: A review. *Applied Sciences*, *8*(1), 143.

Liu, S., Kromann, E. B., Krueger, W. D., Bewersdorf, J., & Lidke, K. A. (2013). Three dimensional single molecule localization using a phase retrieved pupil function. *Optics express*, *21*(24), 29462–29487.

Liu, S., Mlodzianoski, M. J., Hu, Z., Ren, Y., McElmurry, K., Suter, D. M., & Huang, F. (2017). Scmos noise-correction algorithm for microscopy images. *Nature methods*, *14*(8), 760.

Liu, Z., Lee, H., Xiong, Y., Sun, C., & Zhang, X. (2007). Far-field optical hyperlens magnifying sub-diffraction-limited objects. *science*, *315*(5819), 1686–1686.

Löschberger, A., van de Linde, S., Dabauvalle, M.-C., Rieger, B., Heilemann, M., Krohne, G., & Sauer, M. (2012). Super-resolution imaging visualizes the eightfold symmetry of gp210 proteins

around the nuclear pore complex and resolves the central channel with nanometer resolution. *Journal of cell science*, *125*(3), 570–575.

Ma, H., Xu, J., Jin, J., Huang, Y., & Liu, Y. (2017). A simple marker-assisted 3d nanometer drift correction method for superresolution microscopy. *Biophysical journal*, *112*(10), 2196–2208.

Maiman, T. H. (1960). Stimulated optical radiation in ruby. *Nature*, *187*(4736), 493–494.

Maiman, T. H., Hoskins, R., d'Haenens, I., Asawa, C. K., & Evtuhov, V. (1961). Stimulated optical emission in fluorescent solids. ii. spectroscopy and stimulated emission in ruby. *Physical Review*, *123*(4), 1151.

Man, T., Wan, Y., Yan, W., Wang, X.-H., Peterman, E. J., & Wang, D. (2018). Adaptive optics via self-interference digital holography for non-scanning three-dimensional imaging in biological samples. *Biomedical optics express*, *9*(6), 2614–2626.

Manzo, C., & Garcia-Parajo, M. F. (2015). A review of progress in single particle tracking: From methods to biophysical insights. *Reports on progress in physics*, *78*(12), 124601.

Marar, A., & Kner, P. (2019). Three-dimensional localization microscopy by incoherent holography. *Single Molecule Spectroscopy and Superresolution Imaging XII*, *10884*, 108840I.

Marar, A., & Kner, P. (2020a). Self-interference digital holography (SIDH) for far-field three-dimensional nanoscale localization of fluorescent nanoparticles. *Single Molecule Spectroscopy and Superresolution Imaging XIII*, *11246*, 112460M.

Marar, A., & Kner, P. (2020b). Three-dimensional nanoscale localization of point-like objects using self-interference digital holography. *Optics letters*, *45*(2), 591–594.

Marathay, A. S., & McCalmont, J. F. (2004). On the usual approximation used in the rayleigh–sommerfeld diffraction theory. *JOSA A*, *21*(4), 510–516.

Marsh, R. J., Pfisterer, K., Bennett, P., Hirvonen, L. M., Gautel, M., Jones, G. E., & Cox, S. (2018). Artifact-free high-density localization microscopy analysis. *Nature methods*, *15*(9), 689.

Marvin, M. (1961). Microscopy apparatus [US Patent 3,013,467].

Maxwell, J. C. (1861). On physical lines of force. *The London, Edinburgh, and Dublin Philosophical Magazine and Journal of Science*, *21*(141), 338–348.

McGorty, R., Kamiyama, D., & Huang, B. (2013). Active microscope stabilization in three dimensions using image correlation. *Optical nanoscopy*, *2*(1), 3.

Meddens, M. B., Liu, S., Finnegan, P. S., Edwards, T. L., James, C. D., & Lidke, K. A. (2016). Single objective light-sheet microscopy for high-speed whole-cell 3d super-resolution. *Biomedical optics express*, *7*(6), 2219–2236.

Merkle, F., Kern, P., Léna, P., Rigaut, F., Fontanella, J., Rousset, G., Boyer, C., Gaffard, J., & Jagourel, P. (1989). Successful tests of adaptive optics. *The Messenger*, *58*, 1–4.

Mertz, J. (2019). *Introduction to optical microscopy*. Cambridge University Press.

Miao, J., Ishikawa, T., Shen, Q., & Earnest, T. (2008). Extending x-ray crystallography to allow the imaging of noncrystalline materials, cells, and single protein complexes. *Annu. Rev. Phys. Chem.*, *59*, 387–410.

Middendorff, C. v., Egner, A., Geisler, C., Hell, S., & Schönle, A. (2008). Isotropic 3d nanoscopy based on single emitter switching. *Optics express*, *16*(25), 20774–20788.

Mlodzianoski, M. J., Cheng-Hathaway, P. J., Bemiller, S. M., McCray, T. J., Liu, S., Miller, D. A., Lamb, B. T., Landreth, G. E., & Huang, F. (2018). Active psf shaping and adaptive optics enable volumetric localization microscopy through brain sections. *Nature methods*, *15*(8), 583.

Mlodzianoski, M. J., Juette, M. F., Beane, G. L., & Bewersdorf, J. (2009). Experimental characterization of 3d localization techniques for particle-tracking and super-resolution microscopy. *Optics express*, *17*(10), 8264–8277.

Mlodzianoski, M. J., Schreiner, J. M., Callahan, S. P., Smolková, K., Dlasková, A., Šantorová, J., Ježek, P., & Bewersdorf, J. (2011). Sample drift correction in 3d fluorescence photoactivation localization microscopy. *Optics express*, *19*(16), 15009–15019.

Moerner, W., & Basche, T. (1993). Optical spectroscopy of single impurity molecules in solids. *Angewandte Chemie International Edition in English*, *32*(4), 457–476.

Moerner, W. E., & Kador, L. (1989). Optical detection and spectroscopy of single molecules in a solid. *Physical review letters*, *62*(21), 2535.

Mortensen, K. I., Churchman, L. S., Spudich, J. A., & Flyvbjerg, H. (2010). Optimized localization analysis for single-molecule tracking and super-resolution microscopy. *Nature methods*, *7*(5), 377.

Mukamel, E. A., Babcock, H., & Zhuang, X. (2012). Statistical deconvolution for superresolution fluorescence microscopy. *Biophysical journal*, *102*(10), 2391–2400.

Müller, D. J., Helenius, J., Alsteens, D., & Dufrêne, Y. F. (2009). Force probing surfaces of living cells to molecular resolution. *Nature chemical biology*, *5*(6), 383.

Nazarathy, M., & Shamir, J. (1980). Fourier optics described by operator algebra. *JOSA*, *70*(2), 150–159.

Neil, M., Juškaitis, R., & Wilson, T. (1998). Real time 3d fluorescence microscopy by two beam interference illumination. *Optics communications*, *153*(1-3), 1–4.

Neil, M. A., Juškaitis, R., & Wilson, T. (1997). Method of obtaining optical sectioning by using structured light in a conventional microscope. *Optics letters*, *22*(24), 1905–1907.

Niekamp, S., Stuurman, N., & Vale, R. D. (2020). A 6-nm ultra-photostable dna fluorocube for fluorescence imaging. *Nature Methods*, *17*(4), 437–441.

Nieuwenhuizen, R. P., Lidke, K. A., Bates, M., Puig, D. L., Grünwald, D., Stallinga, S., & Rieger, B. (2013). Measuring image resolution in optical nanoscopy. *Nature methods*, *10*(6), 557.

Nobukawa, T., Muroi, T., Katano, Y., Kinoshita, N., & Ishii, N. (2018). Single-shot phase-shifting incoherent digital holography with multiplexed checkerboard phase gratings. *Optics letters*, *43*(8), 1698–1701.

Nyquist, H. (1928). Certain topics in telegraph transmission theory. *Transactions of the American Institute of Electrical Engineers*, *47*(2), 617–644.

Ober, R. J., Ram, S., & Ward, E. S. (2004a). Localization accuracy in single-molecule microscopy. *Biophysical Journal*, *86*(2), 1185–1200. https://doi.org/http://dx.doi.org/10.1016/S0006-3495(04)74193-4

Ober, R. J., Ram, S., & Ward, E. S. (2004b). Localization accuracy in single-molecule microscopy. *Biophysical journal*, *86*(2), 1185–1200.

Oster, G., & Nishijima, Y. (1963). Moiré patterns. *Scientific American*, *208*(5), 54–63.

Oudjedi, L., Fiche, J.-B., Abrahamsson, S., Mazenq, L., Lecestre, A., Calmon, P.-F., Cerf, A., & Nöllmann, M. (2016). Astigmatic multifocus microscopy enables deep 3d super-resolved imaging. *Biomedical optics express*, *7*(6), 2163–2173.

Ovesný, M. (2016). Computational methods in single molecule localization microscopy.

Ovesný, M., Křížek, P., Borkovec, J., Švindrych, Z., & Hagen, G. M. (2014). Thunderstorm: A comprehensive imagej plug-in for palm and storm data analysis and super-resolution imaging. *Bioinformatics*, *30*(16), 2389–2390.

Parthasarathy, R. (2012). Rapid, accurate particle tracking by calculation of radial symmetry centers. *Nature methods*, *9*(7), 724.

Pavani, S. R. P., Thompson, M. A., Biteen, J. S., Lord, S. J., Liu, N., Twieg, R. J., Piestun, R., & Moerner, W. (2009). Three-dimensional, single-molecule fluorescence imaging beyond the diffraction limit by using a double-helix point spread function. *Proceedings of the National Academy of Sciences*, *106*(9), 2995–2999.

Pawley, J. (2010). *Handbook of biological confocal microscopy*. Springer Science & Business Media.

Peatross, J., & Ware, M. (2011). *Physics of light and optics*. Brigham Young University, Department of Physics.

Pendry, J. B. (2000). Negative refraction makes a perfect lens. *Physical review letters*, *85*(18), 3966.

Ploem, J. (1967). The use of a vertical illuminator with interchangeable dichroic mirrors for fluorescence microscopy with incidental light. *Zeitschrift fur wissenschaftliche Mikroskopie und mikroskopische Technik*, *68*(3), 129–142.

Pohl, D. W., Denk, W., & Lanz, M. (1984). Optical stethoscopy: Image recording with resolution $\lambda/20$. *Applied physics letters*, *44*(7), 651–653.

Poon, T.-C., & Indebetouw, G. (2003). Three-dimensional point spread functions of an optical heterodyne scanning image processor. *Applied optics*, *42*(8), 1485–1492.

Prabhat, P., Ram, S., Ward, E. S., & Ober, R. J. (2006). Simultaneous imaging of several focal planes in fluorescence microscopy for the study of cellular dynamics in 3d. *Three-Dimensional and Multidimensional Microscopy: Image Acquisition and Processing XIII*, *6090*, 60900L.

Quan, X., Matoba, O., & Awatsuji, Y. (2017). Single-shot incoherent digital holography using a dual-focusing lens with diffraction gratings. *Optics Letters*, *42*(3), 383–386.

Ram, S., Prabhat, P., Chao, J., Ward, E. S., & Ober, R. J. (2008). High accuracy 3d quantum dot tracking with multifocal plane microscopy for the study of fast intracellular dynamics in live cells. *Biophysical journal*, *95*(12), 6025–6043.

Ram, S., Prabhat, P., Ward, E. S., & Ober, R. J. (2009). Improved single particle localization accuracy with dual objective multifocal plane microscopy. *Optics express*, *17*(8), 6881–6898.

Ram, S., Ward, E. S., & Ober, R. J. (2006). A stochastic analysis of performance limits for optical microscopes. *Multidimensional Systems and Signal Processing*, *17*(1), 27–57.

Rao, C. R. (1973). *Linear statistical inference and its applications* (Vol. 2). Wiley New York.

Rayleigh, J. (1896). On the theory of optical images, with special reference to the microscope. *Phil. Mag*, *42*, 167–195.

Rees, E. J., Erdelyi, M., Schierle, G. S. K., Knight, A., & Kaminski, C. F. (2013). Elements of image processing in localization microscopy. *Journal of Optics*, *15*(9), 094012.

Rego, E. H., Shao, L., Macklin, J. J., Winoto, L., Johansson, G. A., Kamps-Hughes, N., Davidson, M. W., & Gustafsson, M. G. (2012). Nonlinear structured-illumination microscopy with a photoswitchable protein reveals cellular structures at 50-nm resolution. *Proceedings of the National Academy of Sciences*, *109*(3), E135–E143.

Richards, B., & Wolf, E. (1959). Electromagnetic diffraction in optical systems, ii. structure of the image field in an aplanatic system. *Proceedings of the Royal Society of London. Series A. Mathematical and Physical Sciences*, *253*(1274), 358–379.

Rieger, B., Nieuwenhuizen, R., & Stallinga, S. (2014). Image processing and analysis for single-molecule localization microscopy: Computation for nanoscale imaging. *IEEE Signal Processing Magazine*, *32*(1), 49–57.

Rieger, B., & Stallinga, S. (2014). The lateral and axial localization uncertainty in super-resolution light microscopy. *ChemPhysChem*, *15*(4), 664–670.

Rivenson, Y., Stern, A., & Rosen, J. (2011). Compressive multiple view projection incoherent holography. *Optics express*, *19*(7), 6109–6118.

Rivenson, Y., Zhang, Y., Günaydın, H., Teng, D., & Ozcan, A. (2018). Phase recovery and holographic image reconstruction using deep learning in neural networks. *Light: Science & Applications*, *7*(2), 17141–17141.

Rogers, G. L. (1952). Xiv.—experiments in diffraction microscopy. *Proceedings of the Royal Society of Edinburgh Section A: Mathematics*, *63*(3), 193–221.

Rosen, J., & Brooker, G. (2007). Digital spatially incoherent fresnel holography. *Optics letters*, *32*(8), 912–914.

Rosen, J., Brooker, G., Indebetouw, G., & Shaked, N. T. (2009). A review of incoherent digital fresnel holography. *Journal of Holography and speckle*, *5*(2), 124–140.

Rosen, J., Vijayakumar, A., Kumar, M., Rai, M. R., Kelner, R., Kashter, Y., Bulbul, A., & Mukherjee, S. (2019). Recent advances in self-interference incoherent digital holography. *Advances in Optics and Photonics*, *11*(1), 1–66.

Rousset, G., Fontanella, J., Kern, P., Gigan, P., & Rigaut, F. (1990). First diffraction-limited astronomical images with adaptive optics. *Astronomy and Astrophysics*, *230*, L29–L32.

Ruska, E. (1934). Über fortschritte im bau und in der leistung des magnetischen elektronenmikroskops. *Zeitschrift für Physik A Hadrons and Nuclei*, *87*(9), 580–602.

Ruska, E. (1987). The development of the electron microscope and of electron microscopy (nobel lecture). *Angewandte Chemie International Edition in English*, *26*(7), 595–605.

Rust, M. J., Bates, M., & Zhuang, X. (2006). Sub-diffraction-limit imaging by stochastic optical reconstruction microscopy (storm). *Nature methods*, *3*(10), 793.

Sage, D., Pham, T.-A., Babcock, H., Lukes, T., Pengo, T., Chao, J., Velmurugan, R., Herbert, A., Agrawal, A., Colabrese, S., Wheeler, A., Archetti, A., Rieger, B., Ober, R., Hagen, G. M., Sibarita, J.-B., Ries, J., Henriques, R., Unser, M., & Holden, S. (2019). Super-resolution fight club: Assessment of 2d and 3d single-molecule localization microscopy software. *Nature Methods*, *16*(5), 387–395.

Sakamaki, S., Yoneda, N., & Nomura, T. (2020). Single-shot in-line fresnel incoherent holography using a dual-focus checkerboard lens. *Applied Optics*, *59*(22), 6612–6618.

Sako, Y., Minoghchi, S., & Yanagida, T. (2000). Single-molecule imaging of egfr signalling on the surface of living cells. *Nature cell biology*, *2*(3), 168.

Saleh, B. E., & Teich, M. C. (2019). *Fundamentals of photonics*. John Wiley & Sons.

Sauer, M., & Heilemann, M. (2017). Single-molecule localization microscopy in eukaryotes. *Chemical reviews*, *117*(11), 7478–7509.

Schawlow, A. L., & Townes, C. H. (1958). Infrared and optical masers. *Physical Review*, *112*(6), 1940.

Schermelleh, L., Carlton, P. M., Haase, S., Shao, L., Winoto, L., Kner, P., Burke, B., Cardoso, M. C., Agard, D. A., Gustafsson, M. G., et al. (2008). Subdiffraction multicolor imaging of the nuclear periphery with 3d structured illumination microscopy. *Science*, *320*(5881), 1332–1336.

Schilling, B. W., Poon, T.-C., Indebetouw, G., Storrie, B., Shinoda, K., Suzuki, Y., & Wu, M. H. (1997). Three-dimensional holographic fluorescence microscopy. *Optics Letters*, *22*(19), 1506–1508.

Schmidt, N. C., Kahms, M., Hüve, J., & Klingauf, J. (2018). Intrinsic refractive index matched 3d dstorm with two objectives: Comparison of detection techniques. *Scientific reports*, *8*(1), 1–12.

Schmidt, T., Schütz, G., Baumgartner, W., Gruber, H., & Schindler, H. (1996). Imaging of single molecule diffusion. *Proceedings of the National Academy of Sciences*, *93*(7), 2926–2929.

Scott, D. W. (1985). Averaged shifted histograms: Effective nonparametric density estimators in several dimensions. *The Annals of Statistics*, 1024–1040.

Shaked, N. T., Katz, B., & Rosen, J. (2009). Review of three-dimensional holographic imaging by multiple-viewpoint-projection based methods. *Appl. Opt.*, *48*(34), H120–H136.

Shannon, C. E. (1949). Communication in the presence of noise. *Proceedings of the IRE*, *37*(1), 10–21.

Shao, L., Isaac, B., Uzawa, S., Agard, D. A., Sedat, J. W., & Gustafsson, M. G. (2008). I5s: Wide-field light microscopy with 100-nm-scale resolution in three dimensions. *Biophysical journal*, *94*(12), 4971–4983.

Sharonov, A., & Hochstrasser, R. M. (2006). Wide-field subdiffraction imaging by accumulated binding of diffusing probes. *Proceedings of the National Academy of Sciences*, *103*(50), 18911–18916.

Shashkova, S., & Leake, M. C. (2017). Single-molecule fluorescence microscopy review: Shedding new light on old problems. *Bioscience reports*, *37*(4), BSR20170031.

Shechtman, Y., Sahl, S. J., Backer, A. S., & Moerner, W. (2014). Optimal point spread function design for 3d imaging. *Physical review letters*, *113*(13), 133902.

Shechtman, Y., Weiss, L. E., Backer, A. S., Lee, M. Y., & Moerner, W. (2016). Multicolour localization microscopy by point-spread-function engineering. *Nature photonics*, *10*(9), 590–594.

Shechtman, Y., Weiss, L. E., Backer, A. S., Sahl, S. J., & Moerner, W. (2015). Precise three-dimensional scan-free multiple-particle tracking over large axial ranges with tetrapod point spread functions. *Nano letters*, *15*(6), 4194–4199.

Shim, S.-H., Xia, C., Zhong, G., Babcock, H. P., Vaughan, J. C., Huang, B., Wang, X., Xu, C., Bi, G.-Q., & Zhuang, X. (2012). Super-resolution fluorescence imaging of organelles in live cells with photoswitchable membrane probes. *Proceedings of the National Academy of Sciences*, *109*(35), 13978–13983.

Shimomura, O., Johnson, F. H., & Saiga, Y. (1962). Extraction, purification and properties of aequorin, a bioluminescent protein from the luminous hydromedusan, aequorea. *Journal of cellular and comparative physiology*, *59*(3), 223–239.

Shroff, H., Galbraith, C. G., Galbraith, J. A., & Betzig, E. (2008). Live-cell photoactivated localization microscopy of nanoscale adhesion dynamics. *Nature methods*, *5*(5), 417.

Shroff, H., Galbraith, C. G., Galbraith, J. A., White, H., Gillette, J., Olenych, S., Davidson, M. W., & Betzig, E. (2007). Dual-color superresolution imaging of genetically expressed probes within individual adhesion complexes. *Proceedings of the National Academy of Sciences*, *104*(51), 20308–20313.

Shtengel, G., Galbraith, J. A., Galbraith, C. G., Lippincott-Schwartz, J., Gillette, J. M., Manley, S., Sougrat, R., Waterman, C. M., Kanchanawong, P., Davidson, M. W., et al. (2009). Interferometric fluorescent super-resolution microscopy resolves 3d cellular ultrastructure. *Proceedings of the National Academy of Sciences*, *106*(9), 3125–3130.

Siedentopf, H., & Zsigmondy, R. (1902). Uber sichtbarmachung und größenbestimmung ultramikoskopischer teilchen, mit besonderer anwendung auf goldrubingläser. *Annalen der Physik*, *315*(1), 1–39.

Siegel, N., Rosen, J., & Brooker, G. (2012). Reconstruction of objects above and below the objective focal plane with dimensional fidelity by finch fluorescence microscopy. *Optics express*, *20*(18), 19822–19835.

Sims, R. R., Abdul Rehman, S., Lenz, M. O., Clark, A., Sanders, E. W., Ponjavic, A., Muresan, L., Lee, S. F., & O'Holleran, K. (2020). Single molecule light field microscopy. *bioRxiv*.

Small, A., & Stahlheber, S. (2014). Fluorophore localization algorithms for super-resolution microscopy. *Nature methods*, *11*(3), 267.

Small, A. R., & Parthasarathy, R. (2014). Superresolution localization methods. *Annual review of physical chemistry*, *65*, 107–125.

Smith, C. S., Joseph, N., Rieger, B., & Lidke, K. A. (2010). Fast, single-molecule localization that achieves theoretically minimum uncertainty. *Nature methods*, *7*(5), 373.

Stallinga, S., & Rieger, B. (2012). Position and orientation estimation of fixed dipole emitters using an effective hermite point spread function model. *Optics express*, *20*(6), 5896–5921.

Stephenson, J. (1877). Observations on professor abbe's experiments illustrating his theory of microscopic vision. *The Monthly Microscopical Journal*, *17*(2), 82–88.

Stöckle, R. M., Suh, Y. D., Deckert, V., & Zenobi, R. (2000). Nanoscale chemical analysis by tip-enhanced raman spectroscopy. *Chemical Physics Letters*, *318*(1-3), 131–136.

Stokes, G. G. (1852). On the change of refrangibility of light. *Philosophical transactions of the Royal Society of London*, (142), 463–562.

Subach, F. V., Patterson, G. H., Manley, S., Gillette, J. M., Lippincott-Schwartz, J., & Verkhusha, V. V. (2009). Photoactivatable mcherry for high-resolution two-color fluorescence microscopy. *Nature methods*, *6*(2), 153.

Synge, E. (1928). Xxxviii. a suggested method for extending microscopic resolution into the ultra-microscopic region. *The London, Edinburgh, and Dublin Philosophical Magazine and Journal of Science*, *6*(35), 356–362.

Tafteh, R., Abraham, L., Seo, D., Lu, H. Y., Gold, M. R., & Chou, K. C. (2016). Real-time 3d stabilization of a super-resolution microscope using an electrically tunable lens. *Optics express*, *24*(20), 22959–22970.

Tehrani, K. F., Xu, J., Zhang, Y., Shen, P., & Kner, P. (2015). Adaptive optics stochastic optical reconstruction microscopy (ao-storm) using a genetic algorithm. *Optics express*, *23*(10), 13677–13692.

Tehrani, K. F., Zhang, Y., Shen, P., & Kner, P. (2017). Adaptive optics stochastic optical reconstruction microscopy (ao-storm) by particle swarm optimization. *Biomedical optics express*, *8*(11), 5087–5097.

Testa, I., Wurm, C. A., Medda, R., Rothermel, E., Von Middendorf, C., Fölling, J., Jakobs, S., Schönle, A., Hell, S. W., & Eggeling, C. (2010). Multicolor fluorescence nanoscopy in fixed and living cells by exciting conventional fluorophores with a single wavelength. *Biophysical journal*, *99*(8), 2686–2694.

Thompson, M. A., Lew, M. D., Badieirostami, M., & Moerner, W. (2010). Localizing and tracking single nanoscale emitters in three dimensions with high spatiotemporal resolution using a double-helix point spread function. *Nano letters*, *10*(1), 211–218.

Thompson, M. A., Lew, M. D., & Moerner, W. (2012). Extending microscopic resolution with single-molecule imaging and active control. *Annual review of biophysics*, *41*, 321–342.

Thompson, R. E., Larson, D. R., & Webb, W. W. (2002). Precise nanometer localization analysis for individual fluorescent probes. *Biophysical journal*, *82*(5), 2775–2783.

Tokunaga, M., Imamoto, N., & Sakata-Sogawa, K. (2008). Highly inclined thin illumination enables clear single-molecule imaging in cells. *Nature methods*, *5*(2), 159.

Tsien, R. Y. (1998). The green fluorescent protein. *Annual Review of Biochemistry*, *67*(1), 509–544.

van de Linde, S., Endesfelder, U., Mukherjee, A., Schüttpelz, M., Wiebusch, G., Wolter, S., Heilemann, M., & Sauer, M. (2009). Multicolor photoswitching microscopy for subdiffraction-resolution fluorescence imaging. *Photochemical & Photobiological Sciences*, *8*(4), 465–469.

van de Linde, S., Kasper, R., Heilemann, M., & Sauer, M. (2008). Photoswitching microscopy with standard fluorophores. *Applied Physics B*, *93*(4), 725.

Verdet, M. (1869). *Leçons d'optique physique* (Vol. 1). Masson.

Veselago, V. G. (1967). Properties of materials having simultaneously negative values of the dielectric (ϵ) and magnetic (μ) susceptibilities. *Soviet Physics Solid State USSR*, *8*, 2854–2856.

Veselago, V. G. (1968). The electrodynamics of substances with simultaneously negative values of ϵ and μ. *Soviet Physics Uspekhi*, *10*(4), 509–514.

Vijayakumar, A., Kashter, Y., Kelner, R., & Rosen, J. (2016). Coded aperture correlation holography–a new type of incoherent digital holograms. *Optics express*, *24*(11), 12430–12441.

Vijayakumar, A., Katkus, T., Lundgaard, S., Linklater, D. P., Ivanova, E. P., Ng, S. H., & Juodkazis, S. (2020). Fresnel incoherent correlation holography with single camera shot. *Opto-Electronic Advances*, *3*(08), 200004.

Vogelsang, J., Cordes, T., Forthmann, C., Steinhauer, C., & Tinnefeld, P. (2009). Controlling the fluorescence of ordinary oxazine dyes for single-molecule switching and superresolution microscopy. *Proceedings of the National Academy of Sciences*, *106*(20), 8107–8112.

von Diezmann, A., Shechtman, Y., & Moerner, W. (2017). Three-dimensional localization of single molecules for super-resolution imaging and single-particle tracking. *Chemical reviews*, *117*(11), 7244–7275.

Wang, Y., Quan, T., Zeng, S., & Huang, Z.-L. (2012). Palmer: A method capable of parallel localization of multiple emitters for high-density localization microscopy. *Optics express*, *20*(14), 16039–16049.

Weber, H.-J., & Arfken, G. B. (2005). *Mathematical methods for physicists*. Elsevier Academic.

Weng, J., Clark, D. C., & Kim, M. K. (2016). Compressive sensing sectional imaging for single-shot in-line self-interference incoherent holography. *Optics Communications*, *366*, 88–93.

Westphal, V., & Hell, S. W. (2005). Nanoscale resolution in the focal plane of an optical microscope. *Physical review letters*, *94*(14), 143903.

Wilson, T. (1989). Optical sectioning in confocal fluorescent microscopes. *Journal of microscopy*, *154*(2), 143–156.

Wilson, T. (2011). Resolution and optical sectioning in the confocal microscope. *Journal of microscopy*, *244*(2), 113–121.

Winterflood, C. M., Platonova, E., Albrecht, D., & Ewers, H. (2015). Dual-color 3d superresolution microscopy by combined spectral-demixing and biplane imaging. *Biophysical journal*, *109*(1), 3–6.

Wu, Y., & Shroff, H. (2018). Faster, sharper, and deeper: Structured illumination microscopy for biological imaging. *Nature methods*, 1.

Xie, X. S. (1996). Single-molecule spectroscopy and dynamics at room temperature. *Accounts of chemical research*, *29*(12), 598–606.

Xu, J., Tehrani, K. F., & Kner, P. (2015). Multicolor 3d super-resolution imaging by quantum dot stochastic optical reconstruction microscopy. *Acs Nano*, *9*(3), 2917–2925.

Yamaguchi, I., & Zhang, T. (1997). Phase-shifting digital holography. *Optics letters*, *22*(16), 1268–1270.

Yang, B., Chen, X., Wang, Y., Feng, S., Pessino, V., Stuurman, N., Cho, N. H., Cheng, K. W., Lord, S. J., Xu, L., et al. (2019). Epi-illumination spim for volumetric imaging with high spatial-temporal resolution. *Nature methods*, *16*(6), 501.

Zhou, Y., & Carles, G. (2020). Precise 3d particle localization over large axial ranges using secondary astigmatism. *Optics Letters*, *45*(8), 2466–2469.

Zhou, Y., Handley, M., Carles, G., & Harvey, A. R. (2019). Advances in 3d single particle localization microscopy. *APL Photonics*, *4*(6), 060901.

Zhu, L., Zhang, W., Elnatan, D., & Huang, B. (2012). Faster storm using compressed sensing. *Nature methods*, *9*(7), 721.

Zipfel, W. R., Williams, R. M., & Webb, W. W. (2003). Nonlinear magic: Multiphoton microscopy in the biosciences. *Nature biotechnology*, *21*(11), 1369.